Novel Chalcogenide Nanomaterials

Production and Application



Arunvinay Prabakaran

Oriel College

A thesis submitted in partial fulfilment

of the requirements for the degree of

Doctor of Philosophy in Materials

Department of Materials

Trinity Term 2015

Abstract

In this work, chemical vapour deposition (CVD) using chloride precursors has been employed for the synthesis of various nanostructures of tungsten disulphide (WS_2). By tuning the synthesis conditions and precursors, the process was successfully employed for synthesis of 3D nanoflowers of WS_2, 2D WS_2 domains and mixed metal dichalcogenides of Mo and W. The structural evolution of the nanoflowers has been presented along with the composition changes which sheds light on the nucleation and growth mechanism. The presence of few-layered WS_2 along the edges of the nanoflowers was revealed using high resolution microscopy. Various exfoliation techniques were employed to isolate these nanosheets from the nanoflower. Solvent exfoliation produced a cluster of nanosheets with increased amount of edge sites which exhibited excellent catalytic activity for hydrogen evolution reaction (HER) when in combination with commercial fuel cell grade carbon black (BP 2000), shown by studies using a electrochemical setup. The growth of 2D WS_2 domains was also investigated using a similar CVD strategy, as employed for nanoflowers, to study the influence of various parameters such as sulphur sublimation temperature, synthesis temperature, time period, substrates position and precursors on the final deposit. It was observed that the shape, thickness and size of the domains vary within the substrates depending on the growth condition and parameters. The composition-controlled synthesis of $Mo_xW_{1-x}S_2$ was achieved by employing the same atmospheric-pressure CVD using Mo and W chloride precursors. By controlling the sublimation temperature of the precursors it was shown that the growth temperature, which was varied from 650 ˚C to 800 ˚C, dictates the alloy composition with W dopant composition varied from as little as a few percent (x=0.98), to over 50% (x=0.42). This work shows the versatility of the CVD process to produce different morphologies of WS_2- 3D nanoflowers to 2D domains- making it ideal for wide range of applications from catalysis to optoelectronic devices, and could be extended for synthesis of analogous TMD compounds.

Dedication

This thesis is dedicated

To my Amma for dedicating her entire life for my well-being, for her love, care and affection.

To my Dad, for showing me how to lead a respectable and honourable life, silently motivating, guiding and watching over me.

To my wife, Divya, for her love, patience and dedication.

To my son, Vidhyuth Ilamaran, who has brought pure joy and given purpose to all our lives.

To my friends, supervisors, teachers and well-wishers without whom I won't be where I'm today.

And at last the almighty, for providing me this wonderful life and rewarding opportunity.

Eternally grateful



Arunvinay

Acknowledgements

This thesis represents an arduous, intellectually stimulating, joyful, challenging and highly rewarding journey which would not have been possible without the help and support of various generous people and organisations. I acknowledge the financial support received from Felix scholarship which made my study at Oxford possible. Further assistance from Oriel College in the form of hardship grant was gratefully received.

First and foremost, I would like to thank my supervisors Professor Nicole Grobert and Dr Frank Dillon for their patience, encouragement and support throughout my DPhil. Nicole was a wonderful mentor who oversaw my metamorphosis as a researcher and allowed me to take control of my own project. Frank has supported me through the past four years be it for experiments in lab, analysing and discussing the data, talking through my day at the office, a pint at the pub or a banter and laugh, They willed me on to keep improving and always kept their sense of humour even when I lost mine. I'm also thankful l to Professor Kylie Vincent for collaborating with the catalysis work and allowing me to use her lab facilities. I would like to acknowledge and appreciate the outstanding researchers I collaborated with during this project including Dr Matteo Duca, Mr Jonathan Quinson, Mr Vitaliy Babenko, Ms Jude Britton, Dr Rebecca Nicholls, Dr Adrian Murdock, Dr Juan Lozano, Dr Phil Holdway, Dr Alison Crossley, Dr Lewys Jones and Professor Peter Nellist. It was a pleasure working together and learning from them. It was an incredible opportunity for me to work with great microscopists who helped study my sample. I acknowledge Dr Lewys Jones, Dr Rebbecca Nicholls, Ms Jude Britton, Dr Juan Lozano and Dr Adrian Murdock for providing their valuable expertise and time to obtain brilliant high

resolution transmission electron microscopy images. I would also like to thank Dr Neil Young, Mrs. Gabriella Chapman, Mr. Greg Cook, Dr Gareth Hughes and Dr Colin Johnston for training me on various characterisation techniques and providing technical support. My sincere thanks to, Dr Adrian Murdock, Dr Frank Dillon, Dr. Juan Lozano and Dr. Shayan Meysami and Professor Nicole Grobert for reviewing my thesis and providing very useful feedback which significantly shaped the document to its current form. I would also like to thank the members of Nanomaterials by Design for their valuable scientific discussions and friendship over the years. I'm was lucky to be part of such a diverse, thoughtful, fun-loving and friendly research group.

To all the amazing people I met and friends I made at Oxford who made my life here so memorable. It has been an absolute honour and privilege to have had the opportunity to get to know them. A special mention to Oriel MCR where I made numerous friends, my cricket club Oxenford where I spent most of weekends in summer playing and my home 11 Norham Gardens which provided me a wonderful community to be part of, which I would I cherish through my life and stay in touch with. I'm indebted to all the wonderful friends who have willed me on with their love, care and amazing food. Amogh, Usha and Abhilasha deserve a special mention.

Finally, I'm eternally grateful to my family, my Amma and Dad, for providing me the best of everything in life. I wouldn't be where I'm today without their love, sacrifices, unwavering support and encouragement. I'm also indebted to my fiancée Divya Seshadri for taking up this long and often pain-staking journey with me, for her never ending love, encouragement, support and understanding through the hard times. I'm very excited for our future together. My gratitude also goes to all my previous teachers who have inspired and moulded me to be the individual I'm today.

Contents

Abstract i
Dedication ii
Acknowledgements iii
Contents v
List of figures viii
List of tables xx
List of publications xxii
Chapter 1. Introduction 1
1.1. Outline 1
1.2. Plan of thesis 2
1.3. Literature Review 4
1.3.1. Layered Transition Metal Dichalcogenides (TMDs) 4
1.3.2. Insight into inorganic nanostructures of WS_2 and MoS_2 8
1.3.3. Synthesis of inorganic nanostructures 13
1.3.3.1. Synthesis of Inorganic Fullerene-like nanoparticles, Inorganic Nanotubes, Nanoflowers and other forms of WS_2 and MoS_2 17
1.3.3.2. Synthesis of Inorganic Graphene Analogues (IGAs) 29
1.3.4. Properties of inorganic nanostructures 41
1.3.4.1. Electronic Properties 42
1.3.4.2. Mechanical Properties 44
1.3.4.3. Tribological Properties 47
1.3.5. Application of inorganic nanostructures 47
1.3.5.1. Electronic Applications and Devices 48
1.3.5.2. Optoelectronic devices 50
1.3.5.3. Sensing, Catalysis and Electrochemical applications 52
1.4. Summary 54
Chapter 2. Chemical vapour deposition of tungsten disulphide (WS_2) nanoflowers 56
2.1. Introduction 56
2.2. Experimental 57
2.3. Results and Discussion 59
2.3.1. Parameters for synthesis of WS_2 nanoflowers using CVD 59
2.3.2. Diameter distribution of WS_2 nanoflowers 63
2.3.3. Characterisation of WS_2 nanoflowers 65
2.3.3.1. Electron microscopy 65

2.3.3.2. XRD of WS_2 nanoflowers 66
2.3.3.3. Raman spectroscopy of WS_2 nanoflowers 67
2.3.4. Dissection of WS_2 nanoflowers using Focussed Ion Beam (FIB) 68
2.3.5. Evolution of nanoflower structure 69
2.3.6. Nucleation and growth mechanism for nanoflower formation 73
2.3.7. Structural investigation of nanoflowers using Scanning Transmission Electron Microscopy (STEM) 77
2.3.8. Deposits inside the quartz tube 79
2.4. Conclusion 82
Chapter 3. Exfoliation of nanoflowers and their use in catalysis of hydrogen evolution reaction (HER) 83
3.1. Introduction 83
3.2. Experimental 86
3.3. Results and Discussion 89
3.3.1. Mechanical grinding of WS_2 nanoflowers 89
3.3.2. Liquid exfoliation of WS_2 nanoflowers 95
3.3.2.1. Liquid exfoliation using sodium dodecylsulphonate (SDS) as surfactant 96
3.3.2.2. Liquid exfoliation using sodium cholate (SC) as surfactant 99
3.3.3. Exfoliation of WS_2 nanoflowers by sonication in simple solvents 102
3.3.4. Electrochemical studies for hydrogen evolution reaction (HER) 105
3.3.4.1. Linear sweep voltammetry 106
3.3.4.2. Electrochemical impedance spectroscopy 109
3.3.4.3. Cyclic voltammetry 111
3.4. Conclusion 112
Chapter 4. Growth study of two-dimensional WS_2 by Chemical Vapour Deposition (CVD) 113
4.1. Introduction 113
4.2. Experimental 114
4.3. Results and Discussion 118
4.3.1. Influence of sulphur sublimation temperature 118
4.3.2. Influence of synthesis temperature 125
4.3.3. Influence of substrates position 126
4.3.4. Influence of synthesis time 128
4.3.5. Influence of substrate 129
4.3.6. Influence of precursors 137
4.4. Conclusion 140

Chapter 5. Mixed transition metal dichalcogenide $Mo_xW_{1-x}S_2$ alloy synthesis by Chemical Vapour Deposition (CVD) 142
5.1. Introduction 142
5.2. Experimental 143
5.3. Results and Discussion 147
5.3.1. Growth of mixed metal dichalcogenides using single stage furnace. 147
5.3.1.1. Molar ratio 1:3 of WCl_6:$MoCl_5$ precursors 147
5.3.1.2. Molar ratio 1:1 of WCl_6:$MoCl_5$ precursors 148
5.3.1.3. Molar ratio 3:2 of WCl_6:$MoCl_5$ precursors 153
5.3.1.4. Molar ratio 3:1 of WCl_6:$MoCl_5$ precursors 156
5.3.1.5. Summary of single stage furnace 158
5.3.2. Growth of mixed metal dichalcogenides using two stage furnace 159
5.3.2.1. SEM of deposits from 2-stage furnace 160
5.3.2.2. Raman Spectroscopy of mixed metal dichalcogenides 161
5.3.2.3. Electron microscopy of mixed metal dichalcogenides 162
5.3.2.4. X-ray Photoelectron Spectroscopy of substrates 165
5.3.2.5. STEM imaging of mixed metal dichalcogenides 167
5.4. Conclusion 168
Chapter 6. Summary and Future Work 170
6.1. Summary of research 170
6.2. Future work 173
6.2.1. Upscaling synthesis of nanoflower morphology 173
6.2.2. Improved electrocatalysts for HER 174
6.2.3. Low-pressure CVD to form thin films 175
6.2.4. Control of atomic percentage and formation of 2D TMD alloys 176
Bibliography 177
Appendix 194
Dissection of nanoflowers using FIB 194
Growth of nanoflowers on carbon paper 194
HER activity using different proportions of catalysts+BP 195
HER activity using rotation of electrode hosting catalysts+BP 196
Sulphurisation of metal foils 197
Exfoliation using PMMA 199
Exfoliation using scotch tape 200
Sulphurisation of metal oxide templates 201
Raman spectroscopy of blank substrates and bulk powders 205

List of figures

Figure 1. Layered structure of graphite and WS_2. The graphite is composed of stacking of single layers in which the bonding between the carbon atoms is sp^2. The repeating motif in WS_2 is a sandwich of three layers S-W-S with covalent tetrahedral W-S bond.[39] 4

Figure 2. About 40 different layered TMD compounds exist. The transition metals and the three chalcogen elements that predominantly crystallise in those layered structure are highlighted in the periodic table. Partial highlights for Co, Rh, Ir and Ni indicate that only some of the dichalcogenides form layered structures. Reproduced with permission from Nature Chemistry.[42] 5

Figure 3. Summary of the stability analysis and semiconducting properties of 44 different TMD (MX_2) compounds with transition metal indicated by M divided into 3d, 4d and 5d groups.MX_2 compounds shaded light gray form neither stable H (2H-MX_2) nor T (1T-MX_2) structure. In each box, the lower lying structure (H or T) is the ground state. The resulting structures (T or H) can be half metallic (+), metallic (*), or semiconducting (**) with direct or indirect band gaps. Reproduced with permission.[48] 7

Figure 4. Electron micrographs of polyhedral crystals of WS_2. a) Spheroidal crystal; b) Stir-bar crystal. The spacing between fringes is 0.615±0.005 nm, which agrees with the distance between two neighbouring layers (c/2) of WS_2. Scale bar is 10 nm. Reproduced with permission.[3] 8

Figure 5. (a) Structures constructed from a hexagonal MoS_2 monolayer: triangle faces cut in two possible ways, (b) the ideal apex (with a square-like defect) of stoichiometric MoS_2 fullerene, (c) the DFTB-optimized structure of an $(MoS_2)_{576}$ fullerene, which degraded to $Mo_{576}S_{1140}$, and (d) the structure of $Mo_{576}S_{1140}$ fullerene after an MD simulation at 300K. Mo red, S yellow.[47] 10

Figure 6. (a) TEM images of a three layer nano-octahedron at various tilt angles and; (b) corresponding views of the model structures of an $(MoS_2)_{784}$,$(MoS_2)_{1296}$ and $(MoS_2)_{1936}$ fullerene. The similarity between the experimentally observed and model structures is evident. Reproduced with permission.[47] 10

Figure 7. i) Armchair (8,8) MoS_2 nanotube (left) and zigzag (14,0) MoS2 nanotube (right). ii) MoS_2 nanotube tips a) zigzag (12,0) tube closed with three square-like defects. B) Armchair (8,8) tube closed with four square-like defects and one octagonal-like defect c) square-like defect. d) octagonal-like defect. Light atoms are S; dark atoms are Mo. Reproduced with permission.[11] 11

Figure 8. c-Axis and section view of a single-layer TMD with trigonal prismatic (a) and octahedral (b) coordinations. Atom colour code: purple, metal; yellow, chalcogen. The labels AbA and AbC represent the stacking sequence where the upper- and lower-case letters represent chalcogen and metal elements, respectively. Reproduced with permission from Nature Chemistry.[42] 12

Figure 9. (a) The atomic structure of layered MoS_2. Different sheets of MoS_2 are composed of three atomic layers S−Mo−S, where Mo and S are covalently bonded. (b) A top view of the honeycomb lattice, emphasizing the inversion symmetry breaking. Reproduced with permission.[48,61] 13

Figure 10. a) Schematic of the fluidised bed reactor, b) temperature profile along furnace (z) axis. Reproduced with permission.[69] 18

Figure 11. SEM images of WS_2 products obtained at 600 °C (a–c) and 500 °C (d). Reproduced with permission.[81] 21

Figure 12. TEM images and SAED pattern (inset) of the WS2 nanosheets. Reproduced with permission.[81] 22

Figure 13. WS_2 nanobuds: (a) an early stage of growth with typically elongated thin walled buds along the nanotube support, which serves as a reservoir of material. The nanotube grow in the relaxed hexagonal 2Hb stacking (inset). (b) Some faceted nanoparticles joined to the supported thin-walled nanotube with their V-shaped parts. (c) The final stage of growth with nearly spherical thick-walled fullerenes. Reproduced with permission.[32] 23

Figure 14. A schematic top view of PACVD experimental setup. Two evaporation ovens for S and $MoCl_5$ (T=150ºC) are used. Vapours are flushed with argon and led through the main oven (T_{max}-460ºC). In the main oven reaction gases H_2 and H_2S are admixed to allow MoS_2 formation. The reaction mixture flows into the reactor chamber and nanoparticles are collected on a silicon substrate. Reproduced with permission.[101] 24

Figure 15. Schematic of the quartz glass set up used for MOCVD. Reproduced with permission.[77] 26

Figure 16. SEM images of WS_2 a) Low magnification and b) high magnification SEM images of WS_2 nanoflowers c, d) SEM images of WS_2 nanotubes. Reproduced with permission.[28] 28

Figure 17.SEM images of MoS_2 a) nanoflowers b) nanotubes. Reproduced with permission.[28] 28

Figure 18. Schematic of main liquid exfoliation method mechanisms. A. Ion intercalation. Ions (yellow spheres) are intercalated between the layers in a liquid enviquid environment, swelling the crystal and weakening the interlayer attraction. Then, agitation (such as shear, ultrasonification, or thermal) can completely separate the layers, resulting in an exfoliated dispersion. B. Ion exchange. Some layered compounds contain ions between the layers so as to balance surface charge on the layers. These ions (red spheres) can be exchanged in a liquid environment for other, often large ions (yellow spheres). As above, agitaion results in exfoliated dispersion. C. Sonification-assisted exfoliation. This layered crystal is sonicated in a solvent, resulting in exfoliation and nanosheets formation. In "good" solvants-those with the appropriate surface energy-the exfolaited nanosheets are stabilised against reaggregation. Otherwise, for "bad" solvents, regarregation and sedimentation wll occur. Reproduced with permission.[111] 31

Figure 19. HRTEM images of MoS_2 (a), WS_2 (b), and BN (c) nanosheets. The insets show the corresponding electron diffraction images. The scale bars are 100, 50, and 200 nm, respectively. d–f) Atomic resolution HRTEM images. Reproduced with permission.[84] 32

Figure 20. Schematic of the electrochemical lithiation process for the synthesis of 2D nanosheets from layered bulk materials. The cut-off voltage used to optimize the electrochemical lithiation conditions for preparations of few-layer TMDs is indicated. Reproduced with permission.[115] 33

Figure 21. a) Schematic of method for the growth of a MoS_2 monolayer, also on a substrate (sample) from MoO_3 and S powders through a gas-phase reaction.[118]; b) Wafer-scale deposition of mono- to few-layered MoS_2 films obtained by direct sulfurization of MoO_3 thin films, and their transfer onto arbitrary substrates. Reproduced with permission.[119] 35

Figure 22. a) Schematic of the synthesis and cleavage of MoS_2. b), c) Pictures showing the as-synthesised MoS_2/MoO_2 layers on SiO_2/Si wafer and the peeled off MoS_2 layers after removing MoO_2 with atomic force microscope images as insets. Reproduced with permission.[120] 36

Figure 23. Large-grain MoS_2 growth. a. Optical reflection image of a CVD growth of a typical large-grain MoS_2 on SiO_2 (285nm)/Si substrate. b, Optical image of a monolayer MoS_2 triangle. Reproduced with permission.[86] 37

Figure 24. SEM images showing the growth of MoS2 from small triangles to continuous film. Reproduced with permission.[87] 37

Figure 25. Schematic of MoS_2 layer deposited by two-step thermolysis, and the films obtained on a sapphire and silica substrate. Reproduced with permission.[125] 38

Figure 26. a) CVD of ultrathin TMDs by vaporization and decomposition of a single precursor in solution and (b) by vaporization and decomposition of metal and chalcogen precursors in solid forms. Reproduced with permission.[42] 39

Figure 27. a) Schematic of the experimental setup used for the synthesis of WS_2 films involving high temperature treatments under a sulphur/argon environment at low pressures (450 mTorr). b) Schematic of PMMA assisted transfer method onto different substrates. Reproduced with permission.[88] 40

Figure 28. Atmospheric pressure CVD synthesis of large-area WS_2 crystal domains on the SiO_2/Si substrate. (a) Schematic of the corresponding CVD experimental set-up with a highlighted WS_2 reaction chamber (black dashed line). (b) Temperature profiles employed for formation of WS_2 on the SiO_2/Si substrate with sulphur introduced at 0, -10 and -20 min due to the target reaction temperature of 1070 ^oC/ 860 ^oC. (c) Photo of large triangular WS_2 crystals deposited on a 2 cm SiO_2/Si substrate. (d and e) Zoom-in images chosen from the selected area (red dashed line) in (c) and (blue dashed line) in (d), respectively, showing triangular WS_2 domains. Reproduced with permission.[126] 40

Figure 29. (A) Calculated band structures of (a) bulk MoS_2, (b) quadric-layer MoS_2, (c) bi-layer MoS_2, and (d) monolayer MoS_2. (B) Photoluminescence spectra normalized by Raman intensity for MoS_2 layers with different thickness. (C) Raman spectra of thin-layer and bulk MoS_2 films. (D) Frequencies of E^1_{2g} and A_{1g} Raman modes (left vertical axis) and their difference (right vertical axis) as a function of layer number. Reproduced with permission.[131] 43

Figure 30. Sample preparation and the measurement method a) Optical image of a monolayer MoS_2 flake transferred onto a prepatterned SiO_2 substrate; b) AFM image of the same single layer MoS_2 as in part c) schematic of the indentation experiment. Reproduced with permission.[138] 46

Figure 31. Schematic of HfO_2-top-gated monolayer MoS2 FET device c, Integrated circuit based on single-layer MoS2. Figure reproduced with permission.[63] 49

Figure 32. A five-stage ring oscillator based on bilayer MoS2. (a) Schematic of the electronic circuit of the five-stage ring oscillator. (b) Optical micrograph of the ring oscillator constructed on a bilayer MoS2 thin film. Reproduced with permission.[149]50

Figure 33. Current and proposed optoelectronic devices. a, Atomic force microscopy image of MoS_2 monolayer flake (left) and optical microscopy image of this flake made

into a device with metal contacts (right). b, Proposed solar-cell device with parallel structures that may be fabricated using lift-off and printing techniques for patterning the semiconductor layers and a micro- or nanophotonic spectrum-splitting layer. The various bandgaps available from the different TMDCs are promising for use in such multi-junction photovoltaic devices. Reproduced with permission.[63] 51

Figure 34. (A) Optical image of a bilayer (2L) MoS_2 deposited onto a Si substrate coated with 300 nm thick SiO_2. (B) Optical image of a FET device fabricated with the 2L MoS_2 film shown in (A), where Au electrodes work as the source and drain electrodes, and SiO_2 acts as the back gate. (C) Photograph of a fabricated flexible TFT array based on rGO electrodes and MoS_2 channel. Reproduced with permission.[162] 52

Figure 35. Schematic of experimental setup for chemical vapour deposition of WS_2 nanoflowers..... 58

Figure 36. SEM chart showing the nanoflower morphologies obtained with rapid cooling/ quenching at various temperature (left axis) and time period (x axis). 61

Figure 37. SEM chart showing the nanoflower morphologies obtained with controlled cooling at various temperature (left axis) and time period (x axis). 62

Figure 38. Average diameter distribution of nanoflowers with changes in temperature, time and cooling conditions. 64

Figure 39. SEM micrograph showing non-homogenous growth of nanoflowers with increase in synthesis time 30 min. 64

Figure 40. SEM micrograph showing homogenous growth of nanoflowers with increase in synthesis time period to 1 hour. 64

Figure 41. a) SEM micrograph of nanoflower b) TEM micrograph of a flake/ petal from the nanoflower obtain by dissociating it using sonication for 1 min. 65

Figure 42. XRD of nanoflower deposits annealed at 850 ^oC showing characteristic peaks of crystalline WS_2 phase. 66

Figure 43. Raman spectroscopy of nanoflowers deposits annealed at 850^oC showing characteristic first order peaks and second order peaks corresponding to WS_2. 67

Figure 44. FIB cross section of nanoflower morphology showing the core of the 3D structures. 68

Figure 45. Scanning and Transmission electron micrographs showing the changes in morphology of the nanoflowers with variation in synthesis time, temperature and cooling conditions. 69

Figure 46. TEM micrographs showing the nanoflowers with rolled up flakes and higher magnification show curling of the flakes as pointed by the arrow. 70

Figure 47. SEM micrographs showing (a) homogenous distribution of nanoflower with nanowires on silicon substrates; b) nanowires grown on nanoflower morphology... 70

Figure 48. TEM micrographs of nanoflowers with nanowires growing on them..... 71

Figure 49. a) TEM micrograph showing nanowires; b) High magnification TEM of nanowires showing lattice fringe. 71

Figure 50. EDX mapping of nanowires found on nanoflowers under TEM showing elemental mapping of tungsten, oxygen and sulphur. 72

Figure 51. EDX mapping show the difference in composition of a flake and nanowire under TEM using elemental maps of tungsten, oxygen and sulphur. 73

Figure 52. Evolution of nanoflower structure with progress in time periods from 10s to 1800s at 850ºC 74

Figure 53. XRD of deposits deposits nucleating at various time periods from 10 s to 1800 s at 850 ºC which would form nanoflowers eventually. 75

Figure 54. Raman spectroscopy of deposits nucleating at various time periods from 10 s to 1800 s at 850 ºC which would form nanoflowers eventually. 76

Figure 55. Schematic of WS_2 crystal structure along with models depicting the atomic arrangement of the lattice along different axes. 77

Figure. 56 STEM image showing stacked layers in the petals of nanoflowers dissociated by sonication 78

Figure. 57 STEM image showing few-layered WS_2 at edges in WS_2 nanoflower after dissociation. 79

Figure 58. SEM micrograph of deposits obtained on the inside walls quartz tube in which the synthesis is carried out. 80

Figure 59. XRD of deposits inside quartz tube showing presence of WS_2 and $WO_3.H_2O$ phases. 81

Figure 60. Surface analysis of deposits inside quartz tube using BET indicating type IV mesoporous structures. 81

Figure 61. TEM micrographs of mechanically grinded WS_2 nanoflowers showing, a) agglomerates of crushed nanoflowers; b) cluster of exfoliated flakes; c) agglomerate of thin broken up flakes d) exfoliated large thin flakes (the ideal morphology). 90

Figure 62. TEM micrographs and SAED patterns of thin regions obtained by mechanically grinding WS_2 nanoflowers showing the presence of a) amorphous regions b) crystalline regions. 91

Figure 63. EDX spectrum along with elemental composition of thin regions obtained by mechanically grinding WS_2 nanoflowers showing a) presence of SiO_2 along with, b) WS_2 regions. 91

Figure 64. STEM image of thin regions of exfoliated WS_2 seen as islands of crystalline regions (pointed by arrows) supported on amorphous SiO_2 obtained by mechanically grinding of WS_2 nanoflowers. 92

Figure 65. Intensity profile measured on a STEM image across the thin regions of WS_2 on amorphous SiO_2 obtained by mechanically grinding WS_2 nanoflowers 93

Figure 66. STEM image and its false coloured form to differentiate mono-, bi-, and tri-layer regions supported on amorphous SiO_2 obtained by mechanically grinding WS_2 nanoflowers. 94

Figure 67. STEM images of exfoliated regions obtained by mechanically grinding WS_2 nanoflowers: a) agglomerates of exfoliated flakes, and b) cluster of thin regions. ... 95

Figure 68. Schematic of the sonication assisted exfoliation of WS_2 nanoflowers 95

Figure 69. Liquid exfoliation using sodium dodecyl sulfonate (SDS) as surfactant of WS_2 nanoflowers at various tip sonication times as specified in the micrograph. The highlighted regions are contamination. 97

Figure 70. High-resolution TEM micrographs of liquid exfoliated WS_2 nanoflowers using sodium dodecyl sulfonate (SDS) as surfactant for 30 min under the tip sonication showing a) broken up pieces on flakes on thin regions; b) contamination at the edges. 98

Figure 71. EDX spectrum along with elemental composition of liquid exfoliated nanoflowers using sodium dodecyl sulfonate (SDS) as surfactant after 30 min of tip sonication confirming WS_2 composition along with the presence of other elements possibly contamination. 98

Figure 72. Liquid exfoliation using sodium cholate (SC) as surfactant of WS_2 nanoflowers subjected to tip sonication for different time periods as highlighted in the micrograph. 99

Figure 73. High-resolution TEM micrographs of liquid exfoliated WS_2 nanoflowers using sodium cholate (SC) as surfactant for 30 min under the tip showing a) crystalline flakes with diffraction pattern as inset showing hexagonal packing, b) contamination of amorphous layer at edges. 100

Figure 74. EDX spectrum along with elemental composition of liquid exfoliated nanoflowers using sodium cholate (SC) as surfactant after 30 min of tip sonication confirming the WS_2 composition. 100

Figure 75. TEM micrographs of undesirable morphologies formed by liquid exfoliation using aqueous surfactant of WS_2 nanoflowers which include a) agglomerates; b) rolled up nanoflowers; c) rolled up exfoliated flakes; d) contaminations accumulating on flakes. 101

Figure 76. TEM micrographs showing a) cluster of exfoliated flakes, b) edges of exfoliated flakes; HRTEM micrographs showing c) few-layered thick edges, d) lattice and crystal packing of flakes exfoliated using ethanol/water with tip sonication for 15 min. 103

Figure 77. EDX spectrum along with elemental composition of nanoflowers exfoliated using simple solvent with tip sonication for 15 min confirming the WS_2 composition. 103

Figure 78. STEM micrographs of WS_2 nanoflowers exfoliated using simple solvent with tip sonication for 15 min showing the presence of a), b) cluster of exfoliated thin flakes; c), d) thin exfoliated regions showing abundance of edges. 104

Figure 79. a) Polarization performance curves and b) the corresponding Tafel curves and slope obtained in 0.5M H_2SO_4 for various electrocatalysts 108

Figure 80. Nyquist plots showing the electrode kinetics of exfoliated WS_2 nanoflowers with BP at -0.36V vs RHE..... 110

Figure 81. Durability test of WS_2 NF Ex+BP electrocatalysts using cyclic voltammetry curves obtained by continuous cycling, with in the first and after 100 cycles showing minimal change in performance. 111

Figure 82. a) Schematic of experimental setup for two stage furnace chemical vapour deposition setup; b) Temperature profile of furnaces separated by 3 cm and maintained at 250 ^oC and 800 ^oC..... 115

Figure 83. (1) SEM micrographs showing change in nucleation density with sulphurisation temperature a) 300 ºC, e) 250 ºC, i) 200 ºC ; (2) SEM micrographs showing morphology of 2D deposits obtained at sulphur sublimation temperatures of b) 300 ºC, f) 250 ºC, j) 200 ºC; (3) AFM results of individual flakes obtained at sulphurisation temperature of c) 300 ºC, g) 250 ºC, k) 200 ºC; (4) AFM profile obtained across the region shown in (3) at sulphurisation temperatures of d) 300 ºC, h) 250 ºC, l) 200 ºC with sulphurisation temperatures specified along the left axis ... 119

Figure 84. SEM micrographs of deposits produced at sulphur sublimation temperature of 300 ºC with synthesis temperature of 850 ºC on silicon substrates along with schematic showing the growth of isolated domains and 3D flakes from the domains. 120

Figure 85. Schematic of three basic growth modes: (a) layer-by-layer growth mode; (b) island growth mode; and (c) Stranski–Krastanov mode. Reproduced with permission. ref. [215] 122

Figure 86. SEM micrographs of deposits obtained at sulphur sublimation temperature of 350 ºC showing the presence of 3D wire-like structures. 123

Figure 87. Raman spectroscopy representing deposits at different sulphur sublimation temperature with synthesis temperature of 850 ºC on silicon substrates revealing presence of WS_2. 124

Figure 88. XRD pattern of deposits obtained at 300 ºC sulphur sublimation temperatures with synthesis temperature of 850 ºC on silicon substrates showing the presence of WS_2 crystal phase. 124

Figure 89. a) Experimental setup showing the variation in synthesis temperature and position of precursors; SEM micrographs of deposits produced at sulphur sublimation temperature of 250 ºC with different synthesis temperature of b) 900 ºC, c) 800 ºC, d) 750 ºC, e) 600 ºC on silicon substrates. 126

Figure 90. (i) Temperature of furnace showing the position of substrates; (ii) SEM micrographs of deposits produced at sulphur sublimation temperature of 250 ºC with synthesis temperature of 800 ºC and 850 ºC with silicon substrates at positions of (a) 44.5 cm, (b) 47 cm, (c) 49.5 cm which would be 5 cm, 7.5 cm, 10 cm with respect to precursor respectively. 127

Figure 91. SEM micrographs of deposits produced at sulphur sublimation temperature of 250 ºC with synthesis temperature of 800 ºC and 850 ºC showing increase in thickness of domains and formation of 3D flakes with longer synthesis time. 128

Figure 92. SEM and optical micrographs of deposits produced on silicon and sapphire substrates exposed to the same synthesis condition with sulphur sublimation temperature from 100-250 ^{o}C. 131

Figure 93. Raman spectroscopy of deposits on different substrates with sulphur sublimation temperature of 150 ^{o}C and synthesis temperature of 850 ^{o}C for 1 hours showing peaks corresponding to WS_2. 132

Figure 94. Raman spectroscopy of deposits on sapphire substrate with different sulphur sublimation temperature with synthesis temperature of 850 ^{o}C for 1 hour indicating the softening of the A_{1g} mode which could represent reduction in thickness..... 133

Figure 95. AFM topography and profile of bi-layer WS_2 deposits produced at sulphur sublimation temperature of 150 ^{o}C with synthesis temperature of 850 ^{o}C on 300 nm SiO_2/Si substrate. 134

Figure 96. AFM topography and profile of multilayer WS_2 deposits produced at sulphur sublimation temperature of 150 ^{o}C with synthesis temperature of 850 ^{o}C on 300 nm SiO_2/Si substrate. 135

Figure 97. AFM topography and profile of multilayer WS_2 deposits produced at sulphur sublimation temperature of 150 ^{o}C with synthesis temperature of 850 ^{o}C on sapphire substrate. 136

Figure 98. AFM topography and profile of multilayer WS2 deposits produced at sulphur sublimation temperature of 125 ^{o}C with synthesis temperature of 850 ^{o}C on sapphire substrate. 136

Figure 99. EDX results of 80% pure colloidal sulphur precursor 138

Figure 100. SEM micrographs WS_2 deposits produced at sulphur sublimation temperature of 150 ^{o}C with synthesis temperature of 850 ^{o}C on silicon substrate using 99.5% sulphur. 139

Figure 101. WS_2 deposits produced at sulphur sublimation temperature of 150 ^{o}C with synthesis temperature of 850 ^{o}C using 99.5% sulphur, a) on silicon substrates; b) on sapphire substrates, c) AFM image of deposit on sapphire substrate; d) profile of deposit on sapphire substrate. 140

Figure 102. Schematic of experimental setup using single zone furnace and different proportion of chloride precursor mixed together. 144

Figure 103. a) Schematic of experimental setup for two stage furnace chemical vapour deposition setup for synthesis of mixed chalcogenides; b) Temperature profile of furnaces separated by 3 cm and maintained at 250 ºC and 800 ºC. 145

Figure 104. a) SEM micrograph of thick deposits formed on silicon substrates b) SEM micrograph of nanoflower morphology c) Raman spectroscopy showing MoS2 peaks d) XRD showing MoS2 crystal phase obtained by using mixed in the molar ratio of 1:3 148

Figure 105. a) SEM micrograph of mixture of morphologies consisting of flowers and flakes b) SEM micrograph of spiral-like structures along with nanoflowers and flakes; c) XRD showing peak matching for both WS_2 and MoS_2; d) Raman spectroscopy showing MoS_2 first order modes e) Raman spectroscopy showing MoS_2 first order modes along with WS_2 E_{2g} peak in addition to second order peaks obtained by using mixed in the molar ratio of 1:1. 150

Figure 106. TEM and EDX of MoS_2 nanoflowers obtained on silicon substrates by using CVD with $WCl_6$and $MoCl_5$ mixed in the molar ratio of 1:1. 151

Figure 107. TEM and EDX of flakes obtained on silicon substrates by using CVD with $WCl_6$and $MoCl_5$ mixed in the molar ratio of 1:1. 151

Figure 108. TEM and EDX of spiral structures obtained on silicon substrates by using CVD with $WCl_6$and $MoCl_5$ mixed in the molar ratio of 1:1. 152

Figure 109. a) SEM micrograph of mixture of morphologies of nanoflowers and platelet-like structures b) SEM micrograph of platelet-like structures; c) XRD showing peak matching for both WS_2 and MoS_2; Raman spectroscopy showing d) MoS_2 first order modes e) MoS_2 first order modes along with WS_2 E_{2g} peak obtained by using mixed in the molar ratio of 3:2. 154

Figure 110. TEM and EDX of nanoflowers obtained on silicon substrates by using CVD with $WCl_6$and $MoCl_5$ mixed in the molar ratio of 3:2. 155

Figure 111. TEM and EDX of platelet-like structures obtained on silicon substrates by using CVD with $WCl_6$and $MoCl_5$ mixed in the molar ratio of 3:2. 156

Figure 112. a) SEM micrograph of cluster nanoflowers on silion substratesb) SEM micrograph of nanoflowers; c) XRD showing peak matching for both WS_2 and MoS_2 in addition to MoO_3; d) Raman spectroscopy showing WoS_2 first order modes along with MoO_3 peak obtained by using mixed in the molar ratio of 3:1. 157

Figure 113. SEM micrographs of deposits showing flakes obtained on silicon substrates maintained at different positions and growth temperatures by using CVD in a two stage furnace. 161

Figure 114. Raman Spectroscopy of deposits obtained on silicon substrates by using CVD in a two stage furnace showing the presence of first order of both MoS_2 and WS_2 peaks indicating formation of $Mo_{1-x}W_xS_2$ 162

Figure 115. TEM micrographs of deposits on different silicon substrates maintained at different positions obtained by using CVD in a two stage furnace. 163

Figure 116. EDX results indicating the atomic percentage of Mo and W of mixed metal dichalcogenide flakes obtained on different substrates by using CVD in a two stage furnace. 164

Figure. 117. XPS spectra of deposits at various points on silicon substrates showing the variation of W peaks along the furnace with different growth temperature. 166

Figure 118. STEM images indicating Mo and W atoms in mixed chalcogenide flakes obtained by using CVD in a two stage furnace of substrates a) S_{800u}; b) S_{800d}; c) S_{750} and d) S_{650}. 168

Figure 119. 3D MoS2/Graphene framework and its electrocatalytic activity for HER. Reproduced with permission.[235] 174

Figure 120. Optical micrographs of MoS_2 deposits under different total pressure of system along with their Raman spectra. Reproduced with permission.[214] 175

Figure 121. Schematic of proposed CVD setup for synthesis of 2D TMD alloys .. 176

List of tables

Table 1.Electronic Character of different layered TMDs. Reproduced with permission from Nature Chemistry. ref. 42 6

Table 2. Summary of synthesis processes employed to form different inorganic nanostructures 17

Table 3. Mechanical properties of strong materials reproduced from Kaplan-Ashiri 2005 & 2007 (ref.133, 135). 45

Table 4. Electrochemical impedance spectroscopy measurements giving charge transfer resistance of various catalysts measured at -0.41V vs RHE. * Fitting is poor and the Nyquist plot tends to become a straight line. 110

Table 5. Summary of morphologies, phases and atomic percentage of W obtained by varying the molar ratio of WCl_6:$MoCl_5$ 159

List of publications

Publications

- A Prabakaran, F Dillon, J Melbourne, L Jones, RJ Nicholls, P Holdway, J Britton, AA Koós, A Crossley, PD Nellist, N Grobert, "WS_2 2D nanosheets in 3D nanoflowers", Chemical Communications **50**, 12360-12362 (2014).

Manuscripts in preparation

- A Prabakaran, M Ducca, J Lozano, J Quinson, F Dillon, K Vincent, N Grobert, "WS_2 nanoflowers and its exfoliated forms as catalysts for hydrogen evolution reaction", *to be submitted*
- A Murdock, A Prabakaran, J Lozano, F Dillon, N Grobert, "Mixed metal dichalcogenides synthesis using CVD" *in preparation*.

Talks

- A Prabakaran, J Melbourne, F Dillon, L Jones, R Nicholls, J Britton, P D Nellist, N Grobert, "Novel Chalcogenide nanostructures**"** Flatland Beyond Graphene, Bremen, Germany, 21 June 2013.
- A Prabakaran, J Melbourne, F Dillon, N Grobert, "Novel chalcogenide nanostructures**"** 2nd Year Talk, Oxford Materials, Oxford, UK, 28 February 2013.

Posters

- A Prabakaran, J Melbourne, F Dillon, L Jones, R Nicholls, J Britton, P D Nellist, N Grobert," Novel Chalcogenide nanostructures**",** 3rd year poster competition, Oxford Materials, Oxford, UK, 20 February 2014.
- A Prabakaran, J Melbourne, F Dillon, L Jones, R Nicholls, J Britton, P D Nellist, N Grobert," Novel Chalcogenide nanostructures**",** *NanoteC 12*, Brighton – United Kingdom, 29.8 – 1.9.2012

Chapter 1. Introduction

1.1. Outline

The discovery of fullerenes by Kroto, Smalley and Curl[1] in 1985 and carbon nanotubes by Iijima[2] in 1991, initiated a revolution in material science. Equally important was the discovery of inorganic nanostructures in 1992 by Tenne[3] in the form of WS_2 inorganic nanotubes (INTs)[4] and inorganic fullerene-like nanoparticles (IFs)[5]. Since then, numerous new IF and INT have been synthesised using different precursors such as metal oxides,[6, 7] metal halides,[8] and metal chalcogenides.[9] MoS_2 and WS_2 are the most investigated of the non-carbon nanostructures owing to their semiconducting properties,[10,11] amongst others which include super catalytic behaviour[12–14] and tribological properties[15,16]. These properties coupled with high stability at normal conditions could cater to a wide range of promising applications such as solid lubrications,[16–19] solid-state secondary lithium battery cathodes,[20,21] industrial catalysts for hydro-desulfurization of crude oil,[22–24] hydrogen storage,[25] scanning probe microscopy tips,[26,27] and nanocomposites[28]. Currently commercial quantities of IFs, INTs nanostructures of WS_2 and MoS_2 are synthesised using template metal oxide precursors by companies such as ApNanoMaterials, Inc.[29] In addition to these well-studied morphologies, the MS_2 (M=W, Mo) compounds have been synthesised in other less known forms such as nanoflowers,[30,31] nanoribbons,[32,33] nanobuds,[34] and nanocubes.[35] Nevertheless, to exploit the properties of these nanomaterials, methods that enable precise control of the morphology by means of chemistry of precursors rather than using predetermined templates is required.

With the discovery of graphene and its widespread interest[36]- two dimensional (2D) sheets of carbon- synthesis of inorganic graphene analogues such as layered metal chalcogenides have gained significant interest. Despite its exceptional properties, pristine graphene lacks a bandgap, which suggests field effect transistors (FETs) made from graphene cannot be switched off. Transition metal dichalcogenides (TMDs), on the other hand, possess sizeable bandgaps around 1-2 eV, which could complement semi-metal graphene in various state-of-the-art applications[37]. However, the reliable production of atomically thin 2D TMDs is lacking, which is essential for translating their electronic and optical properties into applications. Despite the research being carried worldwide on MoS_2 and WS_2 nanostructures, there are plenty of ground to cover in terms of understanding the synthesis chemistry, structure and properties of these material systems which would improve their use in commercial applications such as catalysts, batteries, lubricants, electronics and optoelectronic devices. A conventional and effective method for the synthesis of these materials is a prerequisite to enable extensive studies on their structure, properties and application.

1.2. Plan of thesis

This research work was centred on the synthesis of different forms of layered metal chalcogenides, WS_2 in particular, using a simple, versatile and scalable chemical vapour deposition (CVD) technique. A detailed study of the synthesis process and parameters influencing the final morphology of the product has been undertaken. In chapter 1 a review of the literature on the synthesis, properties and applications of TMDs, with emphasis on MoS_2 and WS_2, is covered. In Chapter 2, the synthesis of WS_2 nanoflowers is discussed in detail along with their time dependent structural and compositional evolution which has not been shown previously. High-resolution

microscopy revealed the presence of few-layered nanosheets at the edges of these nanoflowers- 2D nanosheets in 3D nanoflowers. Attempts were made to isolate these nanosheets with the aid of various exfoliation techniques. The exfoliation methods employed along with the structural changes they introduced is discussed in Chapter 3. Solvent exfoliation resulted in increased edge sites in the nanoflowers, which is shown using high-resolution electron microscopy. These could serve as active sites for electrocatalysis of hydrogen evolution reaction (HER). The nanoflowers and their solvent exfoliated forms in combination with commercially available carbon (BP2000) are employed as electrocatalysts for HER. In Chapter 4, by tuning the various parameters such as the ratio and temperature of the precursors, a similar atmospheric pressure CVD strategy was employed to form 2D WS_2 domains. The bottom-up approach of CVD has shown promise to generate high-quality TMD layers with scalable size, controllable thickness and excellent electronic properties. However, despite the initial success of CVD synthesis of TMDs, sufficient understanding of the growth process is still lacking. In this work, the effect of various experimental parameters on the growth and morphology of the deposits has been studied. In Chapter 5, the synthesis of mixed metal chalcogenides using the same CVD process and detailed characterisation of the doping with variation to growth temperature (650-850 ^{o}C) is discussed. It is shown that a composition-controlled synthesis of $Mo_xW_{1-x}S_2$ can be achieved by using the atmospheric-pressure CVD. This would offer tremendous opportunities for large-scale synthesis of ternary alloys, which so far has been limited to exfoliation of flakes from single crystals produced by vapour transport. Finally, Chapter 6 provides a summary of the important findings and observations along with future directions that would help to further advance the field.

1.3. Literature Review

1.3.1. Layered Transition Metal Dichalcogenides (TMDs)

TMDs in the form MX_2 (where M is transition metal; X is chalcogen) are the most investigated of the inorganic compounds[38] due to their structural analogy to the layered structures of graphite, as seen in Figure1. However, in contrast to graphite, which is composed of stacked layers of sheets of carbon atoms arranged in hexagonal honeycomb lattice and held together by van der Waals force, the two dimensional layered compounds (MX_2) consists of stacked molecular sheets. In the case of WS_2, the molecular sheets are composed of a six fold-bonded tungsten atom layer sandwiched between two threefold-bonded sulphur layers which are held together by van der Waals force.

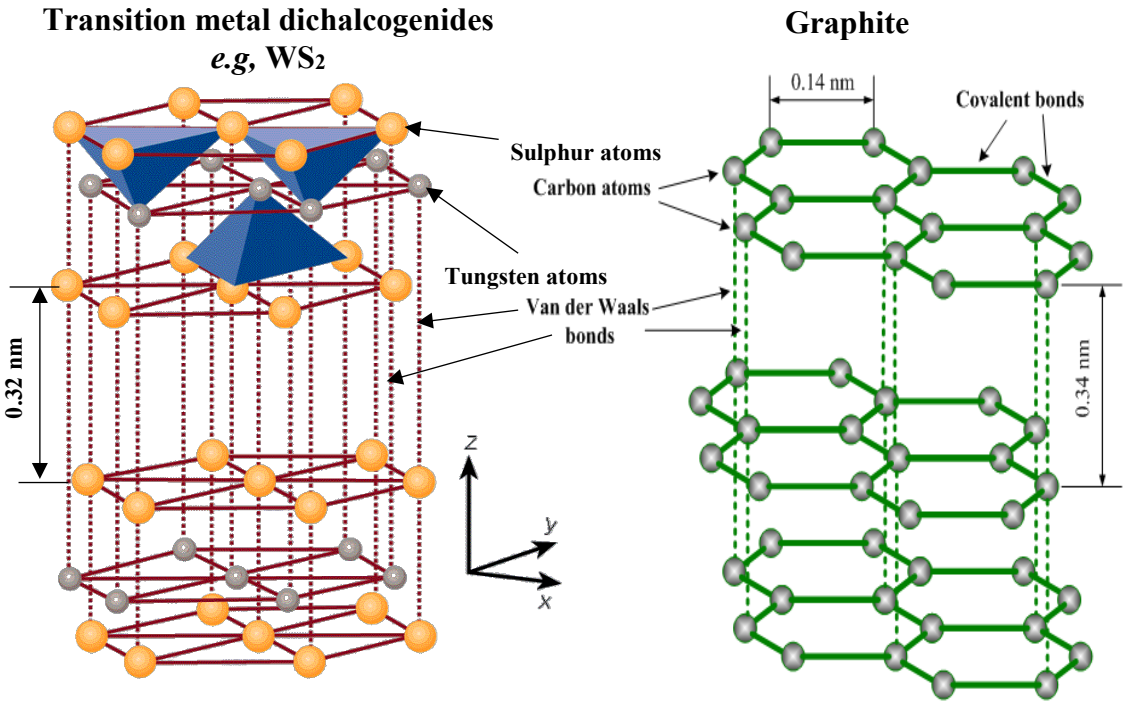


Figure 1. Layered structure of graphite and WS_2. The graphite is composed of stacking of single layers in which the bonding between the carbon atoms is sp^2. The repeating motif in WS_2 is a sandwich of three layers S-W-S with covalent tetrahedral W-S bond.[39]

TMDs are formed when a transition metal (Group 4-7 predominantly for layered TMDs; Group 8-10 non-layered structures) combines with a chalcogen (usually sulphur, selenium, tellurium of Group 16) to form a compound as highlighted in Figure 2. There are about 88 possible combinations of MX_2 compounds of which about 60 TMDs are stable and two-thirds (around 44) possess a layered structure.[40] They are highly anisotropic and the layers are considered to be quasi two-dimensional. Similar to graphite and other van der Waal solids, they are characterised by strong in-plane covalent bonding and weak inter-planar bonding. Although these forces are often referred to as van der Waals forces, the work by Friend and Yoffe[41] argue that the interactions can have covalent character or, Coulombic bonding, in some cases.

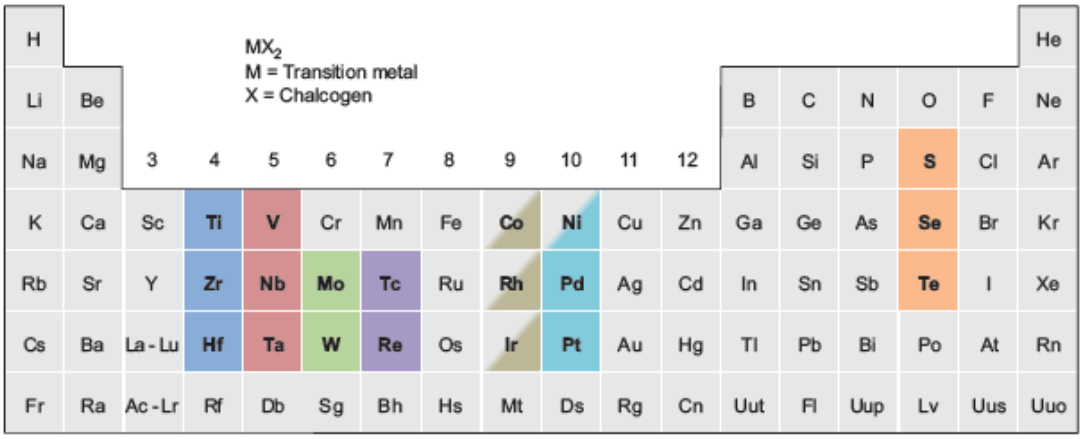


Figure 2. About 40 different layered TMD compounds exist. The transition metals and the three chalcogen elements that predominantly crystallise in those layered structure are highlighted in the periodic table. Partial highlights for Co, Rh, Ir and Ni indicate that only some of the dichalcogenides form layered structures. Reproduced with permission from Nature Chemistry.[42]

The general formulae of transition metal chalcogenides are MX, MX_2, MPX_3, AMX_2 or AMX_3, where M-transition metal, X-chalcogen and A, P- are second metal or chalcogen. The differences in formulae arise due to the variable oxidation state of the d-block transition metals, and the number of elements which constitute the chalcogenides. Also the molecular layers in these compounds can be stacked in different ways leading to hexagonal polymorphs. The polymorphs are classified by the

number of layers per unit cell, as hexagonal (2H), rhombohedral (3R) and trigonal (1T) with two, three and one layer per unit cell respectively. They exhibit diverse properties depending on their chemical composition as summarised in Table 1, and cover a wide spectrum from semiconductors (*e.g.,* MoS_2, WS_2), semi metals (*e.g.,* WTe_2, TeS_2), true metals (*e.g.*, $NbSe_2$ and VS_2) and insulators (*e.g.,* HfS_2).[40] Also, some of the TMDs such as $NbSe_2$, and TaS_2 exhibit low temperature superconductivity[43], charge density wave (CDW, a periodic distortion of crystal lattice)[44,45], and Mott transition (metal to non-metal transition)[46].

Group	M	X	Properties
4	Ti, Hf, Zr	S, Se, Te	Semiconducting (E_g= 0.2~2 eV). Diamagnetic.
5	V, Nb, Ta	S, Se, Te	Narrow band metals (ρ ~10–4 Ω.cm) or semimetals. Superconducting. Charge density wave (CDW). Paramagnetic, antiferromagnetic, or diamagnetic.
6	Mo, W	S, Se, Te	Sulfides and selenides are semiconducting (E_g~1 eV). Tellurides are semimetallic (ρ ~10–3 Ω cm). Diamagnetic.
7	Tc, Re	S, Se, Te	Small-gap semiconductors. Diamagnetic.
10	Pd, Pt	S, Se, Te	Sulfides and selenides are semiconducting (E_g = 0.4eV) and diamagnetic. Tellurides are metallic and paramagnetic. $PdTe_2$ is superconducting.

Table 1.Electronic Character of different layered TMDs. Reproduced with permission from Nature Chemistry.[42]

Even though single and few-layered compounds of many TMDs have been synthesised, first-principle structure optimisation and phonon calculations based DFT predict that not all of the possible 88 combination of MX_2 compounds were stable in free-standing, single layer honeycomb-like structures. The stability analysis and

electronic properties of 44 stable monolayer MX_2 sheets according to Ataca *et al*.[47], is summarised in Figure 3.

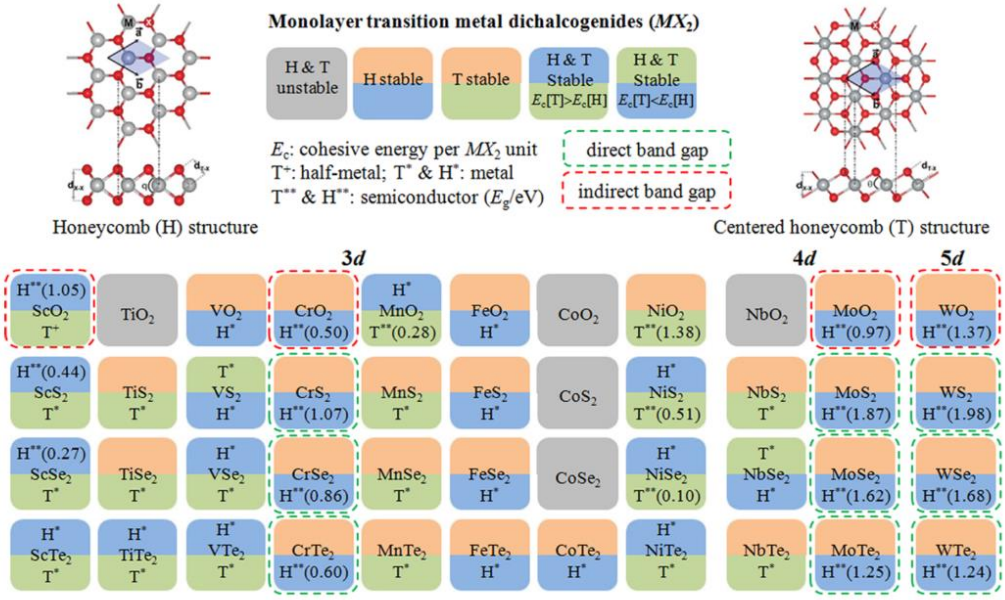


Figure 3. Summary of the stability analysis and semiconducting properties of 44 different TMD (MX_2) compounds with transition metal indicated by M divided into 3d, 4d and 5d groups.MX_2 compounds shaded light gray form neither stable H (2H-MX_2) nor T (1T-MX_2) structure. In each box, the lower lying structure (H or T) is the ground state. The resulting structures (T or H) can be half metallic (+), metallic (*), or semiconducting (**) with direct or indirect band gaps. Reproduced with permission.[48]

WS_2 and MoS_2, the most investigated materials of the layered metal dichalcogenide family, have been synthesised in different forms which include thin films[49], fullerene-like structures (zero-dimensional)[50], nanotubes (one-dimensional)[51], graphene analogues (two-dimensional)[52] and nanoflowers (three-dimensional)[30]. The structure of the layered dichalcogenides dictates their properties and therefore their applications. An insight into discovery, the structure, properties and application of WS_2 and MoS_2 is discussed in the following section.

1.3.2. Insight into inorganic nanostructures of WS_2 and MoS_2

The first formation of stable closed structures for inorganic nanostructures was reported from layered semiconductor tungsten disulphide by Tenne *et al.,* in 1992.[3] They were formed by heating tungsten films on quartz substrate in a reducing atmosphere of hydrogen sulphide at high temperatures (1000 ^{o}C). Although extensive details on the experimental procedure was not presented, the transmission electron microscopy (TEM) images shown in Figure 4 revealed a variety of concentric polyhedral and cylindrical structures (in the range of <10 nm and >100 nm) growing from the amorphous tungsten matrix. Electron diffraction and lattice imaging confirmed the closed nature of the nanostructures and the distance between the lattice fringes was found to be in agreement with the lattice spacing for WS_2.

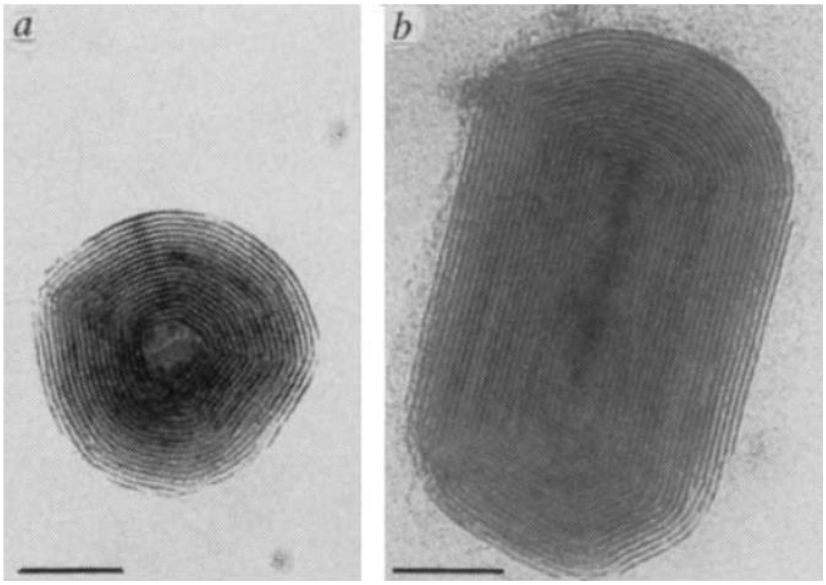


Figure 4. Electron micrographs of polyhedral crystals of WS_2. a) Spheroidal crystal; b) Stir-bar crystal. The spacing between fringes is 0.615±0.005 nm, which agrees with the distance between two neighbouring layers (c/2) of WS_2. Scale bar is 10 nm. Reproduced with permission.[3]

The stability of these nanostructures was confirmed when they remained unchanged over a period of one year at atmospheric conditions. The reason for WS_2 forming these closed structures was investigated from the energetic and geometrical point of view.

The main stimulus for the closure of sheets from the energetic considerations was assumed to be the elimination of dangling bonds at the edges, as reported in graphitic sheets[53]. As for geometrical consideration, the complete closure would require the replacement of hexagons by other polygonal units, or generation of structural defects like edge dislocations which were reported in the resultant polyhedral crystals. The unit cell of WS_2 is made up of two layers in hexagonal arrangement (2H). The edge W and S atoms, abundant in the nano-regime, were four- and two-fold bonded respectively. This could suggest these nanostructures are unstable in the planar form. Therefore the molecular sheets were thought to fold and stitch at the edge atoms together to form seamless stable nanotubular (one-dimensional) and spherical (zero dimensional structures) structures with all W and S atoms being six- and three-fold bonded respectively. This universal observation of nanostructures in layered compounds led to them being classified as inorganic fullerene-like structures (IF) and inorganic nanotubes (INT).

A detailed study to understand the structure and physical properties of closed cage inorganic nanostructures was undertaken by Enyashin *et al.* in 2007 using MoS_2 fullerene-like nanoparticles.[54] Structural models of single layer fullerene-like MoS_2 nanoparticle with square-like defects was investigated using density functional tight-binding coupled with molecular dynamics (DFTB-MD). Theoretical analysis of MoS_2 nano-octahedra was performed with direct comparison to the experimental data obtained from TEM. The authors showed the triangular nanoplatelets can be cut in two ways from a MoS_2 monolayer with the Mo-S bonds perpendicular to the edges of the triangle (I^{st} case) or parallel to the edges of the triangle (II^{nd} case), Figure 5. The association of these triangles lead to a closed stoichiometric polyhedra of octahedral

shape with stable $Mo_{576}S_{1140}$ at 0 K, as shown in Figure 5c. After MD simulation to 300K square-like defects occur at the corners (Figure 5d). These computer generated images and models were found to agree well with TEM image (Figure 6) of the three layer octahedra obtained at various tilt angles thereby providing credibility to the analysis.

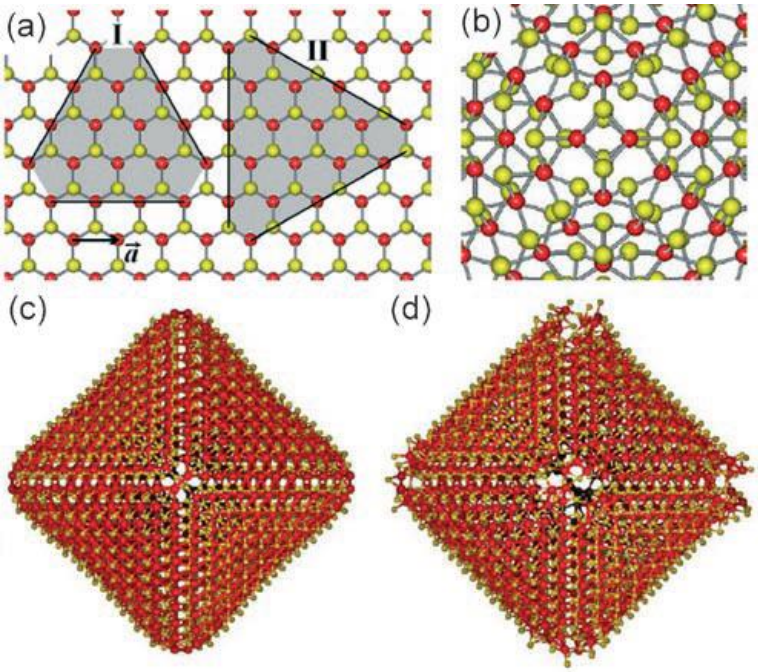


Figure 5. (a) Structures constructed from a hexagonal MoS_2 monolayer: triangle faces cut in two possible ways, (b) the ideal apex (with a square-like defect) of stoichiometric MoS_2 fullerene, (c) the DFTB-optimized structure of an $(MoS_2)_{576}$ fullerene, which degraded to $Mo_{576}S_{1140}$, and (d) the structure of $Mo_{576}S_{1140}$ fullerene after an MD simulation at 300K. Mo red, S yellow.[47]

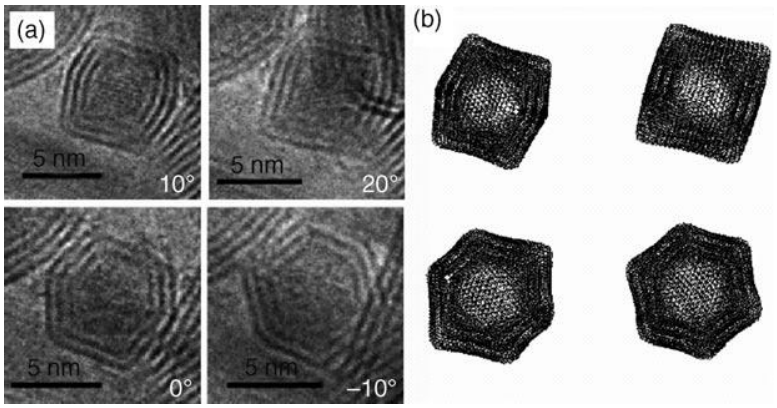


Figure 6. (a) TEM images of a three layer nano-octahedron at various tilt angles and; (b) corresponding views of the model structures of an $(MoS_2)_{784}$,$(MoS_2)_{1296}$ and $(MoS_2)_{1936}$ fullerene. The similarity between the experimentally observed and model structures is evident. Reproduced with permission.[47]

The stability and electronic property (covered in section 1.3.4.2) of zigzag and arm-chair MoS_2 nanotubes was studied by Seifert *et al.*[11], using density functional tight-binding (DFTB) method. The most stable form of MoS_2, also applicable for WS_2, consists of a metal layer sandwiched between two sulphur layers. This was used to construct tubular structures by rolling them on cylindrical surfaces along specific directions in the 2D lattice, as shown in Figure 7(i) to form zigzag and arm chair configurations. To explain the INT tips and the structure of polyhedral particles, topological defects were introduced into the structure to preserve the stoichiometry of the system as shown in Figure 7(ii).

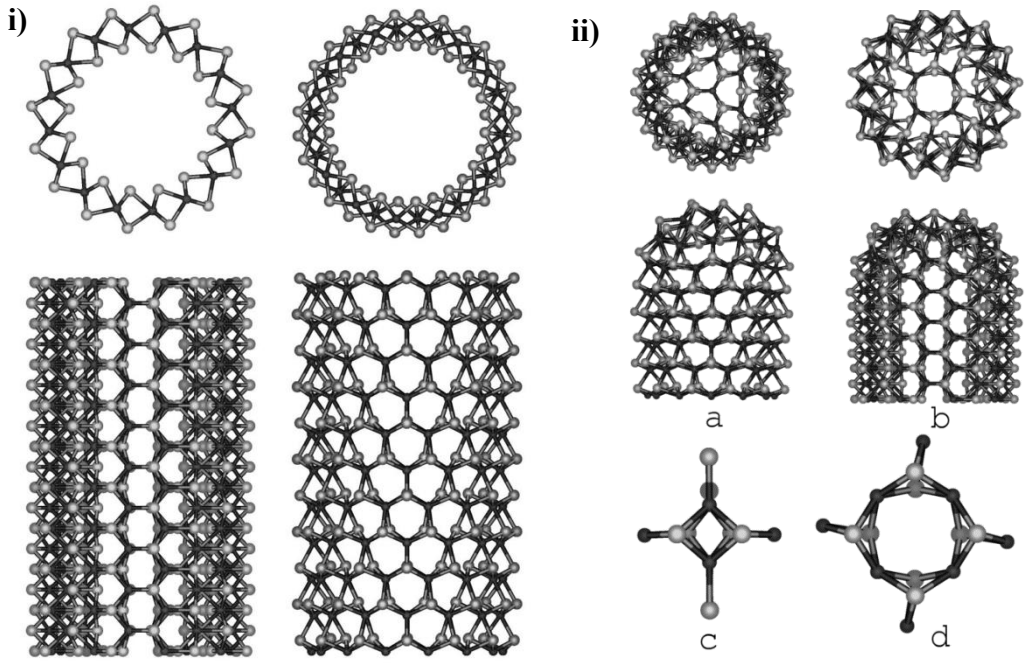


Figure 7. i) Armchair (8,8) MoS_2 nanotube (left) and zigzag (14,0) MoS2 nanotube (right). ii) MoS_2 nanotube tips a) zigzag (12,0) tube closed with three square-like defects. B) Armchair (8,8) tube closed with four square-like defects and one octagonal-like defect c) square-like defect. d) octagonal-like defect. Light atoms are S; dark atoms are Mo. Reproduced with permission.[11]

The quasi spherical shaped fullerene-like MS_2 (M=W, Mo) nanoparticles possessed excellent tribological properties (section 1.3.4.3), making them superb lubricants in the form of additives to lubrications fluids, greases and for self-lubricating coatings.[55]

The excellent mechanical properties of the INT structure (section 1.3.4.2.1) makes them attractive for ultrahigh strength composites. Other applications explored for INT of WS_2 were as scanning probe microscopy tips [26], cathode materials for Li intercalation batteries and the catalytic methanation of CO[56].

The recent interest in graphene, due to its exceptional properties, has encouraged the exploration of other kinds of 2D materials with layered bulk crystals analogous to graphite. The IGAs, in particular TMDs, have received significant interest because some of them are semiconductors with sizeable bandgaps and are naturally abundant.[57] In layered TMDs, the single layer typically has a thickness of 6-7 Å with hexagonally packed layer of metal atoms sandwiched between two layers of chalcogen atoms. The two hexagonal lattices of MX_2 are present depending on the coordination number of the transition metal to the chalcogens.[58] In 2H-MX_2, the coordination (honeycombs) is trigonal prismatic and the coordination in 1T-MX_2 is octahedral (centered honeycombs) as shown in Figure 8.[59]

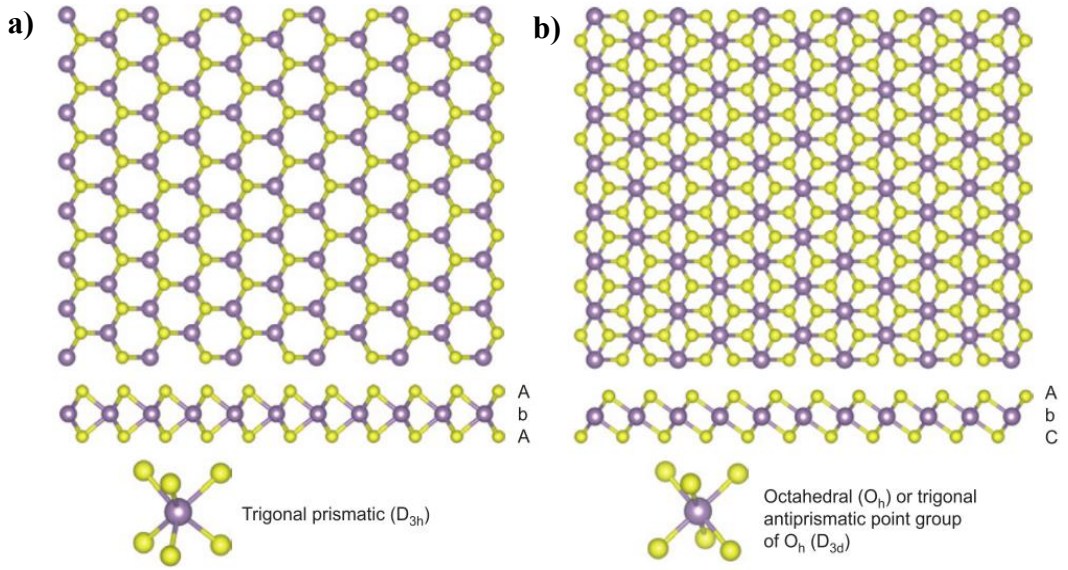


Figure 8. c-Axis and section view of a single-layer TMD with trigonal prismatic (a) and octahedral (b) coordinations. Atom colour code: purple, metal; yellow, chalcogen. The labels AbA and AbC represent the stacking sequence where the upper- and lower-case letters represent chalcogen and metal elements, respectively. Reproduced with permission from Nature Chemistry.[42]

The single layers are stabilised by the development of ripple structures as in the case of graphene.[60] MoS_2 is one such prototypical TMD with layers made of hexagons of Mo and S_2 atoms located at alternating corners as shown in Figure9.

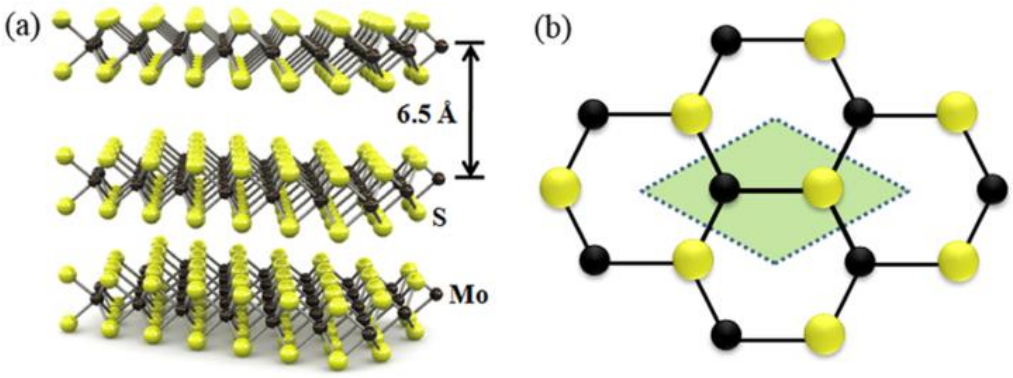


Figure 9. (a) The atomic structure of layered MoS_2. Different sheets of MoS_2 are composed of three atomic layers S−Mo−S, where Mo and S are covalently bonded. (b) A top view of the honeycomb lattice, emphasizing the inversion symmetry breaking. Reproduced with permission.[48,61]

The 2D TMDs, such as MoS_2 and WS_2, with excellent electronic, optical properties (section 1.3.4.1) and sizeable bandgaps make them attractive for applications such as field-effect transistors,[62] photodetectors,[63,64] and electroluminescent devices (section 1.3.5.1 and 1.3.5.2). Moreover, they are also promising materials for catalytic hydrogenation (section 1.3.5.4), potential building blocks of thermoelectrics, energy storage devices, chemical and biological gas sensors (section 1.3.5.3), spin- and valley-tronics,[65,66] thermoelectrics,[67] and topological insulators.[68]

1.3.3. Synthesis of inorganic nanostructures

The synthesis of inorganic nanostructures have been carried out using a number of strategies. Initially, synthesis was limited to sulphurisation of metal foils in extreme environments to form TMDs. Since then, various bottom-up approaches have been developed using different precursors to form IF and INT nanostructures, covered in section 1.3.3.1. The reaction of a metal oxide template with sulphur source is a widely

employed process to produce commercial quantities of the IF and INT nanostructures. With the advent of graphene, top-down approaches have been employed extensively for preparing IGA nanosheets by processing bulk crystals/powder, covered later in section 1.3.3.2.1. However, top-down methods lack the ability to form high quality, large-area films with controlled thickness and size. To address this, the bottom-up synthesis method of chemical vapour deposition (CVD) has been widely researched. The chemical strategies and precursors employed for IF and INT were adopted for bottom-up growth of 2D materials using the CVD process, which is covered in detail in section 1.3.3.2.2.

The synthesis of TMDs can be performed by a relatively simple reaction at elevated temperature, where the transition metal reacts with stoichiometric amounts of sulphur, selenium or tellurium. Such a reaction is relatively straightforward for some compounds, such as MoS_2 and WS_2, but exceedingly difficult for others such as $NiCl_2$[69] and CsO_2[70]. The synthesis can also be accomplished from the respective oxide nanoparticles in a slow diffusion-controlled process[6,71]. However, this process is limited to reactive oxides like WO_3 and would not be applicable to less reactive oxides such as those of titanium and niobium. The synthesis of TMDs can also be achieved at low temperatures in solid state reactions, especially when the final product is unstable at the elevated temperature or highly crystalline product of high temperature reactions is unsuitable[72]. High surface area single crystals suitable for use in catalysis have been created using the process of chemical vapour transport[73]. However, this process requires long time periods, sometimes over 24/48 hours, which is a major drawback. Highly crystalline products can also be formed by vapour phase synthesis at high temperature using the metal chloride and hydrogen sulphide gas as

precursors.[74] However, hydrogen sulphide, being a toxic gas, requires extreme caution for use in laboratory setups making the process complicated.

To overcome these shortcoming, researchers have developed a strategy to employ metal halides or carbonyls as precursors. The high vapour pressure of these precursors at temperatures below 300 ^{o}C facilitates their reaction with a sulphur source, normally H_2S vapour or elemental sulphur, instantaneously leading to fast nucleation of MX_2 nuclei growing outward in a layer–by-layer fashion. Fullerenes-like NbS_2 nanoparticles were the first to synthesised using this strategy.[75] Subsequently TiS_2[76] nanotubes, fullerene-like MoS_2[77], WS_2[8] and TiS_2[78] nanoparticles were synthesised from their respective metal halide and a sulphur reagent. This process offers excellent control over the final morphology synthesised due to the ability to control the precursors. It also offers the distinct advantages of high vapour pressure of precursors and low synthesis temperature, making it an attractive process for TMD synthesis. Hence I adopted the synthesis strategy using metal halides and elemental sulphur for my research work.

The method of preparation must be carefully selected to deliver a product tailored for specific applications. An overview of the various key processes employed for the synthesis of different morphologies of MoS_2 and WS_2 along with their key advantages and limitation has been summarised Table 3. Each process is described in detail in section 1.3.3.1 and 1.3.3.2.

Structures	Process employed	Author & Year	Advantages/Highlights and Limitations
Inorganic fullerene-like particles	Fluidised bed reactor	Y.Feldman *et al.* 2000[7]	Large scale synthesis, uniform shape and size of IF particles.
	Metal Organic CVD	Etzkorn *et al.* 2005[77]	Facile large scale synthesis method enabling size and morphology of particles
	Atmospheric Pressure CVD	Li *et al.* 2004[30]	Large scale synthesis process with morphology control to form nanoflowers, nanotubes and IF particles.
Inorganic Nanotubes	Solid template synthesis	Dorhout *et al.* 1998[79]	Control of size and size distribution of nanofibers or tubules of MoS_2
	Decomposition	Rao *et al.* 2001[80]	Simple synthesis process by direct transformation of precursor without any side products.
	Chemical vapour transport	Tenne *et al.* 2002[50]	Standard growth technique for TMD's. Length and size of nanotubes controlled.
Inorganic Nanobuds	Chemical transport	Remskar *et al.2008*[34]	First inorganic nanobuds to be reported. Reproducibility still an issue which restricts synthesis of large quantities.
Inorganic nanosheets and nanoflowers	Mechanical Activation Method	Wang *et al.* 2010[81]	Novel mechanical method using ball milled mixture to form potentially large quantity WS_2 nanosheets. Uniform sheets with controllable thickness still challenge.

	Aerosol assisted CVD	Adeogun *et al.* 2006[82]	Limited premature reaction and good quality homogenous films
	Atmospheric Pressure CVD	Li *et al.* 2004[30]	Large scale synthesis process with morphology control to form nanoflowers, nanotubes and IF particles.
Inorganic Graphene Analogues	Chemical Exfoliation	Coleman *et al.* 2011[83] Zhang *et al.* 2012 [84]	Versatile method which can be applied to most inorganic compounds. However, lacks control of thickness, lateral size of flakes, crystallinity and has problems with contamination from chemical residues.
	Chemical Vapour Deposition	Lee *et al*. 2012[85]; Zande *et al.* 2013[86]; Najmei *et al.* 2013[87]; Elias *et al.* 2013[88]	Ideal for synthesis of large area films. Process is still in incumbent stages with limited understanding of nucleation and control of growth mechanisms.

Table 2. Summary of synthesis processes employed to form different inorganic nanostructures

1.3.3.1. Synthesis of Inorganic Fullerene-like nanoparticles, Inorganic Nanotubes, Nanoflowers and other forms of WS_2 and MoS_2

Since the discovery of IF and INT nanostructures,[71,89] there have been multitude of synthesis process explored to produce these structures along with other morphologies such as nanofibers, nanotubules, nanoflowers and nanoribbons. A detailed account of some of the key processes employed to produce these structures for WS_2 and MoS_2, is given below.

1.3.3.1.1. Fluidised bed reactor

The large scale synthesis of IF-WS_2 nanoparticles was accomplished using a fluidised bed reactor.[90] The reactor utilises the gas phase reaction between the oxide precursors and H_2S gas established by Tenne *et al.* in 1996.[6,7] A schematic of the fluidised bed reactor and associated temperature profile is shown in Figure 10. Feeding of the oxide powder is assisted by nitrogen in zone A, through the upper heated zone of the reactor, while the gas stream of H_2S and N_2-H_2 gases enters from the bottom zone C. The sulfurization of the oxide nanoparticles takes place in zone B with the diffusion of H_2S gas. High linear rate of main gas stream in zone C offers fluidised bed conditions for the falling powder. The filter, placed at the end of the tube at constant temperature region of 830 ºC, collects a small part of the powder. However, the largest amount of material stays in fluidised bed region. In this way, this reactor forms 50 g of closed and hollow IF-WS_2 per batch.

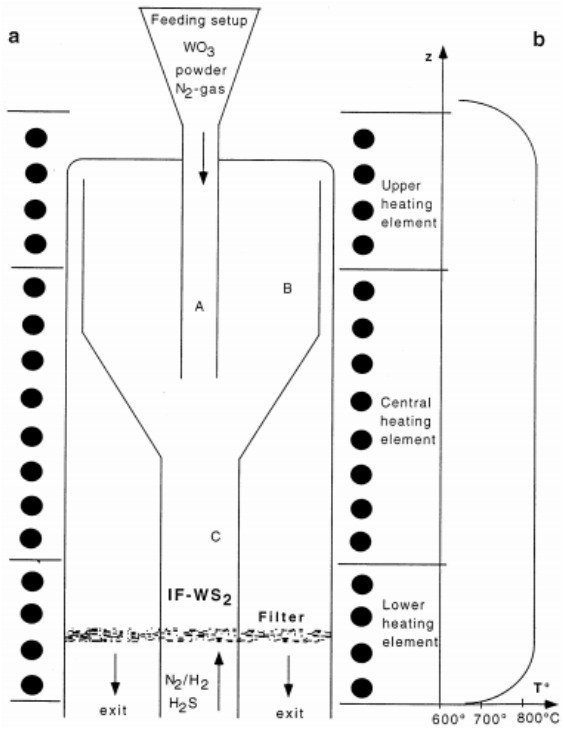


Figure 10. a) Schematic of the fluidised bed reactor, b) temperature profile along furnace (z) axis. Reproduced with permission.[69]

With modifications, the fluidised bed reactor was employed for the industrial production of IF-WS_2 by ApNanoMaterials, Inc.[29] The process was capable of forming pure IF phase particles of 0.5 μm in size with no extra contamination thereby avoiding expensive and time consuming filtration, purification processes. Later this method was also adopted for large scale production of INT- WS_2 and MoS_2.[91]

1.3.3.1.2. Solid Template Synthesis

A solid template synthesis was employed by Zelenski and Dorhout [79] with the aim of controlling the size and distribution of near mono-disperse micro-scale nanofibers or tubules of MoS_2. 2H-MoS_2 structure is a useful catalyst for hydro-desulfurization[22], an electrode in high energy density batteries, and an intercalation host to form new materials. However, for all these applications, the presence of edges or exposed surfaces is of paramount importance. Nanoclusters of MoS_2 provide tremendously increased surface area of exposed edges which would enable this chemistry. Although the reaction mechanism of nanoclusters and tubules have been studied in detail by Tenne *et al.*[7,29,87–92], the control of size and shape had not been realized. The low temperature reactions of Muller *et al.*[96–98] were utilised to produce MoS_2 from solution phase precursors within the porous template of aluminium oxide membranes [99,100]. The process infiltrates soluble ammonium thiomolybdate precursors into well-defined porous aluminium oxide membrane templates. Cylindrical pores sizes and size distributions within these membranes are controllable, with diameters ranging from 50 to 330 nm and lengths approaching 30-60 μm. This in turn dictates the size and shape of the MoS_2 tubules and fibres prepared. This process is attractive for forming nanotubules and fibers with good control over size and shape. However, process is limited only for the nanotube morphology.

1.3.3.1.3. Decomposition

The decomposition method is the result of simplifying the pre-existent chemical strategies widely employed for synthesis of IF and INT TMDs. Originally, the growth of MoS_2 nested IF and INT was established using a gas phase reaction between MoO_{3-x} and H_2S in a reducing atmosphere at elevated temperatures (800 ^oC to 950 ^oC) by Tenne *et al* in 1995.[6] In 2001, CNR Rao *et al.*[80] hypothesised that the reaction between MoO_3 and H_2S would give an amorphous MoS_3, which would further decompose into MoS_2 nanotubes. Their experimental studies on the decomposition of MoS_3 at high temperature in H_2 atmosphere, indeed formed MoS_2 nanotubes. Having produced nanotubes by decomposition of MoS_3, synthesis using ammonium thiomolybdate (MoS_3 precursor) was attempted by thermal decomposition. The MoS_3 formed was heated at high temperature of 1200-1300 ^oC in a stream of H_2 to form MoS_2 nanotubes. Similar reactions were then carried out with ammonium thiotungstate to obtain WS_2 nanotubes. In addition to nanotubes, other forms such as onion-like clusters and nanorods have also been reported using this process. The work is reported to be simplest method for the synthesis of inorganic nanotubes. However, the control over the final morphology is limited and not reported, a clear drawback. Also the quantity of nanotubes produced and their aspect ratio were not discussed in the study.

1.3.3.1.4. Mechanical Activation Method

A mechanical activation method was reported by Wu *et al.*[81] for the synthesis of large quantities of WS_2 nanosheets. It involved ball milling a mixture of WO_3 and S. The effect of temperature on the formation of WS_2 was reported along with a possible formation mechanism. At 500 ^oC only small amounts of WS_2 were formed as indicated

by a small (002) peak in the x-ray diffraction. At 700 ºC WO_3 reacted completely, and resulted in WS_2 as the only product. However, there was an intermediate product of WO_2 with annealing temperatures above 800 ºC. The thickness of the nanosheets were reported to be about 10 nm. An 'outside-in' growth mechanism was suggested where the sulphurisation take place from the outside of the WO_3 particle to the inside. This was proposed due to the coexistence of the inner WO_3 quasi spheres and exterior WS_2 nanosheets, in which the WS_2 nanosheets was produced by the exfoliation of the outer sulphurised layer as seen in Figure 11. The TEM of the nanosheets along with selected area diffraction show that the nanosheets are loosely stacked with slight curvature as shown in Figure 12. The paper also suggests that this strategy can be extended to synthesize other nanomaterials. Even though the process has the ability to form WS_2 nanosheets in large quantities, it has limitations in controlling the lateral size, thickness and reproducibility of the final product.

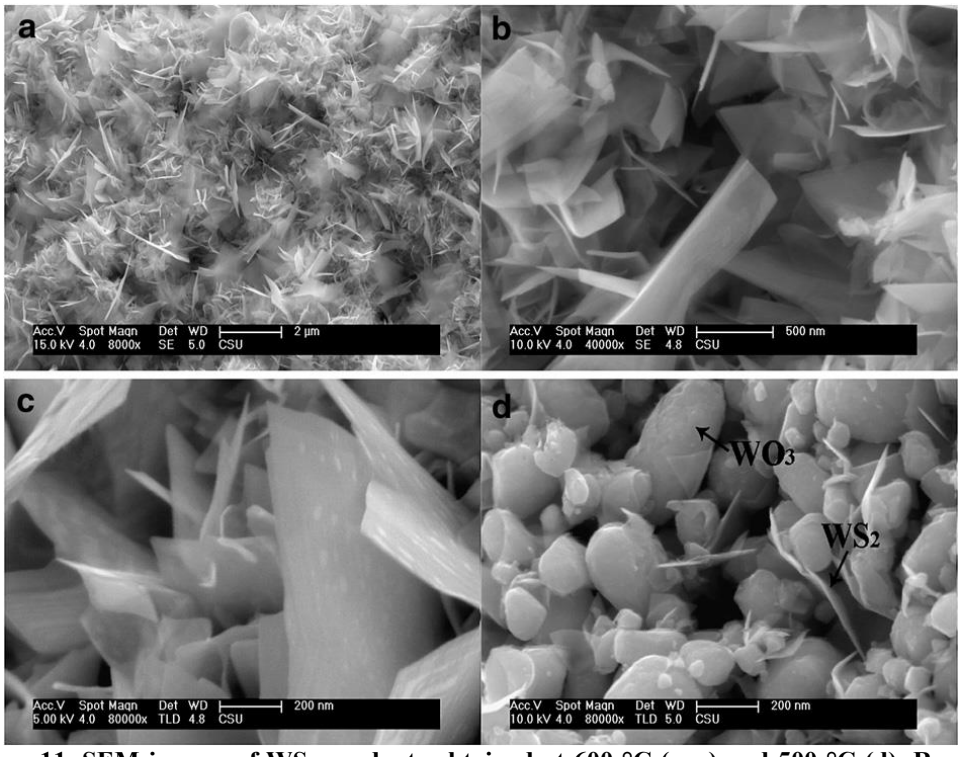


Figure 11. SEM images of WS_2 products obtained at 600 °C (a–c) and 500 °C (d). Reproduced with permission.[81]

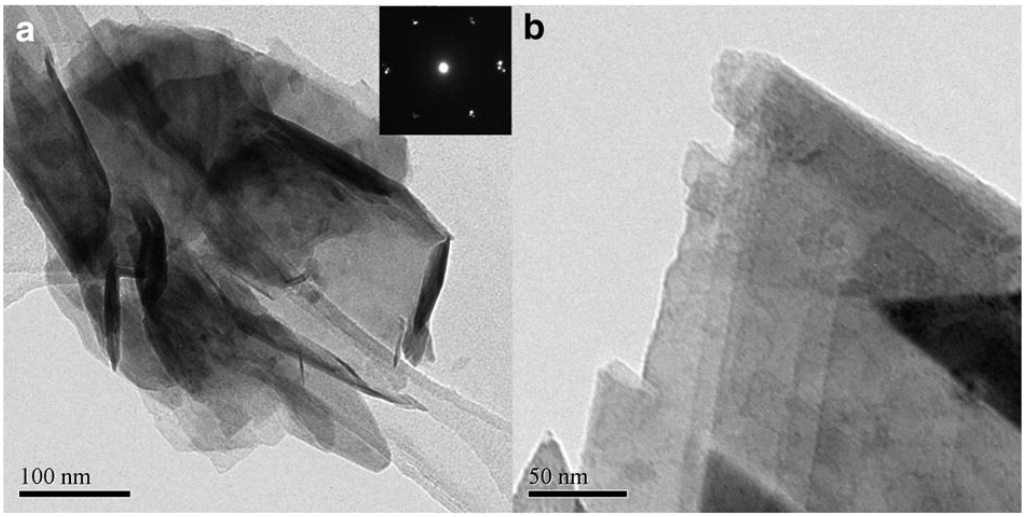


Figure 12. TEM images and SAED pattern (inset) of the WS2 nanosheets. Reproduced with permission.[81]

1.3.3.1.5. Chemical Vapour Deposition

Chemical vapour deposition has been the most successful and commonly employed method for the synthesis of TMDs in various forms. Since the seminal work of Tenne[6], many variations to the chemical vapour deposition (CVD) procedure have been reported which include chemical vapour transport, plasma-assisted chemical vapour deposition (PACVD),[101] metal organic vapour deposition (MOCVD),[77] aerosol-assisted chemical vapour deposition (AACVD),[82] and atmospheric-pressure chemical vapour deposition (APCVD).[30] A detailed description the key aspects of these processes is given below.

1.3.3.1.5.1. Chemical Vapour Transport

Chemical vapour transport has been used abundantly for obtaining single crystals of high melting point or high vapour compounds. It differs from CVD, which entails decomposition of precursors, since it involves volatilization of pertinent precursor of the desired phase in a temperature gradient sealed tube using transport agents. In 2002, Tenne *et al.*[50] employed chemical vapour transport method as a standard growth

technique for high quality single crystals of layered metal dichalcogenide (MX_2) compounds. The pure phase WS_2 nanotube was synthesised by reacting short nanowhiskers of tungsten-oxide, under mild reducing conditions of H_2S. The length of the resulting nanotube was determined by the interplay between three reactions-tip growth of the oxide nanowhisker, reduction and sulfurization. In 2008, Remskar *et al.*[34] employed chemical vapour transport to synthesise the first inorganic nanobuds. WS_2 nanotubes decorated with fullerene-like particles were produced by the sulfurization of W_5O_{14} wires using nickel as a growth promoter as seen in Figure 13. However, the final morphology was not completely controlled as undecorated tubes were also produced. Although chemical vapour transport has the potential to produce single crystals with precise control over the composition, it requires high purity precursors and atmosphere, very long synthesis times. Furthermore, obtaining nanosheets from the crystal will require a second step, such as mechanical cleavage.

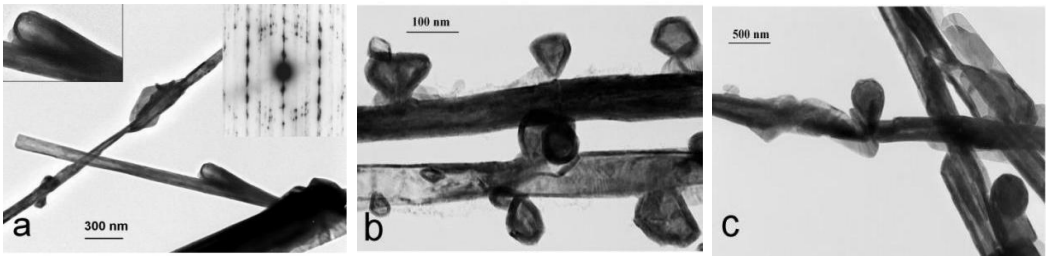


Figure 13. WS_2 nanobuds: (a) an early stage of growth with typically elongated thin walled buds along the nanotube support, which serves as a reservoir of material. The nanotube grow in the relaxed hexagonal 2Hb stacking (inset). (b) Some faceted nanoparticles joined to the supported thin-walled nanotube with their V-shaped parts. (c) The final stage of growth with nearly spherical thick-walled fullerenes. Reproduced with permission.[32]

1.3.3.1.5.2. Plasma assisted chemical vapour deposition

Stoffels *et al.*[101] suggested PACVD for MoS_2 hybrid coatings. The process focusses on the fabrication of layers by CVD/PACVD and simultaneous seeding with nanoparticles. A low pressure PACVD reactor was developed for the formation of

MoS_2 particles as shown in Figure 14. The work aimed at fabricating hybrid titanium nitride coatings with embedded molybdenum sulphide particles. MoS_2 particles formation at pressures between 0.5 and 10 torr was studied with different chemistries: one based on $MoCl_5$ and H_2S, and another on $MoCl_5$ and S. In both cases the particle formation was studied in a thermal oven and in a radio frequency discharge. Nevertheless, the process suffered from limitations such as the low reaction rates at low pressures and no particle formation at high pressures (10 Torr). With sulphur slightly larger particles were produced in comparison to the H_2S which formed particles smaller than 100 nm. Both in thermal and plasma enhanced particle synthesis, excess hydrogen was essential for the stability and purity of the particles.

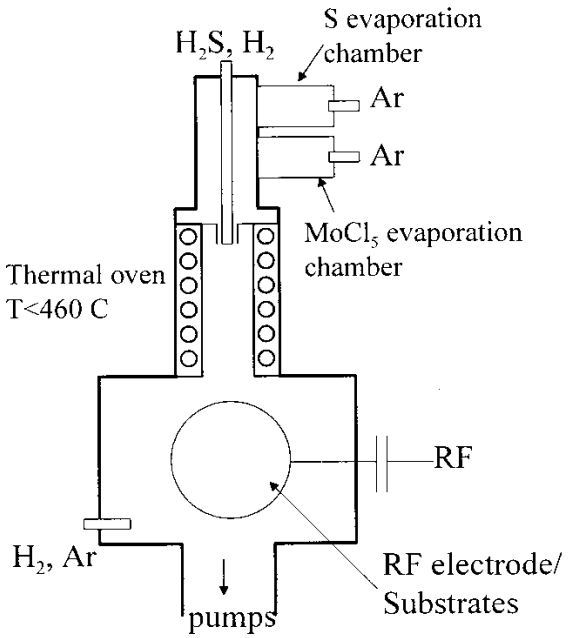


Figure 14. A schematic top view of PACVD experimental setup. Two evaporation ovens for S and $MoCl_5$ (T=150°C) are used. Vapours are flushed with argon and led through the main oven (T_{max}-460°C). In the main oven reaction gases H_2 and H_2S are admixed to allow MoS_2 formation. The reaction mixture flows into the reactor chamber and nanoparticles are collected on a silicon substrate. Reproduced with permission.[101]

1.3.3.1.5.3. Metal organic chemical vapour deposition

Most of the methods previously discussed for the synthesis of nanostructured metal chalcogenides rely on high temperature and/or complicated processes, not ideal for the large scale synthesis of these materials. Since the mechanical, physical and catalytic properties of nanostructured chalcogenides strongly depend on their shape and size, synthesis procedures that enable significant control of the particle size and morphology are desired. From the application point of view, the focus will be on nanoparticle growth with high purity, high yield and thereby low-cost products. Taking these into account, Etzkorn *et al* .[77] reported a facile, large scale synthesis of hollow fullerene-like MoS_2 and $MoSe_2$ nanoparticles by heating the precursors obtained from a metal organic vapour chemical vapour deposition (MOCVD) approach, where $Mo(CO)_6$ and elemental sulphur or selenium were used as the starting material. The schematic of the setup used for the synthesis is shown in Figure 15. Depending on the synthesis temperature, the process formed closed and hollow IF like MoS_2 and $MoSe_2$ nanoparticles in bulk quantities with diameter 5-20 nm, and with onions with diameter between 30-60 nm. The MOCVD setup with gaseous precursors offers the advantage of monitoring using gas phase analytical methods, such as mass spectrometry, to kinetically control the growth process by optimising experimental conditions (precursors, flow rate, *etc.*).

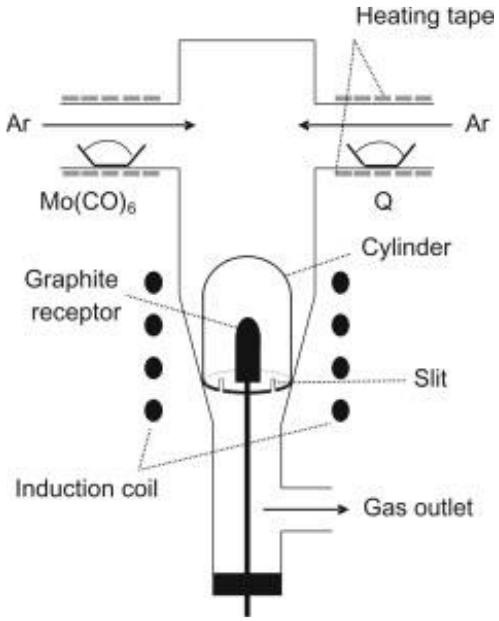


Figure 15. Schematic of the quartz glass set up used for MOCVD. Reproduced with permission.[77]

1.3.3.1.5.4. Aerosol assisted chemical vapour deposition

Adeogun *et al.*[82] reported the synthesis of nanostructures of MoS_2 using single-source precursors (SSPs) which offer advantages such as limited premature reactions and good quality homogenous films. However, only limited work has been reported on the growth of MoS_2 films using SSP such as molybdenum tetra-butyl thiolate complex, $(Mo\text{-}S^tBu)_4$, in a hot wall low pressure LPCVD. The films deposited were amorphous and consists of closely packed granular morphologies when deposited in the temperature range of 110-200 ^oC. Metal dithiocarbamates have been widely used for the deposition of metal sulphides, and recently $[Mo(S_2CNEt_2)_4]$ has been used for the deposition of crystalline MoS_2 films in an ultrahigh vacuum environment using AACVD. Though these precursors do not have sufficient volatility for LPCVD, they are soluble in common organic solvents to be exploited in AACVD. Even though the compounds are relatively easy to synthesize, air-stable, and can be obtained in high

yields, the control of final morphology is often difficult and the setup is complicated and expensive.

1.3.3.1.5.5. Atmospheric pressure chemical vapour deposition

In 2004 Li *et al.*[30] reported a novel atmospheric pressure chemical vapour deposition route for the large scale synthesis of MoS_2 and WS_2 inorganic fullerene (IF) nanostructures. The APCVD process formed elegant 3D nanoflowers by the reaction of chlorides ($MoCl_5$/WCl_6) and sulphur. A reaction mechanism was proposed and their surface area and field emission properties were studied. The morphologies of these structures were controlled by adjusting the deposition position, the deposition temperature and the flux of the carrier gas. The precursor $MoCl_5$/WCl_6 was made to react with excess sulphur at 850^oC with Argon as the carrier gas. Fullerene-like nanoparticles, nanotubes and nanoflowers were deposited at 850 ^oC, 750 ^oC and 650 ^oC respectively. The total yield of MoS_2/WS_2 was calculated to be 95% and it was proposed that by optimising the reaction conditions a product with more than 90% single morphology can be obtained. The morphology of the WS_2 and MoS_2 structures obtained are shown in Figures 16 and 17, respectively. The reaction mechanism proposed was a mixed process of self-redox and metathesis between $MoCl_5$/WCl_6 and S. It was suggested that at elevated temperatures sulphur could act as a reductant and sulphurisation agent simultaneously. With a high yield, simple experimental setup, and the ability to produce different morphologies by varying few parameters, this process possesses huge potential for large scale synthesis of TMDs.

Hence, this CVD synthesis method was adopted for my research. In addition to the advantages listed above, the process offers control over the precursors system and consists of key quantifiable parameters that can control the resultant morphology.

These include the temperature of the process, synthesis time, amount of precursors, and substrates on which the final morphology are obtained.

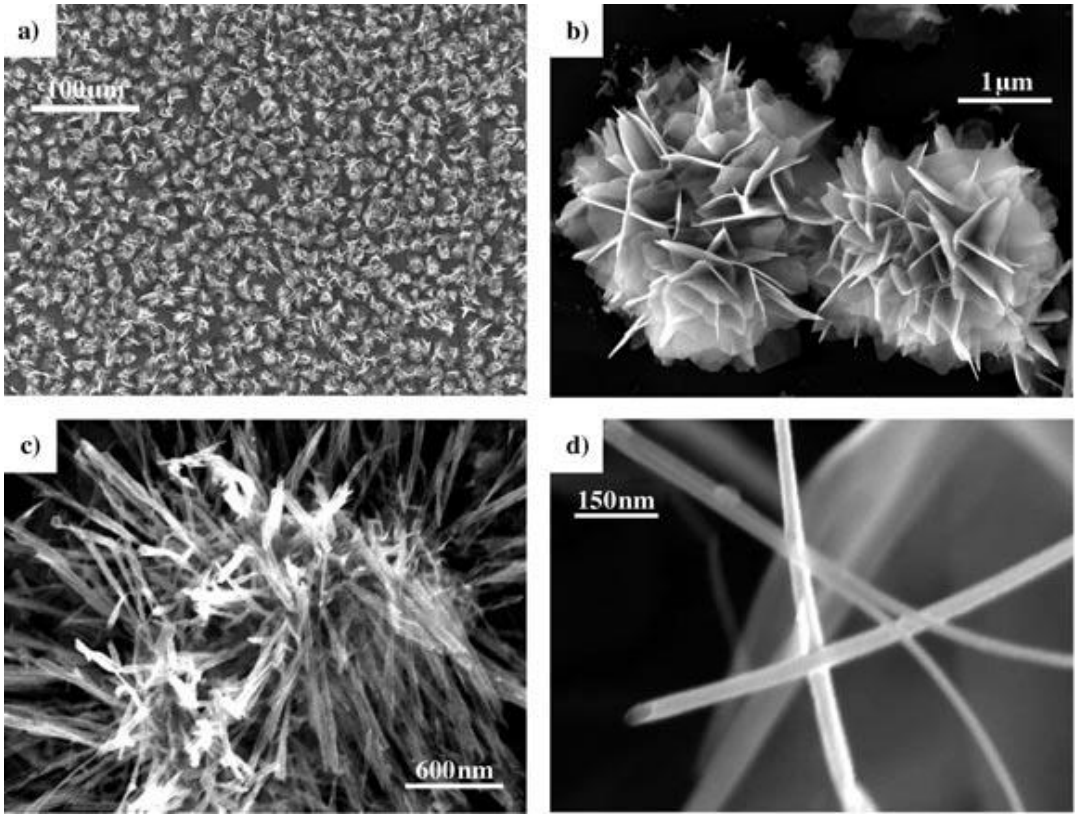


Figure 16. SEM images of WS_2 a) Low magnification and b) high magnification SEM images of WS_2 nanoflowers c, d) SEM images of WS_2 nanotubes. Reproduced with permission.[28]

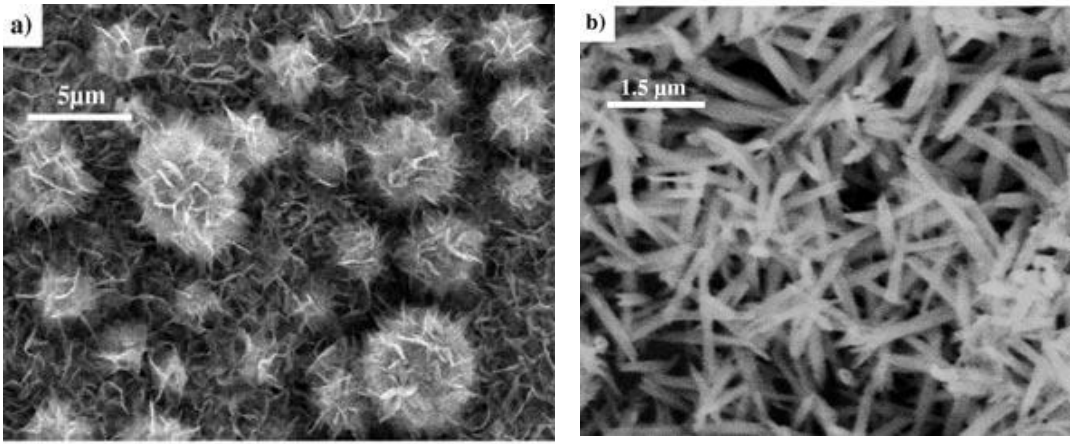


Figure 17.SEM images of MoS_2 a) nanoflowers b) nanotubes. Reproduced with permission.[28]

1.3.3.2. Synthesis of Inorganic Graphene Analogues (IGAs)

With similar layered structure to graphene, a wide range of inorganic layered compounds exists; these are referred to as inorganic graphene analogues (IGAs) or two-dimensional (2D) TMDs. IGAs like WS_2 and MoS_2 with intrinsic band gaps and high mobility, which might complement graphene in electronics[63] and photodetectors[60], are being researched by nimrods in the field. However, investigation of these 2D materials is hindered by the absence of a reliable large-scale synthesis method that is controllable and reproducible. Both top-down and bottom-up approaches have been attempted to obtain single and few-layered IGAs which include micromechanical cleavage[102], liquid exfoliation[103], lithium intercalation[104,105], chemical synthesis[52,106,107], and chemical vapour deposition[85,87,88]. The most relevant of these methods are expanded in the following sections.

1.3.3.2.1. Exfoliation techniques

Micromechanical exfoliation/cleavage revolutionised the field of 2D materials when Novoselov *et al.*[108,109] successfully applied it to peel off single layers/sheets from layered crystals. This method has been routinely used to produce pristine 2D nanosheets which are used to study the fundamental properties of graphene, IGAs and also fabricate electronic devices.[57,61] However, the size of these flakes is limited and their thickness and dimensions are not controllable. Thus, the major drawbacks of this method are irreproducibility and unscalability.

To overcome these limitations, Coleman *et al.*[103] reported a simple, large-scale method to exfoliate transition metal dichalcogenides in aqueous surfactant solutions. In this work a number of layered crystals were exfoliated, resulting in thin flakes

stabilized by a surfactant coating. The surfactant prevents the rapid re-aggregation of the layers, driven by the large surface energy of these materials. MoS_2 powders were subjected to sonification and centrifugation with sodium cholate as surfactant to produce supernatant solution. MoS_2 solutions remained stable over weeks and were also extremely robust to pH changes. Dispersions were also produced for a wide range of layered compunds such as BN, WS_2, $TaSe_2$, $MoTe_2$, $MoSe_2$ and $NbSe_2$. In spite of the ability to exfoliate a wide range of compounds, the process often suffered from contamination caused by the surfactant. Also, the mean size of the flake produced (280 nm) is still relatively small and unsuitable for electronic applications. This makes the process suited for production of wide range of hybrids with tunable conductance and attractive thermoelectric properties, which may be utilised as fillers for composites with enhanced mechanical and thermal properties. A schematic of the different liquid exfoliation processes is explained in Figure 18.

Following this work on liquid exfoliation, a mixed solvent strategy was reported by Zhang *et al.*[84]. By choosing an appropriate composition of solvents they produced highly stable solutions of IGAs in low boiling point mixtures. The theory of Hansen solubility parameters (HSP)[110], a semi empirical correlation, that can be partially used to predict the dispersion of nanomaterials in liquids and explain their dissolution behaviour was employed. This relation sought to demonstrate how two poor solvents, ethanol and water, can be designed to give high solubility for various IGAs making the process very attractive and versatile. The ethanol/water mixture at different compositions were highly stable for up to a week under ambient conditions with concentrations of the dispersions of IGAs strongly dependent on the volume fraction of ethanol in water.

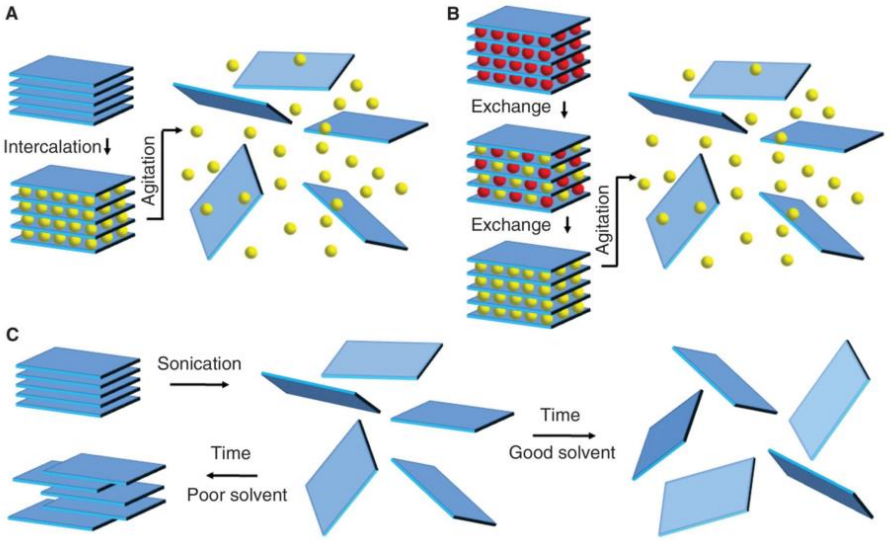


Figure 18. Schematic of main liquid exfoliation method mechanisms. A. Ion intercalation. Ions (yellow spheres) are intercalated between the layers in a liquid enviquid environment, swelling the crystal and weakening the interlayer attraction. Then, agitation (such as shear, ultrasonification, or thermal) can completely separate the layers, resulting in an exfoliated dispersion. B. Ion exchange. Some layered compounds contain ions between the layers so as to balance surface charge on the layers. These ions (red spheres) can be exchanged in a liquid environment for other, often large ions (yellow spheres). As above, agitaion results in exfoliated dispersion. C. Sonification-assisted exfoliation. This layered crystal is sonicated in a solvent, resulting in exfoliation and nanosheets formation. In "good" solvants-those with the appropriate surface energy-the exfolaited nanosheets are stabilised against reaggregation. Otherwise, for "bad" solvents, regarregation and sedimentation wll occur. Reproduced with permission.[111]

The morphology of the IGAs was studied using TEM as shown in Figure 19 along with the AFM studies to reveal thin sheets in the dispersion with thickness in the range of 2-4 nm. However, in general, the control of lateral size and thickness of the flakes remains a challenge. Also, the process struggles to produce uniform nanosheets without contamination as often the sheets produced were uneven with small fragments absorbed on large sheets.

An ion intercalation method was also proposed as a versatile method to produce flakes of inorganic layered compounds.[111] The most common ion-intercalation method is Li-intercalation followed by hydration.[112] The intercalation agent predominantly used is n-butyl lithium (Bu-Li) dissolved in hexane.

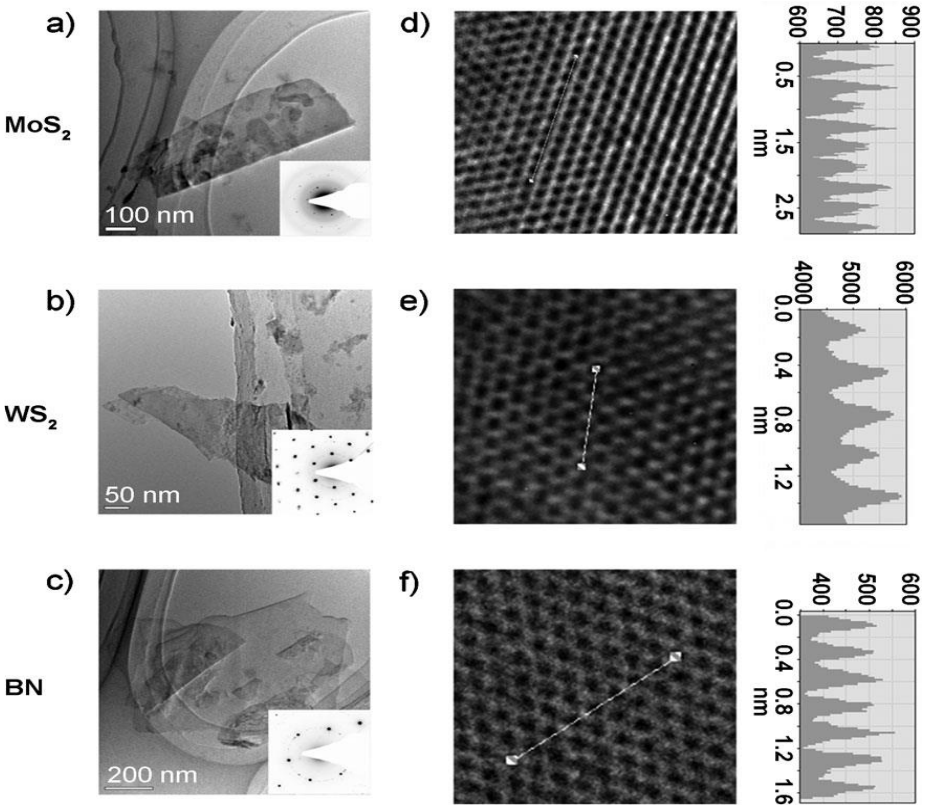


Figure 19. HRTEM images of MoS_2 (a), WS_2 (b), and BN (c) nanosheets. The insets show the corresponding electron diffraction images. The scale bars are 100, 50, and 200 nm, respectively. d–f) Atomic resolution HRTEM images. Reproduced with permission.[84]

The process can produce single layer MoS_2 and WS_2, often with the meta-stable 1T phase.[113] The 1T phase is induced through charge transfer from Li to the TMD. The critical step in this method is the formation of Li_xMS_2 (M=Mo or W), which can be tuned to control the yield of monolayers.[114] The degree of lithiation also influences the amount of 1T phase in the final product. Hexane is employed to remove excess lithium and organic residues from n-butyl lithium. Although the process claims to produce 100% atomically thin layers, challenges do remain in obtaining single layer reproducibility and control over the phase composition of the final product. Other drawbacks are the formation of metal nanoparticles and the precipitation of LiS_2 along with long synthesis time.

To address some of the issue above Zhang *et al*.,[115] developed an electrochemical Li-intercalation method and exfoliation in water/ethanol to produce various 2D TMD's (eg., MoS_2, WS_2, TiS_2, TaS_2, ZrS_2, $NbSe_2$ and WSe_2).[115,116] The layered crystal is employed as the cathode with lithium foil as the anode in a Li-ion battery setup as shown in Figure 20. The vigorous reaction between lithium and water (or ethanol) generates H_2 gas which pushes the adjacent layers apart. In contrast to the chemical Li-intercalation method with Bu-Li, which requires heating (100 ^oC) and long periods of time (3 days), this electrochemical process is conducted at room temperature and within 6 hours. Control of the Li-intercalation process is critical as insufficient Li-insertion leads to low-yield of single layer nanosheets while excessive results in destruction of the 2D nanomaterials. Nevertheless, the process suffers from poor yields and must overcome the limitations of cost and the pyrophoric nature of lithium.

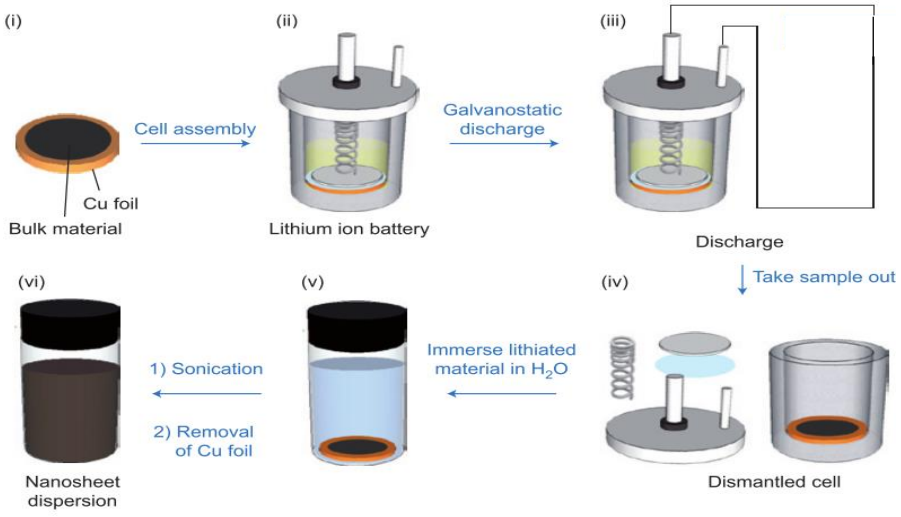


Figure 20. Schematic of the electrochemical lithiation process for the synthesis of 2D nanosheets from layered bulk materials. The cut-off voltage used to optimize the electrochemical lithiation conditions for preparations of few-layer TMDs is indicated. Reproduced with permission.[115]

In general top-down synthesis processes suffer from irreproducibility and poor controllability for producing large-area sheets with defined thickness. However, liquid

exfoliation is ideal for producing large quantities of small area sheets which can be used in composites, inks, batteries and supercapacitors. The 1T phase produced by Li-intercalation has shown excellent potential as electrocatalysts, photo catalysts for hydrogen evolution reaction and electrodes for energy storage devices.

1.3.3.2.2. Chemical vapour deposition

Chemical Vapour Deposition (CVD) is the most common and successfully employed bottom-up synthesis method for 2D materials. Most of the research on TMD growth using CVD has been focussed on MoS_2, since the indirect to direct band-gap transition was established when reduced from bulk to single layer[117]. The ability to grow high-quality, large-area films with scalable size, controllable thickness and excellent electronic properties makes CVD an attractive process. The different strategies employed for the synthesis are summarised below.

The typical precursors used are MoO_3 and sulphur powders, which were adopted from growth of IF and INT nanostructures as discussed in section 1.3.3.1. Initially, Lee *et al*.[118] employed seeding agents such as reduced graphene oxide (rGO), perylene-3,4,9,10-teracarboxylic acid tetrapotassium (PTAS) and perylene-3,4,9,10-teracarboxylic dianhrdride (PTCDA) on SiO_2/Si substrates to create a graphene-like surface to promote layer growth by using a setup as shown in Figure 21a. However, full coverage was a challenge using this method and MoS_2 films with a mixture of layer numbers were formed. Following this, Lin *et al*.[119] employed a wafer scale deposition process using the same chemical strategy by direct sulphurisation of MoO_3 thin layers on 2-inch sapphire substrates to form few-layered MoS_2 film as shown in Figure 21b. These films were polycrystalline and exhibited a high on/off current ratio, which makes them attractive for electronic device fabrication. Also, the superior

quality of MoS_2 layers on sapphire substrates in comparison to SiO_2/Si was emphasized by this method. However, controlling the thickness of the pre-deposited metal oxide was critical to achieve wafer scale uniformity.

a)

b)

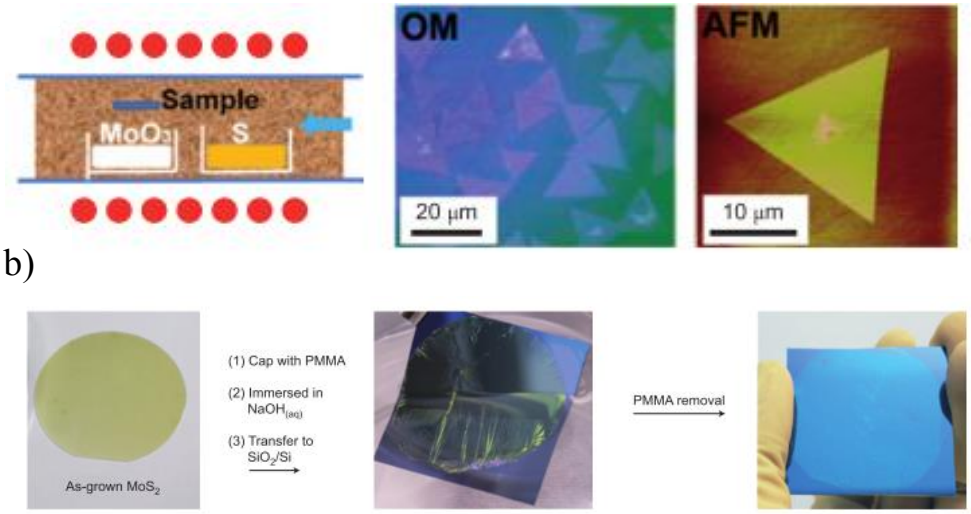


Figure 21. a) Schematic of method for the growth of a MoS_2 monolayer, also on a substrate (sample) from MoO_3 and S powders through a gas-phase reaction.[118]; b) Wafer-scale deposition of mono- to few-layered MoS_2 films obtained by direct sulfurization of MoO_3 thin films, and their transfer onto arbitrary substrates. Reproduced with permission.[119]

To precisely control the thickness of metal oxides, an atomic layer deposition was employed by Wang *et al.*[120]. The synthesis strategy involved thermally evaporating MoO_3 powder and reducing by sulphur to form MoO_2 micro-templates as shown in Figure 22, followed by annealing in sulphur vapour at high temperature. The rhomboidal microplates formed of MoO_2 are sulfurized on the surface and peeled using PMMA thin films. The process nevertheless still faced the limitation of obtaining full coverage. Also, MoS_2 is distributed on randomly isolated islands of MoO_2 flakes and depends on messy transfer procedures to obtain MoS_2 thin layers.

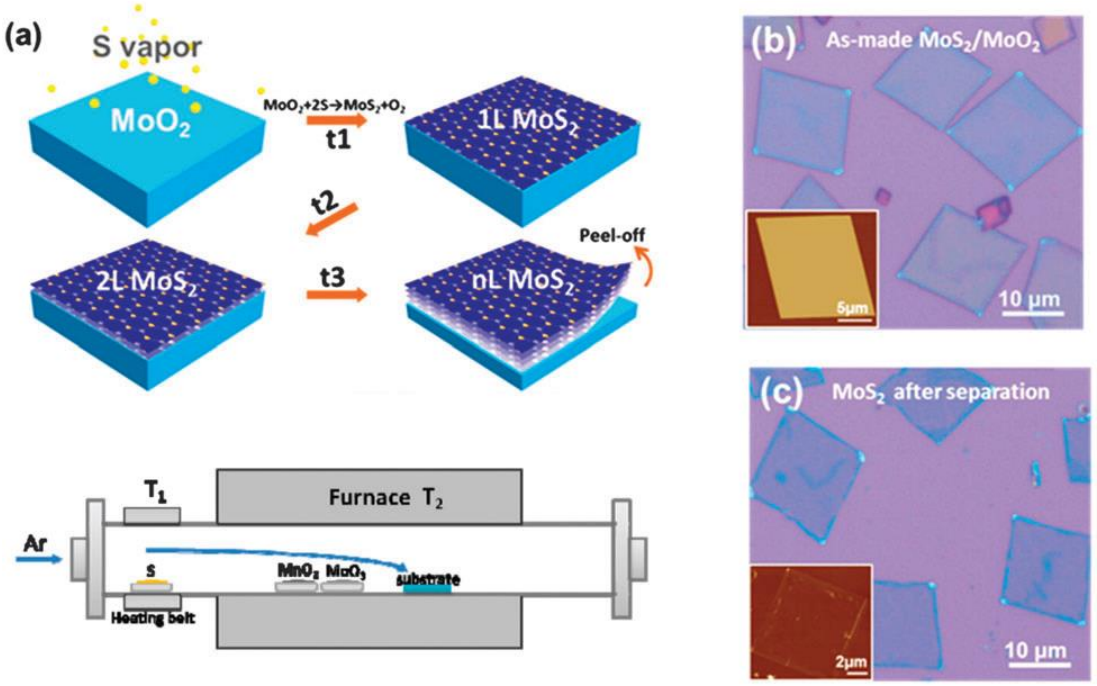


Figure 22. a) Schematic of the synthesis and cleavage of MoS_2. b), c) Pictures showing the as-synthesised MoS_2/MoO_2 layers on SiO_2/Si wafer and the peeled off MoS_2 layers after removing MoO_2 with atomic force microscope images as insets. Reproduced with permission.[120]

Recently, a refined CVD approach was proposed by Zande *et al.,*[86] to grow large, highly crystalline islands of monolayer MoS_2 up to 120 μm in size using solid MoO_3 and S precursors. In contrast to the previous work by Lee *et al.*,[85] this work did not use seeds to nucleate growth but instead emphasised carefully cleaned substrates and minimising exposure of precursors to air during storage. This method produced large single crystal triangular domains as seen in Figure 23, which coalesce to form larger areas in patches. However, there is limited understanding of the nucleation process and poor control over the growth leading to polycrystalline, multilayer films with significant amount of grain boundaries which would serve as defect. A significant reduction in yield was reported when dirty substrates or old precursors are employed.

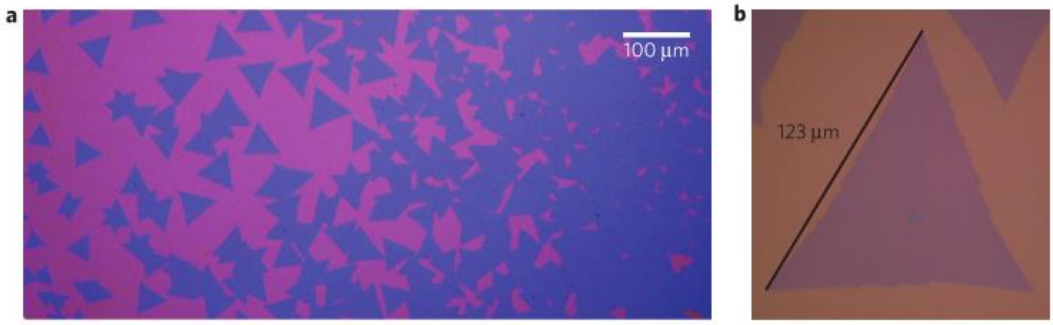


Figure 23. Large-grain MoS_2 growth. a. Optical reflection image of a CVD growth of a typical large-grain MoS_2 on SiO_2 (285nm)/Si substrate. b, Optical image of a monolayer MoS_2 triangle. Reproduced with permission.[86]

A similar growth of MoS_2 was reported by Najmaei *et al*.,[87] as shown in Figure 24. However, this study employed a controlled vapour phase sulphurisation using MoO_3 nanoribbons dispersed on the substrate. The nanoribbons offered a way of controlling the nucleation by varying their concentration on the substrate. The work also studied the grain morphology and grain boundaries structure of polycrystalline MoS_2 films that were formed.

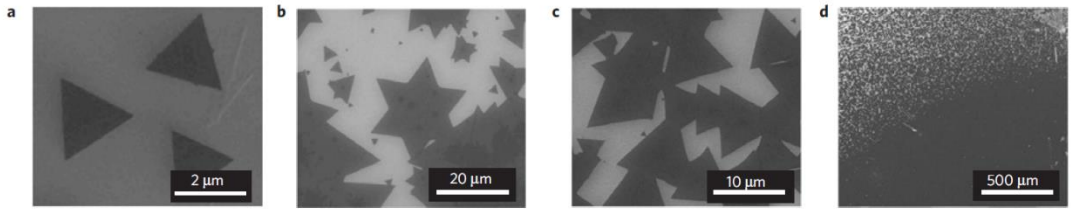


Figure 24. SEM images showing the growth of MoS2 from small triangles to continuous film. Reproduced with permission.[87]

An additional strategy to produce 2D TMDs was based on sulphurisation of Mo metal thin films reported by Zhan *et al*[121]. This approach has been studied since 1970 and it has been shown that sulphur atoms form ordered phases on Mo crystal face.[122] A film is formed by diffusion of sulphur from the nuclei of MoS_2 which appear in conjunction with chemisorbed sulphur species.[123] The process forms large-area polycrystalline few-layered MoS_2 film with limited control over the layer number and

grain sizes ranging from 10-30 nm. Also the MoS_2 layers show a metallic transport property with low on/off current ratio which could be due to the presence of unreacted metal impurities. Attempts have also been made to grow MoS_2 nanosheets on CVD graphene/Cu substrates using van der Waal epitaxy in-spite of the large lattice mismatch.[124] Polycrystalline MoS_2 films were formed on graphene with the similar orientation using ammonium thiomolybdate [$(NH_4)_2MoS_4$] as precursor. However, the formation of a large number of defects in MoS_2 in the form of impurities from precursors at heterogeneous sites and grain boundaries was observed. Another two-step thermolysis process was reported by Liu *et al.*,[125] for the formation large area MoS_2 thin layers by dip coating ammonium thiomolybdates [$(NH_4)_2MoS_4$] on various insulating substrates and converting to MoS_2 by annealing at 500°C followed by sulphurisation at 1000°C as shown in Figure 25. The second step helped to improve the crystallinity of the films that would enhance their photoluminescence intensity and electronic properties for use in field emitting transistors (FET).

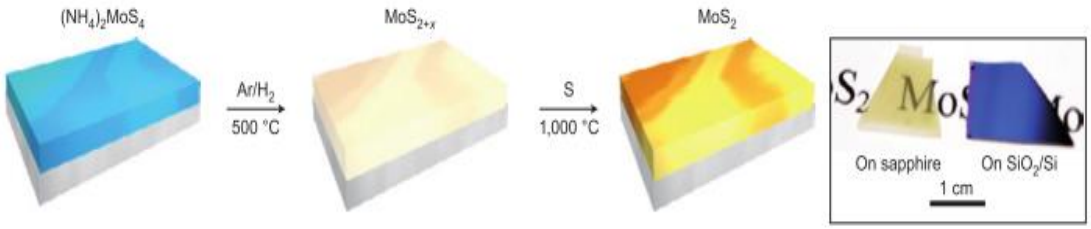


Figure 25. Schematic of MoS_2 layer deposited by two-step thermolysis, and the films obtained on a sapphire and silica substrate. Reproduced with permission.[125]

To enable better control of the precursors, systems have been designed either employing vaporisation and decomposition of single precursors in solution or metal and sulphur precursors in separate chambers as shown in Figure 26. Despite these promising initial reports, growth of large-area, single crystalline and uniform monolayer TMDs still remains a challenge.

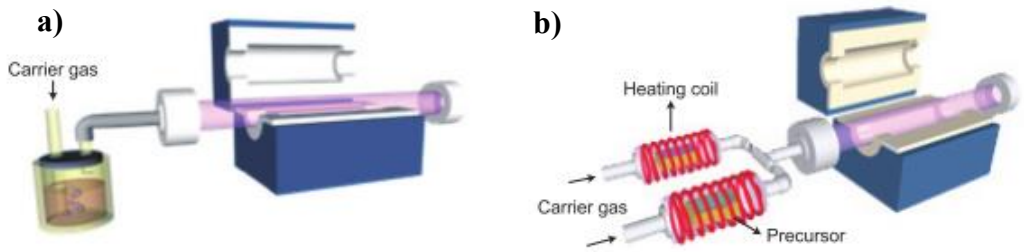


Figure 26. a) CVD of ultrathin TMDs by vaporization and decomposition of a single precursor in solution and (b) by vaporization and decomposition of metal and chalcogen precursors in solid forms. Reproduced with permission.[42]

With regard to work on WS_2, a controlled thermal reduction-sulphurisation was reported by Elias *et al*.,[88] to synthesise WS_2 thin films with thickness ranging from monolayers to few-layered. WO_x films were first deposited on the substrate and sulphurised under vacuum at high temperature (750-950 ^oC) as shown in the schematic in Figure27a. The thickness of the WO_x film prepared was varied to control the layer number, with 1 nm film producing monolayer WS_2. However, the crystallinity of the films formed and their uniformity across the substrates were not established. The work also reported an efficient transfer technique for WS_2 films formed onto different substrates as shown in Fig 27b. This method was also proposed for the synthesis of heterogeneous systems of MoS_2 and WS_2.

Recently Rong *et al*.,[126] showed that controlling the amount of sulphur and its introduction time is critical to achieve growth of large area domains on 300 nm SiO_2 coated Si wafers. The CVD process used a two-stage furnace with WO_3 and S as precursors heated separately as shown in Figure 28. The process formed a large single crystal WS_2 with edges up to 370 μm. Nevertheless, the full coverage with control over thickness of the WS_2 film was still a challenge that was not addressed. The method emphasised the importance of precursor control and its influence on the growth of high quality TMDs.

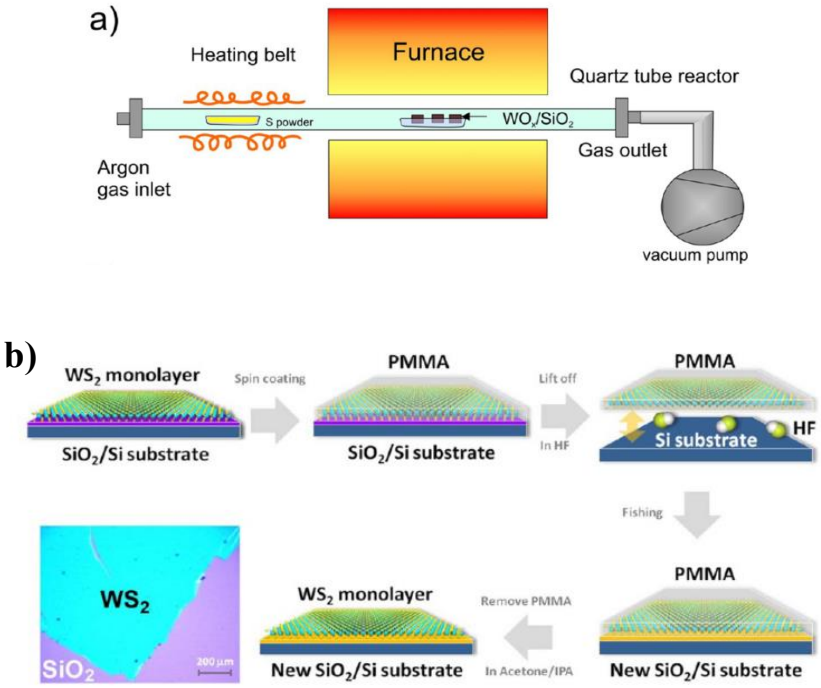


Figure 27. a) Schematic of the experimental setup used for the synthesis of WS_2 films involving high temperature treatments under a sulphur/argon environment at low pressures (450 mTorr). b) Schematic of PMMA assisted transfer method onto different substrates. Reproduced with permission.[88]

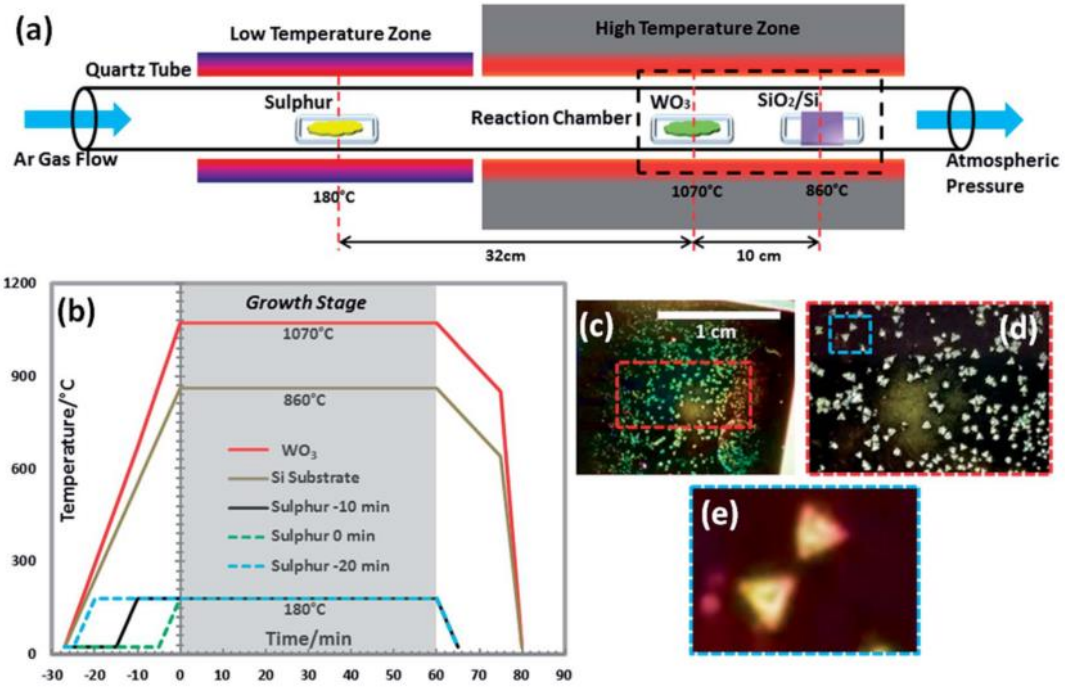


Figure 28. Atmospheric pressure CVD synthesis of large-area WS_2 crystal domains on the SiO_2/Si substrate. (a) Schematic of the corresponding CVD experimental set-up with a highlighted WS_2 reaction chamber (black dashed line). (b) Temperature profiles employed for formation of WS_2 on the SiO_2/Si substrate with sulphur introduced at 0, -10 and -20 min due to the target reaction

temperature of 1070 ºC/ 860 ºC. (c) Photo of large triangular WS_2 crystals deposited on a 2 cm SiO_2/Si substrate. (d and e) Zoom-in images chosen from the selected area (red dashed line) in (c) and (blue dashed line) in (d), respectively, showing triangular WS_2 domains. Reproduced with permission.[126]

The CVD process to form thin films of WS_2 is still in the initial stages of investigation. Nonetheless, methods established for MoS_2 could potentially be translated for the synthesis for WS_2 thin films and large area single crystals. Furthermore, in spite of the different synthesis methods employed for the synthesis of MoS_2 and WS_2 thin films and large crystals with relative success, an understanding of the process of nucleation and growth is still lacking in the field. Additionally, more advanced control of precursors system is necessary to form large area films reproducibly and much development is still required on this front.

1.3.4. Properties of inorganic nanostructures

The properties of nanostructured materials are predominantly determined by their intrinsic structure and chemical bonding. The structure of the prominent inorganic nanostructures was discussed in section 1.3.2. The physical and chemical properties of inorganic nanostructures are variable and depend to a certain extent on the properties of the bulk compounds from which they are synthesised. For example, BN is an insulator; WS_2, MoS_2 are semiconducting and $NbSe_2$ is superconducting. Thereby, the composition of the material along with its morphology and atomic structure determine the properties of nanostructures. In this section, the key properties of three prominent morphologies (0D-IF, 1D-INT, 2D-IGA) of MoS_2 and WS_2 will be discussed.

1.3.4.1. Electronic Properties

The electronic properties of IF-MoS_2 nano-octahedra were analysed by Enyashin *et al.*[127] using electron energy loss spectroscopy (EELS). In contrast to examples such as nanoplatelets, nanotubes and quasi-spherical nanoparticles of MoS_2 which are semiconductors, irrespective of their size and exact stoichiometry,[54,127] all hollow octahedral MoS_2 fullerenes are metallic as they exhibit a nearly vanishing band gap between the HOMO and LUMO. Thus the electronic property of MoS_2 nano-octahedra is radically different to the bulk material.

Nanotubes of WS_2 and MoS_2 are always semiconducting making them attractive for device applications. The bandgap of semiconducting nanotubes, such as MoS_2, shrinks with decreasing nanotube diameter (although it is never zero). This effect can be explained by two factors: the small quantum size effect of the closed nanostructures, and the deformation of the chemical bonds in the curved sheet leading to a less than perfect hybridization of the atomic orbitals.[128] Armchair nanotubes have an indirect electronic transition, while zig-zag nanotubes, have a direct transition suggesting that they could emit strong luminescence on optical or electrical excitation.[69] Hence, the nanotube tube size and structure can be used to control the band gap to suit a particular application.

For 2D MoS_2 there is an indirect to direct band transition in the d-electron system when the bulk material is thinned down to single layer.[117] This change in band structure is attributed to quantum confinement and the resulting change in hybridization for p_z orbitals of S atoms and d orbitals of Mo atoms. All MoX_2 and WX_2 compounds are expected to undergo this transition with a decrease in layer number to monolayer. This would cover the band gap range from 1.1-1.9 eV.[129] The evolution of this electronic

structure with varying thickness can be characterised using photoluminescence (PL) spectra as seen in Figure 29B.[117] While bulk MoS_2 gives negligible PL, the PL intensity is inversely proportional to the thickness of the MoS_2 layer thickness with monolayer exhibiting the strongest PL intensity and highest quantum efficiency with emissions at 670 and 627 nm. Raman scattering can also be used to differentiate layer thickness of MoS_2 nanosheets as reported by Lee *et al.*[130] and shown in Figure 29C, with the frequency, intensity and width of the E_{2g} (strong in-plane) and A_{1g} (out-of-plane) vibrations strongly influenced by the layer number.

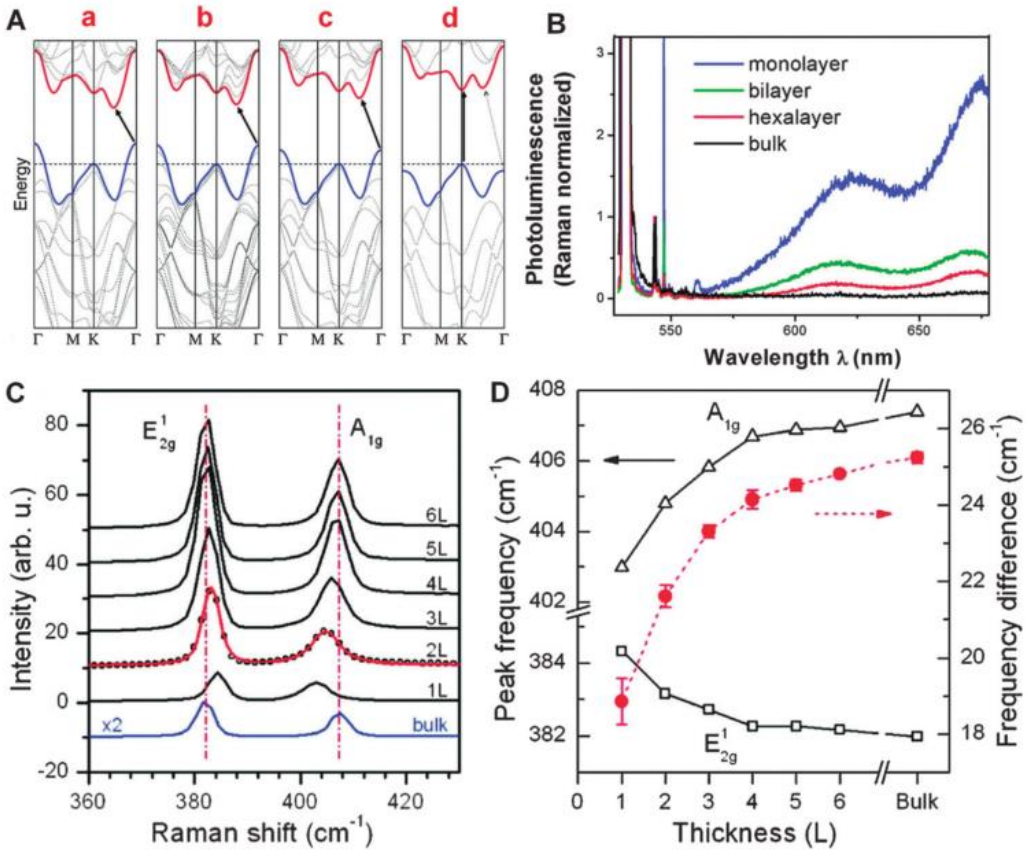


Figure 29. (A) Calculated band structures of (a) bulk MoS_2, (b) quadric-layer MoS_2, (c) bi-layer MoS_2, and (d) monolayer MoS_2. (B) Photoluminescence spectra normalized by Raman intensity for MoS_2 layers with different thickness. (C) Raman spectra of thin-layer and bulk MoS_2 films. (D) Frequencies of E^1_{2g} and A_{1g} Raman modes (left vertical axis) and their difference (right vertical axis) as a function of layer number. Reproduced with permission.[131]

1.3.4.2. Mechanical Properties

The mechanical properties of bulk materials are affected by the presence of defects and thereby the theoretical strength is not generally achievable. On the contrary, nanostructures, which can theoretically be produced to be almost defect free, could achieve close to the theoretical strength which would reflect in superior mechanical properties. Mechanical property of WS_2 and MoS_2 nanoparticles, nanotubes and nanosheets deserve individual discussion.

Mechanical studies show that under mild loads (≤0.5 GPa) the spherical MS_2 (M=W, Mo) nanoparticles exhibit rolling. Under heavier loads the nanoparticles slowly deform and exfoliate giving up MS_2 layers that stick to the underlying surfaces to provide easy shearing.[17] The fullerene-like WS_2 and MoS_2 nanoparticles also have been shown to withstand shockwaves up to 25 and 30 GPa respectively with the concurrent temperatures raising up to 1000ºC.[132] There has been no evidence of significant structural deformation or phase changes, making these materials probably the strongest cage molecules. They offer a wide range of applications for shielding materials for cars and perhaps even as additives to strengthen construction materials. It is noticeable that carbon nanotubes and fullerene are unlikely to be stable under high pressure owing to the 1.7 GPa graphite to diamond transformation[102] whereas these materials show no high resilience with no degradation for hydrostatic pressures up to 20 GPa.

One potentially important application of nanotubes is in composite materials. A comprehensive study by Tenne and Seifert[5] on the mechanical properties of WS_2 and MoS_2 nanotubes using SEM, TEM and scanning probe microscope concluded that they had substantial potential for being part of 'ultra-high strength nanocomposite

technology'. Tensile and buckling experiments of individual WS_2 nanotubes were carried out in a high-resolution scanning electron microscope. The Young's modulus of the WS_2 nanotubes was found to be in good agreement with the value (150 GPa)[133] of the bulk material. The shock resistance of WS_2 nanotube was determined to be 21 GPa. The strength of the WS_2 nanotubes was found to be 16 GPa and elongation to failure was 12%.[134] Deformation of these layered materials occurs through shearing of soft layers as shown by bending test models. Hence the shear deformation is through slip between the adjacent WS_2 layers and the shear modulus was calculated to be 2 GPa[135]. Although the strength of WS_2 nanotube is not as high as single walled carbon nanotubes (SWCNT's), but properties still surpass that of bulk materials as shown in the Table 3.

Material	Modulus of elasticity (GPa)	Tensile Strength (GPa)	Elongation (%)%)
Steel Alloy 4340	**207**	**1.76**	**-**
Stainless alloy 440A	**200**	**1.79**	**12**
Tungsten	**0**	**0.76**	**3.5**
Diamond	**700-1200**	**1.05**	**2**
Silicon nitride	**304**	**0.7-1**	**-**
Zirconia	**205**	**.08-1.5**	**-**
Armid fibre	**60-150**	**3.6-4.1**	**-**
Carbon fibre	**200-750**	**4.65-7.1**	**2.8**
E Glass	**72**	**3.45**	**1.8**
SWCNTs	**1000**	**20-63**	**4.3**
WS_2 Nanotubes	**150**	**16**	**10**

Table 3. Mechanical properties of strong materials reproduced from Kaplan-Ashiri 2005 & 2007 Reproduced with permission.[133,135]

Since the isolation of pristine graphene, the strongest material ever measured with Young's modulus of 1 TPa[136], mechanical properties of 2D nanomaterials are examined with great interest. The elastic properties of freely suspended MoS_2 nanosheets, with thickness ranging from 5 to 25 layers, was examined using AFM by Castellanos-Gomez *et al*.,[137] as shown in Figure 30. A Young's modulus of 0.33±0.77 TPa was reported, which is exceptionally high for MoS_2 nanosheets and comparable to graphene oxide. This value is also higher than the Young's modulus for bulk MoS_2 (0.24 TPa), possibly due to the lower density of stacking faults in the thinner regions. The nanosheets were also shown to exhibit low pre-strain, and were able to withstand the elastic deformations up to tens of nanometers without breaking.

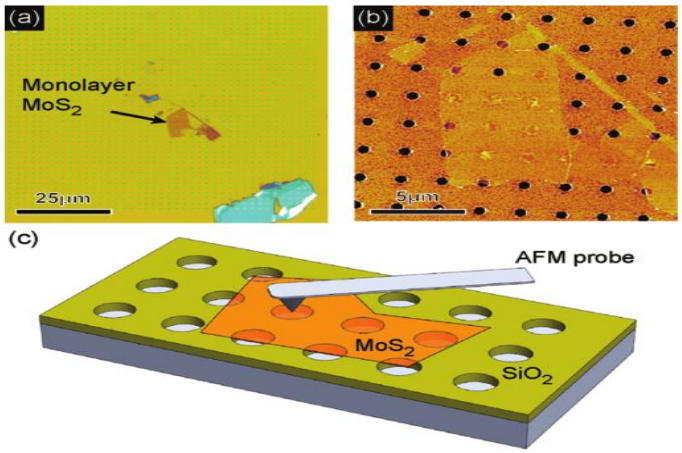


Figure 30. Sample preparation and the measurement method a) Optical image of a monolayer MoS_2 flake transferred onto a prepatterned SiO_2 substrate; b) AFM image of the same single layer MoS_2 as in part c) schematic of the indentation experiment. Reproduced with permission.[138]

In another work by Bertolazzi *et al*.,[60] Young's modulus of 0.27 TPa was reported for monolayer MoS_2. This value is lower than that reported for multilayers but higher than bulk. The measured elastic strength for monolayer MoS_2 was found to be in the range of 6-11% of its Young's modulus, which is the theoretical upper limit of a material's breaking strength, i.e. intrinsic strength of interatomic bond in crystals. This led to the conclusion that the mechanically exfoliated MoS_2 nanosheets are highly

crystalline and almost defect free, which makes them attractive for flexible electronic and optoelectronic devices.

1.3.4.3. Tribological Properties

Despite the impressive mechanical properties, it is the tribological properties of these materials that make them unique. In fact bulk WS_2 was developed by NASA as a lubricant for the Mariner deep space probe.[139] The extremely low dynamic coefficient of friction of 0.03 enables it to perform well as a solid lubricant in space, in vacuum atmosphere and at extremely high temperatures. WS_2 reduced wear in the system contributing to much longer lifetimes of the space probe.[17] The spherical fullerenes of these materials are now exploited as solid lubricants, hypothetically acting as 'nano ball bearings'. Their excellent tribological properties result from factors such as the lack of dangling bond and edge effects, making the IF particles chemically inert. Also the exfoliation of outer layers during wear could possibly lead to coating of the metal surface with extremely low friction WS_2 layers.[140]

1.3.5. Application of inorganic nanostructures

Various applications have been proposed for TMDs in different morphologies of IFs, INTs and IGAs nanostructures. IF MX_2 have shown to exhibit excellent solid lubricant behaviour with potential applications in automotive and aerospace industries, home appliances, and medical technology.[5] Other proposed applications for INT and IF include catalysis, rechargeable batteries, drug delivery, solar cells and electronics.[16] IGAs have intrinsic band gaps and high mobility which might complement graphene in electronics[63] and photodetectors[60]. In this section, potential applications being pursued currently for MoS_2 and WS_2 in various fields are discussed.

1.3.5.1. Electronic Applications and Devices

The desirable properties required for next-generation digital transistors are high charge carrier mobility for fast operation, a high on/off ratio (on-state to off-state conductance) for effective switching, high conductivity product of charge density and mobility, low off-state conductance for low power consumption during operation, flexibility and transparency for flexible electronics.[141,142] There has been substantially interest recently in using 2D TMD nanosheets for high performance field effect transistors (FETs) and other optoelectronic devices.[143] Being semiconducting by nature, the most important application of this class of materials is in digital electronics as transistors. The challenge in the field of digital electronics is to scale down the size of the transistors. However, with the reduction in size, the dissipation of heat is difficult due to limitations from quantum effects. Currently silicon based metal oxide semiconductor FETs (MOSFETs) with feature length of 22 nm are the state of the art material system.[144] 2D semiconductor TMDs such as MoS_2 offer an important advantage when compared with classical 3D electronic materials because of their sub-nanometre thickness. This is coupled with tuneable bandgaps, typically in the 1–2 eV range that can offer for high on/off ratios[61], and more efficient control over switching[145], which are the main limiting factors to transistor miniaturization. 2D TMDs also offers attractive processability, lack short channel circuits and less power dissipation that could enhance device performance.[146]

The majority of the work has focussed on using single-layer MoS_2 with a direct band gap of 1.83 eV obtained using mechanical exfoliation. Initially back-gate configuration was employed for transistors based on MoS_2 nanosheets with SiO_2 as dielectric to achieve carrier mobility of 10 $cm^2 V^{-1} s^{-1}$. Subsequently Radisavljevic *et*

al.[61], reported the use of an atomic layer deposited (ALD)-HfO_2, with a high-k gate dielectric to improve the FET performance as shown in Figure 31. This led to significant increase in carrier mobility to over 200 $cm^2\ V^{-1}\ s^{-1}$ at room temperature, and a large on/off ratio of 1 x 10^8 and an ultralow standby power dissipation. Following this the performance of HfO_2 as dielectric was studied by Yoon *et al*.,[147] The results revealed the distinct advantages obtained using MoS_2 based FET such as large on/off ratios, immunity to short channel effects, and abrupt switching behaviour. Although the relatively low carrier mobility restricts its use in high-performance devices, the wide gap and 2D morphology of TMDs make them ideal candidates for low-power electronic applications.[142]

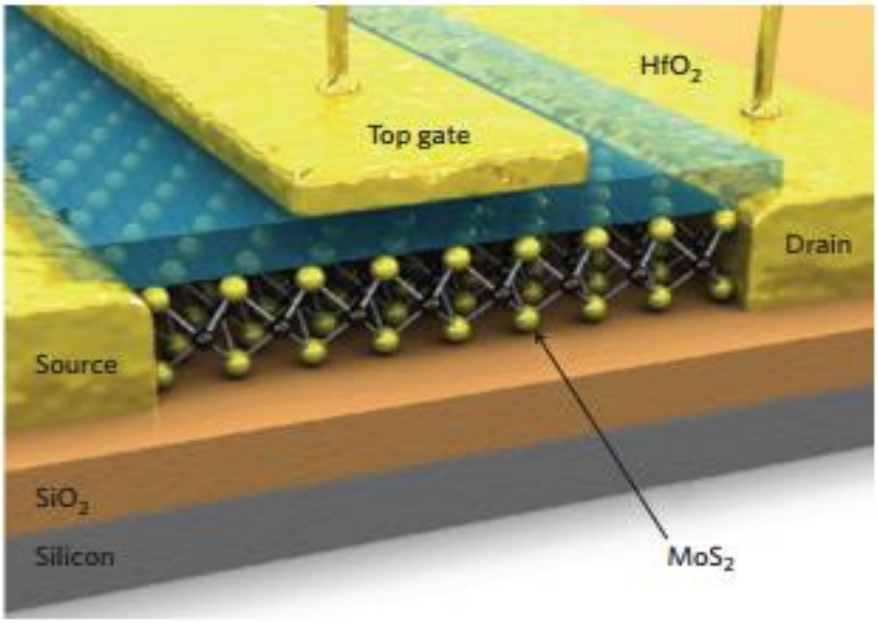


Figure 31. Schematic of HfO_2-top-gated monolayer MoS2 FET device c, Integrated circuit based on single-layer MoS2. Figure reproduced with permission.[63]

The next step towards practical electronic devices is the integration of individual transistors into a logic circuit. A simple circuit consisting of two-transistors has been demonstrated by Radisavljevic *et al*.[148] to amplify signals and perform basic logic operations. Wang *et al*.[149] further demonstrated the feasibility of incorporating MoS_2

transistors into complex circuits. In this work, they incorporated 12 transistors side by side on a single sheet of bilayer MoS_2 to perform multiple functions such as NAND(Negated AND or NOT AND) gate, a static random access memory and a five-stage ring oscillator as shown in Figure 32.

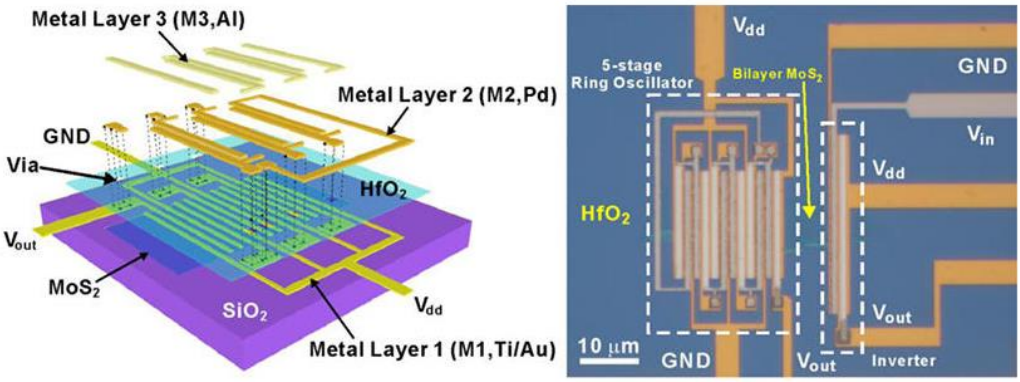


Figure 32. A five-stage ring oscillator based on bilayer MoS2. (a) Schematic of the electronic circuit of the five-stage ring oscillator. (b) Optical micrograph of the ring oscillator constructed on a bilayer MoS2 thin film. Reproduced with permission.[149]

1.3.5.2. Optoelectronic devices

Optoelectronic applications such as lasers, LEDs, solar cells, optical switches, photodetectors and displays have studied the use of nanomaterials such as carbon nanotubes, semiconductor quantum dots and nanowires.[150–153] 2D semiconductors with direct band gap at monolayer would be ideal components required for these future applications as they are atomically thin and processable. TMDs, such as MoS_2, are a promising candidate for optoelectronic devices mainly due to their wide band gap (1.2-1.9 eV for MoS_2, depending on thickness) which can interact with light especially in the visible region.[61,148] These devices could enable the generation, detection, and control of light. Flexible and transparent electronic devices are a corner stone of solar arrays, wearable electronics and transparent displays. For transparent conductors, graphene's high conductivity and low broadband absorption makes it an ideal

candidate[154], while for 2D dielectrics layered perovskites and BN[155] are promising. TMDs are also attractive as light-absorbing material in thin-film solar cells[156]. The band gap of these materials can also be tuned by intercalation of metal ions and organic molecules[41,112], which allows optical absorbance to be tuned in photovoltaic applications. A variety of photovoltaics and photodetectors based on TMDs have been demonstrated including photosensitive MoS_2 and WS_2 thin films[157], single layer MoS_2 phototransistor with potential as a photodetector[158] and multi-junction solar cells which incorporate materials with different bandgaps to allow photons of different energies in the full solar spectrum to be absorbed, reducing losses due to thermalisation[159]. Also, TMDs as light emitters for electroluminescence (photons emitted in response to electrical stimulus) and photoluminescence (material absorbs a photon and radiates a photon at sometimes different energy) are useful in devices such as LEDs and diode lasers. Examples of electroluminescence include MoS_2 emitting light by electrical excitation using Au nano-contacts and photoluminescence with MoS_2 monolayer.

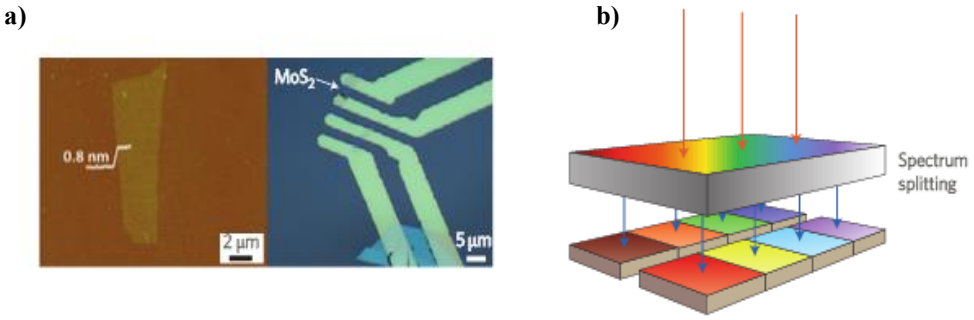


Figure 33. Current and proposed optoelectronic devices. a, Atomic force microscopy image of MoS_2 monolayer flake (left) and optical microscopy image of this flake made into a device with metal contacts (right). b, Proposed solar-cell device with parallel structures that may be fabricated using lift-off and printing techniques for patterning the semiconductor layers and a micro- or nanophotonic spectrum-splitting layer. The various bandgaps available from the different TMDCs are promising for use in such multi-junction photovoltaic devices. Reproduced with permission.[63]

1.3.5.3. Sensing, Catalysis and Electrochemical applications

Chemical, biological and gas sensors based on FETs have been receiving considerable attention recently. The FET-based detection relies on change in conductance of FET channel upon absorption of target molecules[160]. Following success with graphene FETs providing low noise and highly sensitive detection for various molecules[161], mechanically cleaved single- and multi-layer MoS_2 nanosheets have been investigated for NO detection[162]. MoS_2 sheets are n-type semiconductors but exposure to NO, which is an electron-withdrawing molecule, causes p-doping of the channel resulting in an increased channel resistance and a decrease in current. Additionally, FET-sensors based on bi-, tri-, and quadri-layers have been reported to exhibit high sensitivity for NO with detection limit down to 0.8 ppm, while single-layer devices show a rapid but unstable response. Nevertheless the low throughout of the fabrication procedure and poor reproducibility of sensing results have limited their wider use. In addition, a flexible gas sensor array on polyethylene terephthalate (PET) substrates has been demonstrated with MoS_2 thin films made from dispersions for NO_2 detection[163]. Further functionalization with Pt nano-particles increased the sensing sensitivity by 3 times with a detection limit of as low as 2 ppb.

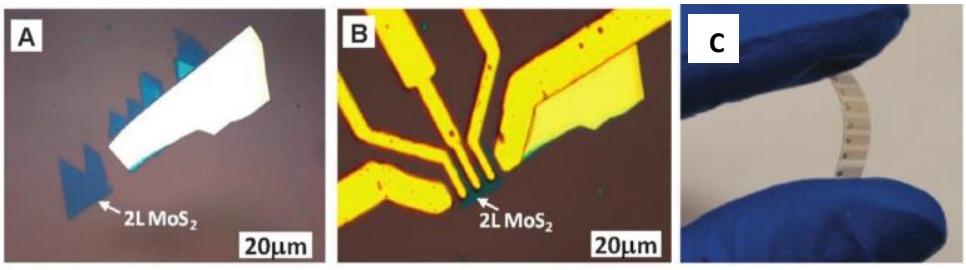


Figure 34. (A) Optical image of a bilayer (2L) MoS_2 deposited onto a Si substrate coated with 300 nm thick SiO_2. (B) Optical image of a FET device fabricated with the 2L MoS_2 film shown in (A), where Au electrodes work as the source and drain electrodes, and SiO_2 acts as the back gate. (C) Photograph of a fabricated flexible TFT array based on rGO electrodes and MoS_2 channel. Reproduced with permission.[162]

Electrochemical sensing enables detection of chemical and biological species. Reduced MoS_2 (r-MoS_2) modified electrodes have been shown to exhibit good conductivity and fast electron transfer rates in redox systems which could be reliably used for glucose sensing, and selective detection of dopamine in the presence of uric acid and ascorbic acid.[164]

Originally the interest in MX_2 compounds stemmed from their application in hydrodesulphurisation (HDS) of petroleum products where they were used to remove sulphur from crude oil.[22] Different forms of MoS_2 have been tested for their HER activity in recent years.[165] Hollow nanoparticles of MoS_2 with non-perfect crystallinity were shown to have high reactivity and selectivity towards hydrodesulphurization of thiophene[22]. The deposition of Ni nanoparticles onto a MoS_2 nanotube was found to produce a very reactive and selective catalyst for hydrodesulphurization of thiophene and its derivative[24]. These kind of catalysts could play a major role in mitigating the environmental impact of sulphur-rich gasoline.

Recently, non-noble catalysts, in particular chalcogenides derivatives, have shown potential towards Hydrogen Evolution Reaction (HER). To date platinum has been the most electroactive catalyst that contributes to excellent reaction yield and low overpotential.[166] However, earth abundant and inexpensive catalysts still have to be pursed to make hydrogen production more viable. The identification of active edge sites for catalytic activity in MoS_2 nanostructures has paved way for exploring TMDs.[167] The MoS_2 catalysts for HER are compared by two metrics: namely, the intrinsic activity as measured by turn-over frequency (TOF) per surface of exposed Mo atom, and the total electrode activity measured by the potential to reach a current density of 10 mA/cm^2. MoS_2 HER catalysts have been applied in photoelectrochemical

devices where they serve as both light emitters and catalysts, but so far they exhibit poor performance for hydrogen production and require further work on surface engineering strategies.[168–170] Nonetheless, MoS_2 in combination with other semiconductor light absorbers has been successful for photocatalytic and photoelectrochemical water splitting[171–174]. MoS_2 with silicon can yield highly active complete water splitting cathodes[175]. Also the conformal MoS_2 protective layer will prevent corrosion of the silicon surface while simultaneously catalysing HER. In my research, WS_2 nanoflowers and exfoliated forms have been synthesised and investigated as electrocatalysts for HER in Chapter 3. The morphology ideal for this application is determined by the ability of the nanostructure to maximise the number of active sites with respect to the bulk structure. Attempts were made to improve the HER activity by increasing the number of active edge sites.

1.4. Summary

Inorganic nanomaterials are a relatively new class of compounds that have potential application in various fields. Investigation into WS_2 and MoS_2 is at the forefront of research in this field. Although extensive research is being carried out in this field, a detailed understanding of the synthesis method and properties of material tailored to the specific applications is needed to enable commercial applications in areas such as catalysts, electronics, and batteries. Different forms of these materials including inorganic fullerene-like (IF) structures, inorganic nanotubes (INT) and inorganic graphene analogues (IGAs) have been synthesized using a number of processes. These methods have been discussed in detail in this review along with their advantages and drawbacks. Of these methods, chemical vapour deposition, is very favourable as it enables synthesis of different structures selectively and reproducibly. The synthesis

and properties of IF and IN structures for WS_2 and MoS_2 have been studied to some extent and attractive for applications such as lubrication. Extensive investigation of the synthesis and properties of 2D TMDs still needs to be accomplished to enable critical applications. The IGAs show potential to complement carbon nanostructures for application in fields such as electrochemistry, catalysis, electronics *etc*. However, applications of WS_2 and MoS_2 are limited to a selected few which exploit their mechanical properties. My work aims to establish a simple synthesis method using CVD that would cater to production of different morphologies of inorganic nanostructures. This would enable study of properties of the different structures, mainly with respect to electronics and catalysis, which in turn would allow potential applications such as optoelectronic devices and electrocatalysis to be exploited.

Chapter 2. Chemical vapour deposition of tungsten disulphide (WS_2) nanoflowers

2.1. Introduction

WS_2 nanostructures have been synthesized through a variety different routes, including gas-phase reactions of oxides with H_2S/H_2 [6,7,176], decomposition of metal trisulfides[79,80], catalysed transport method[177,178], decomposition of ammonium salts[4], chemical vapour transport[179], plasma assisted chemical vapour deposition (CVD)[101], metal vapour CVD[77], aerosol assisted CVD[82] and solid template synthesis[7,79]. With all but the last of these techniques, there was limited control over the morphology of the resulting IF and INT nanostructures. Commercial quantities of these structures are synthesised from an oxide template which limit the morphology and enhance control.[6] In addition to these well-studied morphologies, the MS_2 (M=W, Mo) layered materials have been produced in other lesser known forms such as nanoflowers [30,31], nanoribbons [32,33], nanobuds [34] and nanocubes [35]. However, a reliable method to synthesize large quantities of these materials has not yet been established. To exploit the properties of WS_2 nanomaterials, methods that enable precise control of the morphology by means of chemistry of precursors rather than using predetermined templates are required.

In this chapter we outline a fast, catalyst free and easily scalable chemical vapour deposition technique for the controlled synthesis of well-defined tungsten disulphide (WS_2) nanomaterials on (100) silicon-based substrates using tungsten(VI)chloride (WCl_6) and sulphur as precursors. Though a similar strategy has been employed previously to obtain nanostructures of WS_2 and MoS_2 [30], here-in the process has been simplified greatly by limiting the number of critical parameters and using shorter time

periods to enhance control and scalability. Moreover attempts have been made to understand the structure and nucleation process of the resultant nanoflower morphology, along with a detailed parameter study to identify the window of formation for various morphologies.

2.2. Experimental

The synthesis process was carried out by chemical vapour deposition (CVD) inside a quartz tube in a conventional tube furnace (Instron SFL furnace model: 4850A). The synthesis of WS_2 using CVD process can be performed in a number of ways.[30,126,180] The widely used precursors are chlorides, owing to their high vapour pressures at relatively low temperatures (< 300 ^oC). Either elemental sulphur or H_2S can be used as the sulphuring agent. In this work, tungsten chloride is used as the precursor along with elemental sulphur. The precursors WCl_6 (2 mmol-99.9% purity) and colloidal sulphur (20 mmol-80% purity) were placed at definite positions inside the quartz tube: sulphur at 13.5 cm from one end of the quartz tube, WCl_6 at 18.5 cm further away along the tube and a (100) silicon substrate at 23.5 cm. This arrangement ensured that the precursors and substrate were at the core of the furnace during the reaction. The schematic of the experimental setup is shown in Figure 35. This setup was connected to argon flow of 100 sccm with the precursors as far away from the hot zone of the furnace as possible, to prevent any reactions whilst heating the furnace.

The parameter space for the CVD synthesis was chosen carefully after considering previously established work on the reaction between the chloride precursor and sulphur to form transition metal sulphides, which does not begin until 300 ^oC. Also the sulphides (MoS_2 and WS_2) form only at temperatures above 550 ^oC, initially in the rhombohedral structure, which subsequently transforms to the hexagonal phase with

increase in temperature. At intermediate temperatures of 615 °C, they form a mixture of rhombohedral and hexagonal phases.[30] Hence, temperature window between 650-850 °C was studied with the aim of producing the hexagonal phase of WS_2. Short reaction time periods of 5 minutes and 10 minutes were chosen in contrast to one hour time period employed widely, since 2H-WS_2 forms in as little as 2 minutes.[30]

Once the furnace reached the desired temperature, the reactants were positioned in the hot zone. The precursors remained in the hot zone of the furnace for the stipulated time (5 min or 10 min) for usual experiments and for studying nucleation, much shorter time periods (10s to 1800s) were employed. After this stipulated reaction time, the tube was either taken out (instant cooling or quenching) or left in the furnace to cool to room temperature (controlled cooling or annealing) with the furnace switched off and the argon flow at 100 sccm. The products were collected both from the silicon substrate marked as 1 in the schematic and also by-products from inner surface of the quartz tube marked 2 as shown in Figure 35. The simplicity and ease of the process makes it potentially suitable for up-scaling, which has been discussed under future work in section 6.2.1.

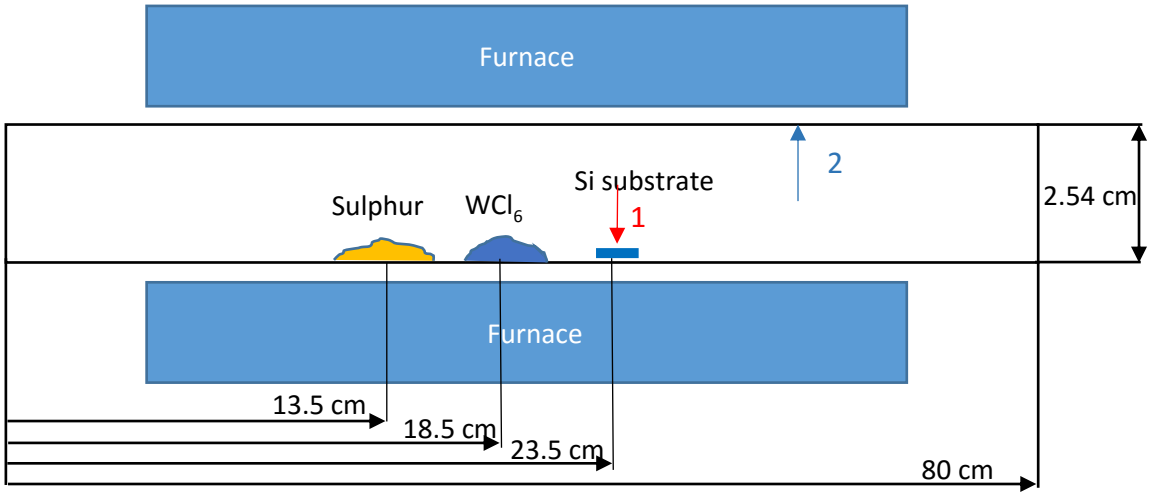


Figure 35. Schematic of experimental setup for chemical vapour deposition of WS_2 nanoflowers

For scanning electron microscopy (SEM) studies, the as-grown deposit on the silicon substrates were used. The morphology of the material deposited on the substrate was studied using SEM (JEOL-840F, JSM 6500F) operating at 5 and 10 kV acceleration voltages. The diameter of the nanoflowers were determined using the SEM micrograph by employing image processing software GIMP. At least three images were processed for each condition and close to 100 readings were obtained from each micrograph to obtain the average and the error bar. The size and morphology of the deposits were determined by a JOEL 2000FX, JOEL-2010 and JOEL-3000F transmission electron microscopes (TEM) operated at an accelerating voltage of 200 kV and 300kV respectively. For TEM, few milligrams of deposit was collected from the substrates, dispersed in ethanol and sonicated for a minute using an ultrasonic tip. A few droplets of the suspension were dropped onto a TEM grid and dried in air for a few minutes. EDX mapping was obtained using JOEL-3000F, operated at 300 kV with field emission gun to confirm composition. The Raman spectra of the deposits were obtained using a JY Horiba Labram Aramis imaging confocal Raman microscope with a 532 nm green laser using as the grown samples. X-ray diffraction of the as-synthesised deposits was carried out on a Siemens D5000 X-ray powder diffractometer. The range of 2θ employed was 10^{o}-60^{o} with a step size of 0.050^{o} and count time of 10 sec.

2.3. Results and Discussion

2.3.1. Parameters for synthesis of WS_2 nanoflowers using CVD

The Scanning electron micrographs (SEM) provides an overview of the parameter space that has been studied with the help of the CVD process. The structures obtained

by systematically varying the temperature and time for the two different methods of cooling, namely rapid and controlled cooling are presented in Figure 36 and 37 respectively. By systematic variation of the temperature and time, their role on the final morphology and the amount of deposits have been studied.

The predominant morphology (>90 %) obtained by this synthesis process is that of the nanoflowers. The morphology, structure and composition of these nanoflowers have been discussed in detail in the following section on characterisation (section 2.3.3). With variation in temperature and time, subtle but significant changes have been obtained in the nanoflower morphology, which are presented under evolution of nanoflower morphology (section 2.3.5) later in this chapter. Apart from the time and temperature of the process, the method of cooling was found to play a role in determining the final deposits as well. Controlled cooling generally led to an increase in nanoflower deposits, sometimes with slight changes in morphology (detailed in section 2.3.5), while instant cooling formed very crystalline and distinct looking nanoflowers as shown in Figure 37a.

From the scanning electron micrographs, the size distribution of the nanoflowers have been derived and presented in the following section (2.3.2), which discusses the effect of the synthesis parameters on the diameter distribution of the nanoflowers. Of the synthesis parameters, the temperature of the process has been found to have the biggest influence on the resultant morphology and size distribution. The time period of the synthesis process dictates the amount of deposits and its influence on the size distribution. The influence of the synthesis time on the nanoflower morphology is limited primarily due to the short time periods employed in this work.

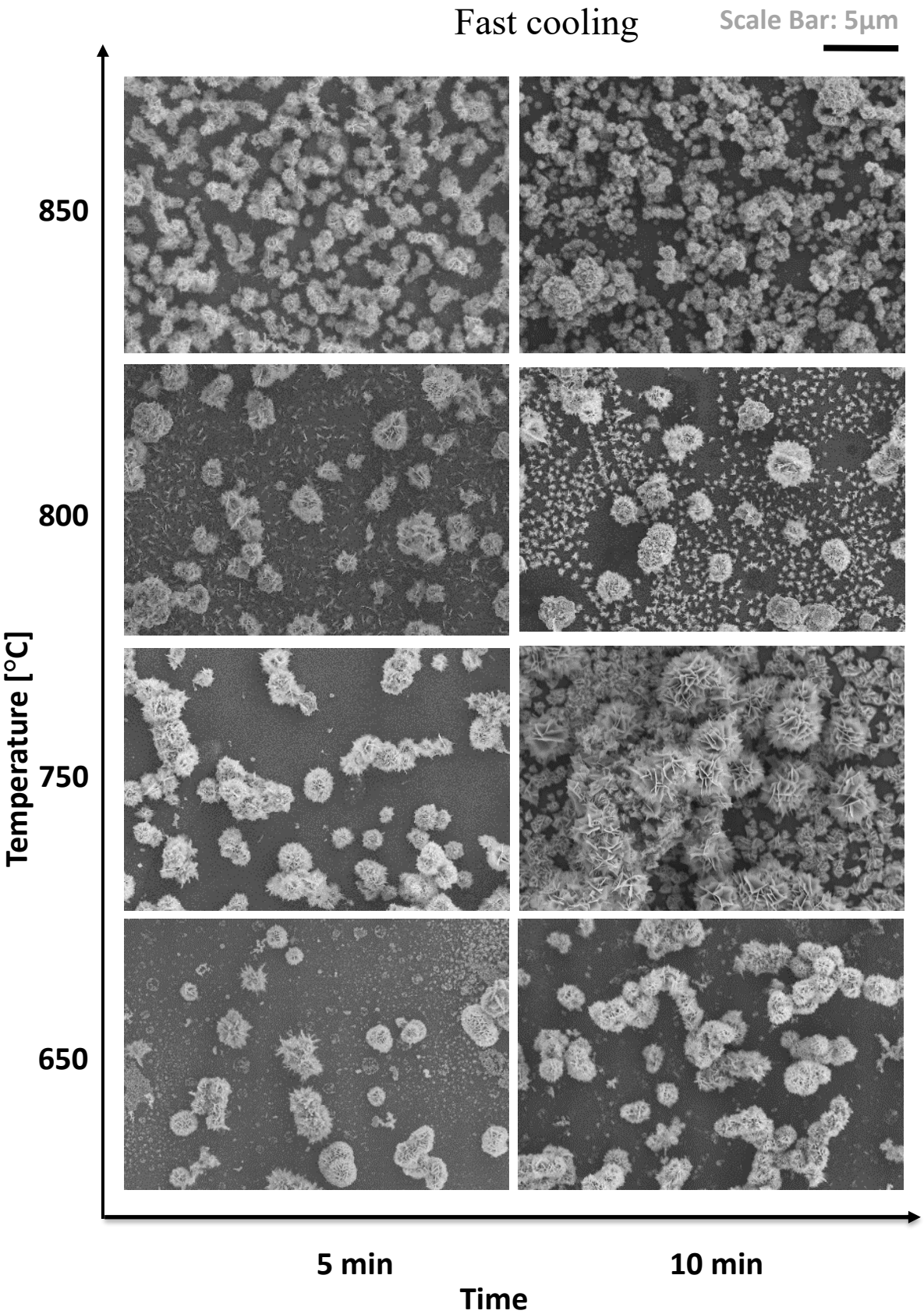


Figure 36. SEM chart showing the nanoflower morphologies obtained with rapid cooling/ quenching at various temperature (left axis) and time period (x axis).

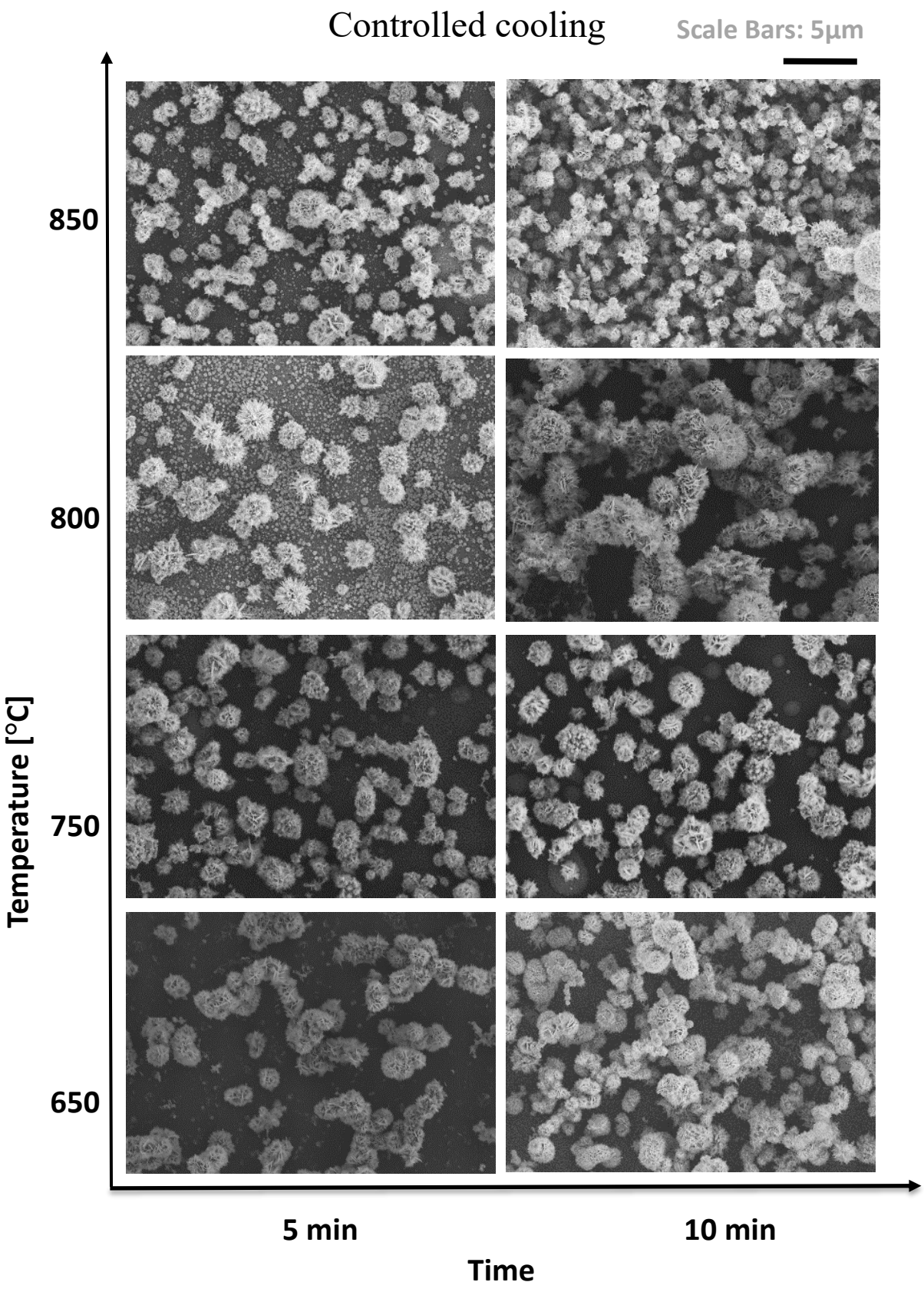


Figure 37. SEM chart showing the nanoflower morphologies obtained with controlled cooling at various temperature (left axis) and time period (x axis).

2.3.2. Diameter distribution of WS_2 nanoflowers

The average size of nanoflowers decreased from 2.68 μm to 1.07 μm when the temperature was stepped up from 650 ^oC to 850 ^oC, for quenched condition after 5 min. Hence, with respect to size distribution, increasing the temperature from 650 ^oC to 850 ^oC results in the reduction of the average size of the nanoflowers. This could be attributed to the increase in number of nucleation sites with temperature. The plot of the average size of the nanoflowers in Figure 38 shows the trend. Increasing the time period, in general leads to an increase in the size of the nanoflowers. However, there were exceptions for temperatures of 800 ^oC and 850 ^oC where the size of nanoflowers decreased. The reason could be the greater influence of temperature, as discussed earlier, in comparison to the time, leading to an increase in nucleation sites and consequently, a higher density of nanoflowers. Also it needs to be taken into account that shorter time periods are employed in this work, therefore their influence on the final deposit is rather limited. As a consequence of this shorter time period in almost all the conditions a wide distribution in the size of the nanoflowers formed is observed. This explains the large error bars in the plot Figure 38. At certain condition, tiny flakes covering the background were observed, as found in the 800 ^oC, 5 min, and controlled cooled condition. For the synthesis time of 30 min the average size of the nanoflowers were 1.07 μm but the distribution was not homogenous as shown in Figure 39. In many cases, the nanoflowers were agglomerated together, making it difficult to differentiate between them. With the increase in time period to 1 hour the average size increased to 1.28 μm and the nanoflowers were very homogenous as seen in Figure 40. This shows that with significant increase in time period, the size distribution of the nanoflower becomes more homogenous.

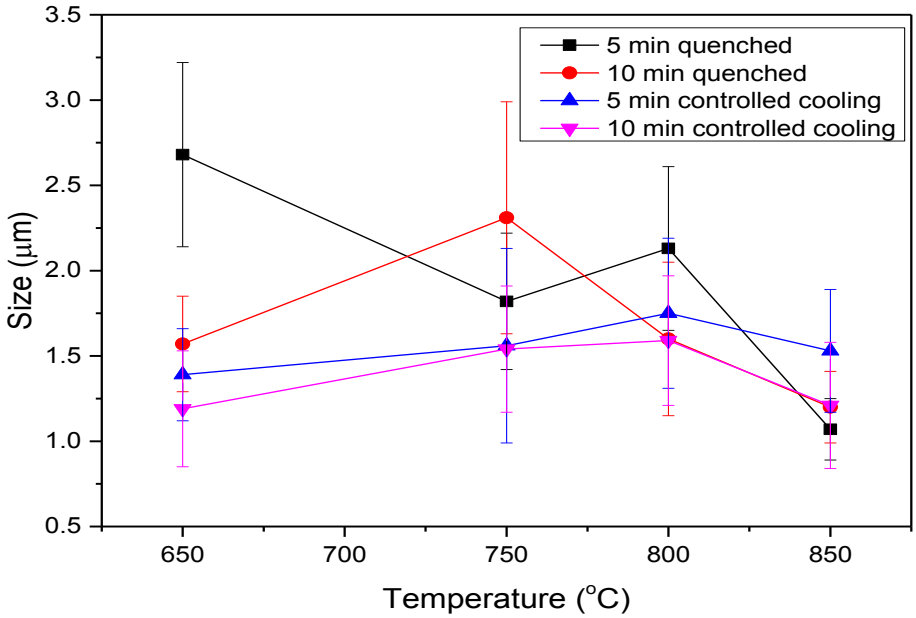


Figure 38. Average diameter distribution of nanoflowers with changes in temperature, time and cooling conditions.

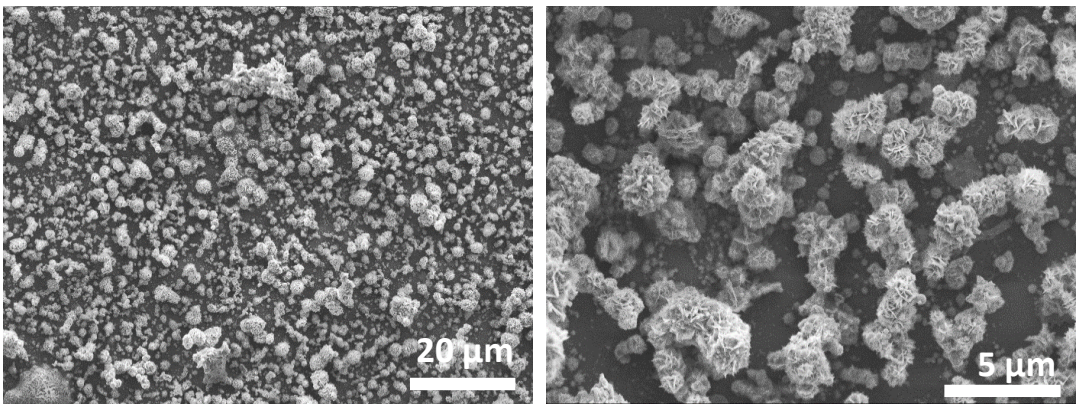


Figure 39. SEM micrograph showing non-homogenous growth of nanoflowers with increase in synthesis time 30 min.

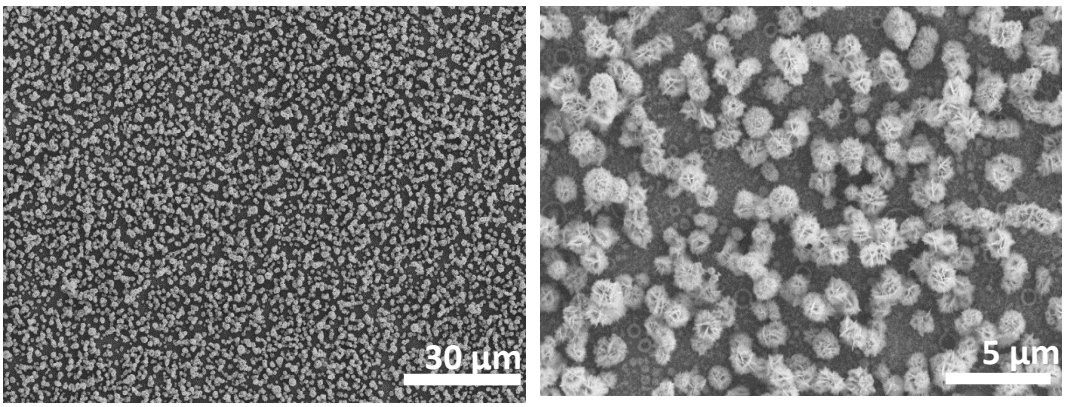


Figure 40. SEM micrograph showing homogenous growth of nanoflowers with increase in synthesis time period to 1 hour.

2.3.3. Characterisation of WS_2 nanoflowers

2.3.3.1. Electron microscopy

The nanoflower morphology obtained using CVD process and characterised by electron microscopy is shown in Figure 41a. The nanoflowers morphology is constituted by petals as clearly visible in the SEM micrograph. This has been reported previously by Li *et al.*,[30] where presence of 10-100's of petals combine together to form, spherical nanoflower structure. However, to help prove this and also to study the nanoflower morphology in detail sonification has been employed to dissociate the nanoflowers. The nanoflowers on sonification disassociated into triangular petals (flakes) with one corner always broken as highlighted in the Transmission Electron Microscope (TEM) micrograph in Figure41b, where the petal is broken at the left bottom corner. This suggests that these triangles were connected at only one of the edges to form the assembly of 3D nanoflowers, which is a novel observation that helps to understand these structures better. Further structural investigation of these nanoflowers using high-resolution TEM will be presented later in this chapter (section 2.3.7).

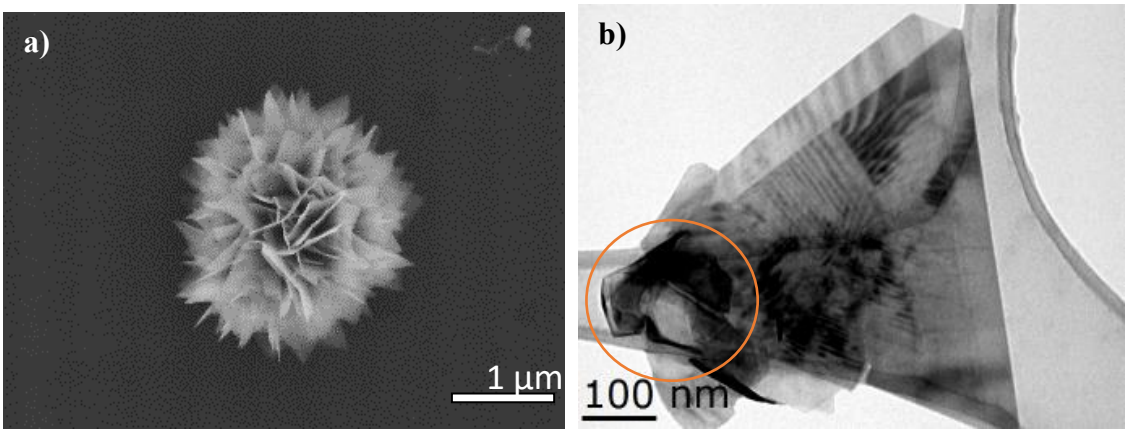


Figure 41. a) SEM micrograph of nanoflower b) TEM micrograph of a flake/ petal from the nanoflower obtain by dissociating it using sonication for 1 min.

2.3.3.2. XRD of WS_2 nanoflowers

X-Ray Diffraction (XRD) (Figure42) was used to determine the chemical composition of the material deposited and the presence of crystal phase belonging to the WS_2 crystalline phase was observed. The prominent signal of the (002) peak indicates the presence of well-stacked layered structure in the material deposited. The XRD plot has been indexed to the hexagonal structure of WS_2 with lattice constants: a=3.153, c=12.32 A^{o} (JCPDS card No: 84-1398).

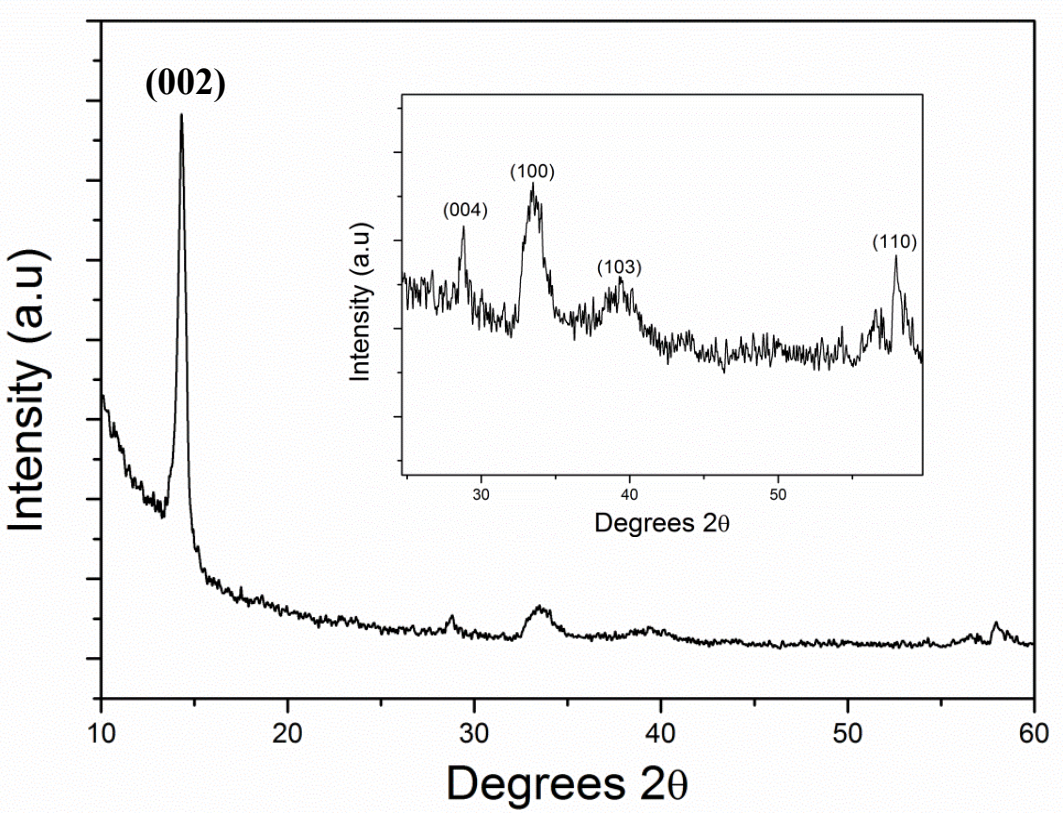


Figure 42. XRD of nanoflower deposits annealed at 850 ^{o}C showing characteristic peaks of crystalline WS_2 phase.

2.3.3.3. Raman spectroscopy of WS_2 nanoflowers

2H-WS_2 single crystals belong to the space group P 6_3/m m c (D_{6h}^4) and have 4 Raman active crystal vibrations at the τ-point of the reciprocal unit cell: A_{1g} (421 cm^{-1}), E_{2g} $^{(1)}$ (356 cm^{-1}), E_{1g} (306 cm^{-1}), and E_{2g} $^{(2)}$ (27 cm^{-1}).[181] Moreover, second and higher Raman transitions have been observed for excitation energies close to the band gap and the A and B exciton at 2.05 eV, 1.95 eV, and 2.36 eV, respectively.[182] The strongest of them, 352 cm^{-1} is attributed to the overtone of the LA-phonon at K-point [2LA(K)].[182] The Raman spectroscopy obtained from all the samples at different synthesis temperatures ranging from 650-850 ºC showed the characteristic peaks of A_{1g} (420 cm^{-1}) and E_{2g} (351 cm^{-1}) belonging to WS_2 for nanoflower sample deposit along with second order modes.

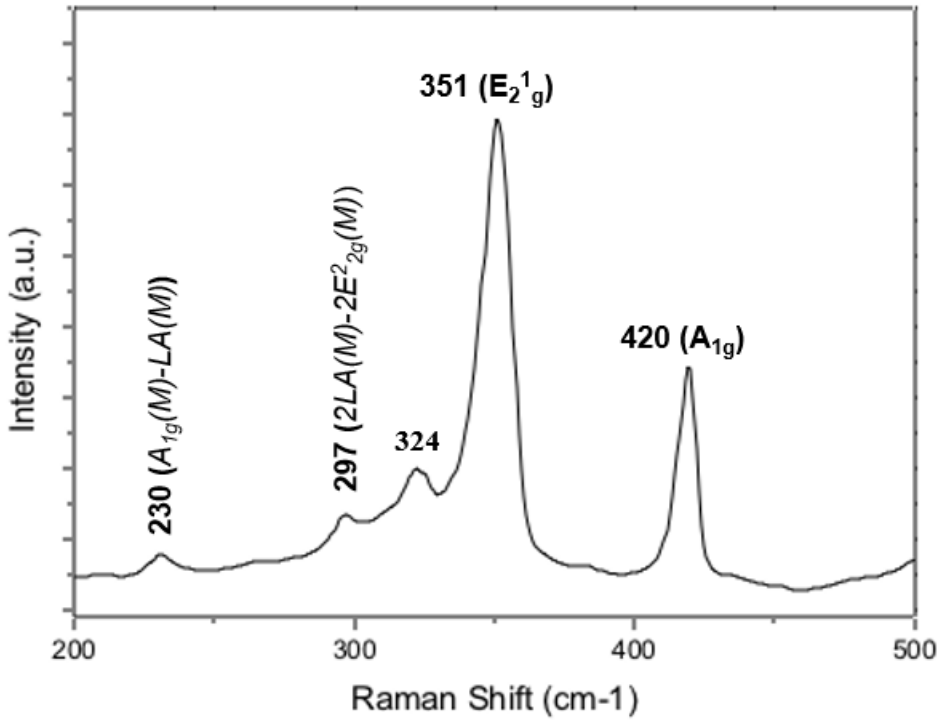


Figure 43. Raman spectroscopy of nanoflowers deposits annealed at 850ºC showing characteristic first order peaks and second order peaks corresponding to WS_2.

2.3.4. Dissection of WS_2 nanoflowers using Focussed Ion Beam (FIB)

To improve our understanding of the structure of nanoflowers and to also analyse the core of these self-assembled three dimensional (3D) structures, attempts were made to dissect them using a focussed ion beam (FIB) of gallium ions. This is a new approach that would give an insight into the core of the 3D nanoflower morphology. The difficulty with this technique is that gallium tends to deposit back on the surface of the cross section. Consequently to reduce this, a lower current was used and the dissection was carried out in small steps (shown in appendix). The resultant image in Figure 44 showed that the WS_2 petals were oriented in random directions and that there appears to be a core constituting the centre that did not contain any nanosheets. The core could have been initiated by a nanoparticle, which we believe is the source from which nanoflowers originate. This will be discussed in detail in the later part of the chapter (section 2.3.6) under nucleation and evolution of the nanoflower morphology.

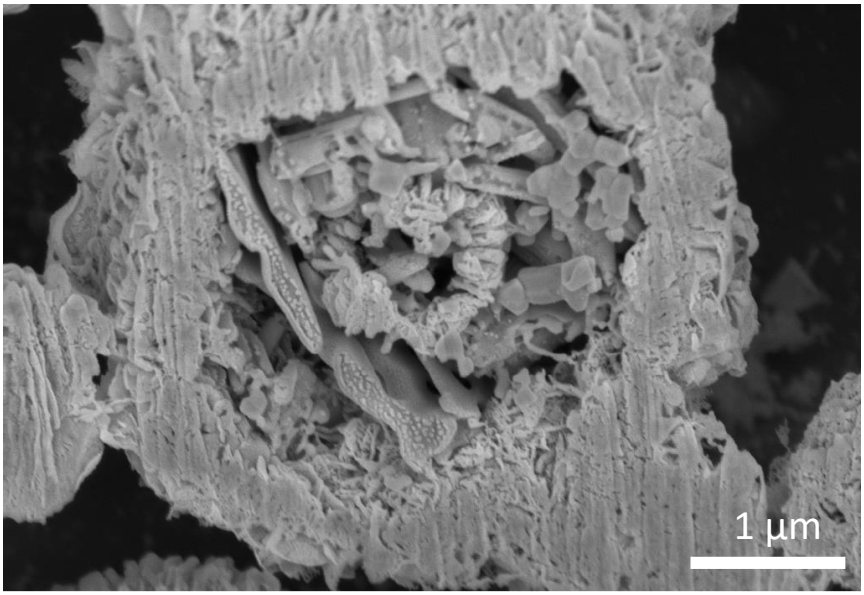


Figure 44. FIB cross section of nanoflower morphology showing the core of the 3D structures.

2.3.5. Evolution of nanoflower structure

The nanoflower morphology was studied using the different characterisation techniques, which helped us establish the morphology, structure and composition. Using electron microscopy, the subtle but significant changes in morphology of the nanoflower with variation of the synthesis parameters have been studied. These changes in morphology of nanoflower are summarised in Figure 45 with the help of SEM and TEM micrographs.

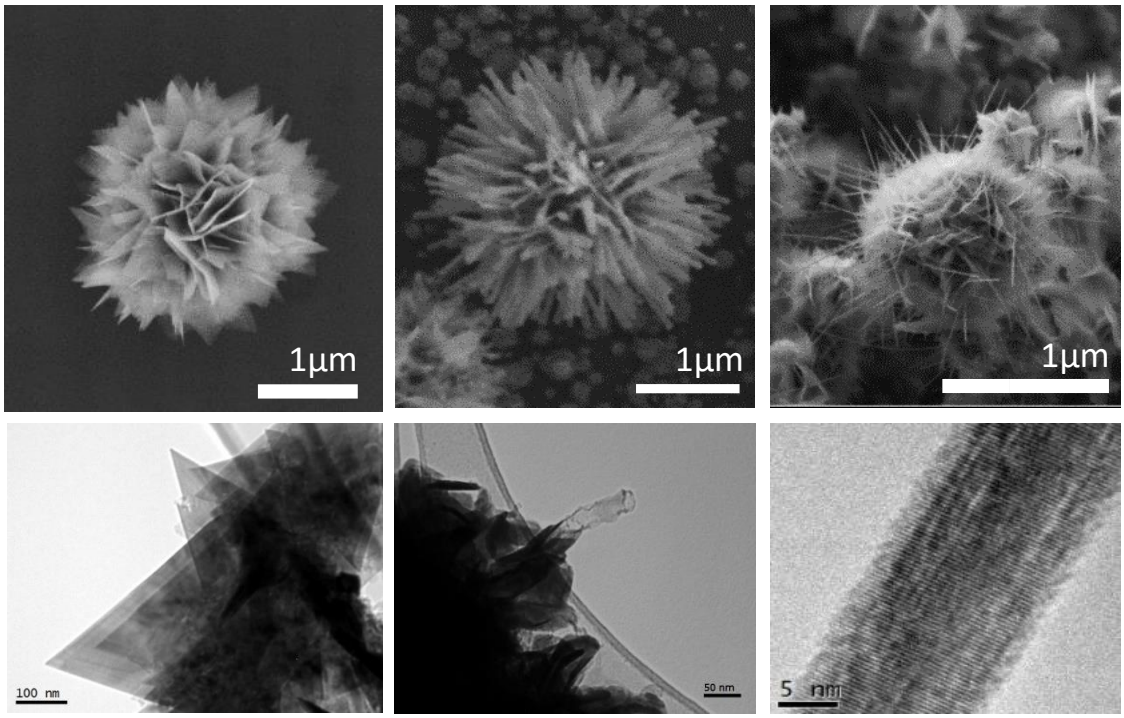


Figure 45. Scanning and Transmission electron micrographs showing the changes in morphology of the nanoflowers with variation in synthesis time, temperature and cooling conditions.

The structure of conventional and predominant nanoflower morphology have been explained using electron microscopy and FIB cross section. This conventional morphology is generally observed at a lower synthesis temperature and with longer time periods. Apart from the conventional nanoflowers, we observed the presence of nanoflowers as shown in Figure 41 where the petals constituting the nanoflower appear more tubular. Under TEM, the rolling of the petal to form the tubular structures was

observed as highlighted in Figure 46. These tubular nanoflower seem to form at a moderate temperature (750 ^{o}C) and at time periods of 5 minutes and 10 minutes, usually in combination with the conventional nanoflower morphology.

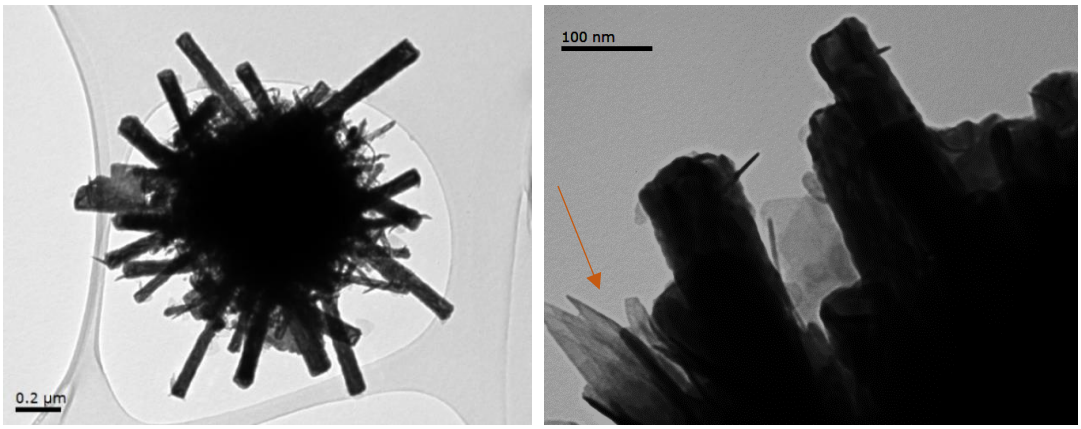


Figure 46. TEM micrographs showing the nanoflowers with rolled up flakes and higher magnification show curling of the flakes as pointed by the arrow.

The nanoflowers with nanowires attached are observed at a higher synthesis temperature (850 ^{o}C) and at lower time periods (5 min). This morphology is sighted for the first time and requires detailed investigation. Firstly, the morphology was characterised using SEM. These nanoflowers were slightly smaller than the conventional nanoflower, with size usually less than 1 µm. Also, it is evident from the SEM micrograph that predominantly, the nanoflowers are covered with nanowires and this morphology is homogenous across the substrate as shown in Figure 47.

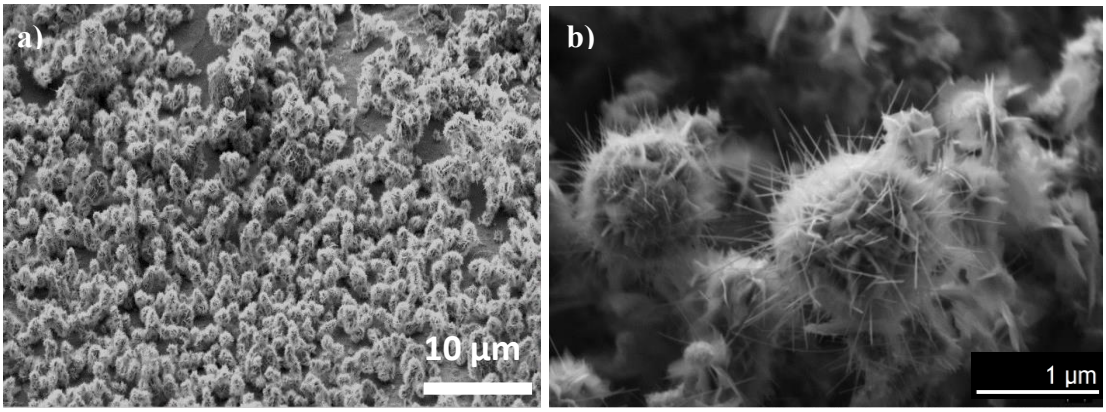


Figure 47. SEM micrographs showing (a) homogenous distribution of nanoflower with nanowires on silicon substrates; b) nanowires grown on nanoflower morphology.

The nanoflowers with nanowires were then characterised using TEM as shown in Figure 50. Firstly, the tubular structures were confirmed to be nanowires with the absence of a hollow core (present in nanotube) and presence of lattice fringes across the length of the tube as shown in the high magnification TEM micrograph in Figure 51b. Also, the diameter of these nanowires were between 20-50 nm and lengths in the range of 300-500 nm.

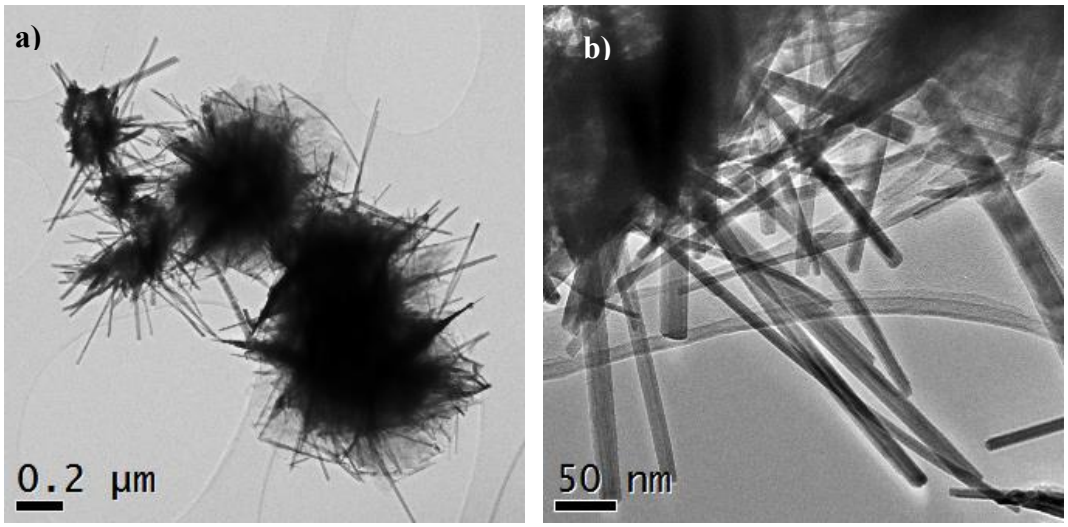


Figure 48. TEM micrographs of nanoflowers with nanowires growing on them.

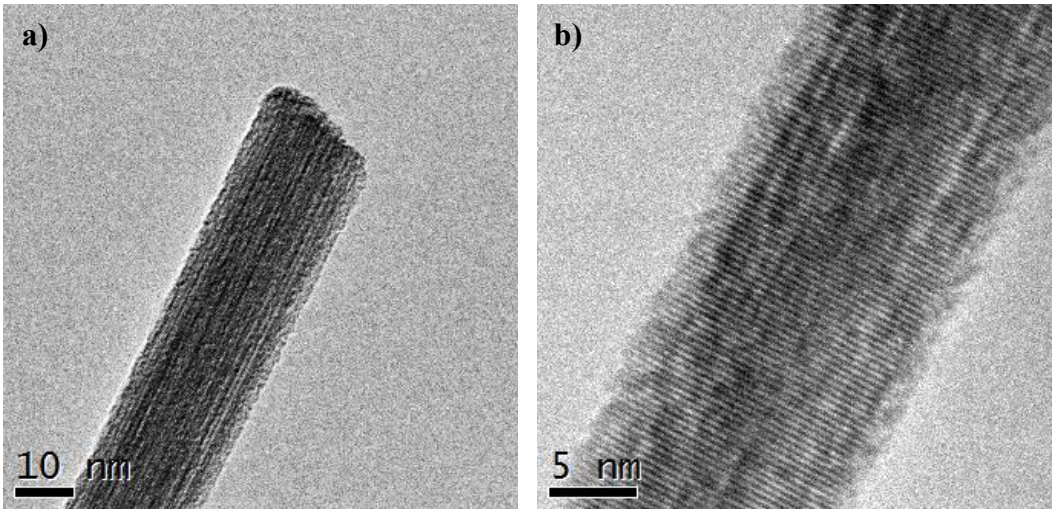


Figure 49. a) TEM micrograph showing nanowires; b) High magnification TEM of nanowires showing lattice fringe.

To shed light on the composition of this morphology, EDX mapping was performed on TEM as shown in Figure 50. The nanowires showed significant amount of oxygen in their structure, which led to the conclusion that these nanowires are tungsten oxide, in contrast to the WS_2 nanoflower on which they are formed. To compare and contrast the tungsten oxide nanowires to the tungsten disulphide nanoflower, EDX mapping has been acquired with both the flake and nanowire in the same frame as shown in Figure 51. The nanowire and the flake were not at the same height for imaging but nonetheless the maps show the presence of significant amount of sulphur in the flake while large amount of oxygen on the nanowire. The difference in the amount of tungsten on the nanostructures could be attributed to the difference in the distance of the deposits from the detector with the flake being farther from the detector, compared to the nanowire. The reason for the formation of these structures will be discussed in the section 2.3.6.

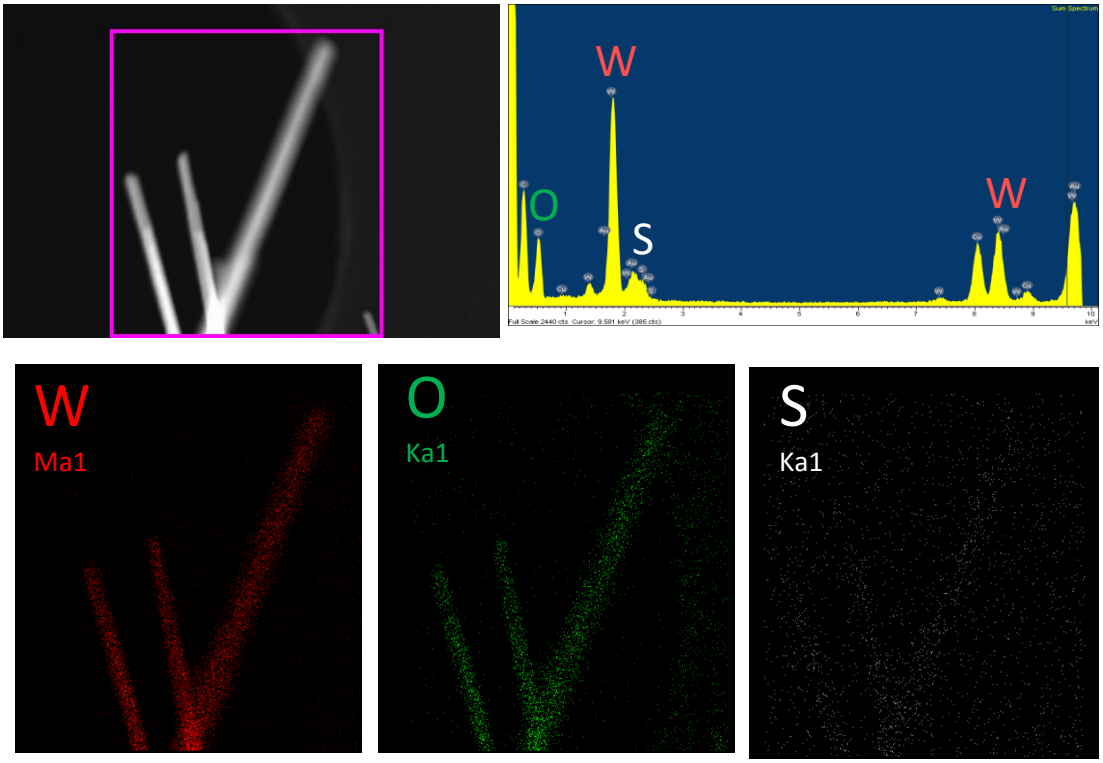


Figure 50. EDX mapping of nanowires found on nanoflowers under TEM showing elemental mapping of tungsten, oxygen and sulphur.

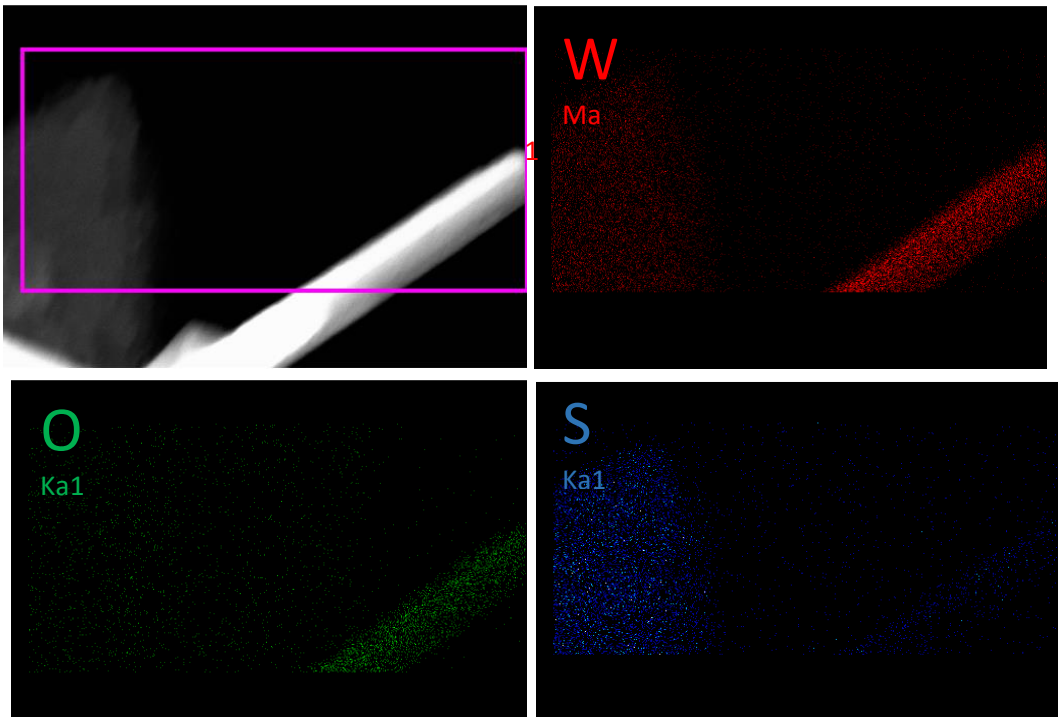


Figure 51. EDX mapping show the difference in composition of a flake and nanowire under TEM using elemental maps of tungsten, oxygen and sulphur.

2.3.6. Nucleation and growth mechanism for nanoflower formation

In order to understand the evolution of these structures, short time nucleation experiments were carried out. The process parameters were similar to the CVD experiments employed to produce nanoflowers. However, the nucleation experiments were performed at very short time periods ranging from 10 s, 30 s, 60 s, and 120 s to 1800 s. The different stages of nucleation of the nanoflower are shown in Fig 52 and it clearly shows the evolution process involved in forming these nanostructures. These different stages of evolution have been studied using XRD and Raman spectroscopy presented in Figure 53 and 54 respectively. This would help understand the composition changes involved with the growth of these nanostructures.

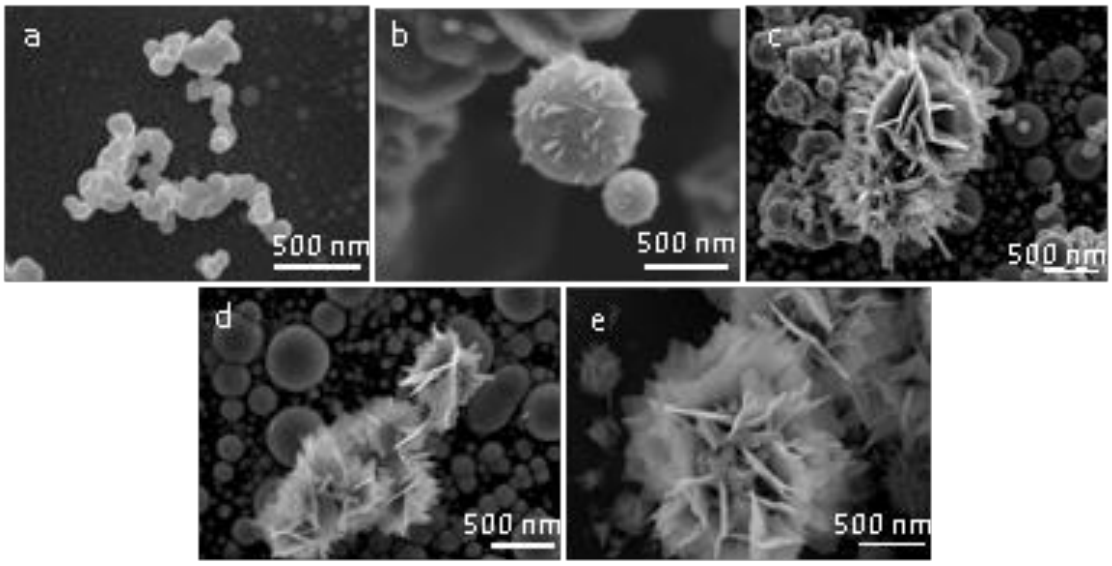


Figure 52. Evolution of nanoflower structure with progress in time periods from 10s to 1800s at 850°C

Initially, nanoparticles of tungsten are formed, as confirmed by XRD at 10 s in Fig 55. These particles are usually agglomerated as seen in Figure 52a. As reaction time was increased to 30 s, intermediate phases of tungsten- oxide and sulphide were observed, as evident from the WO_3 and WS_2 peaks in XRD. This could be sulphur progressively reacting with the oxide nanoparticles, as proposed by Tenne *et al*. [8], forming flake-like structures on the surface, visible in Figure 52b. The oxides may have also been formed when particles are exposed to the atmosphere while transferring them for characterisation. The morphology after 60 s in Figure 54c shows the formation of petals from these particles and also the presence of tubular structures. With time, the tubular morphology disappears and only flakes are observed, as in Figure 52d. With longer time periods of 1800 s all of the tubular structures observed in Figure 52c & 52d are converted to flakes and flowers with predominantly large flakes/ petals as observed from Figure 52e and they exhibit characteristic WS_2 signals in Raman and XRD.

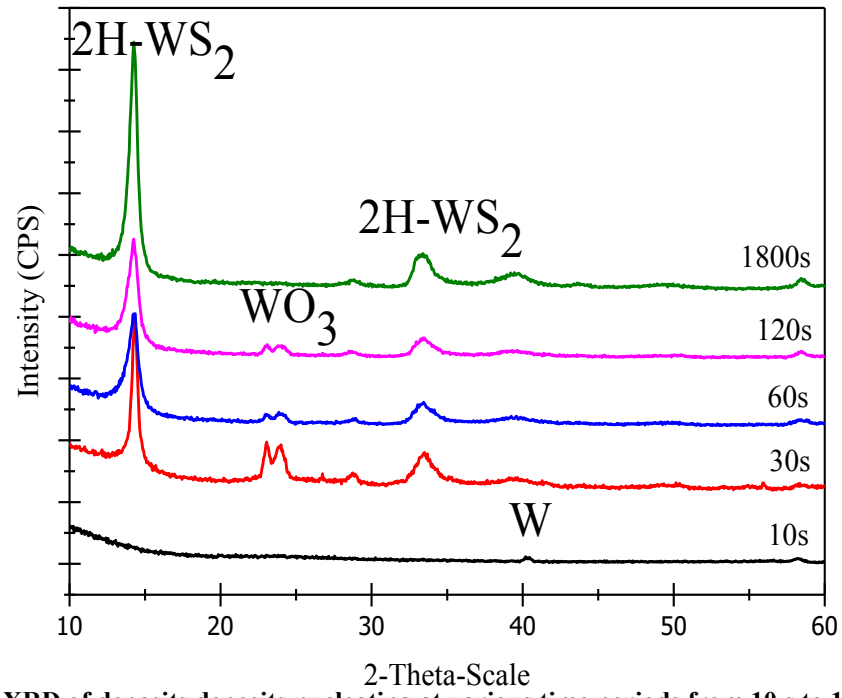


Figure 53. XRD of deposits deposits nucleating at various time periods from 10 s to 1800 s at 850 ^{o}C which would form nanoflowers eventually.

The synthesis process observed in this work seems to follow a combination of the mechanisms described previously in literature. W species are formed in the first 10 s, which are transformed into intermediate species of WO_xS_y over 120 s, which eventually form a pure WS_2 phase after 300 s (5 min). This is determined by XRD, which clearly shows the suppression of oxide phases and the dominance of sulphide phase with an increase in time from 10 s to 1800 s. Raman spectroscopy also shows the characteristic A_1g (352 cm^{-1}) and E_2g (420 cm^{-1}) belonging to WS_2 phase which feature in the later stages of the process along with Si peak at 520 cm^{-1}. Thus the initial phase of the experiment shows the presence of an oxide phase in both XRD and Raman. The source of this oxygen is uncertain and is difficult to trace. It could be from the small ppm level of oxygen present in Argon, which is used as a carrier gas or from

Nitrogen which is used to purge the system in which the experiment has been carried out.

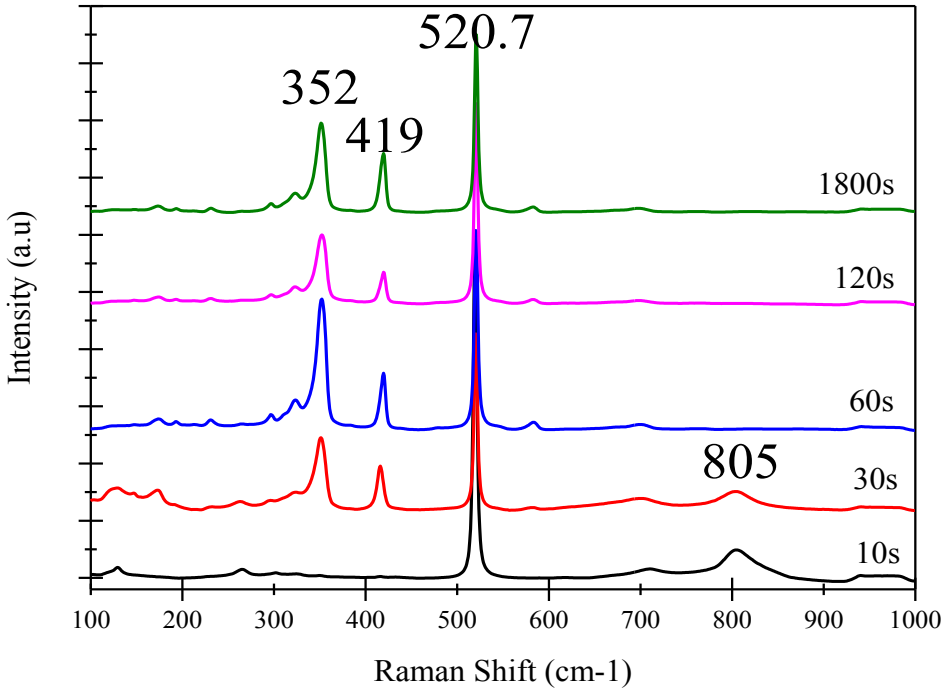


Figure 54. Raman spectroscopy of deposits nucleating at various time periods from 10 s to 1800 s at 850 ºC which would form nanoflowers eventually.

Tenne *et al.*[8] highlight a similar mechanism for the formation of IF-WS_2 nanoparticles using WCl_n and H_2S precursors. A major difference in this work is the formation of WS_2 nanosheets on the surface of the nanoparticle in random directions leading to nanoflower formation, in contrast to the confined growth in IF-WS_2. It has been reported that the WCl_n, on heating first forms W species, possibly WCl_xS_y, which on subsequent reaction leads to the formation of a pure WS_2 phase. Another mechanism proposed based on TEM-EDS, is amorphous WS_3 formation enhancing IF-WS_2 formation through sulphur abstraction and crystallization[22]. Li *et al.*[30] reported the use of sulphur both as a reductant and sulphurisation agent at the same time. They reported a self-redox and metathesis reaction, resulting in a stepwise sulphurisation of $MoCl_5$ to form MoS_xCl_y, an intermediate at low temperatures of 515 ºC and pure MoS_2 phase at 800 ºC. This same mechanism is likely to hold for WS_2.

2.3.7. Structural investigation of nanoflowers using Scanning Transmission Electron Microscopy (STEM)

WS_2 nanoflowers are composed of petals that resemble an equilateral triangular, as shown in Fig 41b. This was established by disassembling the nanoflowers using sonication. Although it has been reported that 10-100's of these triangular petals combine together to form the spherical 3D self-assembled nanoflower, a detailed analysis of their structure has not been undertaken. To achieve this, the petals which are the building blocks of the nanoflower morphology were characterised using STEM. For this purpose, the nanoflowers were subjected to sonification prior to sample preparation which would which isolated the petals from the 3D structure and helped to obtain a good contrast in STEM. Few-layered edges were observed with atomic resolution using a double aberration corrected JEOL 2200 MCO operated at 200kV in Scanning STEM mode and an annular dark field detector. An illustration of the crystal structure along with lattice arrangement along different axes is shown in Fig 55.

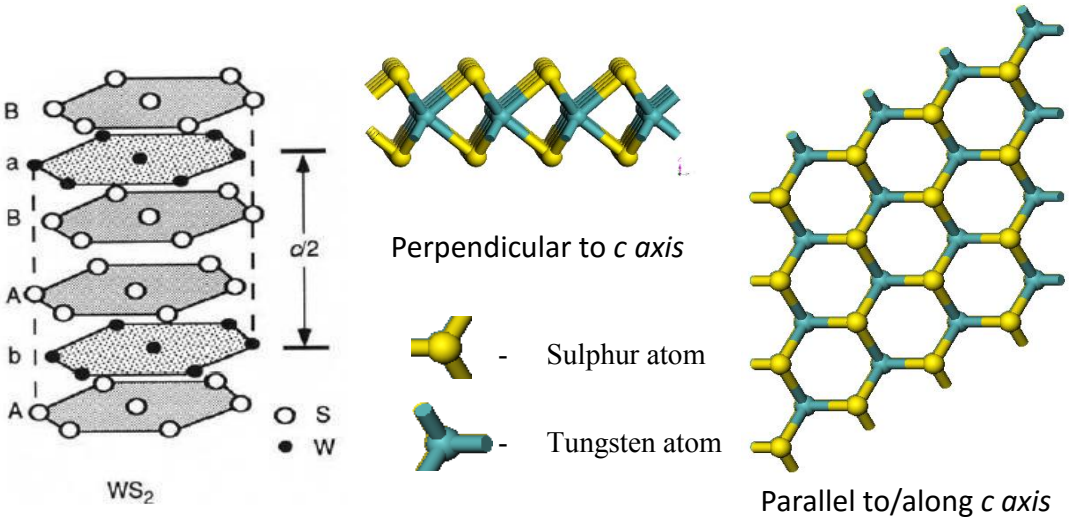


Figure 55. Schematic of WS_2 crystal structure along with models depicting the atomic arrangement of the lattice along different axes.

For WS_2, molecular sheets are stacked together with spacing of 0.62 nm and an in-plane lattice spacing of 0.31 nm. In Fig 56, a cluster of the petals which constitutes a nanoflower is visualised along their edges (beam perpendicular to c-axis), to reveal 6-8 molecular layers of WS_2. These WS_2 were stacked on top of each other to form the petals. The distribution of the number of molecular layers to form the petals is not very uniform and varies from few-layered (2-4) to increased number of layers up to 12-14.

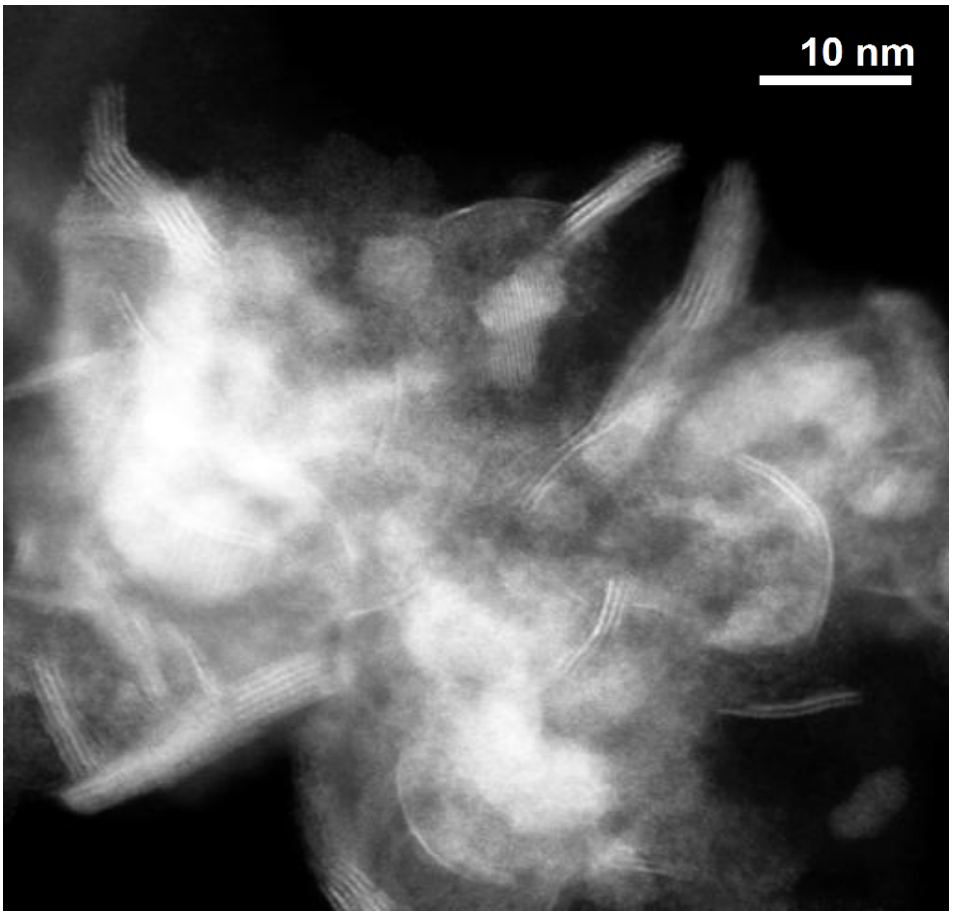


Figure. 56 STEM image showing stacked layers in the petals of nanoflowers dissociated by sonication

With the beam parallel to the c axis, the hexagonal packing can be clearly observed at the edges where the number of layers have reduced considerably to reveal mono- and bi-layer regions. This is a significant observation since it highlights that the nanoflowers are composed of few-layered nanosheets at the edges. These few-layered

(mono- and bi-layer) edges are visible in Fig 57. As we move towards the centre of the petal, the layers stack up progressively forming Moiré fringes which are visible near the centre of the petal.

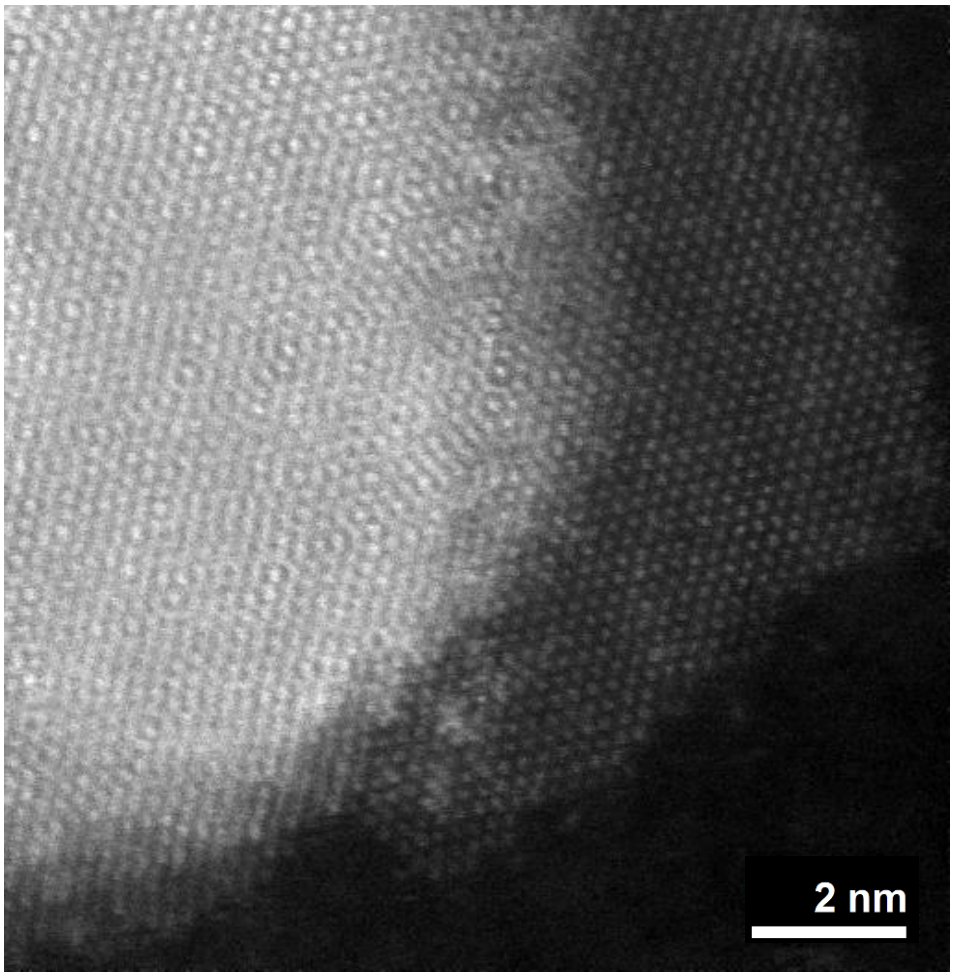


Figure. 57 STEM image showing few-layered WS_2 at edges in WS_2 nanoflower after dissociation.

2.3.8. Deposits inside the quartz tube

As explained in the experimental section, the chemical vapour deposition process was carried out in a quartz tube. In addition to the nanoflower morphology formed on the silicon substrate positioned inside the quartz tube, deposits were also obtained on the inner walls of the quartz tube in the form of a black powder. These deposits consisted predominantly of faceted microtubes and also of sheets and wires in lesser proportions as shown in Figure 58.

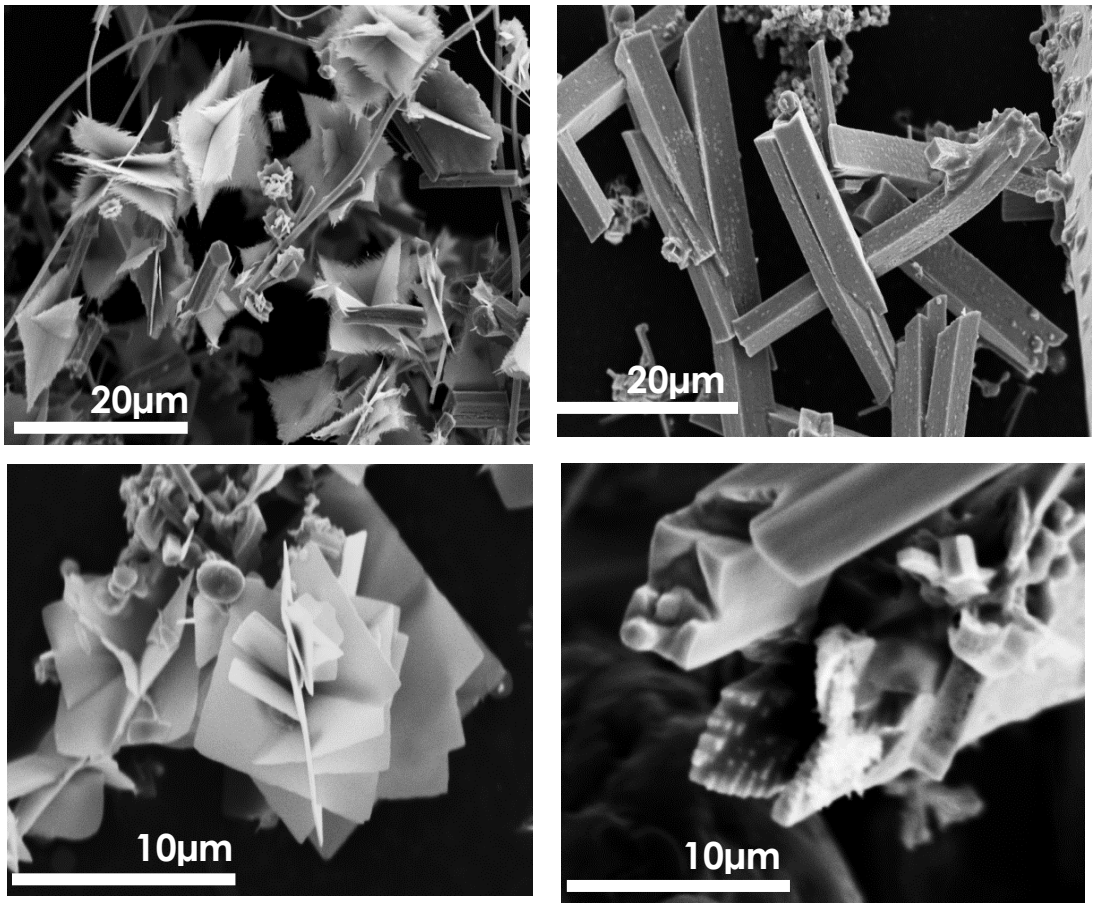


Figure 58. SEM micrograph of deposits obtained on the inside walls quartz tube in which the synthesis is carried out.

The composition of these deposits was a mixture of WS_2 and $WO_3.H_2O$ as confirmed by XRD in Figure 59. Surface area analysis was also performed using Brunauer–Emmett–Teller (BET) characterisation technique, as illustrated in Figure 60. BET result indicates the presence of type IV mesoporous structures with type H3 loops [183,184] associated with aggregates of plate-like particles forming slit-like pores. The surface area of these structures was found to be 33 m^2/g. This novel material could find potential applications in energy storage and catalysis due to its enhanced surface area. Similar faceted MoS_2 structures have been synthesized using molybdenum oxide and thiourea.[185] The amount of powders obtained from this region were much higher in comparison to the deposit on the silicon substrate, making these ideal by-products while considering upscaling synthesis, since they are formed at all conditions.

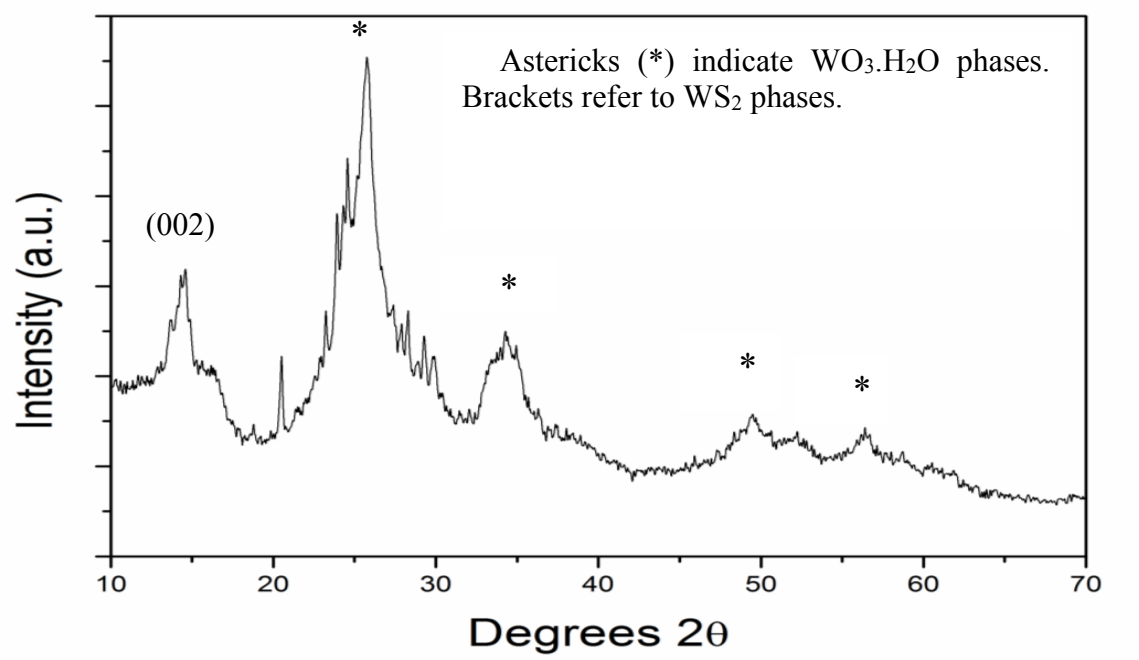


Figure 59. XRD of deposits inside quartz tube showing presence of WS_2 and $WO_3.H_2O$ phases.

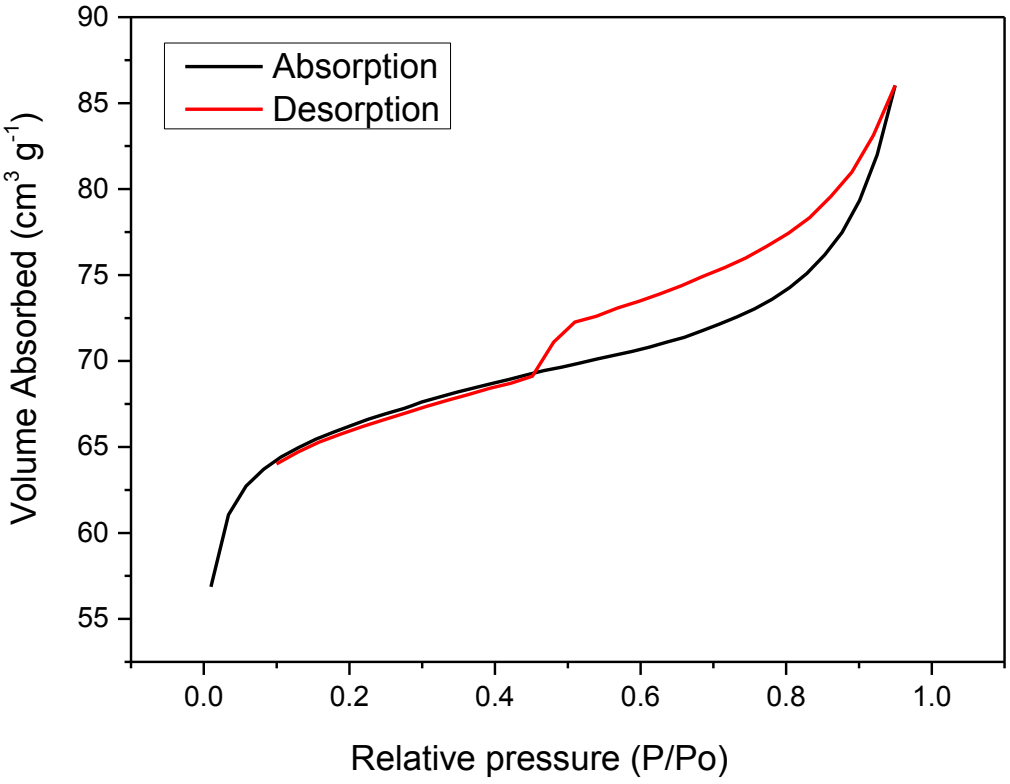


Figure 60. Surface analysis of deposits inside quartz tube using BET indicating type IV mesoporous structures.

2.4. Conclusion

The synthesis of nanoflower morphology using chemical vapour deposition (CVD) was studied in detail. The key findings/results are listed below:

- Reproducible synthesis was established using a simple CVD process.
- Triangular flake/ petal was found to constitute the nanoflower morphology.
- Insights into the core of these 3D structure was revealed by dissecting it using a FIB
- Novel structures of nanoflowers with nanowires showing the presence of tungsten oxide nanowire on WS_2 nanoflowers were synthesised.
- The structural evolution of the nanoflower morphology from oxide nanoparticles along with the compositional changes were shown using nucleation experiments.
- High-resolution microscopy revealed the presence of few-layered WS_2 at the edges of these 2D nanosheets/petals and also the progressive stacking of these layers to form the petals, that in turn constitute the 3D nanoflower morphology.
- Deposits of faceted microtubes, sheets and wires were obtained on the inner walls of the quartz tube, which possess relatively high surface area and could be useful in applications such as catalysis and energy storage.

Chapter 3. Exfoliation of nanoflowers and their use in catalysis of hydrogen evolution reaction (HER)

3.1. Introduction

Exfoliation of layered materials to form atomically thin nanosheets has been of interest for many decades.[104,105] A number of methods have been developed, which span from Li intercalation to solution processing methods such as liquid exfoliation to form monolayer nanosheets.[111] Among these, large-scale liquid exfoliation of bulk material using surfactants[83] and solvents[186] matching the surface energy of material have received significant attention due to their versatility and robustness. Such exfoliation would help produce high aspect ratio nanosheets with high surface activities, which are suited for electrochemical applications such as electrodes in supercapacitors or batteries [187] and catalysis.[188] Moreover, the confinement of electrons on the exfoliated two dimensional nanosheets would lead to unprecedented optical and electrical properties.[63,64] Recently TMDs, in particular MoS_2 and WS_2, have shown potential as catalysts for hydrogen evolution.[189,190]

The need for sustainable technologies and renewable forms of energy has been at forefront of discussion for the past few decades in order to address the most important challenge that faces the twenty first century. Hydrogen holds the promise to fulfil the needs for a clean and sustainable future. However, to realise this potential of hydrogen, efficient methods of production are a prerequisite. Electrochemical hydrogen evolution reaction (HER) provides a feasible approach but requires the use of electrocatalysts to decrease the overpotential of the electrodes.[191] To date, platinum has been the most electroactive catalyst, which contributes to excellent reaction yield

and low overpotential.[166] However, earth abundant and inexpensive non-noble catalysts have to be pursued to make hydrogen production more viable. Identifying materials for electrocatalysts for HER has been a field of active research.[192] Metal alloys,[193] metal oxides,[194] metal dichalcogenides,[195] and even more complex systems which include enzymes,[196] and bio-mimic nanoparticles [197] have all been examined for their role as electrocatalysts for efficient hydrogen evolution.

Chalcogenides derivatives, represented by the general formulae MX_2 (M-transition metal; X-chalcogen) have shown promise as electrocatalysts for HER.[198] However, their bulk form has not been very efficient catalysts due to the absence of catalytically active sites. The identification of active edge sites for catalytic activity in MoS_2 nanostructures[167] has encouraged nanostructuring of TMDs to enhance the concentration of catalytically active sites. Thereby, enriching the edge sites of these MX_2 compounds is a prerequisite for improving their performance as catalysis for HER. The morphology ideal for this application is determined by the ability of the nanostructure to maximise the number of active sites with respect to the bulk structure. Even though MoS_2 in various morphologies have been extensively researched in the MX_2 family, other potential analogous structures such as WS_2 have been largely unexplored. Recently, the role of WS_2 in metallic 1T phase obtained by lithium exfoliation forms has received considerable interest.[188,190] It has been shown that the presence of a metastable 1T phase formed as a result of the process is responsible for enhanced HER activities.[188] This is not the case in bulk forms, which mostly consists of 2H polymorph, where the presence of unsaturated sulphur atoms along the edges of Mo atoms has been attributed to the HER activity.[167] Further theoretical studies have shown that the presence of defects such as sulphur vacancies at the MoS_2 surface, act

as catalytically active sites in otherwise catalytically inactive basal plane of the sulphur sub-lattice.[199] This theory should hold well for WS_2 electrocatalysts as well.

In this chapter, the exfoliation of WS_2 nanoflowers and the application of exfoliated thin sheets in the catalysis of hydrogen evolution reaction has been presented. The synthesis of the WS_2 nanoflowers using a simple, scalable CVD and the presence of thin regions at the edges have been presented in Chapter 2. The nanoflowers with their abundance of exposed edges and thin flakes/petals that constitute them are ideal candidates as catalysts for electrochemical HER. By exfoliating them using various methods such as mechanical grinding, liquid exfoliation using surfactants and sonication in ethanol/water, further enhancement of the edges could be achieved thereby improving the HER activity of this morphology. The WS_2 nanoflowers (WS_2 NF) and its exfoliated forms (WS_2 NF Ex) were employed for the catalysis of hydrogen evolution reaction. The morphology is exfoliated using sonication in non-toxic and environmental benign solvents such as ethanol and water with the aim to produce atomically thin nanosheets with abundance of edges, which are the catalytically active sites. This process is more effective than using toxic solvents such as NMP to exfoliate the bulk materials as it offers better control to form more uniform thin regions with enhanced active sites in the form of edges. The as-synthesised WS_2 nanoflowers and its exfoliated form, produced by sonication in simple solvents, are mixed with commercially available fuel grade carbon powder (BP2000). The simplicity of the CVD process to form the nanoflowers and the use of readily accessible forms of carbon to achieve good HER activity makes this method attractive for commercial purposes.

3.2. Experimental

The WS_2 nanoflowers, with thin regions along the edges of the petals, synthesised by chemical vapour deposition (CVD) as elaborated in Chapter 2, were subjected to different exfoliation techniques with the aim of producing large micrometer (μm) sized few-layered WS_2 with uniform thickness. The three different exfolaition techniques employed include (a) mechanical grinding, (b) liquid exfoliation using surfactants such as sodium dodecylsulphonate (SDS) and sodium cholate (SC), and (c) liquid exfoliation using simple solvents such as ethanol and water along with sonication. In addition to these, complementary (d) liquid exfoliation of bulk materials was performed using NMP and simple solvents such as ethanol and water.

(a) The mechanical grinding process was carried out using a simple pestle and mortar. The nanoflowers were scrapped from the silicon substrates, on which they were synthesised, into the pestle. The nanoflower deposits were then crushed and ground using the mortar until a fine deposit was obtained. Subsequently, the deposits were either suspended in ethanol and dropped onto the grid or transferred directly by rubbing the grid against the deposit, for further characterisation using transmission electron microscopy (TEM).

(b) Liquid exfoliation using surfactants was carried out using sodium dodecylsulphonate and sodium cholate as surfactants at concentrations of 0.1 and 0.15 mg/ml respectively with sonication times varying from 5 min to 2 hours. The ionic surfactants act as stabilizers, which would prevent the rapid reaggregation of the exfoliated flakes. This reaggregation is driven by the large surface energy of TMDs, which by computational studies, was shown to be greater than 250 mJ m^{-2} for both MoS_2 and WS_2.[200] The advantage of using this process is its simplicity and scalability

in comparison to ion intercalation which is time consuming, extremely sensitive to the environment and results in structural deformation of TMDs.[201] For this, the nanoflowers were initially subjected to low power bath sonication whilst still on substrates to dislodge them into solvent. Further to bath sonication, a probe sonication method was employed using ultrasonic processor UP100H (100 W, 30 kHz) to dissociate the nanoflowers and exfoliate them. The samples were subjected to 1 hour of bath sonication and then varying time periods of continuous tip sonication from 15 min to 1 hour. The exfoliated solution was then transferred to TEM grids for further characterisation using microscopy.

(c) Liquid exfoliation of nanoflowers in simple solvents was adopted from the mixed solvent strategy reported by Zhang *et al*.[84] The method employed low boiling point solvent mixtures of ethanol and water to effectively exfoliate MoS_2, WS_2 and BN. This process was better than employing high boiling point solvents such as cyclohexylpyrrolidone (CHP) and N-methyl-pyrrolidone (NMP) mainly due to difficulties in removal of solvents and occurrence of aggregation during the slow evaporation. This process was adopted for the exfoliation of nanoflowers to overcome the shortcomings of the liquid exfoliation process especially with the surfactant contamination. Liquid exfoliation of the nanoflowers in simple solvents such as ethanol and water was carried out by dispersing the nanoflowers in ethanol and dissociating them with tip sonication. The tip sonication method was employed for 15 min using ultrasonic processor UP100H (100 W, 30 kHz) to break the nanoflowers and exfoliate them.

(d) Liquid exfoliation of bulk materials using NMP was carried out by preparing 10 mL of 0.15 mg/ml concentration of bulk WS_2 powder and sonicating it for 60 min

using the tip sonicator. This was followed by centrifugation at 1500 rpm for 45 min. The supernatant was used for characterising the exfoliated flakes and the aggregates were employed as catalysts. This was because the amount of material obtained in the supernatant is very small and would require multiple centrifugation/evaporation of solvent to obtain any reasonable quantity, which is laborious and time consuming. The liquid exfoliation of bulk materials using simple solvents such as ethanol and water was performed by using 35% ethanol/water (EtOH) mixture. 30 mg of bulk WS_2 was mixed with 10 ml of 35% EtOH mixture and sonicated for 15 min using the tip sonicator. This dispersion was centrifuged at 3000 rpm for 20 min to remove aggregates, which was employed as a catalyst for HER.

All electrochemical studies were performed with an Autolab PGSTAT302N potentiostat, equipped with an electrochemical impedance spectroscopy (EIS) module FRA 2.V10.[202,203] A three-electrode setup was used, consisting of Au as the counter electrode, saturated calomel (SCE, +0.2412 V vs SHE) as the reference electrode and glassy carbon as the working electrode (GCE). The reference electrode was calibrated with respect to reversible hydrogen electrode (RHE) using platinum wire as working and counter electrode in the electrolyte solution saturated with hydrogen. In 0.5 M H_2SO_4, E (RHE) = E (SCE) + 0.2412. Au was preferred as the material for the counter electrode to rule out any interference on the measurement: Au is more resistant to oxidation than Pt and less catalytically active. The cell was maintained at a constant temperature by means of a water jacket T = 25 ^{o}C. The sample was obtained as powders after being dried in an oven or scrapped from the substrate and dispersed in milliQ water to achieve a concentration of 10 mg/ml. The solution was sonicated to obtain a homogenous mixture and 1 μL of the mixture was drop casted onto the glassy carbon

electrode (GCE) with 2 mm diameter and dried. The linear sweep voltammetry was conducted at a scan rate of 5 $mV \cdot s^{-1}$ in 0.5M H_2SO_4 electrolyte de-aerated using nitrogen. Electrochemical impedance spectroscopy (EIS) experiments were performed in a quiescent solution at a chosen DC electrode potential (see below for details). The AC component of the electrode potential varies in time according to a sinusoidal function, $E_{ac} = E_0 \sin \omega t$. The experimental routine was based on the procedures of Autolab software NOVA: 50 frequencies were selected in the range 100 kHz – 100 mHz, separated by equal steps on a logarithmic scale. A "single sine" wave type was chosen. The potential amplitude (E_0) was equal to 10 mV. Experimental EIS data were fit to a modified Randles circuit (a resistor in series with a "constant-phase element" and a resistor in parallel) with the NOVA fitting routines.

The morphology and crystallinity of the exfoliated material was investigated using a JOEL 2000FX, JOEL-2010 and JOEL-3000F transmission electron microscopes operated at an accelerating voltage of 200 kV and 300kV. EDX mapping was obtained using JOEL-3000F operated at 300 kV with field emission gun. The atomic resolution images were obtained using a double aberration corrected JEOL 2200 MCO operated at 200kV in scanning transmission electron microscopy (STEM) mode using an annular dark field detector.

3.3. Results and Discussion

3.3.1. Mechanical grinding of WS_2 nanoflowers

The typical morphologies obtained as a result of mechanical grinding process is summarised in the TEM micrographs of Figure 61. The predominant morphologies formed by mechanical grinding are agglomerates of thick deposits shown in Figure

61a and cluster of flakes as shown in Figure 61b. The thick agglomerates could possibly be formed by the crushing of the nanoflowers. If the nanoflowers had dissociated well without crushing, then it would be possible to obtain the flakes as shown in Figure 61b. However, the process does not offer the ability to control the final morphology of the exfoliation nanoflowers in a definitive way. Apart from these predominant morphologies, only a small portion of the sample consisted of thin regions shown in Figure 61c and Figure 61d. The flakes in Figure 61c appeared to be thin with a plenty of broken up flakes agglomerated together. The flakes shown in Figure 61d is close to the ideal morphology expected from the exfoliation.

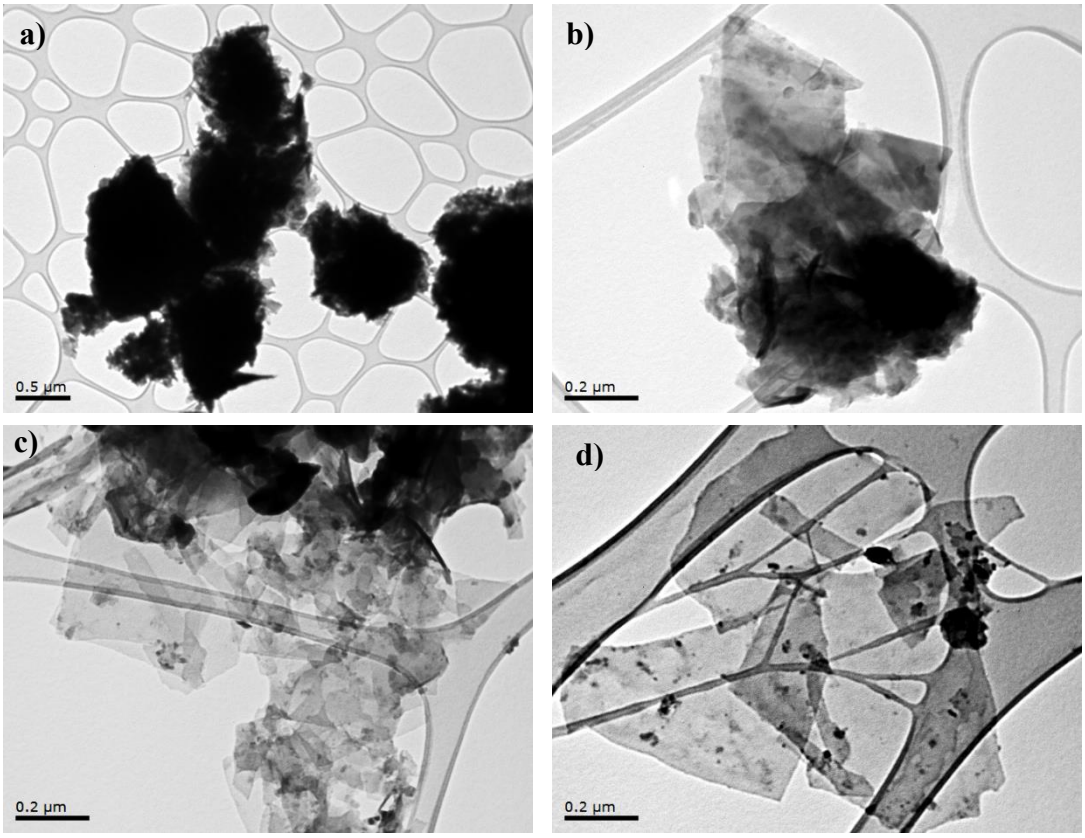


Figure 61. TEM micrographs of mechanically grinded WS_2 nanoflowers showing, a) agglomerates of crushed nanoflowers; b) cluster of exfoliated flakes; c) agglomerate of thin broken up flakes d) exfoliated large thin flakes (the ideal morphology).

Some of these thin regions indicated amorphous character when characterised using selected area electron diffraction (SAED) as shown by the hollow rings in the

diffraction pattern inset of TEM micrograph in Figure 62a and others displayed crystalline hexagonal pattern, which would belong to WS_2 as shown in Figure 62b. EDX results obtained on these amorphous thin regions showed significant amount of silicon and oxygen which could indicate the presence of SiO_2, verified from ratio of their atomic percentages as seen in Figure 63.

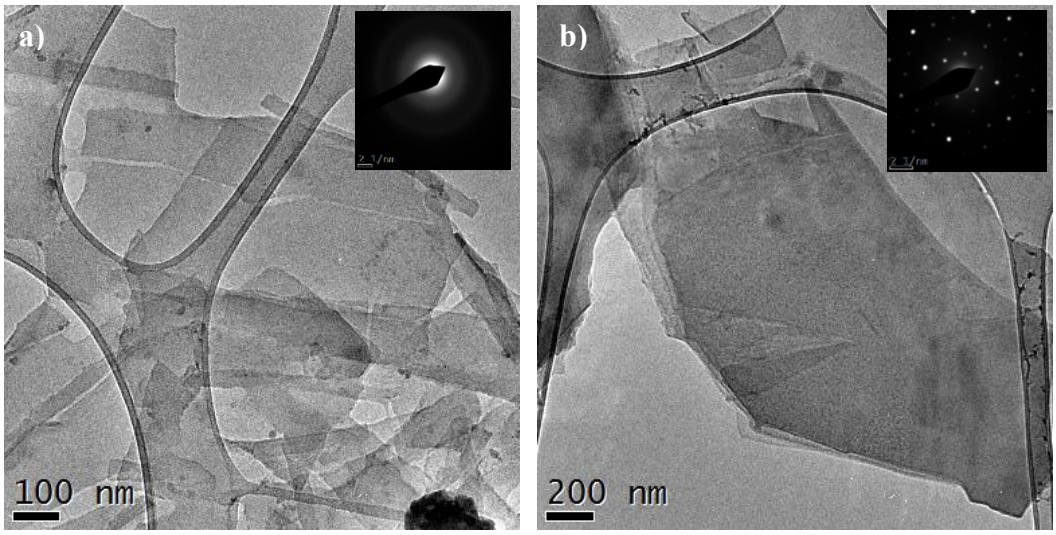
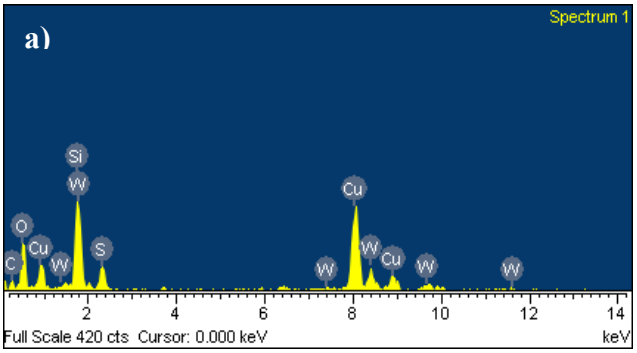
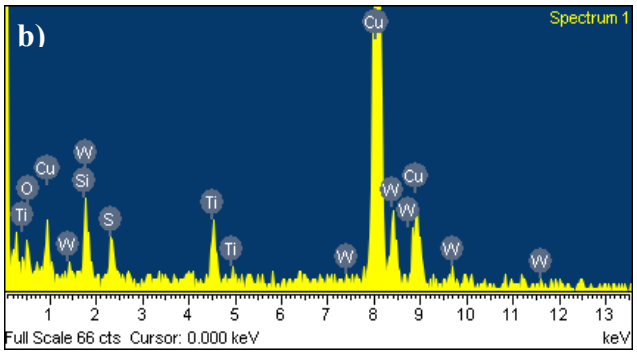


Figure 62. TEM micrographs and SAED patterns of thin regions obtained by mechanically grinding WS_2 nanoflowers showing the presence of a) amorphous regions b) crystalline regions.



Element	Weight%	Atomic%
O K	16.16	35.93
Si K	13.94	17.65
S K	5.07	5.63
W L	20.70	4.01
Totals	100.00	



Element	Weight%	Atomic%
O K	1.23	5.21
Si K	1.01	2.43
S K	2.03	4.28
W L	22.00	8.09
Totals	100.00	

Figure 63. EDX spectrum along with elemental composition of thin regions obtained by mechanically grinding WS_2 nanoflowers showing a) presence of SiO_2 along with, b) WS_2 regions.

The silicon substrate used for the growth of nanoflower is the most likely source of this, as the substrates usually contain an oxidised layer at the surface. This silicon oxide could be introduced into the deposit collected for mechanical grinding during the scrapping process. Apart from SiO_2, the thin regions also contained tungsten and sulphur that would indicate presence of WS_2. The amount of WS_2 and SiO_2 seem to be present in varying proportions across different regions of the thin flakes. To determine the morphology and distribution of SiO_2 and WS_2 on these thin regions, characterisation was performed by scanning transmission electron microscopy (STEM) mode using an annular dark field (ADF) detector.

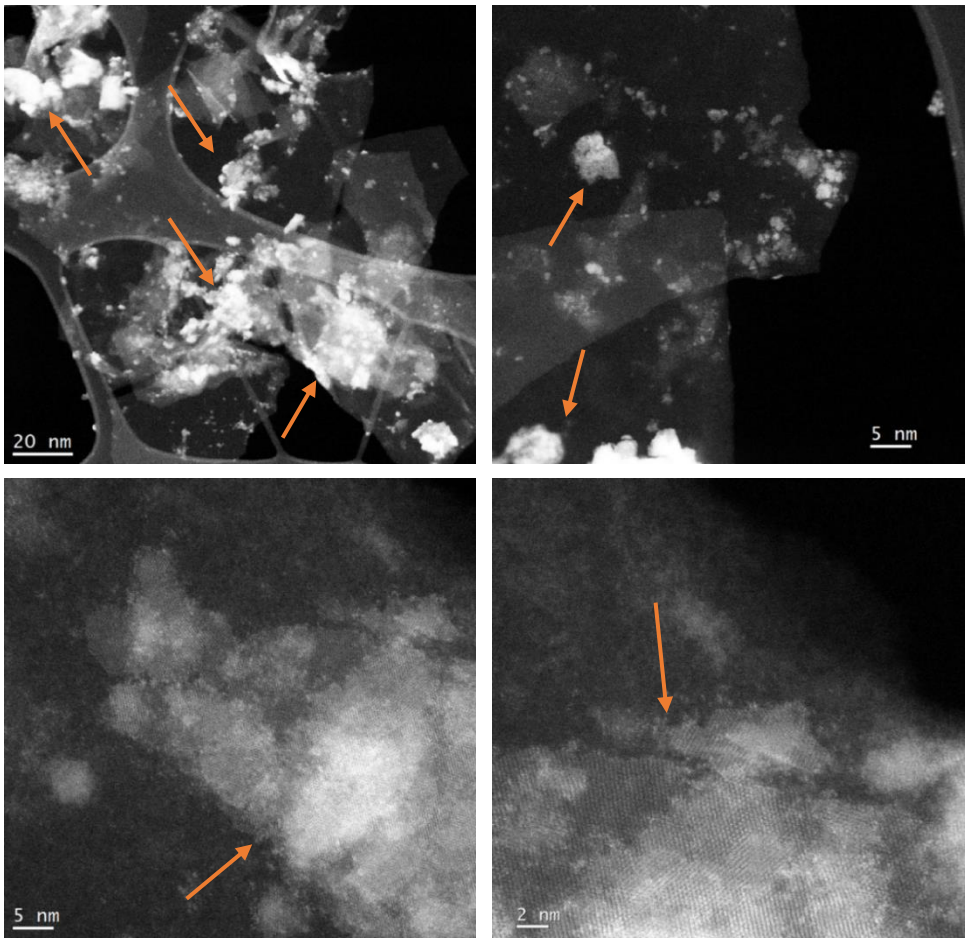


Figure 64. STEM image of thin regions of exfoliated WS_2 seen as islands of crystalline regions (pointed by arrows) supported on amorphous SiO_2 obtained by mechanically grinding of WS_2 nanoflowers.

STEM along with ADF provides contrast that is directly related to the atomic number (z-contrast image). Thereby, the crystalline WS_2 regions appear as brighter region supported on amorphous SiO_2 as seen in Figure 64. High-resolution ADF-STEM showed the presence of large amophous flakes of SiO_2 on which small crystalline islands of WS_2 regions were present. The distribution of these WS_2 islands was not uniform on the flakes and also their thickness varied. To verify the thickness of these small WS_2 islands, an intensity profile was obtained across the region as shown in the Figure 65. However, the presence of an amorphous background makes it difficult to determine the thickness of the crystalline regions.

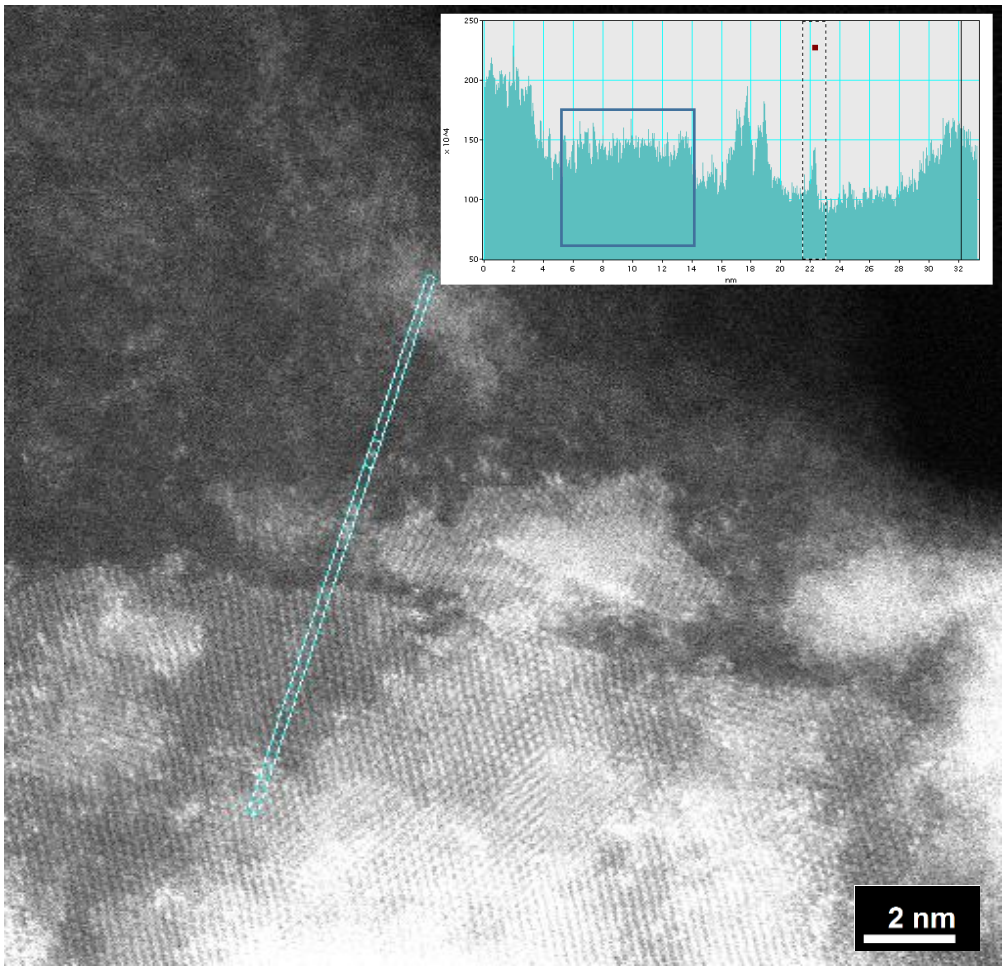


Figure 65. Intensity profile measured on a STEM image across the thin regions of WS_2 on amorphous SiO_2 obtained by mechanically grinding WS_2 nanoflowers

However, if amorphous background is assumed to be uniform, then the intensity of an isolated tungsten atom as highlighted in the intensity profile can be compared to the intensity of the crystalline region. Since the intensity, highlighted by a box in the inset, is quite similar to the single tunsgten atom, it could possibly indicate a monolayer region of WS_2. Using this way, the intensity of the atoms from STEM image can help differentiating the regions of different thickness. By assigning colours to different intensities, a coloured STEM image can be obtained as shown below in Figure 66. With this intensity mapping the thickness of the different regions could be predicted as mono-, bi- and tri-layers of WS_2 for colours blue (green spots as W atoms), green and orange respectively.

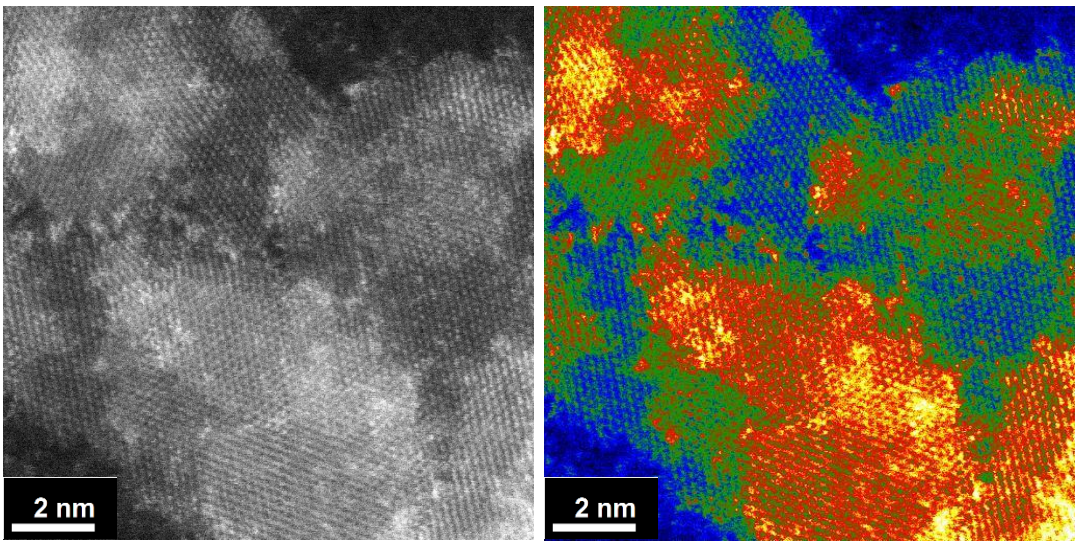


Figure 66. STEM image and its false coloured form to differentiate mono-, bi-, and tri-layer regions supported on amorphous SiO_2 obtained by mechanically grinding WS_2 nanoflowers.

Even though the presence of few-layered WS_2 regions supported on amorphous SiO_2 were shown, the area of these crystalline WS_2 regions were very small (tens of nanometer) and their thickness varies within these regions. A majority of the mechanically exfoliated deposit still contained agglomerates, which were thick with

some few-layered regions as seen in Figure 67a and cluster of few-layered thick flakes as shown in the edge on view micrograph of Figure 67b.

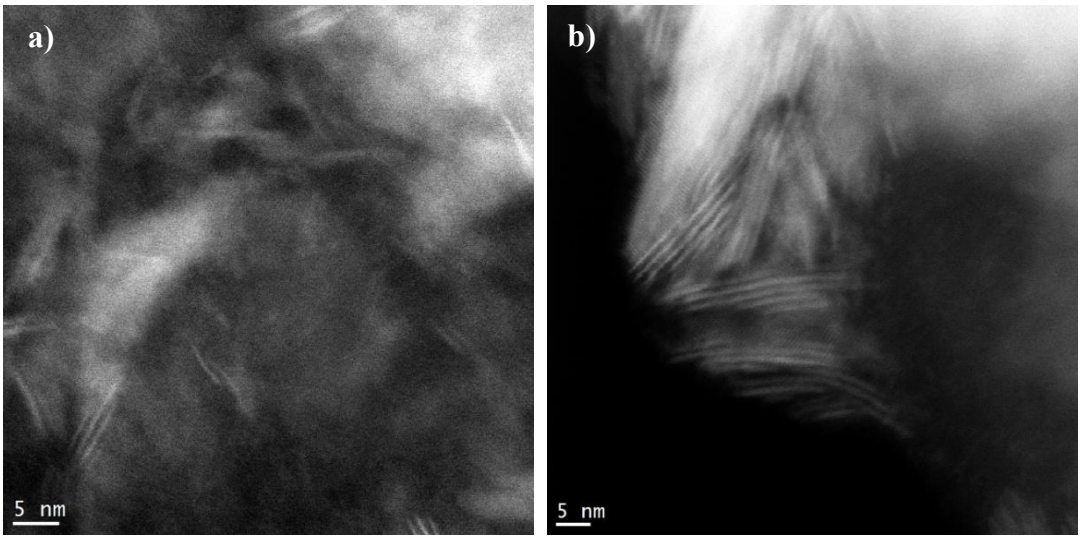


Figure 67. STEM images of exfoliated regions obtained by mechanically grinding WS_2 nanoflowers: a) agglomerates of exfoliated flakes, and b) cluster of thin regions.

Therefore, even though the mechanical grinding technique produced small-area few-layered thick regions WS_2, it offered limited control and hence may not be the ideal method for exfoliating nanoflowers.

3.3.2. Liquid exfoliation of WS_2 nanoflowers

A schematic of the exfoliation of nanoflowers using sonication assisted process is shown in Figure 68.

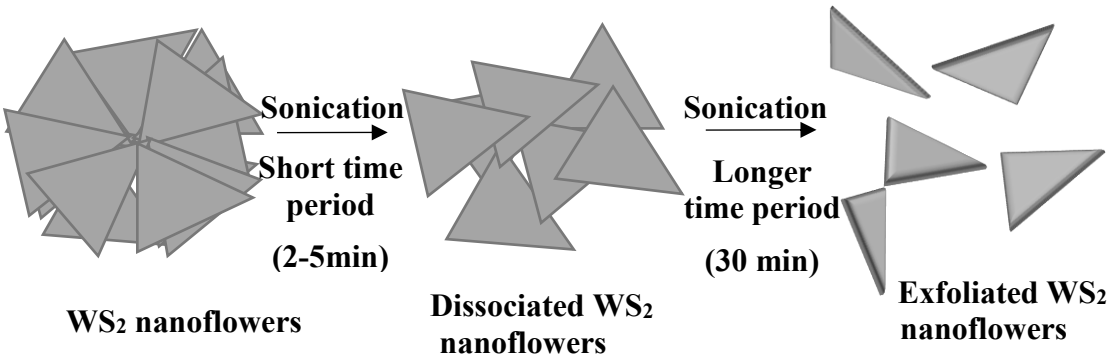


Figure 68. Schematic of the sonication assisted exfoliation of WS_2 nanoflowers

3.3.2.1. Liquid exfoliation using sodium dodecylsulphonate (SDS) as surfactant

The liquid exfoliation was initially attempted using SDS in water using tip sonication with varying times from 5 min to 2 hours. Transmission electron microscopy was the characterisation technique utilized to visualise the extent of the exfoliation and evaluate the process by analysing the resultant morphologies. TEM micrographs in Figure 69 represent the predominant structures/morphology obtained at different sonication times using SDS as the surfactant. The bath sonication has little exfoliation effect with the nanoflower morphology remaining intact. It is evident that the extent of exfoliation varies with the sonication time under the probe and a clear trend was observed. The nanoflowers were intact with 5 min tip sonication time and showed limited signs of dissociation. After 15 min under the tip, the nanoflower morphology was broken. The petals/flakes that constitute the nanoflower were no longer held together in the spherical 3D nanoflower structure but were exfoliated into 2D sheets/flakes. However, the flakes appear to be relatively thick suggesting they are not well exfoliated yet. With increase in sonication time to 30 min the flakes were well dissociated and exfoliated, but were covered by contamination as highlighted in the micrograph. After 1 hour tip sonication, more agglomerates than exfoliated thin flakes were produced and the contamination was still present. This contamination highlighted in Figure 69, could be caused possibly by the surfactant. After 2 hours of exfoliation the flakes lost their crystal structure and broke up to form amorphous flakes. From these results it was clear that SDS was not a suitable surfactant for the exfoliation of WS_2 as it caused a lot contamination and with longer sonication time leading to crystal structure being degraded.

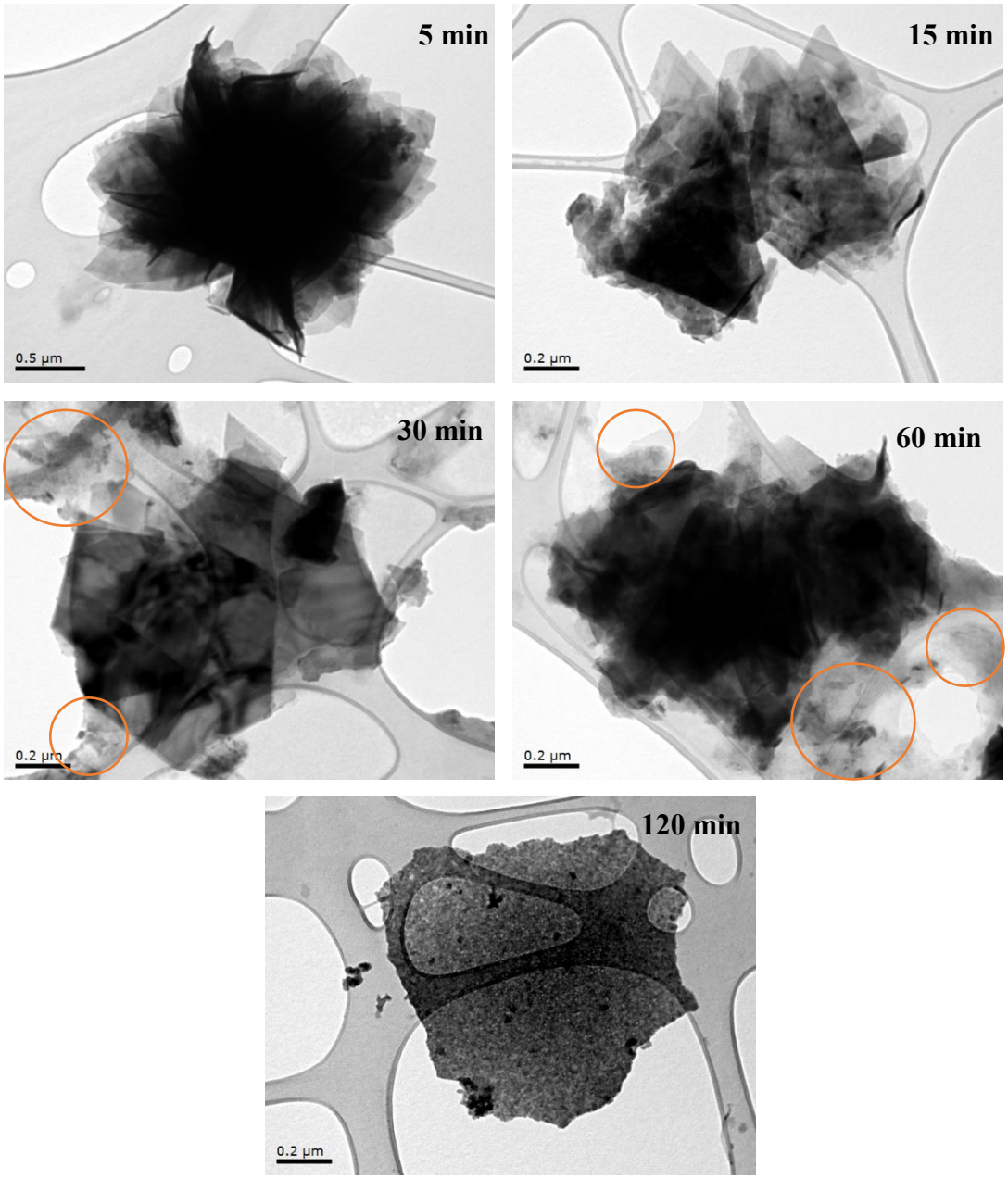


Figure 69. Liquid exfoliation using sodium dodecyl sulfonate (SDS) as surfactant of WS_2 nanoflowers at various tip sonication times as specified in the micrograph. The highlighted regions are contamination.

The well exfoliated flakes obtained after 30 min of tip sonication were characterised further using high-resolution microscopy and representative micrographs are shown in Figure 70. The sample contaminated a lot under the high energy beam making it difficult to characterise, but we were able to observe sections of broken flakes on thin

regions as seen in Figure 70a. Also the edges of these flakes were mostly covered by contamination as seen in Figure 70b.

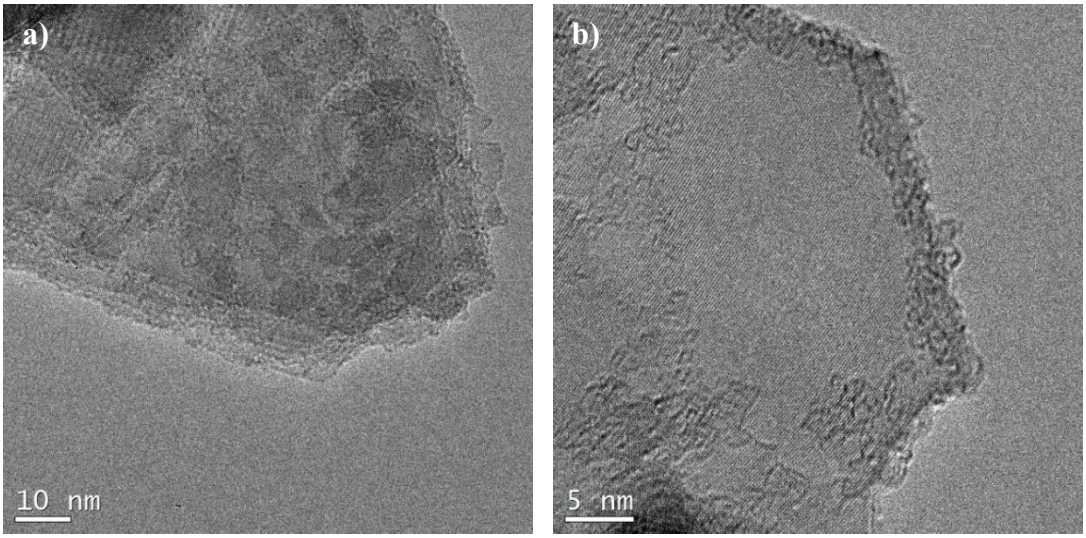
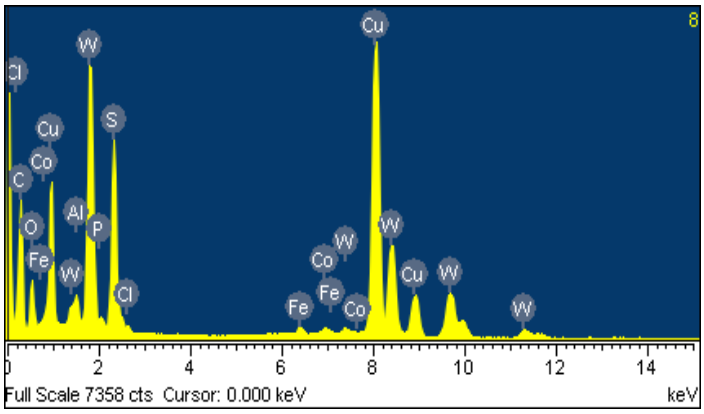


Figure 70. High-resolution TEM micrographs of liquid exfoliated WS_2 nanoflowers using sodium dodecyl sulfonate (SDS) as surfactant for 30 min under the tip sonication showing a) broken up pieces on flakes on thin regions; b) contamination at the edges.

EDX spectrum of the sample shown in Figure 71 predominantly showed the presence of tungsten and sulphur with plenty of other elements possibly present as a result of the contamination.



Element	Weight%	Atomic%
C K	14.20	46.24
O K	3.83	9.36
Al K	1.26	1.83
P K	0.10	0.13
S K	10.91	13.31
Cl K	0.29	0.32
Fe K	0.54	0.38
Co K	0.53	0.35
Cu K	33.62	20.69
W L	34.71	7.38
Totals	100.00	

Figure 71. EDX spectrum along with elemental composition of liquid exfoliated nanoflowers using sodium dodecyl sulfonate (SDS) as surfactant after 30 min of tip sonication confirming WS_2 composition along with the presence of other elements possibly contamination.

3.3.2.2. Liquid exfoliation using sodium cholate (SC) as surfactant

In order to investigate if the SDS surfactant was the reason for the poor exfoliation results, the process was attempted with sodium cholate (SC) as a surfactant for nanoflowers. Even though the predominant morphology obtained was very similar to SDS exfoliation, the amount of contamination was reduced significantly as shown in Figure 72. Similar to SDS, after 5 min tip sonication the nanoflowers had hardly dissociated. After 15 min sonication the nanoflowers were broken up well and had started to be exfoliated into thinner sheets. After 30 min tip sonication the sample was exfoliated well and with longer sonication time of 60 min predominantly agglomerates were formed, similar to SDS surfactants.

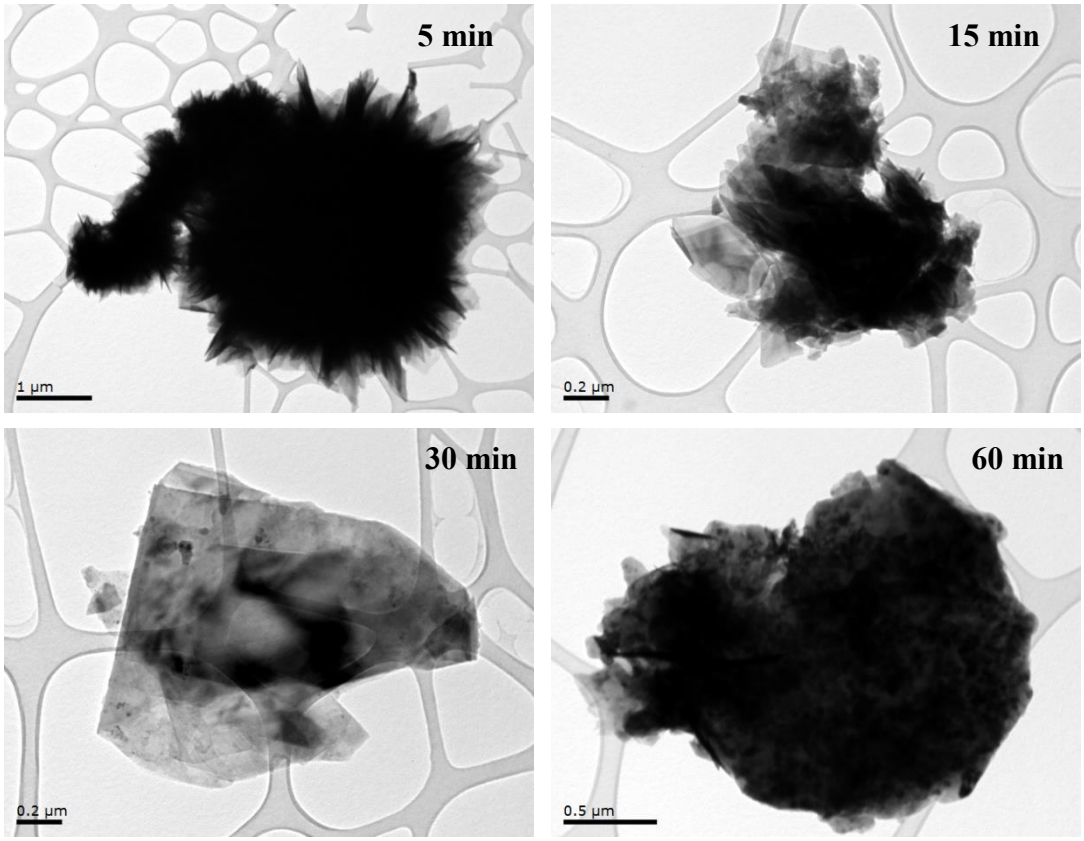


Figure 72. Liquid exfoliation using sodium cholate (SC) as surfactant of WS_2 nanoflowers subjected to tip sonication for different time periods as highlighted in the micrograph.

The exfoliated thin flakes obtained after 30 min tip sonification exfoliation were further characterised using high-resolution TEM and EDX and the results are summarised in Figure 73 and Figure 74 respectively. The flakes were crystalline and quite thin as observed in Figure 73a. The inset of the SAED pattern obtained over the region showed a perfect hexagonal pattern, corresponding to WS_2 as confirmed by EDX in Figure 74. However, the edges of the flakes had been covered with an amorphous layer of possibly surfactant as observed in Fig 73b. The few nanometer thick amorphous coating at the edge of the flake, highlighted in the figure, shows the contamination layer. This made it difficult to quantify the thickness of these flakes.

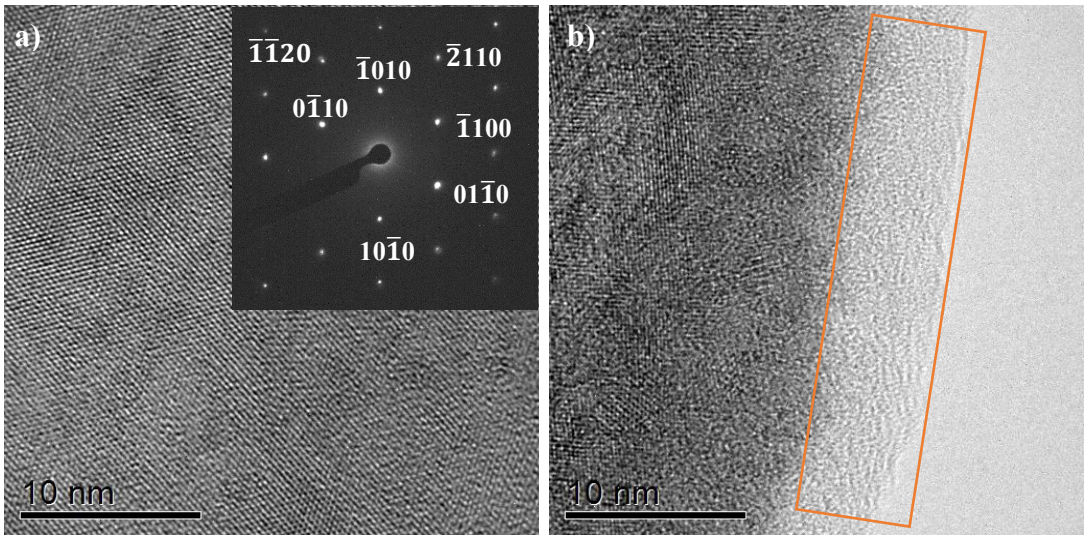
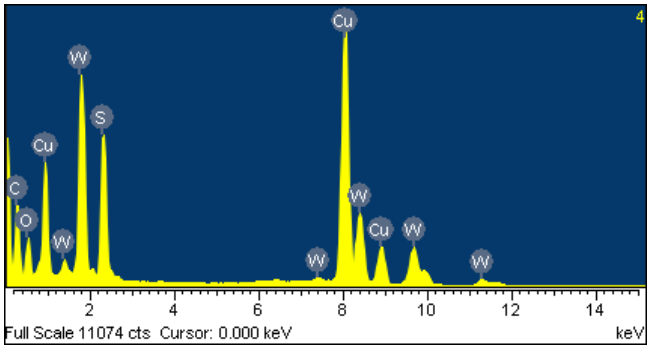


Figure 73. High-resolution TEM micrographs of liquid exfoliated WS_2 nanoflowers using sodium cholate (SC) as surfactant for 30 min under the tip showing a) crystalline flakes with diffraction pattern as inset showing hexagonal packing, b) contamination of amorphous layer at edges.



Element	Weight%	Atomic%
S K	24	14.72
W L	76	8.14
	100	

Figure 74. EDX spectrum along with elemental composition of liquid exfoliated nanoflowers using sodium cholate (SC) as surfactant after 30 min of tip sonication confirming the WS_2 composition.

Though the liquid exfoliation process employing aqueous surfactant solution does dissociate the nanoflowers and reduces the thickness of majority flakes, the process does not provide uniform exfoliation of the nanoflowers. There are undesirable morphologies formed during the exfoliation process as seen in Figure 75. One of the limitation were the agglomerates formed especially with longer sonication times as shown in Figure 75a. The other limitations were rolling up of the flakes/petals of nanoflowers during exfoliation process as seen in Figure 75b and Figure 75c, making it difficult to form few-layered sheets. The problems with contamination in the case of SDS as shown in Figure 75d has been overcome partially by employing SC.

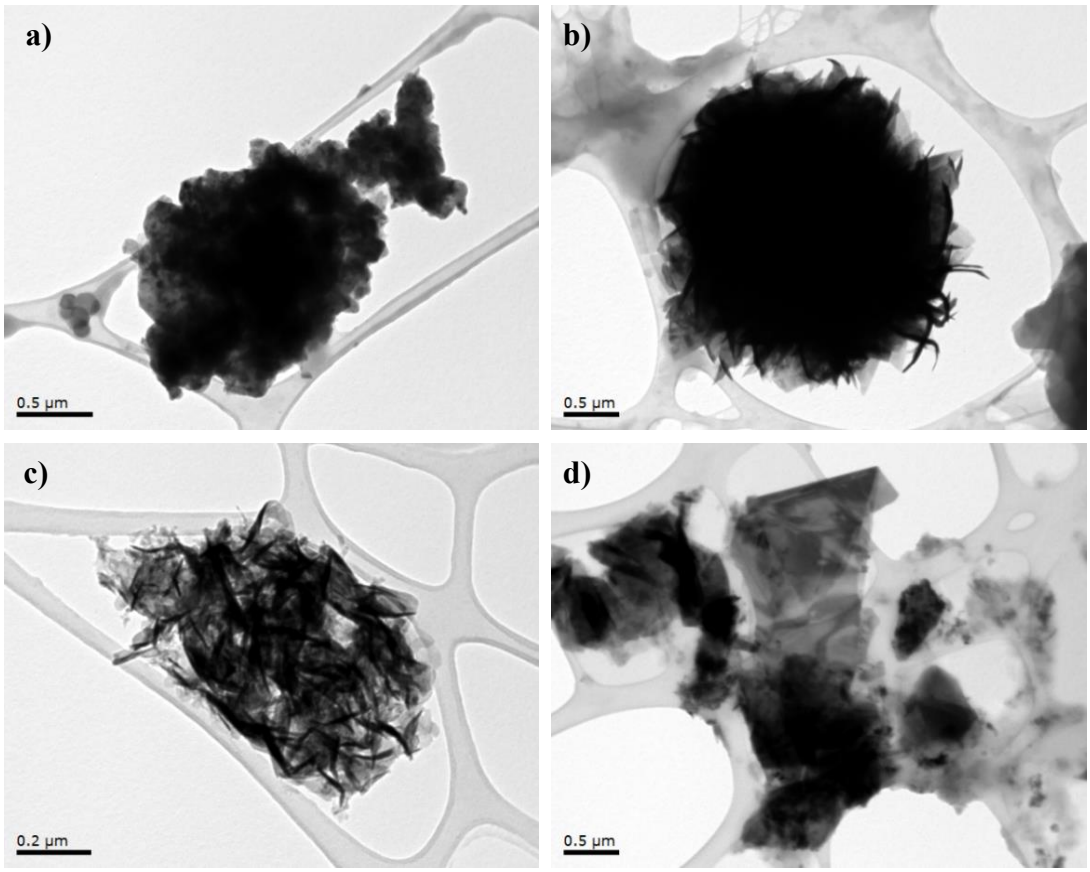


Figure 75. TEM micrographs of undesirable morphologies formed by liquid exfoliation using aqueous surfactant of WS_2 nanoflowers which include a) agglomerates; b) rolled up nanoflowers; c) rolled up exfoliated flakes; d) contaminations accumulating on flakes.

However, even with SC, the exfoliated flakes are covered with an amorphous thin layer of contamination at the edges. This combined with presence of undesirable morphologies in the final product along with the exfoliated flakes are major drawbacks of the liquid exfoliation process. In spite of these drawbacks exfoliation of nanoflowers offers better control than liquid exfoliation of bulk material and it produces significantly larger quantities of thinner regions.

3.3.3. Exfoliation of WS_2 nanoflowers by sonication in simple solvents

Simple solvents such as ethanol and water were employed to exfoliate the nanoflowers. The tip sonication process, which has been shown to be effective in breaking down the nanoflower morphology, was employed for 15 min. TEM micrographs of the resultant morphology are shown in Figure 76. The nanoflowers have been broken up well by the sonication process to form clusters as seen in Fig 76a. These clusters contained broken up flakes which appear to be thin and small with plenty of edges as evident from Figure 76b. The high-resolution TEM micrographs revealed cluster of flakes with plenty of edges exposed and varying thickness of these edges was observed as seen in Fig 76c. The exfoliated flakes were very crystalline and few layers thick with hexagonal packing corresponding to WS_2 as shown in Figure 76d. EDX data in Figure 77 shows the flakes were largely composed of WS_2. The exfoliated flakes were also characterised using STEM, which clearly highlighted the presence of edges and thin flakes in the final deposits. Almost all the deposit obtained by this simple sonication method contained abundance of edges and thin flakes clustered together as shown in Figure 78. This morphology is ideal for applications such as catalysis for hydrogen evolution, which has been shown to take place more actively on the edge states in comparison to the basal planes.[167]

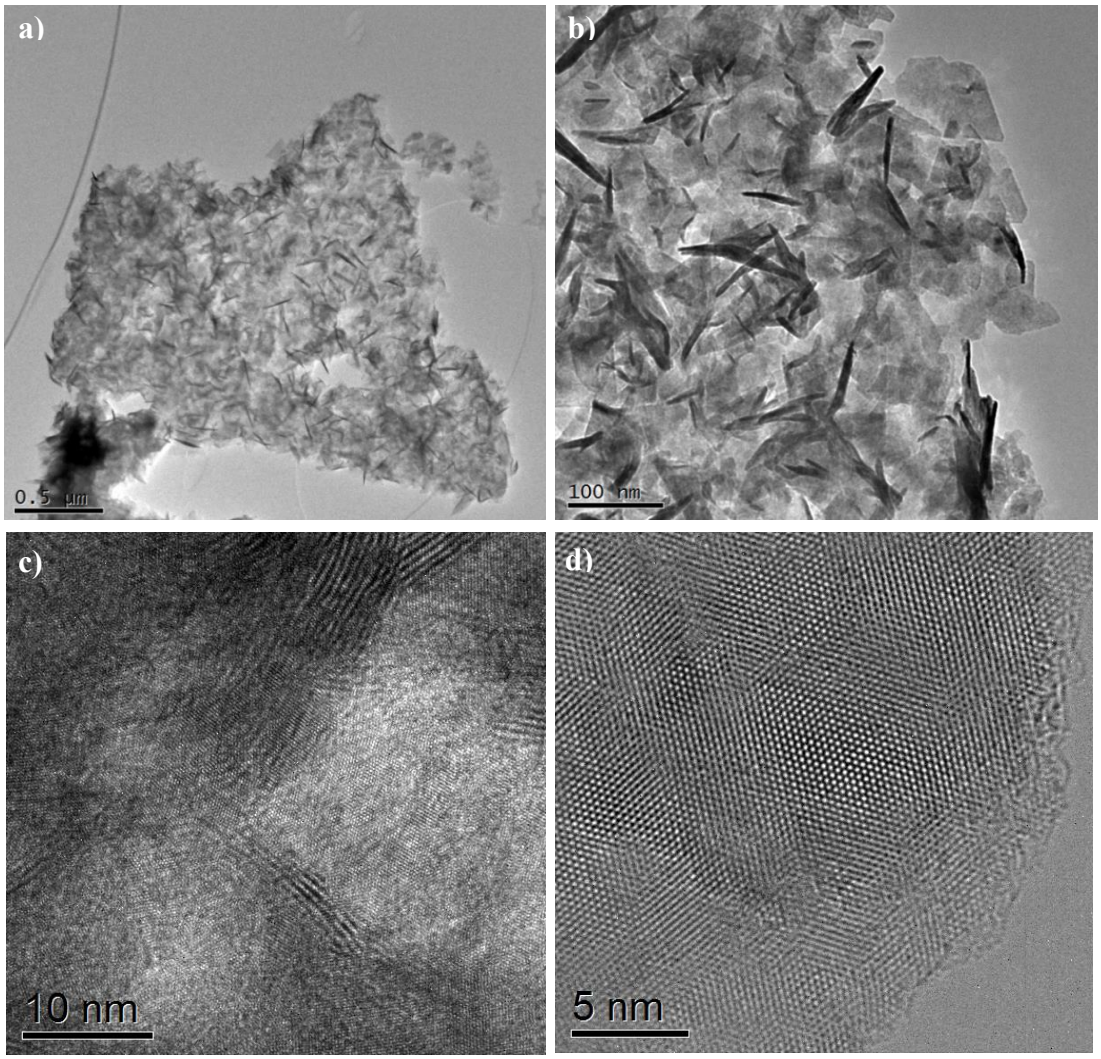
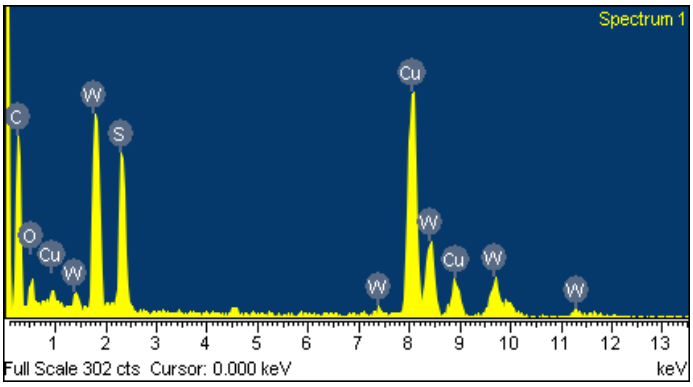


Figure 76. TEM micrographs showing a) cluster of exfoliated flakes, b) edges of exfoliated flakes; HRTEM micrographs showing c) few-layered thick edges, d) lattice and crystal packing of flakes exfoliated using ethanol/water with tip sonication for 15 min.



Element	Weight%	Atomic%
S K	23.2	13.60
W L	76.8	7.85
	100	

Figure 77. EDX spectrum along with elemental composition of nanoflowers exfoliated using simple solvent with tip sonication for 15 min confirming the WS_2 composition.

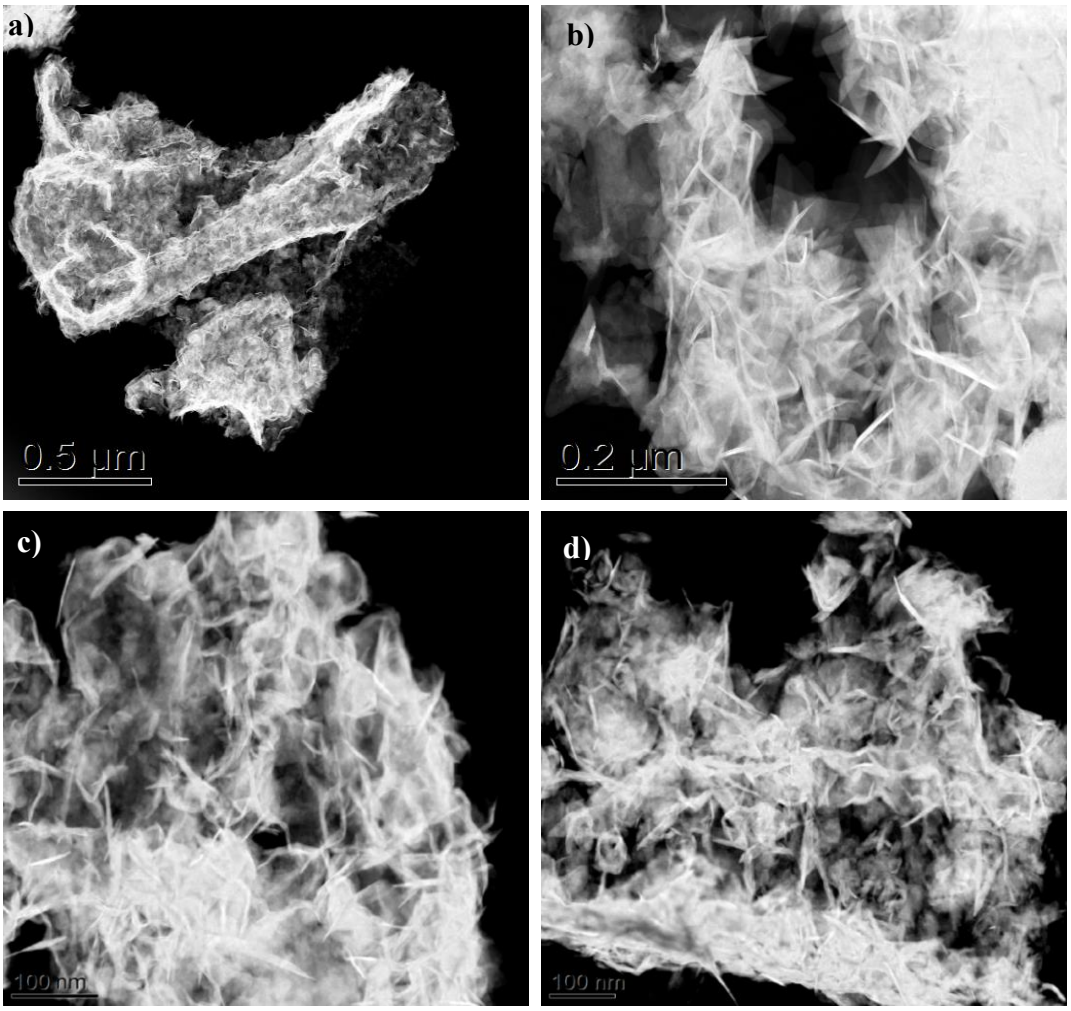


Figure 78. STEM micrographs of WS_2 nanoflowers exfoliated using simple solvent with tip sonication for 15 min showing the presence of a), b) cluster of exfoliated thin flakes; c), d) thin exfoliated regions showing abundance of edges.

Thus the sonication process with ethanol and water helped breaking down the nanoflower morphology into clusters of small flakes, few layers thick and with plenty of exposed edges with better uniformity and lesser time compared to liquid exfoliation of bulk materials. The abundance of edges makes them attractive as electrocatalysts for hydrogen evolution reaction as they would act as active sites. In the following section the performance of these exfoliated nanoflowers as catalysts for hydrogen evolution reaction are tested and compared to other commercially available materials and catalysts.

3.3.4. Electrochemical studies for hydrogen evolution reaction (HER)

The electrocatalytic hydrogen evolution performance of WS_2 nanoflower morphology and its exfoliated flakes form were investigated using linear sweep voltammetry based on polarization curves and Tafel plots. In general, the catalytic performance of nanosized MoS_2 and WS_2 have been compromised due to its poor conductivity.[204] Therefore, a commercial carbon powder material of BP 2000 was mixed with the WS_2 nanomaterials that would help achieve lower overpotential and higher currents by providing a highly conductive matrix and good contact between the nanoflowers. These materials and mixtures were compared to commercially available WS_2, liquid exfoliated WS_2 and vulcanised carbon platinum particles (Pt 20%wt/VC). The polarization curves and the Tafel plots presented in Figure 79, were measured in 0.5M H_2SO_4 with a scan rate of 5 mV/s at a constant temperature of 25 ^oC. Polarization curves can be used to obtain "Tafel plots", which are widespread tools to interrogate the catalytic properties of electrode materials and the reaction mechanism. The absolute values of the recorded current ($|I|$) and the potential (E) are plotted as $E = f(\log |I|)$. The linear branch of this plot is then fit to the equation $E = b \log |I| + a$, where the slope b is commonly called "Tafel slope"). The Tafel slope is an inherent property of the catalyst and is determined by the rate limiting step of the HER. The HER has been suggested to involve three possible reaction steps in an acidic media.[205,206] The corresponding Tafel slope values for each step are calculated using the equation $b = 2.3RT/\alpha F$, where R is the ideal gas constant, T is the absolute temperature, $\alpha \approx 0.5$ is the symmetry coefficient, and F is the Faraday constant. The Volmer reaction is the primary discharge step represented by the equation $H_3O^+ + e^- \rightarrow H_{abs} + H_2O$ with $b \approx$ 120 mV, followed by either an electrochemical desorption step $H_{abs} + H_3O^+ + e^- \rightarrow H_2$

+ H_2O, Heyrovsky reaction $b \approx 40$ mV with or a recombination step represented by Tafel reaction $H_{abs} + H_{abs} \rightarrow H_2$ with $b \approx 30$ mV. The HER may occur via the Volmer-Heyrovsky mechanism or the Volmer-Tafel mechanism and the determination Tafel slope would help in elucidating the elementary steps involved. In both mechanisms, the reaction proceeds through the hydrogen absorption at the electrode and thus the overall reaction is influenced by the free energy of hydrogen adsorption, ΔG_H, as described by Parsons.[207] The optimal HER catalysts have hydrogen adsorption energies close to $\Delta G_H = 0$, which would bind the hydrogen neither too weakly nor too strongly, causing neither the adsorption step or the desorption step to limit the overall reaction rate.

3.3.4.1. Linear sweep voltammetry

Platinum (Pt 20%wt/VC) exhibited the highest HER activity with near zero-overpotential (if the potential is expressed on a RHE scale, the overpotential for hydrogen evolution is equal to the absolute value of the potential) and a Tafel slope of 30 mV is known to proceed through the Volmer-Tafel mechanism with the recombination step as the rate limiting step at low overpotentials. Therefore, promising materials for HER should ideally exhibit a Tafel slope as close as possible to 30 mV. For WS_2 nanoflowers combined with BP (WS_2 NF +BP) an overpotential of 180 mV was calculated from the inset in Figure 79a, with a Tafel slope of 85 mV. In comparison, the exfoliated WS_2 nanoflowers combined with BP (WS_2 NF Ex+BP) exhibited a lower overpotential of 100 mV but a slightly higher Tafel slope of 102 mV. These overpotentials are comparable to MoS_2 edges with typical overpotentials in the range of 150-200 mV.[167,194,208] Lower overpotentials of 80-100mV have been reported for amorphous MoS_2[209], by placing nanocrystals on gold[167], reduced graphene oxide

(rGO)[18] and strained 1T-WS_2 [188]. However the Tafel slope reported for MoS_2 is much lower than WS_2 with 41mV per decade for MoS_2 nanocrystals on graphene being the smallest Tafel slope reported till date. In general, the electrocatalytic activity towards HER has been reported to be better for MoS_2 in comparison to WS_2 with similar nanostructures. For instance, density functional theory (DFT) calculations suggest the hydrogen evolution for MoS_2 is expected to take place at Mo-edge ($\Delta G_H = 0.08$ eV) rather than S-edge ($\Delta G_H = 0.18$ eV), while for WS_2 both edges are equally good ($\Delta G_H = 0.22$ eV). Given these values for hydrogen binding energies (ΔG_H), MoS_2 is predicted to be better than WS_2.[210]

The performance of the mixed materials was certainly better than those obtained for pure WS_2 NF and WS_2 NF Ex with overpotentials of 150 mV and 220 mV respectively, with Tafel slope of around 142 mV. This is attributed to the semiconducting 2H phase of the WS_2 nanoflowers that are formed by self-assembly of nanosheets, which could hinder the charge transfer kinetics primarily due to its high electrical resistance reported in literature.[204] However, the presence of carbon powder with relatively higher conductivity can mitigate this to have a very low percolation threshold for conduction. The commercially available bulk WS_2 and their exfoliated forms obtained by established liquid exfoliation method using NMP[103] (Liq Ex Bulk WS_2 in NMP) and mixed solvent strategy[84](Liq Ex Bulk WS_2 in ethanol) showed poor HER activity. This combined with the usage of toxic and high boiling point solvents such as NMP, laborious and time consuming techniques for preparation of thin regions makes them unfavourable as catalyst for HER.

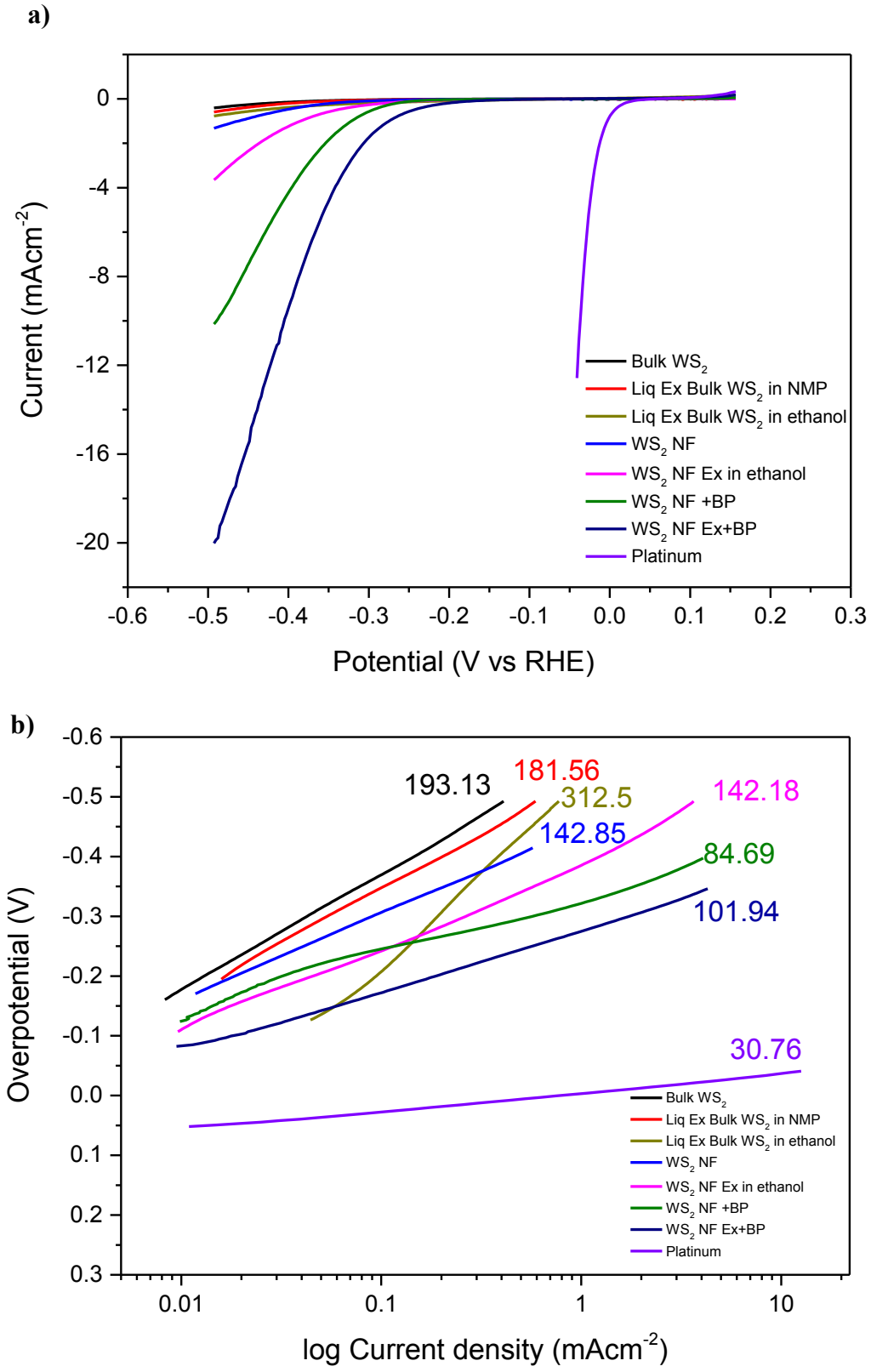


Figure 79. a) Polarization performance curves and b) the corresponding Tafel curves and slope obtained in 0.5M H_2SO_4 for various electrocatalysts

In addition to the Tafel slope, the exchange current density (j_0) is another inherent measure of the HER activity. The WS_2 NF Ex+ BP exhibits a very high j_0 of 15.6 x 10^{-6} Acm^{-2} in comparison to the WS_2 NF+ BP with 1.75 x 10^{-6} Acm^{-2}, mainly attributed to its larger active sites resulting from its unique structural features of few-layered flakes with plenty of exposed edges which would offer abundant catalytic sites for HER and to adsorb hydrogen ions.

3.3.4.2. Electrochemical impedance spectroscopy

Additional evidence on the beneficial role of BP is provided by EIS. In all cases, EIS was recorded at potential values corresponding to the foot, or the first section, of the linear sweep voltammetry downward branch associated with HER (-0.31 / -0.36 V / -0.41 V /-0.56 V vs RHE). Comparison between the EIS response of different materials at the same potential allowed us to evaluate their catalytic activity by comparing the charge-transfer resistance (R_{CT}, see figure 80). The Nyquist plot recorded for WS_2 NF Ex+ BP at -0.36 V is shown in Figure 80 (squares), along with the fitting (line) corresponding to the modified Randles circuit. While the resistance associated with ohmic losses (R_{ohm}) remains constant for all materials at approximately 30 Ω, the charge transfer resistance (R_{CT}), which is a proxy for the kinetics of the reaction, hence the catalytic activity of the material under investigation, is the lowest for WS_2 NF Ex+ BP at all potentials. For the EIS experiment in figure 80, $R_{CT} = 879 \pm 23$ Ω.

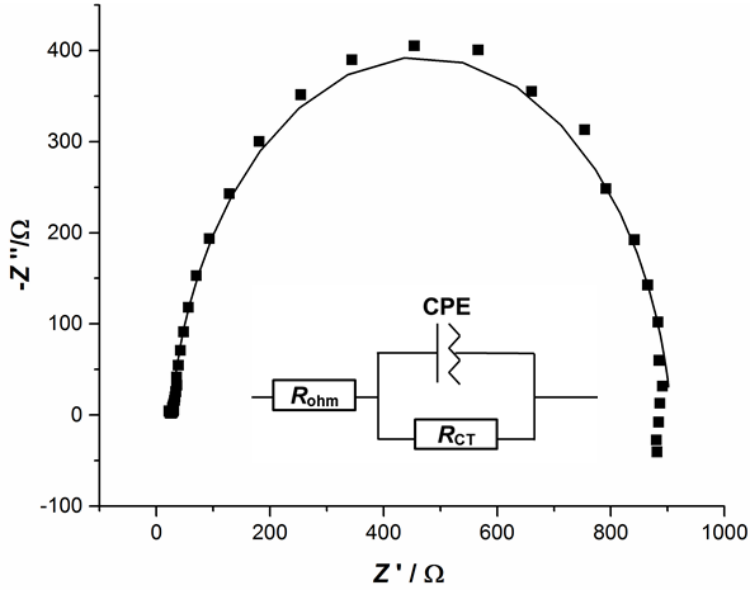


Figure 80. Nyquist plots showing the electrode kinetics of exfoliated WS_2 nanoflowers with BP at -0.36V vs RHE

In table 4, the R_{CT} from fitting of EIS experiments at – 0.41 V for the four catalysts studied has been summarised. The R_{CT} of exfoliated WS_2 nanoflowers obtained at -0.41V is comparable to the charge transfer resistance of 232 Ω reported for as grown MoS_2 nanosheets[189] and 200 Ω for 2H-WS_2 nanostructures[211]. However, the lowest charge transfer resistance reported so far has been for chemically exfoliated 1T-MoS_2 with 4 Ω and metallic 1T- WS_2 with 5-6 Ω mainly due to its metallic nature.[189,211]

Material	R_{CT} (Ω)
WS_2 NF Ex+ BP	386 ± 12
WS_2 NF + BP	576 ± 17
WS_2 NF Ex	15300 ± 1300 *
WS_2 NF	7315 ± 300 *

Table 4. Electrochemical impedance spectroscopy measurements giving charge transfer resistance of various catalysts measured at -0.41V vs RHE. * Fitting is poor and the Nyquist plot tends to become a straight line.

3.3.4.3. Cyclic voltammetry

The stability and durability is another important aspect to measure for a good electrocatalyst. For assessing this, the best catalyst obtained from our experiments, exfoliated nanoflowers in combination with carbon powder (WS_2 NF Ex+BP), was subjected to continuous cycling using cyclic voltammetry for 100 cycles. The polarization curves at end of 100 cycles show minimal loss in cathodic current and a similar I-V curve in comparison to the first one as seen in Figure 81. This suggests a good stability for the WS_2 NF Ex electrocatalysts.

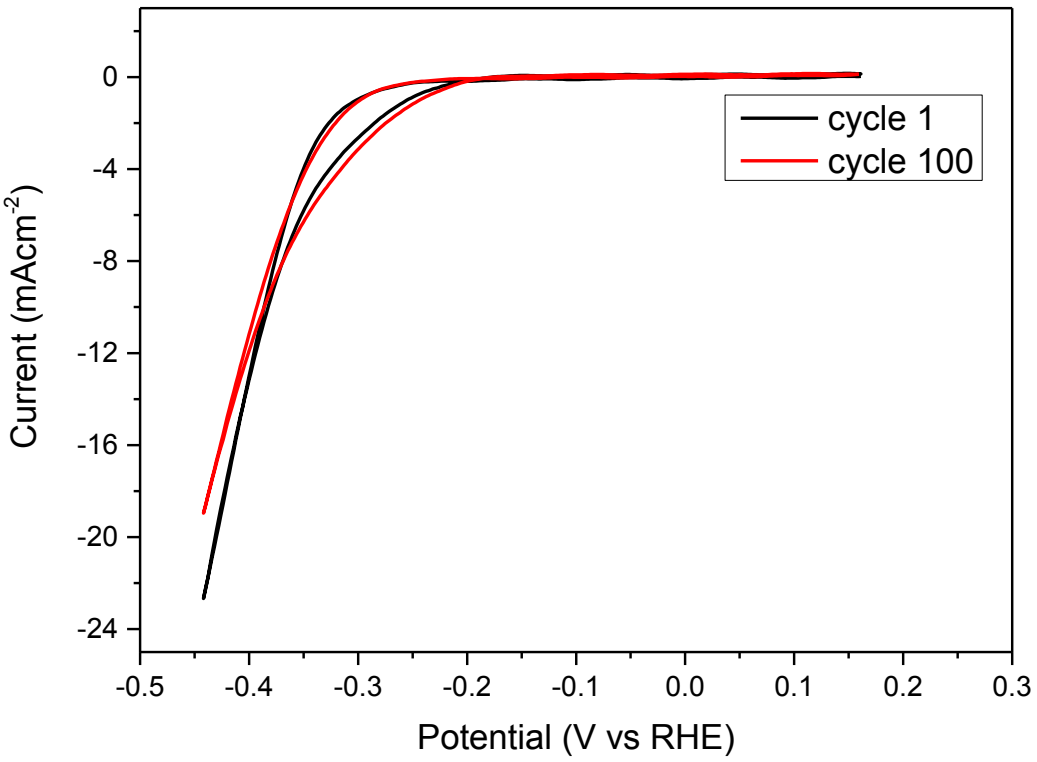


Figure 81. Durability test of WS_2 NF Ex+BP electrocatalysts using cyclic voltammetry curves obtained by continuous cycling, with in the first and after 100 cycles showing minimal change in performance.

3.4. Conclusion

The WS_2 nanoflower morphology synthesised by the simple chemical vapour deposition process as explained in the previous chapter, was used as a starting material for various exfoliation processes and also applied as electrocatalysts for hydrogen evolution reaction (HER). The key findings/results are listed below.

- The mechanical grinding produced small amounts of very thin (one to three layer thick) and small (tens of nanometer) crystalline WS_2 region supported on amorphous SiO_2 (scrapped from substrate) but generally offered limited control over the resultant final morphology.
- Systematic study of exfoliation using surfactants such as sodium dodecylsulfonate (SDS) and sodium cholate (SC) produced few-layered crystalline WS_2 flakes with uniform thickness. However, the process did suffer from drawbacks caused by contamination, rolling up of the flakes, agglomeration and breaking of flakes into very small pieces, which cause contamination.
- Sonification process with simple solvents like ethanol produced a cluster of thin, few-layered flakes with abundance of exposed edges, which were investigated as electrocatalysts for HER in combination with commercially available BP powder as the carbon matrix.
- The exfoliated flakes combined with BP showed excellent HER activity with an overpotential of 100 mV and Tafel slope of 102 mV/decade along with an exchange current density of 15.6×10^{-6} A/cm^2.

Chapter 4. Growth study of two-dimensional WS_2 by Chemical Vapour Deposition (CVD)

4.1. Introduction

An important aspect of TMDs research is the reliable production of atomically thin 2D layers *via* scalable approaches. The utilisation of 2D materials in potential applications is hindered by the absence of a reliable large scale synthesis method which is controllable and reproducible. Various processes including mechanical cleavage, liquid exfoliation and sulfurization of transition metal oxides through CVD employed for the synthesis of 2D TMDs have been discussed in Chapter 1 under section 1.3.3.2. Chemical vapour deposition (CVD) has shown promise to generate high-quality TMD layers with scalable size, controllable thickness and excellent electronic properties. Even though the synthesis of monolayer MoS_2 crystal domains and films have been realised using CVD, the tendency to form nanoparticles[212] and multilayers[119] hinders its effectiveness. In spite of its the initial promise of CVD for synthesising 2D TMDs, sufficient understanding of the influence of various experimental parameters on the growth process is lacking.

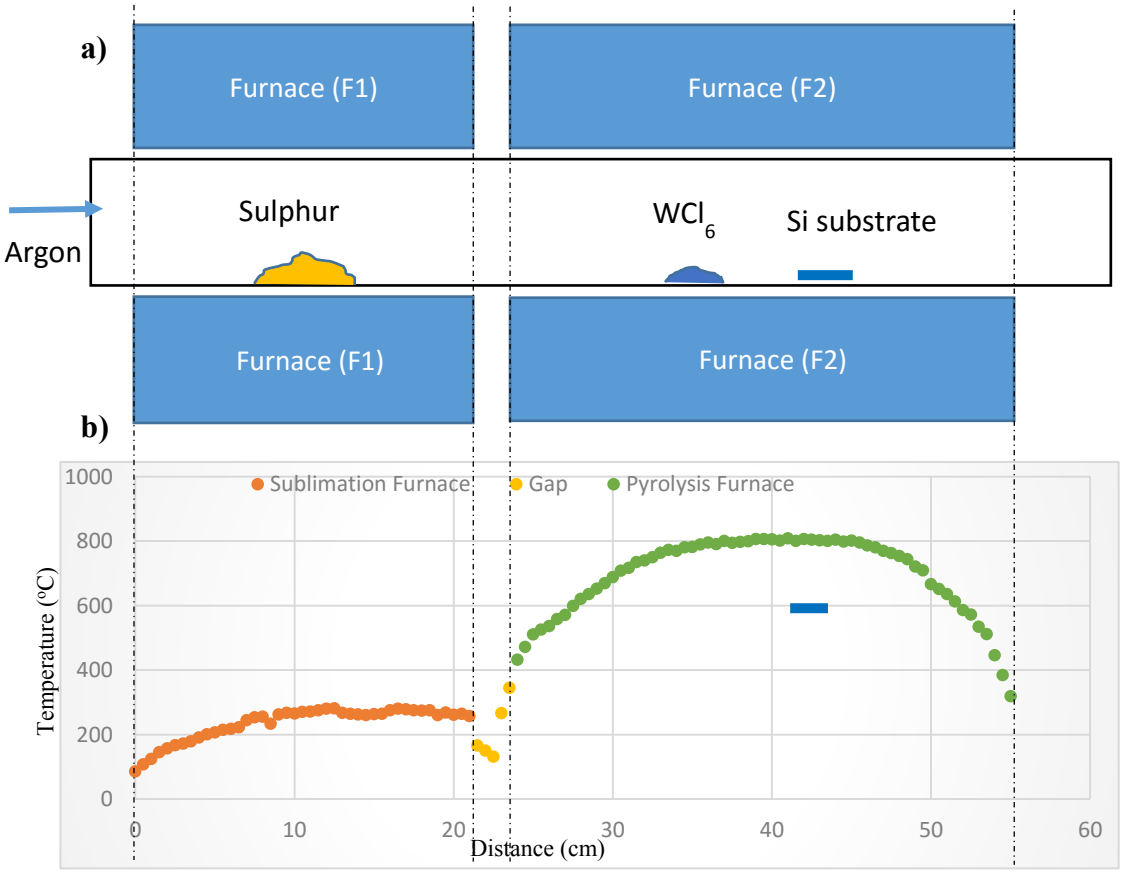
In this work the CVD synthesis of 2D WS_2 has been investigated using WCl_6 and S as precursors, and the influence of experimental parameters on the growth process has been reported. WCl_6 was selected due to its higher volatility and lower melting point. Till date, most CVD growth approaches have used WO_3 as precursor with S at elevated temperature.[88,213] WO_3 as precursor possesses higher melting point and low volatility which would require high growth temperatures. Furthermore, both precursors are usually employed in a single furnace which does not offer control over

the precursors and limits the parameter space for the chemical reaction. To overcome these limitations, I employed CVD method that separates the metal and sulphur precursors into different furnaces. This offers better control over the precursor input, their mass transport to the deposition chamber, and the rate of the gas phase reaction. By controlling the sublimation temperature of sulphur, the amount and rate of sulphur input can be controlled to a large extent. Nevertheless it is still difficult to precisely control the partial pressure of the gas phase precursors when solids are evaporated into a carrier gas stream. The influence of various parameters such as sulphur sublimation temperature, synthesis temperature and time, substrate position and type, and precursor's purity on the growth process have been systematically examined and presented.

4.2. Experimental

The synthesis of 2D inorganic chalcogenides was carried out using CVD process using a two stage furnace setup. The metal source (metal chlorides) and the chalcogen source (elemental sulphur) were placed in two different furnaces which could be operated independently as shown in Figure 82. The precursor colloidal sulphur (80% purity) was loaded into the quartz tube such that it would be placed in the centre of the first furnace (F1) which would be maintained at a lower temperature of 100-350 ^{o}C. The WCl_6 (99.9% purity) was positioned away from the sulphur in such a way that it would be at centre of second furnace (F2), with the substrates placed 5 cm away from the precursor and was maintained at the set temperature of the furnace. The precursors and substrates were loaded at one end of the 150 cm long quartz tube and connected to argon flow of 100 sccm such that the precursors was far away from the hot zone until the furnace reached the set temperature. After the furnaces reached their

respective set temperatures, the quartz tube was slid across to position the precursors and substrates, as shown in the simple schematic of the setup in the Figure. 82a. Also the furnaces the separated by 3 cm to prevent any influence of higher temperature furnace (F2) on the lower temperature furnace (F1). The temperature profile of the furnaces separated by 3 cm with F1 at 250 ºC and F2 at 800 ºC is shown in Figure 82b. The growth of 2D WS_2 was initially attempted on plain silicon substrates at



atmospheric pressure to identify the parameter space.

Figure 82. a) Schematic of experimental setup for two stage furnace chemical vapour deposition setup; b) Temperature profile of furnaces separated by 3 cm and maintained at 250 ºC and 800 ºC

The precursors employed for the CVD method is similar to the one employed for the synthesis of 3D nanoflower detailed in Chapter 2. The difference in the synthesis strategy were the changes to the ratio and quantity of precursors and their respective

sublimation temperature. The amount of the chloride precursor was reduced significantly from 2 mmol to 0.03 mmol based on the observation made by Yu *et al.* [214], where the amount of $MoCl_5$ has been shown to have a direct effect on the thickness of the MoS_2 films. Hence, the amount of WCl_6 used in these set of experiments was reduced to few milligrams (4-15 mg). The amount of sulphur precursors was weighed out such that a molar ratio of WCl_6 and sulphur of 1:1000 was maintained. This would ensure that the reaction of WCl_6 with S to form WS_2 would be complete. Also the sulphur was sublimed in a separate furnace at much lower temperature which offered control over the precursor input. The molar weights of precursors were chosen to be 12 mg (0.03 mmol) of WCl_6 and 960 mg (30 mmol) of sulphur. This is the first time the growth of 2D WS_2 was attempted using the chloride precursors at atmospheric pressure. The biggest challenge was to limit the growth of WS_2 in the third dimension to prevent the formation of 3D structures such as nanoflowers.

The investigation into the role of sulphur sublimation temperature was established by varying the temperature of the low temperature furnace (F1) from 350 ^oC to 200 ^oC in steps of 50 ^oC while maintaining the higher temperature furnace (F2) at 850 ^oC with WCl_6 and the silicon substrate. A synthesis time of 30 min was employed for this set of experiments and the effect of synthesis temperature was studied by maintaining the sulphur sublimation temperature at constant at 250 ^oC while varying the synthesis temperature from 600 ^oC to 900 ^oC with WCl_6 and the silicon substrate positioned at the centre of the furnace. A synthesis time of 30 min was employed similar to the previous study. Having determined the appropriate temperatures for synthesis, the influence of position of the substrate across the length of the furnace on the growth was investigated. For this purpose, substrates were positioned downstream relative to

the precursor WCl_6. The role of synthesis time on the growth was also studied relative to the synthesis and sublimation temperature by using two different time periods of 30 min and 1 hour. To investigate the influence that the substrates would have on the growth of 2D WS_2, three different substrates namely silicon, 300 nm SiO_2 coated silicon and (0001) c-plane oriented sapphire were employed as growth substrates in the same APCVD process. The substrates were positioned around 5 cm from WCl_6 precursors in the synthesis furnace maintained at 850 ^oC. The sulphur sublimation temperature was varied from 250 ^oC to 100 ^oC, since above 250 ^oC the reaction tended to form 3D structures and sulphur sublimes only above 100 ^oC, with a synthesis time of 1 hour. Finally the effect of precursor's purity and the importance of precursor control for the synthesis of 2D TMDs has been discussed.

The morphology of the material deposited on the substrate was studied using scanning electron microscopy (SEM) (JEOL-840F, JSM 6500F) operating at 5 and 10 kV acceleration voltages. The Raman spectra of the deposits were obtained using a JY Horiba Labram Aramis imaging confocal Raman microscope with a 532 nm green laser using as grown samples. Powder X-ray diffraction was carried out on a Siemens D5000 X-ray powder diffractometer. The range of 2θ employed was 10^o-60^o with a step size of 0.050^o and count time of 10 s. The atomic force microscopy was performed using a Park AFM operated in contact mode using Al-BS cantilever.

4.3. Results and Discussion

4.3.1. Influence of sulphur sublimation temperature

SEM studies as shown in Figure 83, revealed that the change in sulphur sublimation temperature has a distinct effect on the morphology of the deposits along with the corresponding AFM profiles of the 2D deposits. At sulphur sublimation temperature of 300 ^{o}C, flat 2D domains of WS_2 start to form along with the presence of flakes grown out-of-plane from the deposit as observed in Figure 83a. These triangular flakes are relatively thick at the centre but taper down to thinner region as seen along the edges in Fig 83b. This morphology has also been verified with the AFM as can be observed from the topography image in Figure 83c. The profile across the domain presented in Figure 83d shows the increase in thickness of the flake towards the centre. The step height of the flake obtained at the edge was 20.43 ± 4.1 nm as inferred from the profile fit shown in Figure 84d. It was difficult to record the topography of flakes with out-of-plane growth using the AFM due to the sharp difference in height. This out-of-plane growth as shown in the schematic 84f, could be possibly due to the relatively high sulphur sublimation temperature. This would result in a larger amount of sulphur being sublimed in shorter time and thus resulting in the faster reaction rates, thereby causing formation of 3D structures. The WS_2 domains also contained large particles which could possibly have formed during the cooling stages of the experiment and have acted as contamination. Consequently, the WS_2 flakes obtained at sulphur sublimation temperature of 300 ^{o}C do not possess uniform thickness across the domain and are characterised by steep edges and thicker regions in the middle.

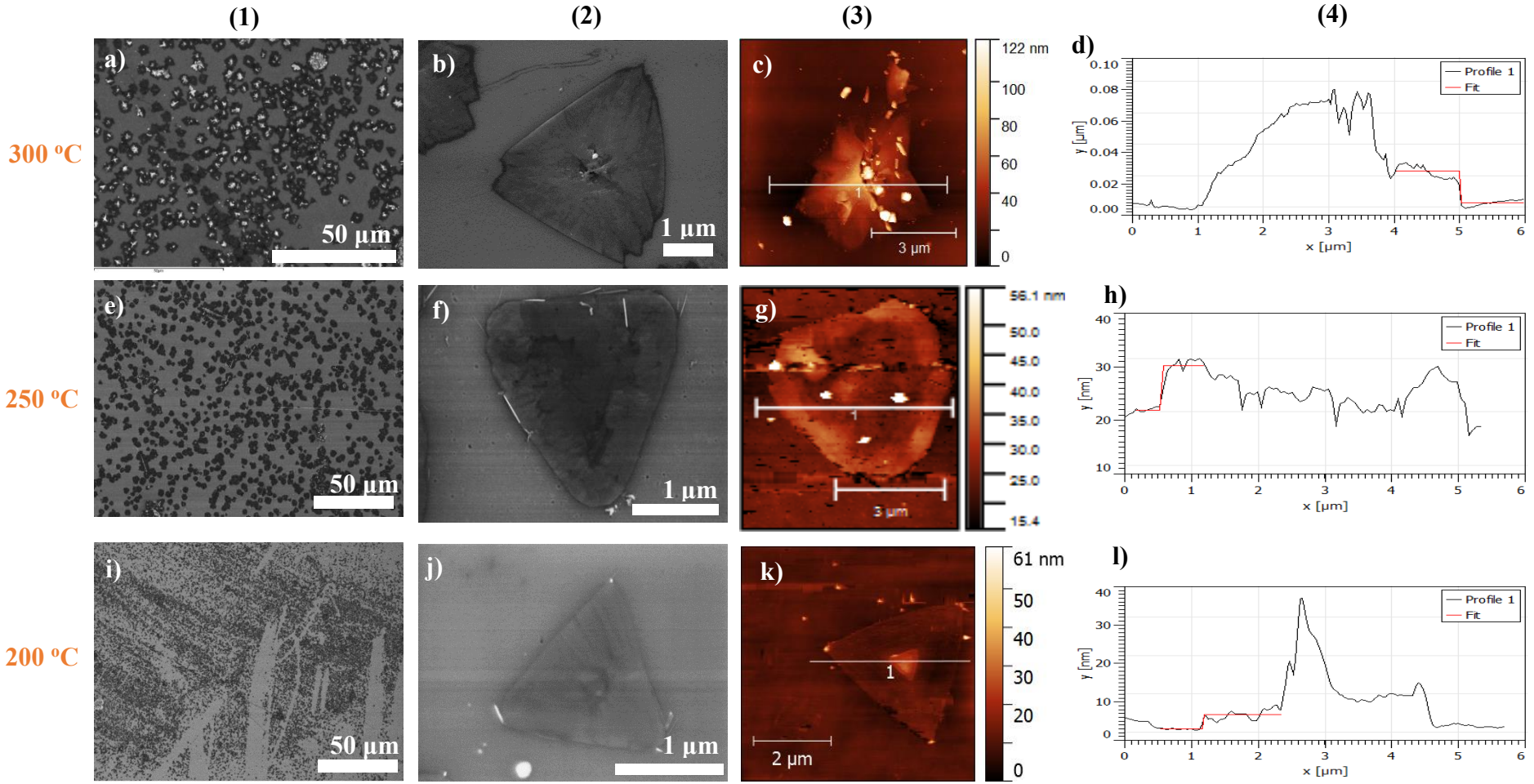


Figure 83. (1) SEM micrographs showing change in nucleation density with sulphurisation temperature a) 300 ºC, e) 250 ºC, i) 200 ºC ; (2) SEM micrographs showing morphology of 2D deposits obtained at sulphur sublimation temperatures of b) 300 ºC, f) 250 ºC, j) 200 ºC; (3) AFM results of individual flakes obtained at sulphurisation temperature of c) 300 ºC, g) 250 ºC, k) 200 ºC; (4) AFM profile obtained across the region shown in (3) at sulphurisation temperatures of d) 300 ºC, h) 250 ºC, l) 200 ºC with sulphurisation temperatures specified along the left axis .

This morphology obtained at 300 °C was studied in further detail as shown in Figure 84 to understand the growth mechanism. The domains nucleate as isolated islands as observed in Figure 84a, but coalesce to form large continuous patches underneath the thicker domain as seen in Figure 84b, and Figure 84c. Also the growth of out-of-plane flakes are observed on some domains forming the 3D nanoflower structure as observed in Figure 84d. These flakes always seem to have grown mostly from the centre of the thicker domains. The schematic of this growth is shown in Figure 84e, and Figure 84f.

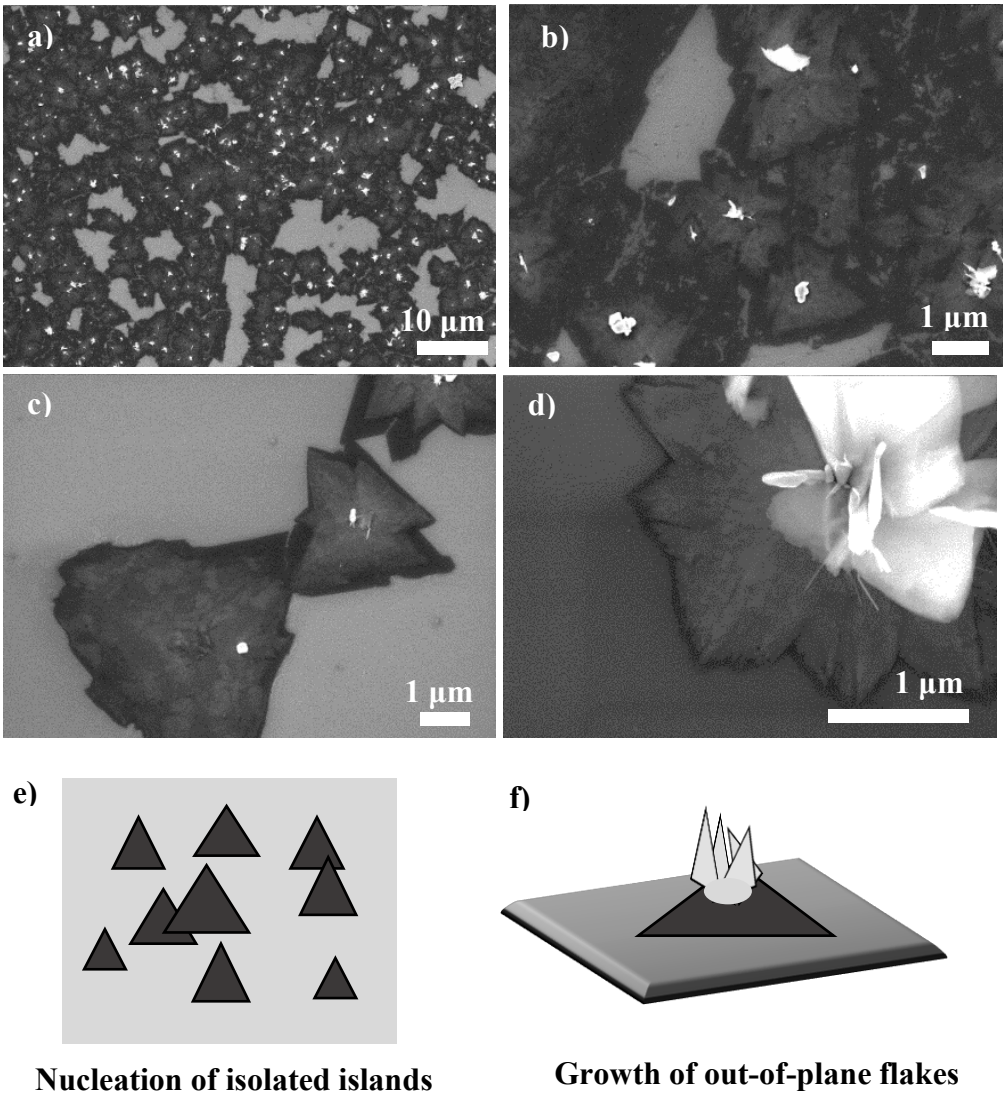


Figure 84. SEM micrographs of deposits produced at sulphur sublimation temperature of 300 °C with synthesis temperature of 850 °C on silicon substrates along with schematic showing the growth of isolated domains and 3D flakes from the domains.

With reduction in sulphur sublimation temperature to 250 ^{o}C, triangular flat domains are formed throughout the sample. It is evident from Figure 83e that the nucleation density of these domains has increased and the size has decreased in comparison to Figure 83a. Normally the increase in nucleation density in CVD process is associated with the presence of impurities, especially carbon. Since colloidal sulphur (80%) contains carbon impurities as will be discussed in detail later in section 4.3.6, it could explain this increase. Similarly, the increase in nucleation density would be normally accompanied by a decrease in domain size as the amount of metal precursor is limited. This could explain the smaller triangular domain observed in Fig 84f, around 3 μm, in comparison with Figure 83b which is around 5 μm. It can also be seen that the flakes growing out of the domains are eliminated. The absence of 3D structures corresponds to the reduction in the rate of sulphur sublimation, which would generally lead to lower growth and reaction rate. Also interestingly the triangular domains formed were more rounded along the corners as seen in Figure 83f. From the AFM profile shown in Figure 83h, it was observed that the edges are thicker than the flake possibly suggesting growth of the flakes with nucleation at the edges. The average thickness of the flake along the edges was found to be 9.22 ± 1.8 nm, which is half the thickness of domains edges obtained at 300 ^{o}C. With further reduction in sulphur sublimation temperature to 200 ^{o}C, the triangular domains reduced in size significantly to around 1 μm, along with a drastic increase in nucleation density, as seen in Figure 83i. This is similar to the trend observed with reduction in sulphur sublimation temperature from 300 ^{o}C to 250 ^{o}C. The domains are considerably thinner, uniform and a smaller triangular region is formed in comparison to the previous condition. The average thickness of the flake at the edges was measured to be 5.83 ± 0.81 nm from

the profile in Figure 83l, which is significantly thinner than the other two conditions. Besides a triangular nucleation centre was observed on the domains as seen Figure 83k, suggesting an outward growth of the flakes from the centre.

The nucleation and growth of these WS_2 domains can be explained using three main growth models for CVD of thin films as shown in Figure 85. Two dimensional layer-by-layer or Frank-van der Merwe occurs when the film atoms are equally or less strongly bound to each other than to the substrate, often in the case of homoepitaxy on clean substrates. In a 3D island growth, often referred to as the Volmer-Weber growth mechanism, small clusters nucleate directly on the substrate initially and grow into three-dimensional islands, which eventually coalesce to form a continuous film. This growth mode takes place when the film atoms are more strongly bound to each other than to the substrate. The layer-plus island growth or Stranski-Krastanov growth mode is combination of the previous mechanisms. After growth of one or more monolayers, subsequent layer growth becomes unfavourable and islands grow on top of initial layers.

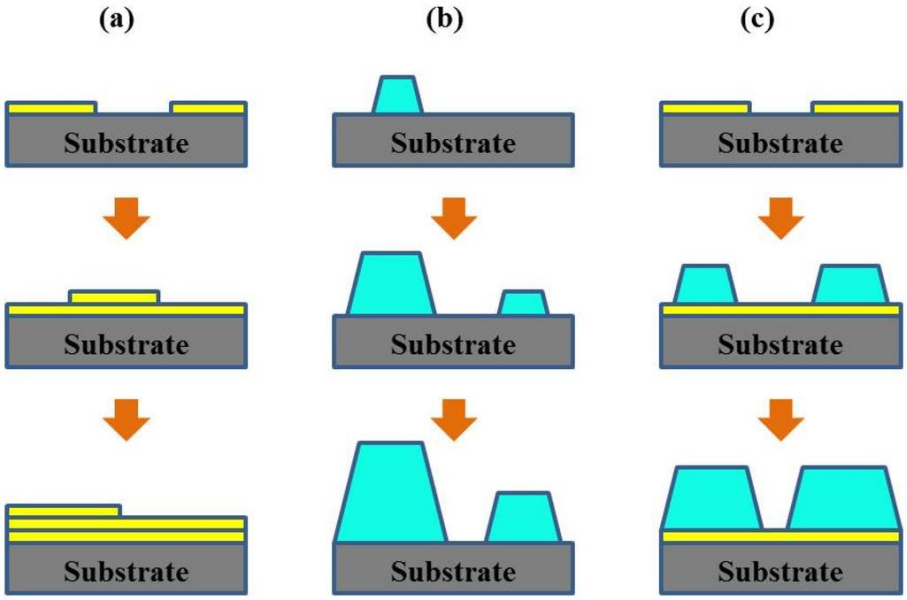


Figure 85. Schematic of three basic growth modes: (a) layer-by-layer growth mode; (b) island growth mode; and (c) Stranski–Krastanov mode. Reproduced with permission. ref. [215]

At higher sulphur sublimation temperature of 350 ºC, 3D structures are formed as shown in Figure 86a. The higher magnification of these structure in Figure 86b, indicates the presence of wire-like structures which is not a desired morphology. These 3D structures were found to form at higher temperatures, which would generally lead to faster nucleation and higher growth rates in comparison to growth at lower sulphur sublimation temperature.

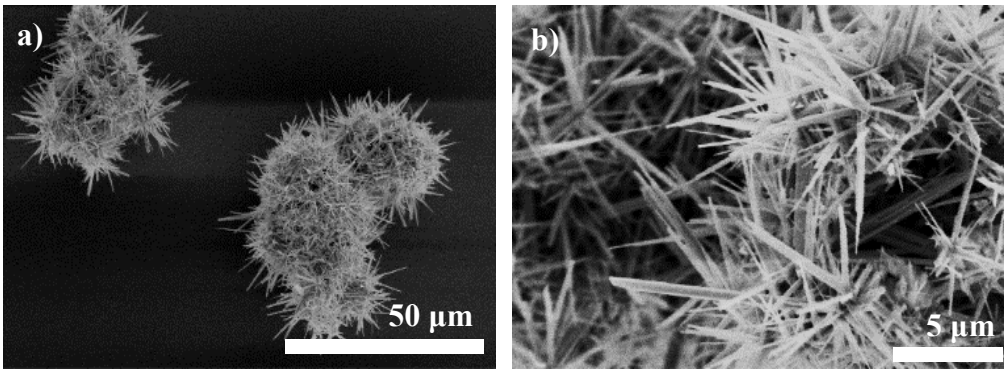


Figure 86. SEM micrographs of deposits obtained at sulphur sublimation temperature of 350 ºC showing the presence of 3D wire-like structures.

Raman Spectroscopy under 532 nm laser excitation was used to confirm WS_2 with peaks corresponding to in-plane vibration of E_{2g} mode at around 350 cm^{-1} and the out-of-plane A_{1g} mode around 420 cm^{-1}. This was observed for all deposits obtained at various sulphur sublimation temperature. The Raman spectrum for the three sulphur sublimation temperatures of interest is shown in Figure 87, in comparison to bulk WS_2 powder. The second order modes are seen in the 2D deposits which are absent in the bulk material. The peak around 521 cm^{-1}corresponds to the silicon substrate on which the deposits were formed. X-Ray Diffraction was further performed on the 300 ºC sulphur sublimation temperature sample, and a spectrum with a prominent signal of (002) peak corresponding to a well stacked WS_2 crystalline phase was observed in Figure 88. It confirmed the absence of any other crystal phases. However, XRD was

not easible at lower sulphur sublimation temperature as the amount of deposits was below the detectable quantity and proved difficult to obtain any significant signal.

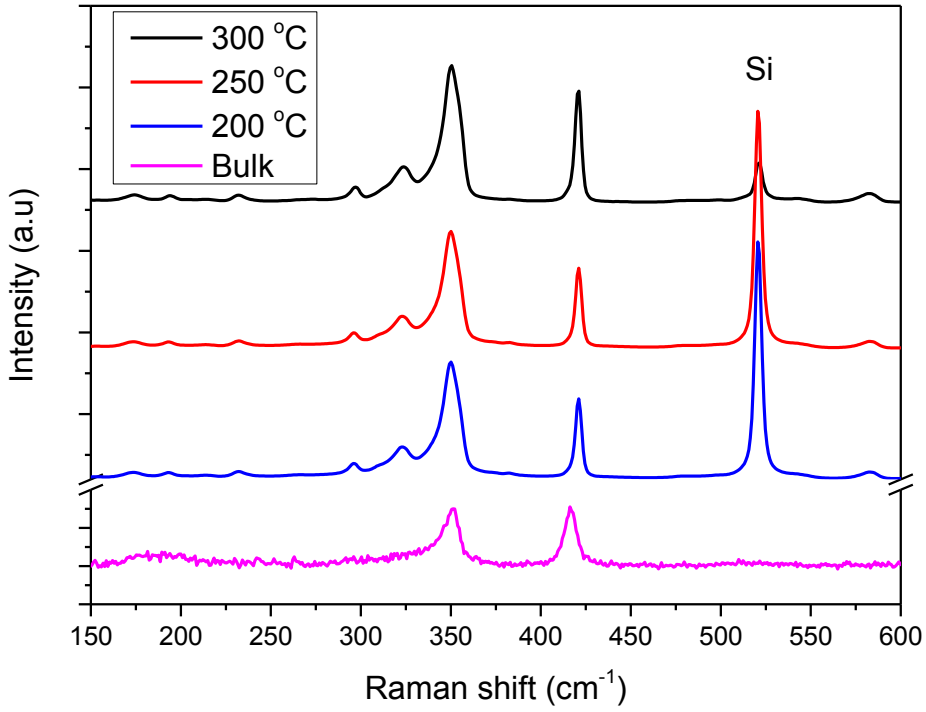


Figure 87. Raman spectroscopy representing deposits at different sulphur sublimation temperature with synthesis temperature of 850 ºC on silicon substrates revealing presence of WS_2.

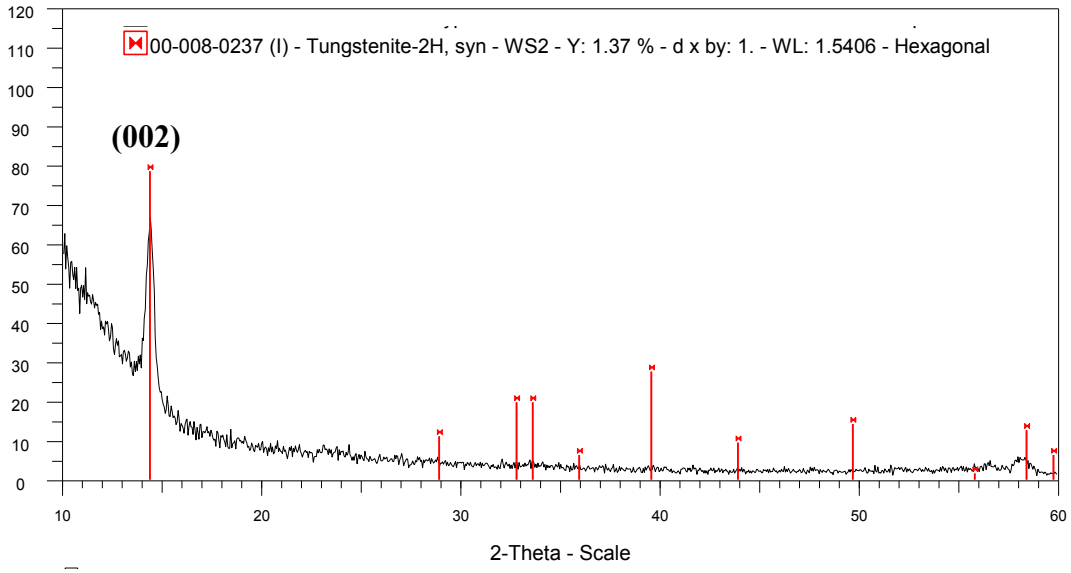


Figure 88. XRD pattern of deposits obtained at 300 ºC sulphur sublimation temperatures with synthesis temperature of 850 ºC on silicon substrates showing the presence of WS_2 crystal phase.

Thus the effect of sulphur sublimation temperature on the morphology, thickness and nucleation density of the WS_2 domains has been discussed in detail. It has been shown with decrease in sulphur sublimation temperature from 300 to 200 ^oC there is an increase in the nucleation density and a reduction in the thickness from 20 nm to about 6 nm, with reduction in the size of the WS_2 domains from 5 μm to 1 μm. The morphology of these domains change quite significantly with out-of-plane growth disappearing and forming more uniform triangular domains. Further, the effect of lower sulphur sublimation temperatures with growth on different substrates have been studied later in this chapter in section 4.3.5.

4.3.2. Influence of synthesis temperature

The influence of synthesis temperature was studied by varying it from 600-900 ^oC whilst maintaining the sulphur sublimation temperature at a constant 250 ^oC. The deposits obtained are summarised in Figure 89 using SEM micrographs. The synthesis temperature controls the diffusion rate of the precursors and thus the rate of the gas phase reaction which determines the nucleation and growth of the WS_2 domains. At higher temperatures of 900 ^oC, wire-like deposits along with agglomerates in the form of potholes were formed as seen in Figure 89a. These 3D structures are often the result of larger diffusion rate of precursors at higher temperatures, leading to faster growth rates. The optimum synthesis temperature for the formation of 2D WS_2 domains was found to be 800-850 ^oC, with large flat domains forming at 800 ^oC as shown in Figure 89b. With reduction in synthesis temperatures to 750 ^oC, thick agglomerates were deposited as presented in Figure 89c, possibly caused by nucleation sites turning into trap centres. At low temperatures with low diffusion rate, the subsequent precursor nucleated at the trap sites leading to thick deposits. At lower synthesis temperature of

600 ºC, particles were formed as seen in Figure 89d possibly due to low diffusion rate of precursor causing them to be trapped in the pre-growth sites of substrate preventing growth.

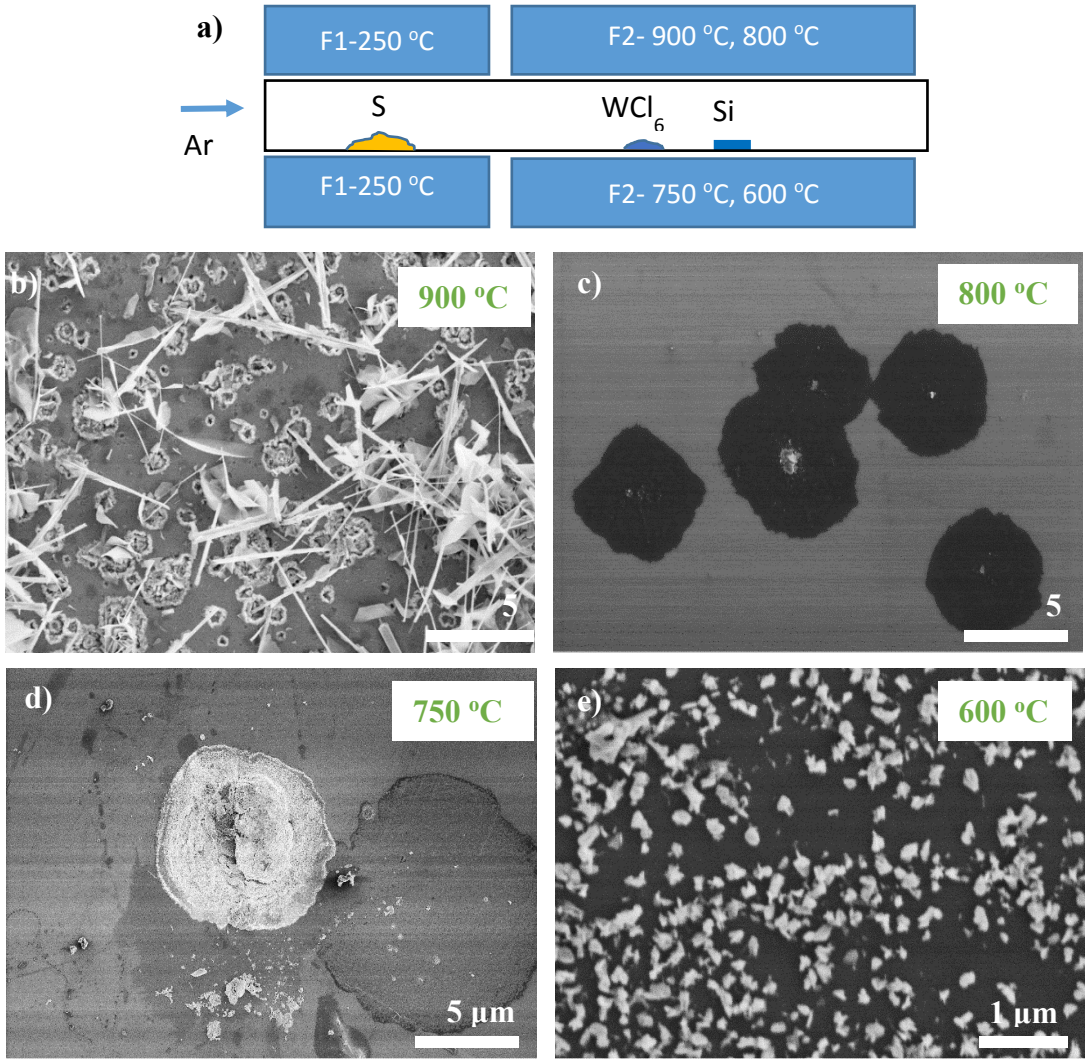


Figure 89. a) Experimental setup showing the variation in synthesis temperature and position of precursors; SEM micrographs of deposits produced at sulphur sublimation temperature of 250 ºC with different synthesis temperature of b) 900 ºC, c) 800 ºC, d) 750 ºC, e) 600 ºC on silicon substrates.

4.3.3. Influence of substrates position

The position of the silicon substrate in the quartz tube seem to have an effect on the deposit of WS_2 formed. This was investigated by placing substrates downstream of the flow at various positions relative to the position of the WCl_6 precursor. With increase

in distance of the substrate from the precursor (placed at 39.5 cm), the deposits formed were thicker as can be seen from the SEM images in Figure 90, obtained for synthesis temperature of 800 ºC and 850 ºC.

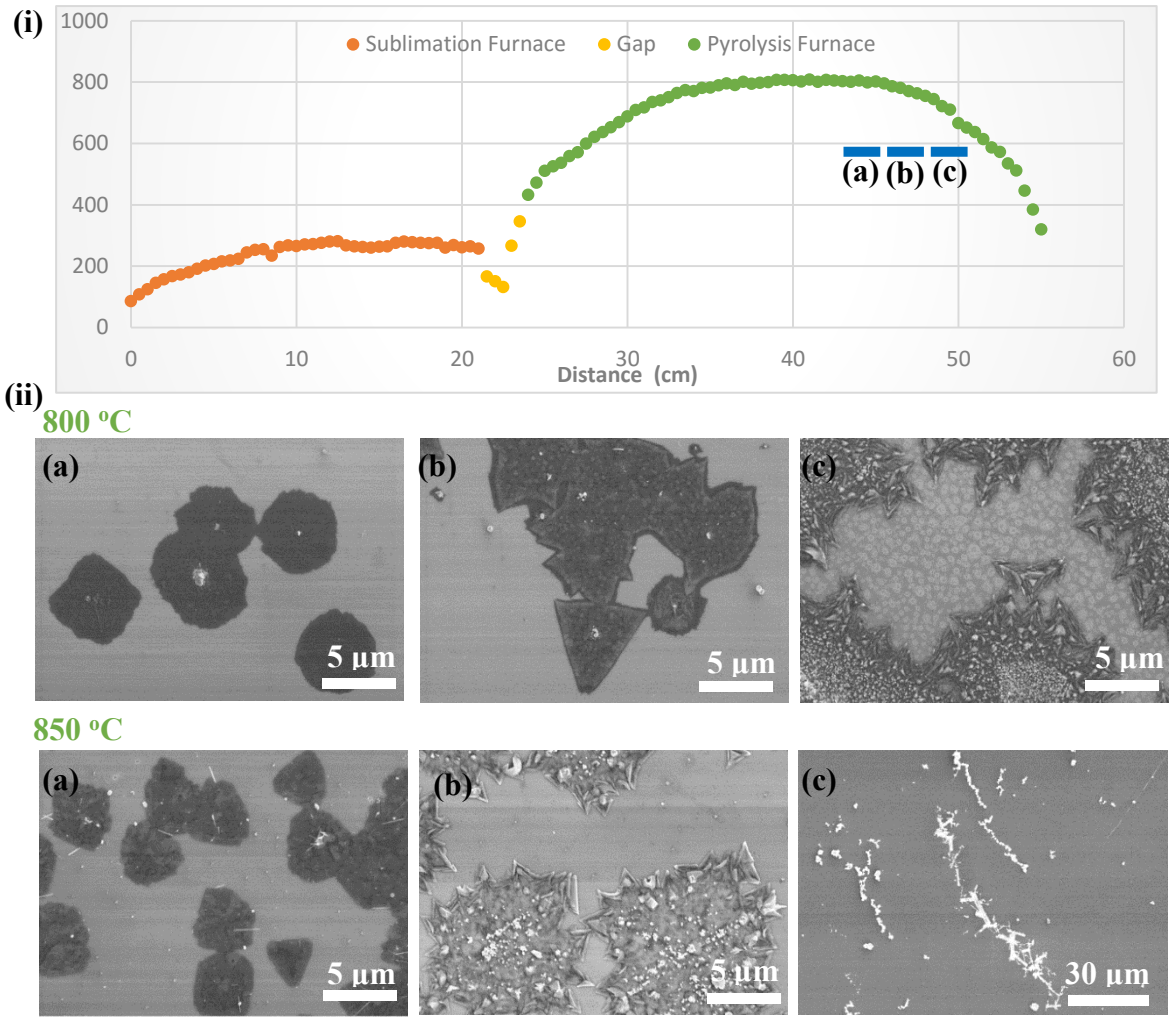


Figure 90. (i) Temperature of furnace showing the position of substrates; (ii) SEM micrographs of deposits produced at sulphur sublimation temperature of 250 ºC with synthesis temperature of 800 ºC and 850 ºC with silicon substrates at positions of (a) 44.5 cm, (b) 47 cm, (c) 49.5 cm which would be 5 cm, 7.5 cm, 10 cm with respect to precursor respectively.

This could be possibly due to the slight decrease in temperature with increase in distance from the centre of the furnace. The set temperature of the furnace is obtained across a plateau region of 15 cm in the middle of the furnace. The silicon substrate at 10 cm relative to the precursor (i.e. 49.5 cm), would be outside this plateau and the

temperature would be 50 °C lower than the set temperature which is determined with the help of a temperature profile. Another reason could be the relative amount of WCl_6 reaching the different substrates that decreases with increasing distance. This would result in the formation of thick crystals of WS_{2+x} which has been shown to form in the early stages of nucleation.[216] The optimal distance for the growth of 2D WS_2 domains was found to be close to 5 cm from the precursor, where substrates were maintained at the set synthesis temperature.

4.3.4. Influence of synthesis time

The synthesis time required for the growth of 2D WS_2 was determined based on the temperature of sulphur sublimation. With sulphur sublimation temperature above 200 °C, the increase in synthesis time from 30 min to 1 hour generally led to the formation of thicker WS_2 domains and out-of-plane growth of WS_2 flakes as shown in Figure 91.

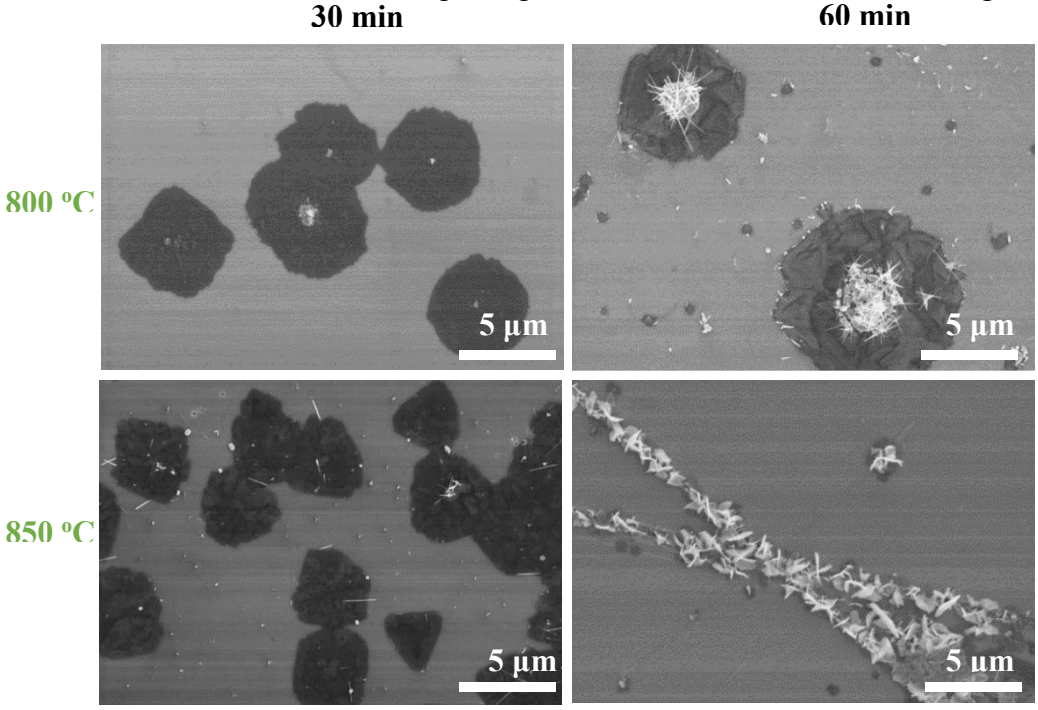


Figure 91. SEM micrographs of deposits produced at sulphur sublimation temperature of 250 °C with synthesis temperature of 800 °C and 850 °C showing increase in thickness of domains and formation of 3D flakes with longer synthesis time.

This could be the result of growth of subsequent layers on top of initial domains with prolonged synthesis time. Also, at higher sublimation temperature, the diffusion of sulphur would be higher leading to faster growth rates and formation of 3D structures. The formation of nanowires could be caused by the depletion of sulphur source due to higher sublimation rate and longer time periods. On the other hand, with lower sulphur sublimation temperature, longer synthesis time of 1 hour was necessary to sublime sufficient amount of sulphur to obtain favourable deposits. The results obtained at lower sulphur sublimation temperature has been discussed in the following section.

4.3.5. Influence of substrate

The influence of substrate on the growth has been studied by employing silicon, 300 nm SiO_2 coated silicon and sapphire substrates in the same experiment and thereby exposing them to similar growth condition. Unlike the synthesis of graphene on metal substrates such as copper, where the substrate acts as a catalyst to break down the precursor and aids growth[217], TMDs are grown on insulating substrates without the need for catalyst. The synthesis of TMDs using various chemical vapour deposition have been attempted on diverse substrates such as silicon, sapphire and glass.[214,218,219] In most reports, SiO_2 coated Si substrates were used as growth substrates since they have the advantage of good compatibility for device fabrication. However, it often results in random orientation of the domains owing to its amorphous nature and relatively high surface roughness. Recently, sapphire substrates (i.e. Al_2O_3, (0001)) have been preferred due to its atomically flat terrace which is suitable to grow on large area, highly crystalline TMDs and the matching lattice symmetry of hexagonally arranged c-plane (0001) with MoS_2 and WS_2.

The WS_2 deposits, confirmed by Raman, on the silicon substrates were characterised by the use of scanning electron microscope. Optical microscopy was employed for sapphire substrates. The results obtained across various sulphur sublimation temperature summarised in Figure 92 shows that the deposits do not change significantly across the substrates exposed to the same condition. As discussed in previous sections, at higher sulphur sublimation temperature of above 200 ^{o}C produced thick deposits with growth of out-of-plane flakes observed on silicon substrates. The sapphire substrates also produced thick deposits with large WS_2 domains at 250 ^{o}C and smaller flakes with higher nucleation density at 200 ^{o}C. The sulphur sublimation temperature of 175 ^{o}C produced thick deposits similar to higher sulphur sublimation temperature with out-of-plane growth of flakes on silicon substrates and similar thick deposits on sapphire. The sulphur sublimation temperature of 150 ^{o}C seemed to be the ideal condition as it produced uniform triangular domains which were quite thin on silicon substrates and some thin regions on sapphire. At lower sulphur sublimation temperature of 125 ^{o}C, the growth of WS_2 seemed to be better on sapphire, forming large thin domains, in comparison to the silicon substrates which formed large domains with flakes growing out-of-plane. This suggests a difference in the ideal growth condition between the silicon and sapphire substrates. The possible reasons for this are discussed later in this section along with their atomic force microscopy (AFM) study. With further decrease in sulphur sublimation temperature to 100 ^{o}C, agglomerates are produced across all substrates with sometimes out-of-plane grown flakes present. This is possibly caused by the poor diffusion of the precursor. The best condition for growth of 2D domains are highlighted in Figure 92.

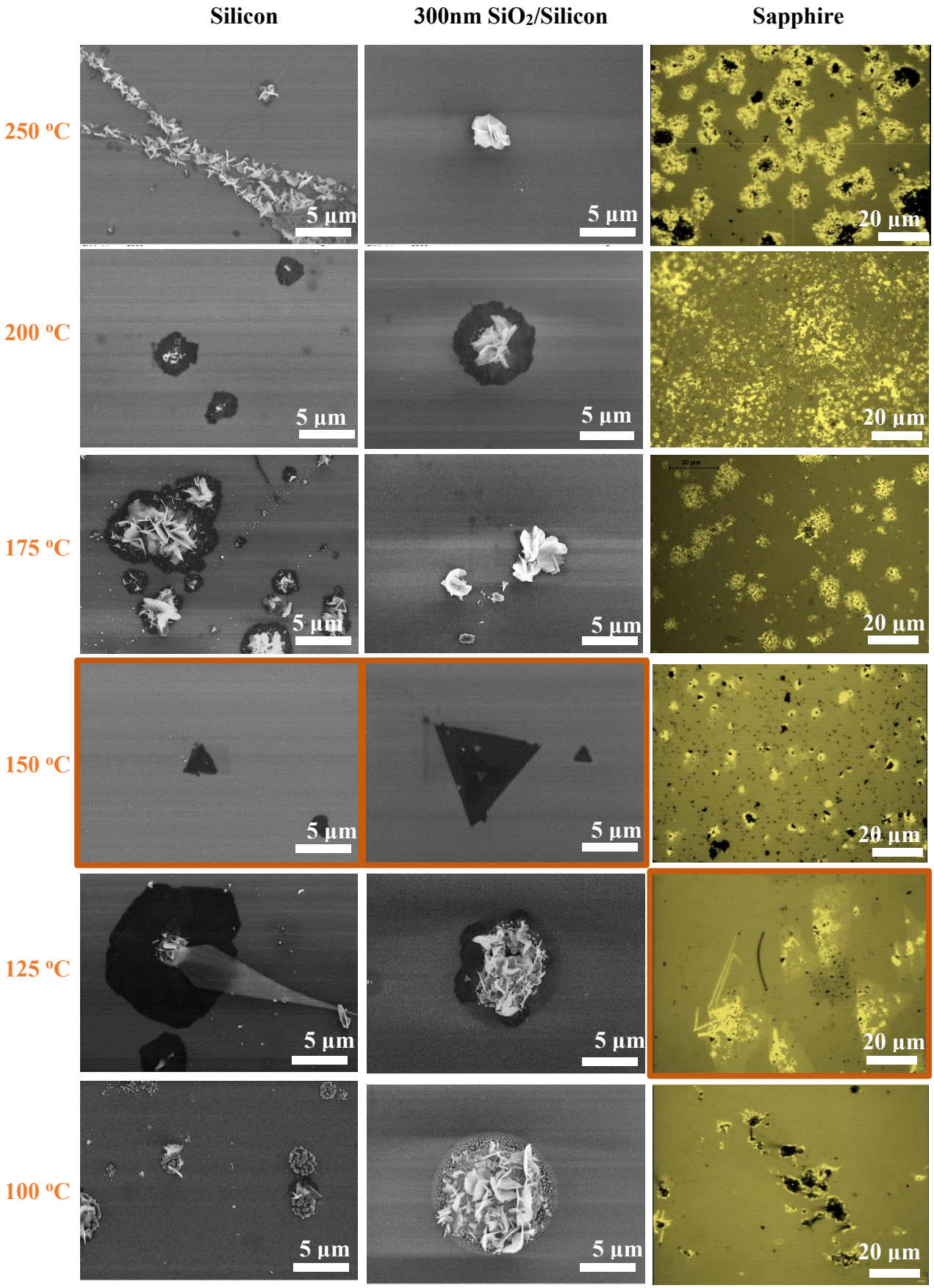


Figure 92. SEM and optical micrographs of deposits produced on silicon and sapphire substrates exposed to the same synthesis condition with sulphur sublimation temperature from 100-250 ºC.

The Raman spectroscopy of the triangular domains obtained at 150 °C were characterised using the 532 nm laser excitation exhibiting the in-plane phonon mode at E^1_{2g} at 350 $cm^{-1}$and out-of-plane phonon mode A_{1g} at 418 cm^{-1} which indicated the presence WS_2 on the different substrates as shown in Figure 93. The silicon substrates show the characteristic peak at 520 cm^{-1} which is absent in the sapphire substrates.

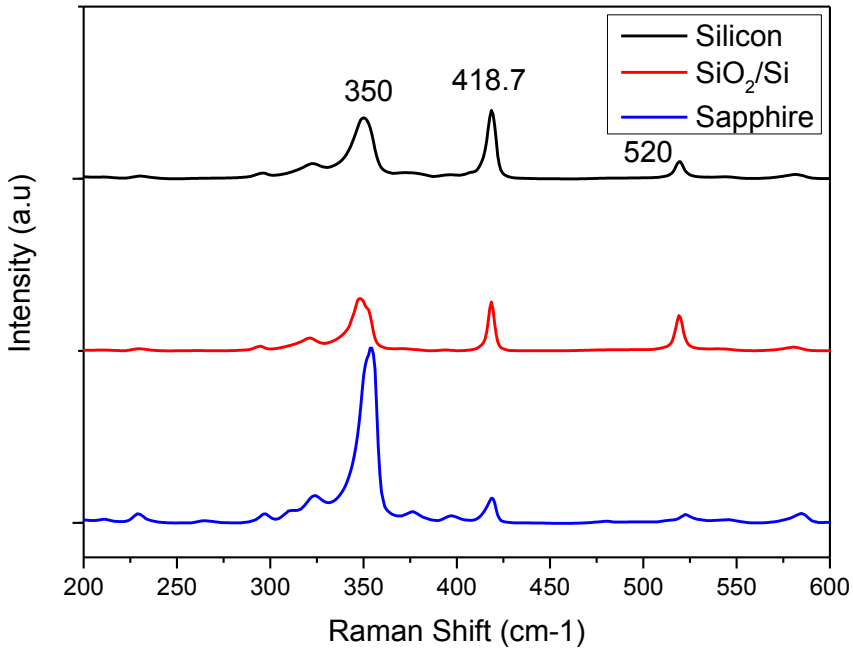


Figure 93. Raman spectroscopy of deposits on different substrates with sulphur sublimation temperature of 150 °C and synthesis temperature of 850 °C for 1 hours showing peaks corresponding to WS_2.

Furthermore, Raman scattering of single- and few-layered WS_2 has been studied to reveal that the A_{1g} mode softens while the 2LA(M) and E^1_{2g} modes present a very subtle hardening with decreasing number of WS_2 layers.[182] To highlight the difference in thickness, the Raman spectra of deposit obtained on sapphire substrates at various sulphur sublimation temperatures from 250 °C to 100 °C is presented in Figure 94. The softening of the A_{1g} mode can be clearly observed at sulphur sublimation temperatures of 150 °C and 125°C in comparison to higher sulphur sublimation temperature of 175-250 °C which would indicate a decrease in thickness. Also the ratio of intensities of

the strongest Raman peaks is more than double for the conditions 125 ºC and 150 ºC which could possibly indicate the presence of monolayer regions.

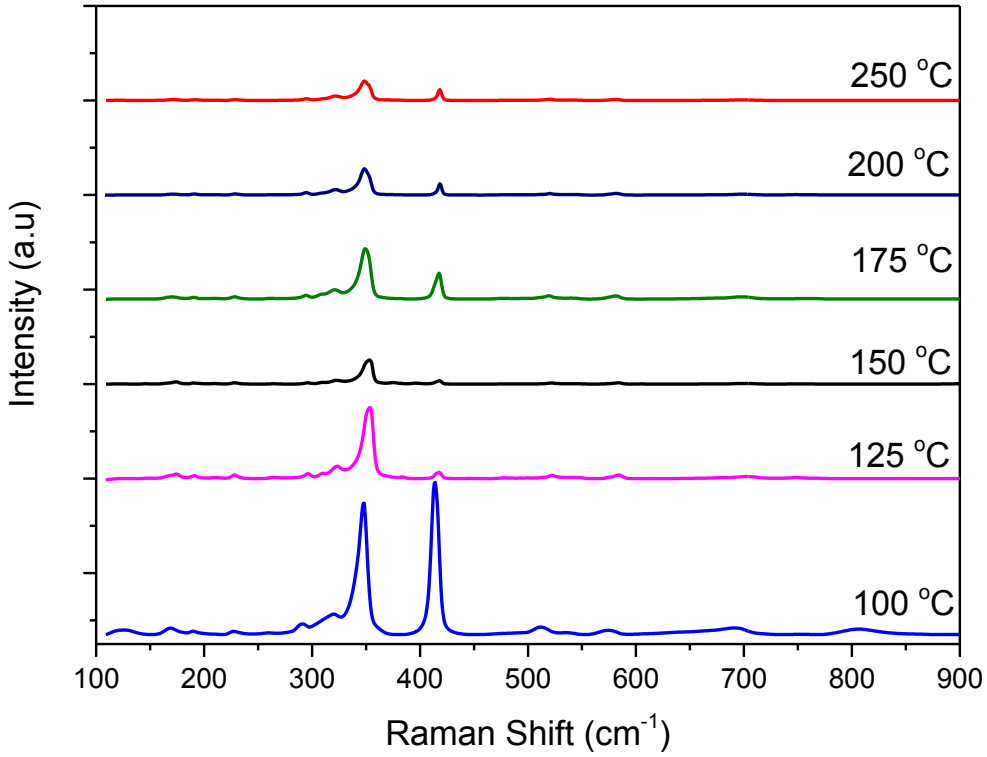


Figure 94. Raman spectroscopy of deposits on sapphire substrate with different sulphur sublimation temperature with synthesis temperature of 850 ºC for 1 hour indicating the softening of the A_{1g} mode which could represent reduction in thickness.

The WS_2 domains obtained at sulphur sublimation temperature of 125 ºC and 150 ºC, which were inferred to be few-layers thick by Raman, were characterised using Atomic Force Microscopy (AFM). The topography of the typical triangular domains obtained at 150 ºC on 300 nm SiO_2 coated silicon substrates along with line profiles is presented in Figure 95. The thickness of these thin regions was found to be around 1.67 ± 0.19 nm, which would correspond to a bilayer WS_2. These thin triangular regions also coalesced at various parts of the sample and one such instance is highlighted in Figure 95b. The thickness does not change at the combined region which indicates that the flakes do not overlap but coalesce. However, secondary nucleation

has been observed in other domains of the sample. One such case of multi-layer domains with secondary nucleation is shown in Figure 96. The thickness of these domains were found to be 4.83 ± 0.84 nm and had thick triangular centres which could possibly have served as nucleation points. Also sometimes secondary nucleation points were observed on these domains which support the initial theory of growth of subsequent layers on top of initial domains as highlighted in Figure 96. In this case the secondary region had a thickness of around 0.68 nm which would represent a monolayer WS_2 region on top of a multi-layer flake. It was evident that WS_2 domains formed on these substrates were always triangular. This could possibly be due to the amorphous nature of the insulating SiO_2 layer which would encourage the deposits to form bonds within itself rather than the substrate, resulting in the deposits to coalesce as triangular domains, the lowest energy form.

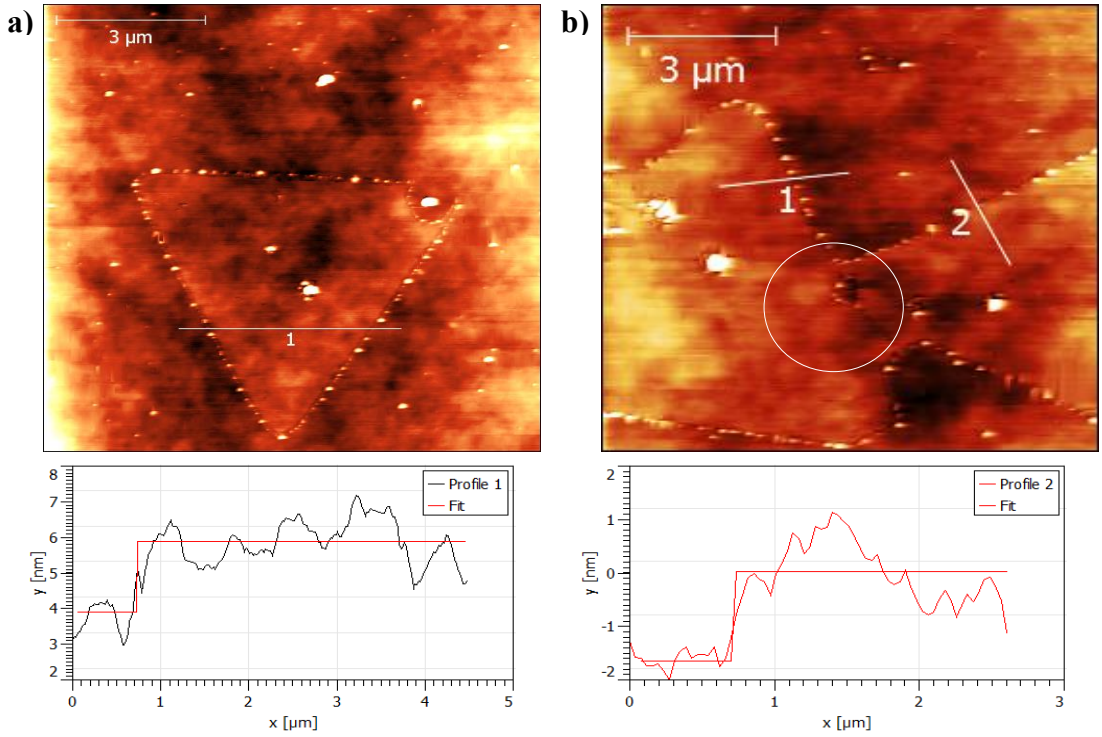


Figure 95. AFM topography and profile of bi-layer WS_2 deposits produced at sulphur sublimation temperature of 150 ºC with synthesis temperature of 850 ºC on 300 nm SiO_2/Si substrate.

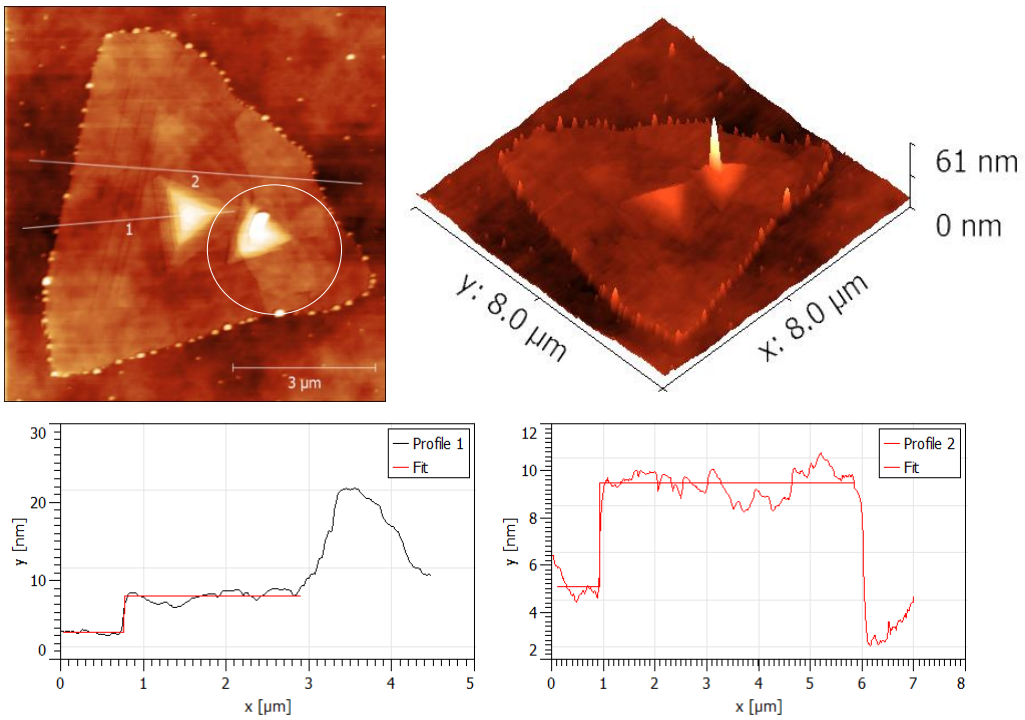


Figure 96. AFM topography and profile of multilayer WS_2 deposits produced at sulphur sublimation temperature of 150 °C with synthesis temperature of 850 °C on 300 nm SiO_2/Si substrate.

Also in these set of experiments, the 300nm-SiO_2 silicon sample were found to contain lesser contamination in comparison to sapphire and mostly the contaminations present were found to agglomerate along the sides of the triangular domains.

The sapphire substrates, on the other hand, at sulphur sublimation temperature of 150 °C formed a mixture of both thin and thick WS_2 regions, which could be inferred from the optical micrograph in Figure 92. The thickness of the WS_2 regions obtained on the sample was measured to be 5.2 nm. The presence of large amounts of contamination particles on the sample was evident as can be seen in Figure 97, which made it difficult to characterise and identify the thin regions. The sulphur sublimation temperature of 125 °C produced large WS_2 domains, which were around 20 µm in size. The thickness of these flakes was measured to be 2.67 ± 0.3 nm. It also had smaller regions nucleating on top of these flakes as can be seen in Figure 98. These triangular

regions nucleating on the large WS_2 domains were found to be 0.68 nm in thickness indicating a monolayer WS_2. The sapphire substrates due to their matching lattice symmetry would encourage epitaxy with the substrate, thereby forming larger domains and thinner regions in comparison to amorphous silicon substrates. However, the secondary regions on WS_2 domains tended to form triangular regions due to bonding within material. Also it has been shown that the growth on sapphire substrate is superior in quality to SiO_2/Si substrates, possibly due to oxygen from SiO_2 reacting with the film.[125]

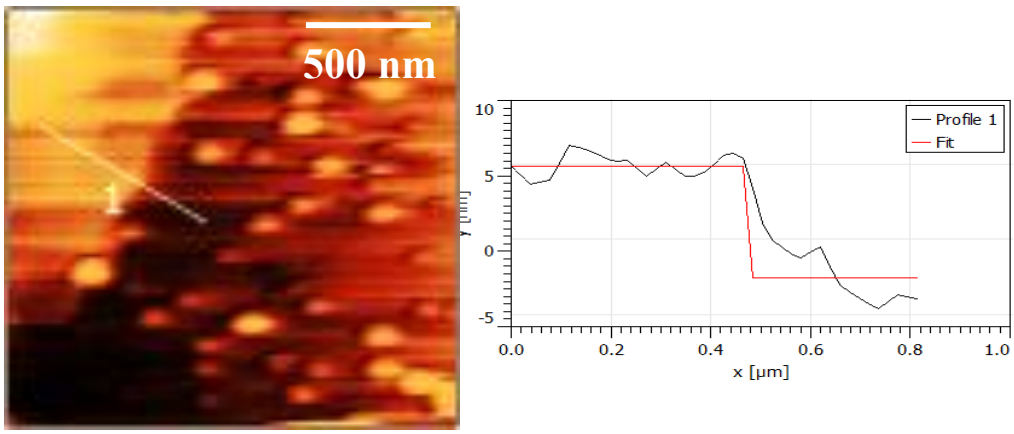


Figure 97. AFM topography and profile of multilayer WS_2 deposits produced at sulphur sublimation temperature of 150 ºC with synthesis temperature of 850 ºC on sapphire substrate.

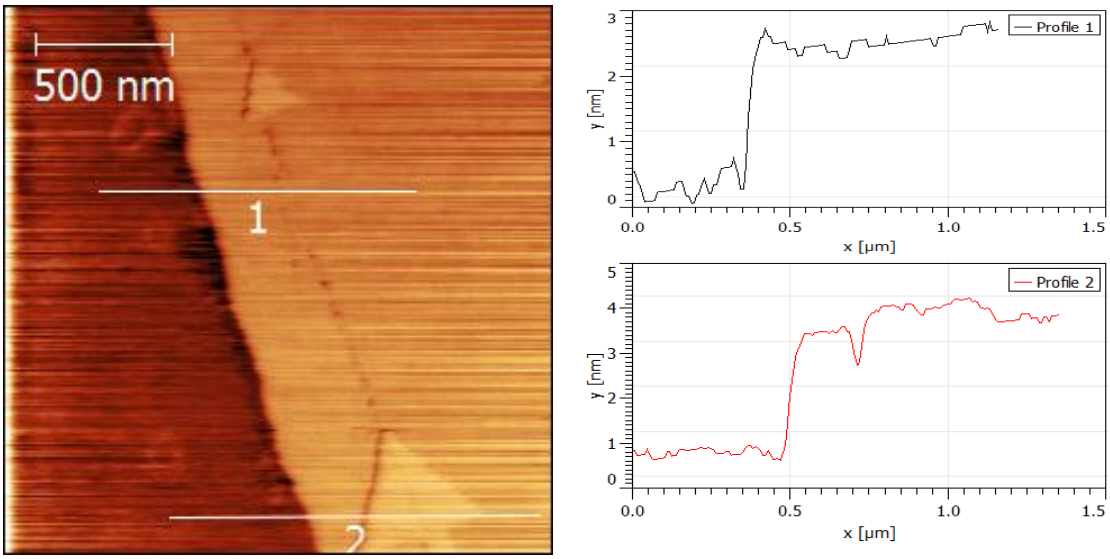


Figure 98. AFM topography and profile of multilayer WS2 deposits produced at sulphur sublimation temperature of 125 ºC with synthesis temperature of 850 ºC on sapphire substrate.

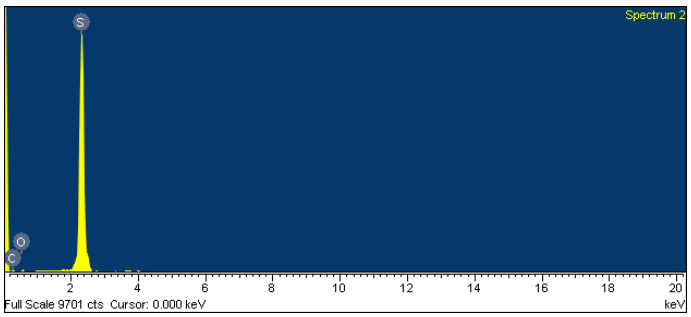
Although it is shown that even though mono and bi-layer regions of WS_2 were synthesised on both silicon and sapphire substrates at the atmospheric pressure, it was difficult to prevent the secondary nucleation which forms thicker domains. This is predominantly due to the inability of the method to control partial pressure of the precursors precisely and independently. To achieve this, low pressure CVD would be necessary to control the total pressure of the system along with the independent control of precursors in separate chambers. By comparing the growth of 2D WS_2 on different substrates exposed to the same condition, it can be observed the shape, thickness and size of the domains vary within the substrates influenced to certain extent by the condition. Thereby, sapphire forms larger and thinner domains at 125 ^{o}C sulphur sublimation temperature, while 150 ^{o}C is more suited for growth of triangular flakes on silicon substrates. The other factors that could affect the growth on different substrates are the lattice matching, cleanliness, and contamination on the substrates.

4.3.6. Influence of precursors

The precursor control is a key aspect for the synthesis of 2D WS_2 using CVD. For atmospheric pressure CVD, initially the amount of WCl_6 precursor had to be controlled and tuned to prevent the growth of out-of-plane flakes and 3D structures. It was found that amount of WCl_6 precursors required for growth of 2D WS_2 was 0.01-0.03 mmol, which was 1000 times less than that which is required to form 3D nanoflowers of WS_2. In the current setup, the W-precursor undergoes pyrolysis when introduced into the high temperature furnace and reacts with sulphur sublimed from the low temperature furnace. The rate of this chemical reaction between WCl_6 and S was possibly controlled to a large extent by the rate of sulphur sublimation. This was perhaps one of the limitations of the current CVD setup. It can be overcome by creating a setup in

which the W-precursor could be sublimed in an independently temperature controlled furnace or ampoule. This would provide greater control over the reaction rate and also enable continuous supply of precursors. This could result in growth of large domains and possibly full coverage. But still the challenge would be to prevent the secondary layer growth which would require control over the partial pressure of precursors and total pressure of the system. Moreover, the WCl_6 precursor tend to get oxidised over time when exposed to air. This would affect the final morphology and introduce defects such as oxides. Hence it is important to use fresh precursors and store them in an inert atmosphere.

Another important aspect that needs to be considered is the purity of the precursor. In this CVD approach 80% pure colloidal sulphur was used as the precursor. The low purity could possibly introduce contamination in the system. To ascertain the impurities in the colloidal sulphur, it was characterised by EDX and the result is summarised in Figure 99. Apart from sulphur it predominantly contained carbon. This carbon was left back in the crucible at the end of the experiment after the sulphur sublimed. Hence, it did not seem to introduce any significant impurities in the final deposit but nonetheless would affect the nucleation and growth. However, the experiment were still repeated using 99.5% sulphur powder as precursor.



Element	Weight%	Atomic%
C K	24.45	44.95
O K	4.37	6.03
S K	71.19	49.03
Totals	100.00	

Figure 99. EDX results of 80% pure colloidal sulphur precursor

The synthesis condition of 850 ºC synthesis temperature and 150 ºC sulphur sublimation temperature, which produced triangular thin regions with the 80% colloidal sulphur powder formed was repeated using 99.5% sulphur. It formed flakes that grew out of the surface on silicon substrates as shown by the SEM micrographs in Figure 100. This could possibly be due to relatively large amount of sulphur being sublimed with an increase in purity leading to higher growth rates.

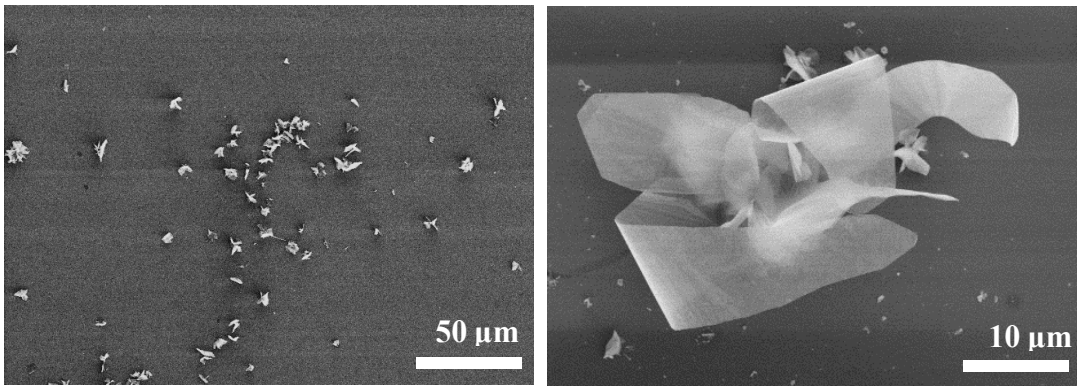


Figure 100. SEM micrographs WS_2 deposits produced at sulphur sublimation temperature of 150 ºC with synthesis temperature of 850 ºC on silicon substrate using 99.5% sulphur.

Hence, the amount of 99.5% sulphur was reduced to one-third its weight and the experiment was repeated using the same growth conditions. The deposits obtained are summarised in Figure 101 with silicon substrates forming large WS_2 regions domains with flakes growing out-of-plane as seen in Figure 101a, while sapphire at the same condition produced very thin and large domains of WS_2 as shown in Figure 101b. The difference in growth could be due to contamination by SiO_2/Si and epitaxy offered by sapphire. The thin WS_2 regions formed on the sapphire were characterised using AFM and the topography presented in Figure 101c. The thickness was found to 1.85 ± 0.29 nm as inferred from the profile in Figure 101d, possibly corresponding to a bi-layer or tri-layer region. Therefore, it can be seen that the 99.5% sulphur can be used as sulphur source but the ratio and amount of precursors needs to be tuned.

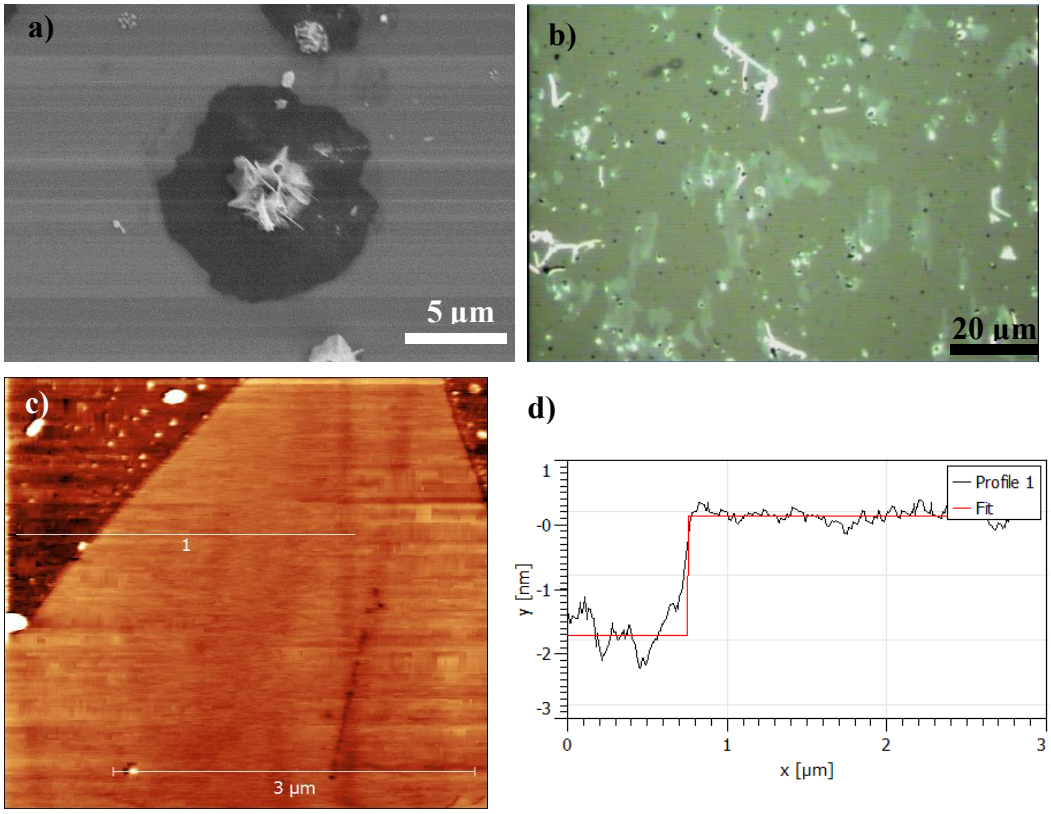


Figure 101. WS_2 deposits produced at sulphur sublimation temperature of 150 ºC with synthesis temperature of 850 ºC using 99.5% sulphur, a) on silicon substrates; b) on sapphire substrates, c) AFM image of deposit on sapphire substrate; d) profile of deposit on sapphire substrate.

4.4. Conclusion

The synthesis of layered 2D WS_2 domains was attempted using chemical vapour deposition at atmospheric pressure using WCl_6 and colloidal sulphur as precursors. The key findings/results are listed below.

- With decrease in sulphur sublimation temperature from 300 to 200 ºC there was an increase in the nucleation density and reduction in the thickness from 20 nm to about 6 nm, with the size of the WS_2 domains shrinking from 5 µm to 1 µm.
- The window for the formation of 2D WS_2 domains was found to be 800-850 ºC.
- The optimum position of the substrates was found to be around 5 cm from the metal precursor and with increase in distance bulk and thick deposits formed.

- The shape, thickness and size of the domains vary within the three widely used substrates namely silicon, 300 nm SiO_2 coated silicon and (0001) c-plane oriented sapphire. This is dependent on the growth condition, contamination and lattice matching.
- The best synthesis condition for sapphire which forms large and thin domains was 125 ^{o}C sulphur sublimation temperature with 850 ^{o}C synthesis. However, 150 ^{o}C sulphur sublimation was more suited for growth of bilayer WS_2 triangular flakes on silicon substrates.

Chapter 5. Mixed transition metal dichalcogenide $Mo_xW_{1-x}S_2$ alloy synthesis by Chemical Vapour Deposition (CVD)

5.1. Introduction

Nanoengineering of transition metal dichalcogenides (TMDs) (MX_2: M = Mo, W, Nb, Re; X = S, Se, Te) offers exciting new prospects for the production of 2D nanomaterials with tailored properties. Band gap engineering has been widely used in bulk semiconductors to alloy different band gap materials.[220] For application in nanodevices modulating the electronic properties in a well-controlled manner is crucial. Band gaps of current 2D materials provide limited choices with 0 eV for graphene, 5.8 eV for hexagonal BN monolayer [221], 1.9 eV for MoS_2 monolayer [57,117], and 2.1 eV for WS_2 monolayer [222]. Heterostructures possess electronic properties beyond those offered by individual constituent parts due to interaction at the interfaces, which is often used to engineer the electronic properties of semiconductors. Creating band gap tuneable material system could be advantageous for new nanoelectronic, optoelectronic or photonic applications.[64,223] Moreover, thin films and powders of such nanostructured materials could also offer improved catalytic capabilities due to optimised edge structures.[224,225]

Recent advances in the growth of vertical and lateral heterostructures of $MoSe_2$-WSe_2 [226], MoS_2-WS_2 [227], and MoS_2-$MoSe_2$ [228] demonstrate the scope for modulating atomically thin materials. Similarly, single layer TMD ternary alloys, including $Mo_xW_{1-x}S_2$ and $MoSe_{2(1-x)}S_{2x}$ (x=0-1), have been shown to have a compositionally modulated electronic structure.[229] The latter approach is effective for band gap modulation because of their good thermodynamic stability at room temperature of the

alloys as predicted by theoretical calculation.[69,230] Composition-dependent band gap modulation from 1.82 eV to 1.99 eV has been shown for $Mo_xW_{1-x}S_2$ monolayer alloys by photoluminescence. However, to date, synthesis of these ternary alloys has been limited to exfoliation of flakes from single crystals that are produced by vapour transport using bulk Mo, W, and S powders [226] or MoS_2 [231], which offers limited prospect for large-scale manufacturing in the future.

In this work, the synthesis of $Mo_xW_{1-x}S_2$ by atmospheric-pressure chemical vapour deposition (CVD) using Mo and W chloride precursors was investigated. The effect of the precursor ratio on the morphology and composition of the resultant deposits was studied by mixing the two metal precursors in various proportions in a single stage furnace. To enhance the control over the precursors, the evaporation condition of the precursors was regulated using a two stage furnace setup. The resultant deposits were characterised in detail using Raman spectroscopy, EDX analysis, atomic-resolution annular dark field (ADF) scanning transmission electron microscopy (STEM) and X-ray photoelectron spectroscopy (XPS) to confirm the synthesis of alloyed dichalcogenides with varying composition.

5.2. Experimental

The synthesis of mixed metal dichalcogenide nanomaterials was conducted using a combination of two precursors, namely tungsten chloride (WCl_6 - 99.9% purity-Sigma Aldrich) and molybdenum chloride ($MoCl_5$ - 99.9% purity- Sigma Aldrich) in conjunction with a sulphur source (colloidal-80% purity or elemental sulphur-99.5% purity-Sigma Aldrich). Two types of setups were employed (for details see Chapter 2 and 4). In order to test the feasibility of the formation of mixed metal dichalcogenides first a simple single stage furnace setup was used. A two stage furnace was then utilised

in order to control the composition of the nanomaterials formed by controlling the evaporation/sublimation of the precursors individually.

For experiments involving the single stage furnace a total of 2 mmol containing mixtures of both metal chloride precursors in the ratios of 1:3, 1:1, 3:2, 3:1 WCl_6:$MoCl_5$ were employed. In addition to this, 20 mmol sulphur (colloidal-80% purity) were introduced into a quartz tube (inner diameter: 2.5 cm) located in a 21 cm tube furnace. Thereby the mixture of the metal chloride precursors were introduced and positioned at the centre of the temperature plateau of this furnace whilst the sulphur was placed upstream with respect to the argon flow. A silicon substrate (on which the products formed) were positioned downstream with respect to the precursors at a distance of 5 cm and 10 cm respectively (see Figure102). All experiments were carried out at a temperature of 800 ^{o}C for 10 minutes and with an argon flow rate of 100 sccm. After 10 minutes, the furnace was switched off and the samples were left to cool inside the furnace to room temperature whilst maintaining the argon flow at 100 sccm before they were removed for analysis.

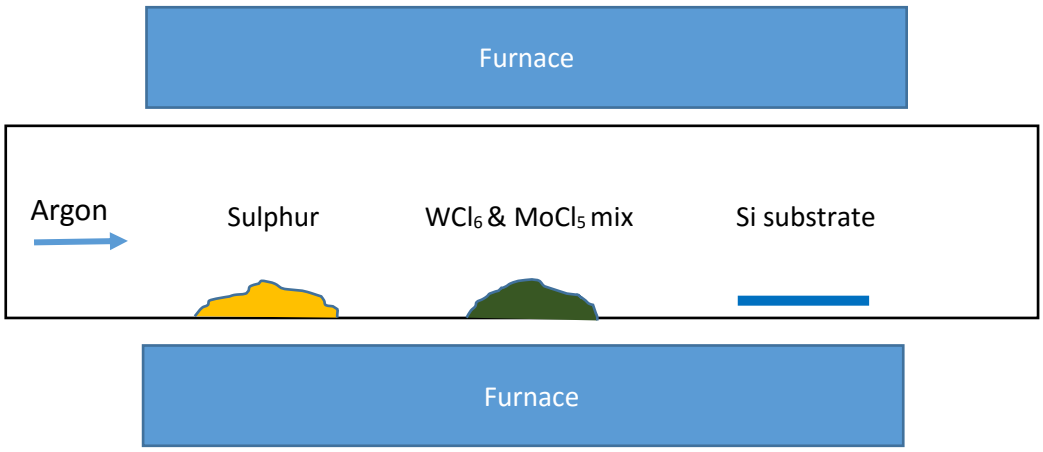


Figure 102. Schematic of experimental setup using single zone furnace and different proportion of chloride precursor mixed together.

For experiments involving the two stage furnace setup, a total of 2 mmol of the chloride precursors (at a ratio of 1:1) along with 20 mmol of elemental sulphur were positioned inside furnace 1 set at 300 ºC in order to maintain them at their respective sublimation/evaporation temperature (see Figure 103). In order to control the precursor release the temperature profile of furnace 1 was exploited. For example, the sulphur was kept at 150 ºC at position of x=3 cm, $MoCl_5$ at 200 ºC at x=4.5 cm and WCl_6 at 300 ºC at x=15.5 cm with x=0 at the edge of the furnace 1.

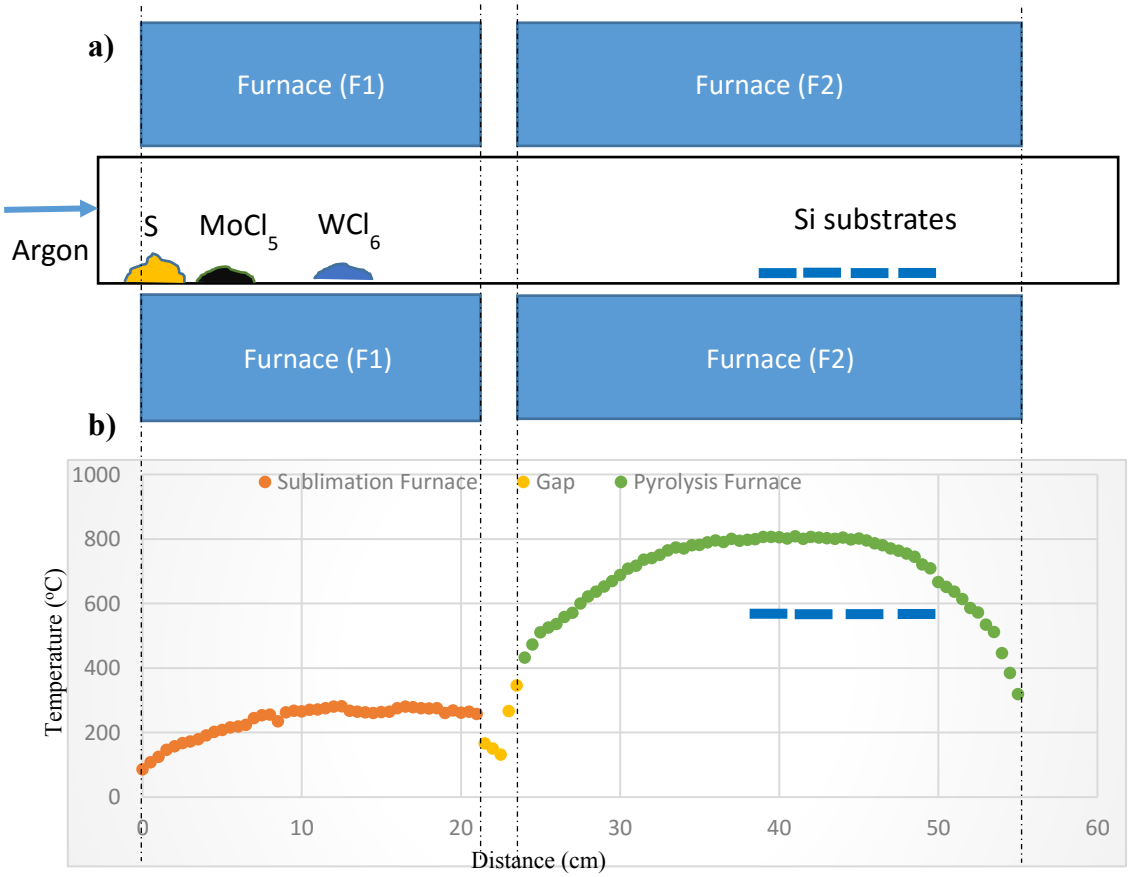


Figure 103. a) Schematic of experimental setup for two stage furnace chemical vapour deposition setup for synthesis of mixed chalcogenides; b) Temperature profile of furnaces separated by 3 cm and maintained at 250 ºC and 800 ºC.

This time four silicon substrates on which later the nanomaterials formed were placed inside furnace 2 which was set to 800 ºC. These substrates were positioned 5 cm apart from each other at fixed points of defined temperature. The substrates were

differentiated by their position in the furnace and labelled as S_{800u} (800 ^oC upstream), S_{800d} (800 ^oC downstream), S_{750} (750 ^oC) and S_{650} (650 ^oC) respectively depending on the temperature at which they were positioned. The synthesis time was again kept at 10 minutes and the products were allowed to cool inside the furnace in an inert argon flow of 100 sccm until it reached room temperature. The products were collected by retrieving the substrates from the furnace.

The substrates were then mounted on a standard aluminium stub using sticky carbon tape and their sample morphology was studied by scanning electron microscopy (SEM; JEOL 840F, JSM 6500F both operated at acceleration voltages of 5 kV and 10 kV). Complementary studies of the bulk deposits were performed using Raman spectroscopy using a JY Horiba Labram Aramis imaging confocal Raman microscope with a 532 nm green laser. The crystalline phases were determined by powder X-ray diffraction using a Siemens D5000 X-ray powder diffractometer. The range of 2θ employed was 10^o-60^o with a step size of 0.050^o and count time of 10 seconds. The variation in the elemental composition with respect to the position in the furnace was investigated using XPS using as-synthesised sample (Thermo Scientific K-Alpha X-ray Photoelectron Spectrometer System). To reveal the structure and morphology of the products TEM samples were prepared by collecting a few milligrams of the deposits from the substrates, dispersing them in ethanol and sonicating for one minute using an ultrasonic tip (UP100H-100W, 30 kHz). A few droplets of the suspension were dropped on a transmission electron microscopy (TEM) grid and dried in air for a few hours. TEM studies were conducted using a JEOL 2000FX, JEOL-2010 and JEOL-3000F operated at an accelerating voltage of 200 kV and 300kV. Energy Dispersive X-ray (EDX) spectroscopy was used to determine the composition of the

products in a JEOL-3000F equipped with field emission gun operated at 300 kV. High-resolution annular dark field (ADF) scanning transmission electron microscopy (STEM) using a Cs probe corrected JEOL ARM 200F (200 kV) was employed to study the atomic distribution of W and Mo.

5.3. Results and Discussion

5.3.1. Growth of mixed metal dichalcogenides using single stage furnace.

The experiment using single stage furnace revealed a variety of morphologies including nanoflowers, flakes, spiral-like and platelet-like structures. The formation of these morphologies was dependent on the molar ratios of the precursors, which influenced the composition of these structures. These are discussed in the following sections.

5.3.1.1. Molar ratio 1:3 of WCl_6:$MoCl_5$ precursors

SEM studies of the samples produced using mixtures of WCl_6:$MoCl_5$ at the molar ratio of 1:3 revealed an uneven but relatively thick powdery deposit which was estimated to be of the order of a few microns (Figure 104a). At higher magnifications these deposits appeared to consist of predominantly nanoflowers (Figure 104b) *ca.*1 μm in diameter. Whilst their morphology appeared to be similar to the nanoflowers reported in Chapter 2, closer inspection revealed that the nature of these structures was more rounded and that the protruding flakes were less dominant. These nanoflowers were inferred to be MoS_2 using XRD (Figure 104c) and Raman presented (Figure 104d). Raman spectroscopy showed the first order Raman modes (E_{2g} and A_{1g})

corresponding to MoS_2 and XRD confirmed 2H-MoS_2 was the only phase formed. The higher vapour pressure and lower sublimation temperature of $MoCl_5$ would have a significant effect on the resultant morphology and hence the predominant formation of MoS_2 nanoflowers.

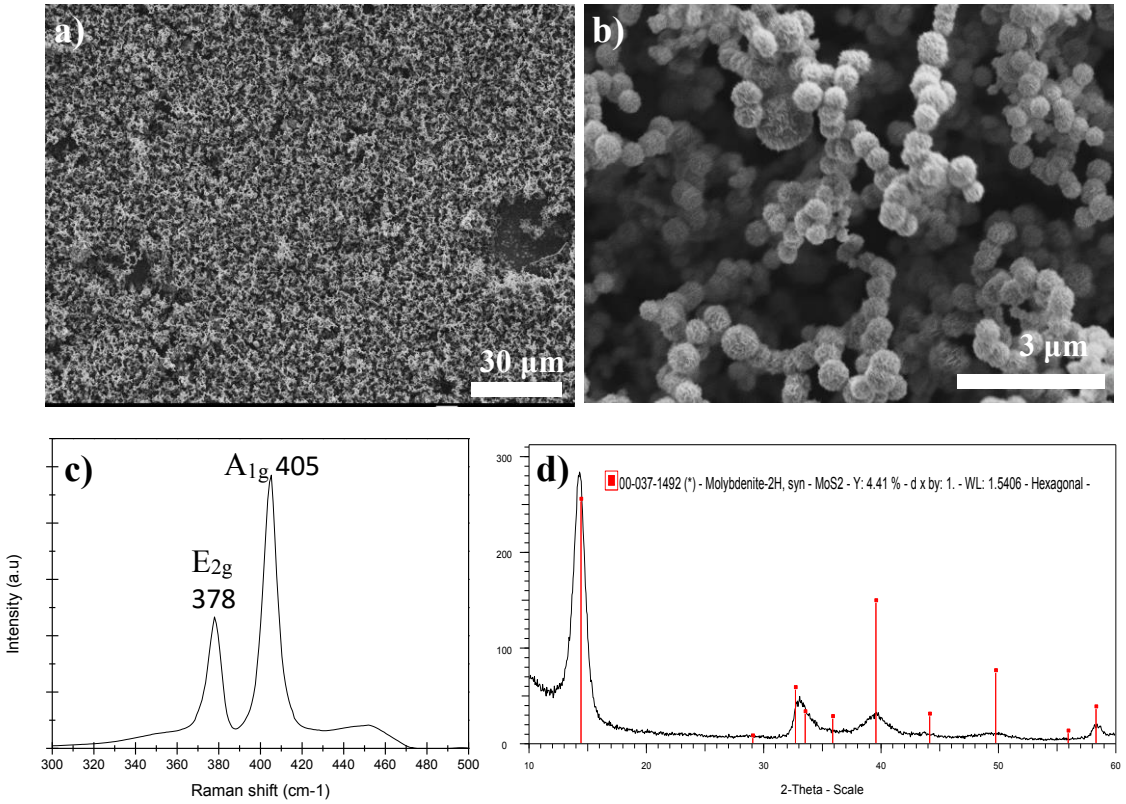


Figure 104. a) SEM micrograph of thick deposits formed on silicon substrates b) SEM micrograph of nanoflower morphology c) Raman spectroscopy showing MoS2 peaks d) XRD showing MoS2 crystal phase obtained by using mixed in the molar ratio of 1:3

5.3.1.2. Molar ratio 1:1 of WCl_6:$MoCl_5$ precursors

SEM of samples produced using mixtures of WCl_6:$MoCl_5$ in the molar ratio of 1:1 consisted of a mixture of various structures including small spherical structures resembling nanoflowers, branched spiral-like structures and flakes (Figure 105b, 105c). The XRD peaks of these deposits showed that the peak position of WS_2 and MoS_2 crystal structures overlapped (Figure 105c). The XRD spectrum could not be classified as either one or the other and hence was unable to differentiate between the

MoS_2 and WS_2 in the deposit. However, the XRD spectrum did confirm the 2H type crystal structure of the resultant morphologies. Raman spectroscopy was employed to differentiate between MoS_2 and WS_2 in the deposits owing to distinct isolated peaks (Figure 105d, Figure 105e). The spectroscopy revealed the presence of 2H-MoS_2 in most parts of the sample as seen in Figure 105d. The spectrum exhibits the first order modes of A_{1g} and E_{2g} close to 380 cm^{-1} and 403 cm^{-1} respectively, along with silicon at 520 cm^{-1} and other second order peaks. However, in some regions of the sample, Figure 105e, an additional peak was observed at 350 cm^{-1} which corresponds to E_{2g} peak of WS_2. It has been shown in Raman study of $Mo_{1-x}W_xS_2$ that for A_{1g} mode only sulphur atoms vibrate giving rise to a one-mode type behaviour.[232] For the E_{2g} mode, the mass difference between the vibrating Mo and W cations causes two mode type behaviour which is similar to the results observed in Figure 105e.

The different morphologies observed by the SEM were characterised individually using the TEM and EDX techniques. The predominant morphology obtained was that of the nanoflowers (Figure 106). EDX determined these nanoflowers are composed of Mo and S. The Cu and Ti obtained on the spectra were part of the TEM grid on which the samples were characterised. These MoS_2 nanoflowers consisted of flakes with much smaller sizes compared to the WS_2 nanoflowers described in Chapter 1. The second morphology was the flakes which are shown in Figure 106. These flakes contained exposed edges as can be observed from the lattice fringes in Figure 107. EDX determined these flakes predominantly consist of Mo and S with very small amount of W (0.32%). Unfortunately identifying the individual W dopants in these morphologies using high-resolution STEM would be difficult as they were not sufficiently thin and electron transparent.

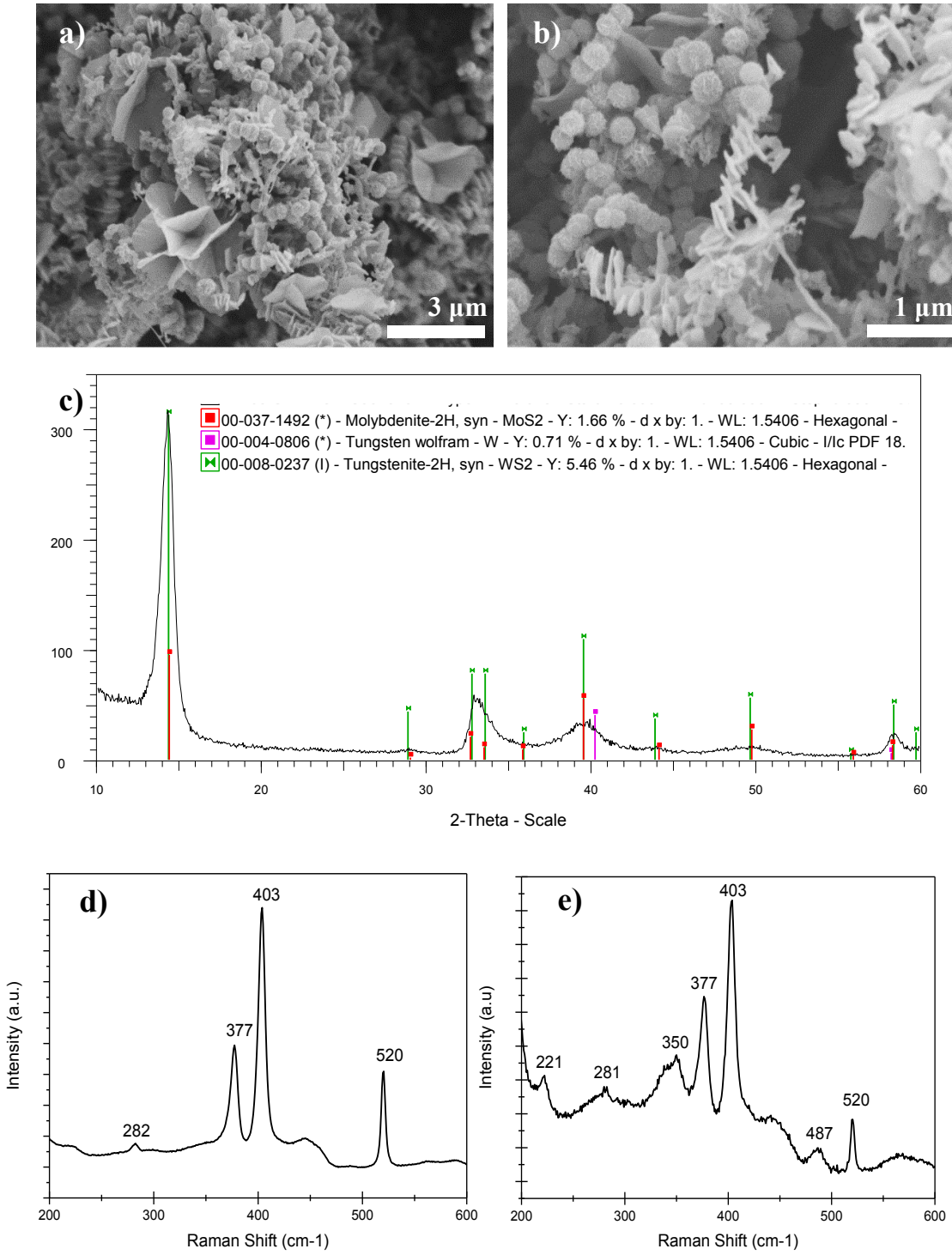
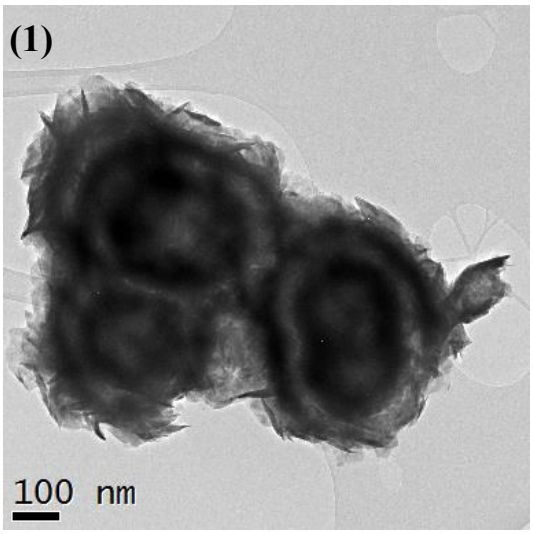
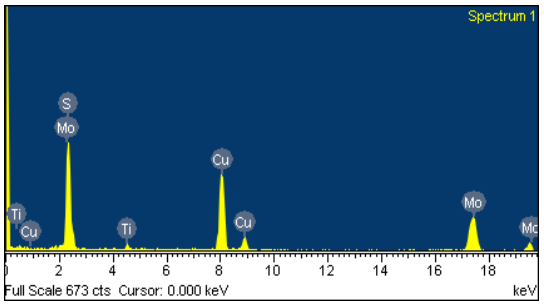


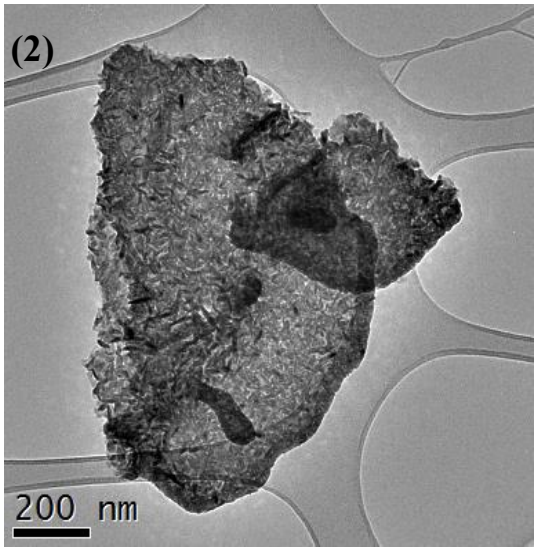
Figure 105. a) SEM micrograph of mixture of morphologies consisting of flowers and flakes b) SEM micrograph of spiral-like structures along with nanoflowers and flakes; c) XRD showing peak matching for both WS_2 and MoS_2; d) Raman spectroscopy showing MoS_2 first order modes e) Raman spectroscopy showing MoS_2 first order modes along with WS_2 E_{2g} peak in addition to second order peaks obtained by using mixed in the molar ratio of 1:1.

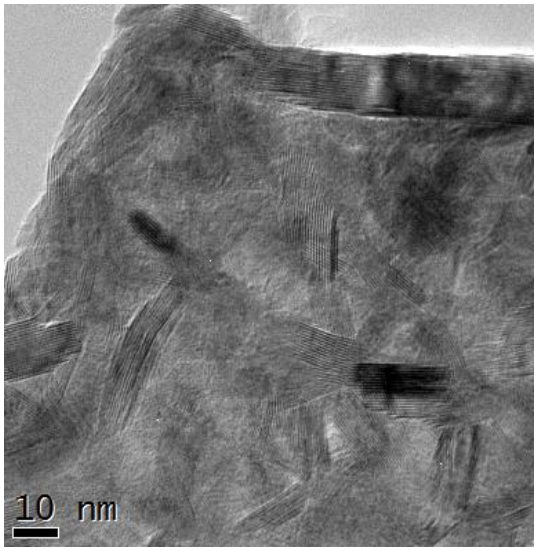


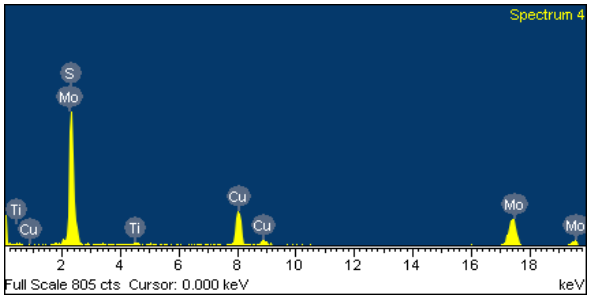


Element	Weight%	Atomic%
S K	14.35	29.3
Mo K	59.1	35.4

Figure 106. TEM and EDX of MoS_2 nanoflowers obtained on silicon substrates by using CVD with $WCl_6$and $MoCl_5$ mixed in the molar ratio of 1:1.





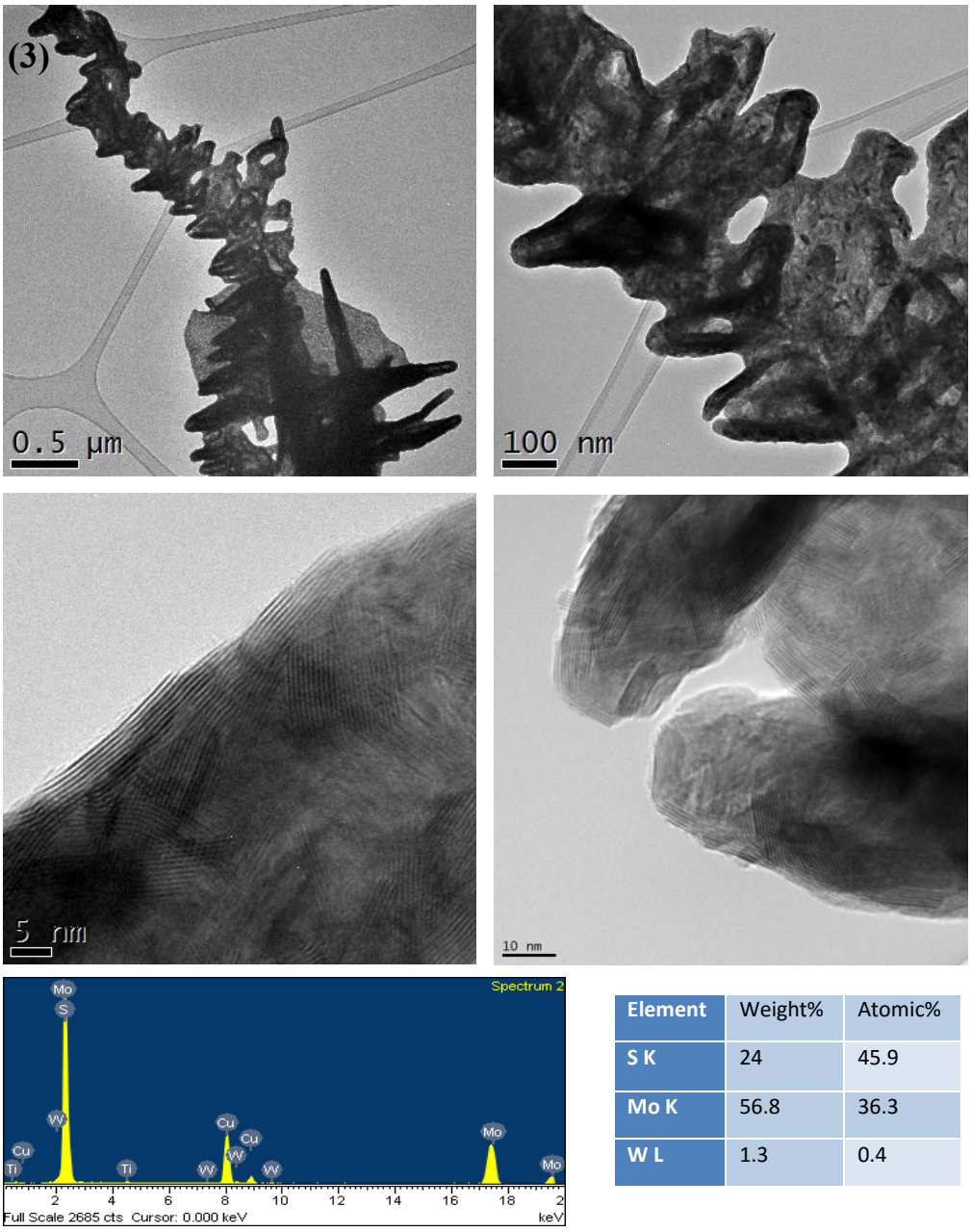


Element	Weight%	Atomic%
S K	25.8	48.0
Mo K	54.5	33.8
W L	1.00	0.32

Figure 107. TEM and EDX of flakes obtained on silicon substrates by using CVD with $WCl_6$and $MoCl_5$ mixed in the molar ratio of 1:1.

The third morphology obtained in this experiment is the branched spiral-like structures as shown in Figure 108. They were found in much smaller quantities in comparison to the nanoflowers and flakes. They also contained exposed edges similar

to the flakes characterised previously. EDX determined the presence of Mo, S and small amounts of W (0.44%) The high-resolution image of the finger like branches of these spiral structures could show the presence of possibly MoS_2 layers stacked along the edges.



Element	Weight%	Atomic%
S K	24	45.9
Mo K	56.8	36.3
W L	1.3	0.4

Figure 108. TEM and EDX of spiral structures obtained on silicon substrates by using CVD with $WCl_6$and $MoCl_5$ mixed in the molar ratio of 1:1.

From the analysis, the CVD synthesis with 1:1 molar ratio of tungsten and $MoCl_5$ precursors formed predominantly MoS_2 structures with small amounts of tungsten (less than 1%). This W may be present as a dopant in $Mo_{1-x}W_xS_2$ or as individual region of WS_2 alongside MoS_2. The results suggest that the $Mo_{1-x}W_xS_2$ is more likely formed given we did not observe any isolated WS_2 flakes. It is hypothesised that the formation of MoS_2 structures could be preferential because of the lower sublimation temperature of 194 ^oC and higher vapour pressure of 131 mmHg (at 250 ^oC) of the molybdenum chloride ($MoCl_5$) precursor in comparison to tungsten chloride (WCl_6) which sublimes at 275 ^oC at a vapour pressure of 43 mmHg (at 215 ^oC). Hence with the precursors mixed together and evaporated at the same condition of 800 ^oC, the partial pressure of $MoCl_5$ would be higher leading to the formation of MoS_2 morphology.

5.3.1.3. Molar ratio 3:2 of WCl_6:$MoCl_5$ precursors

SEM of products obtained with a precursor's ratio of 3:2 consists of a mixture of different morphologies including small nanoflower (Figure 109a) and platelets-like structures stacked on top of each other as shown in Figure 109b. XRD detected peaks corresponding to hexagonal phase of 2H MoS_2/WS_2 as seen in Fig 109c. Raman spectroscopy showed the characteristic peak of MoS_2 for some parts (Figure 109d) and in other parts the presence of two E_{2g} corresponding to MoS_2 and WS_2 indicating formation of the mixed metal dichalcogenides (Fig 109e). The morphologies obtained by SEM were individually characterised using TEM and EDX techniques. In addition, the results based on Raman spectroscopy indicated a shift of 5 cm^{-1} in the first order modes of MoS_2 as illustrated in Figure 109d and Figure 109e. The shift in the peak position has been observed in mixed crystals of Mo1-xWxS2. This is attributed to the

disorder effect introduced by the doping of W which leads to decrease in modes related to 2H-MoS_2.[232]

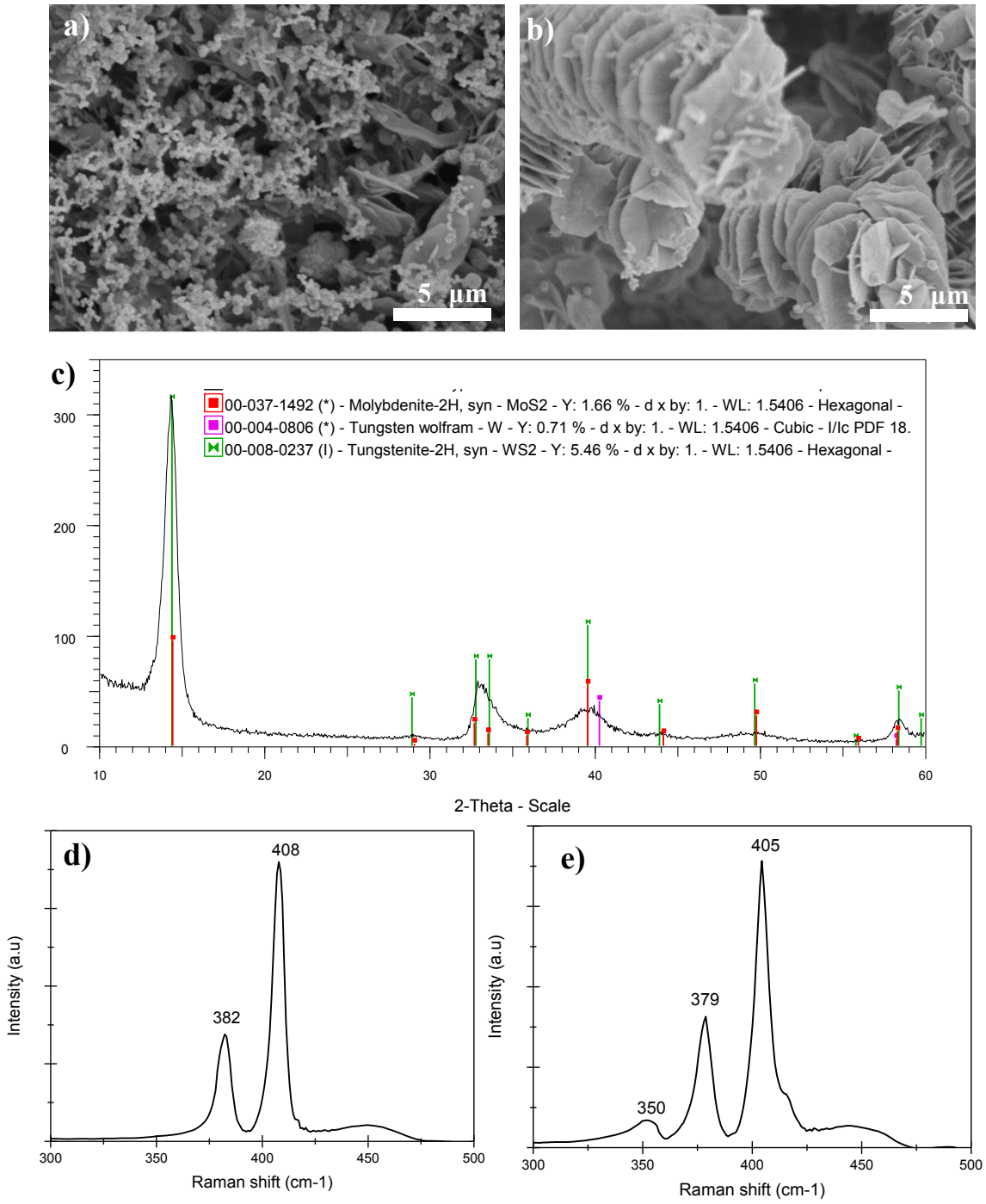
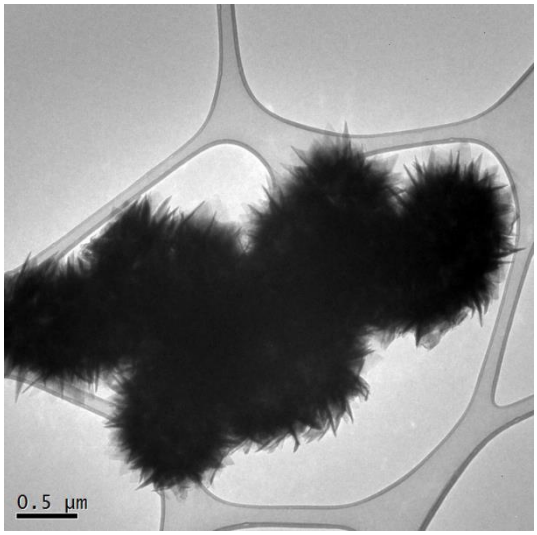
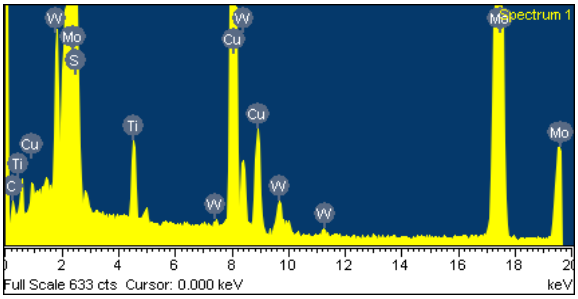


Figure 109. a) SEM micrograph of mixture of morphologies of nanoflowers and platelet-like structures b) SEM micrograph of platelet-like structures; c) XRD showing peak matching for both WS_2 and MoS_2; Raman spectroscopy showing d) MoS_2 first order modes e) MoS_2 first order modes along with WS_2 E_{2g} peak obtained by using mixed in the molar ratio of 3:2.

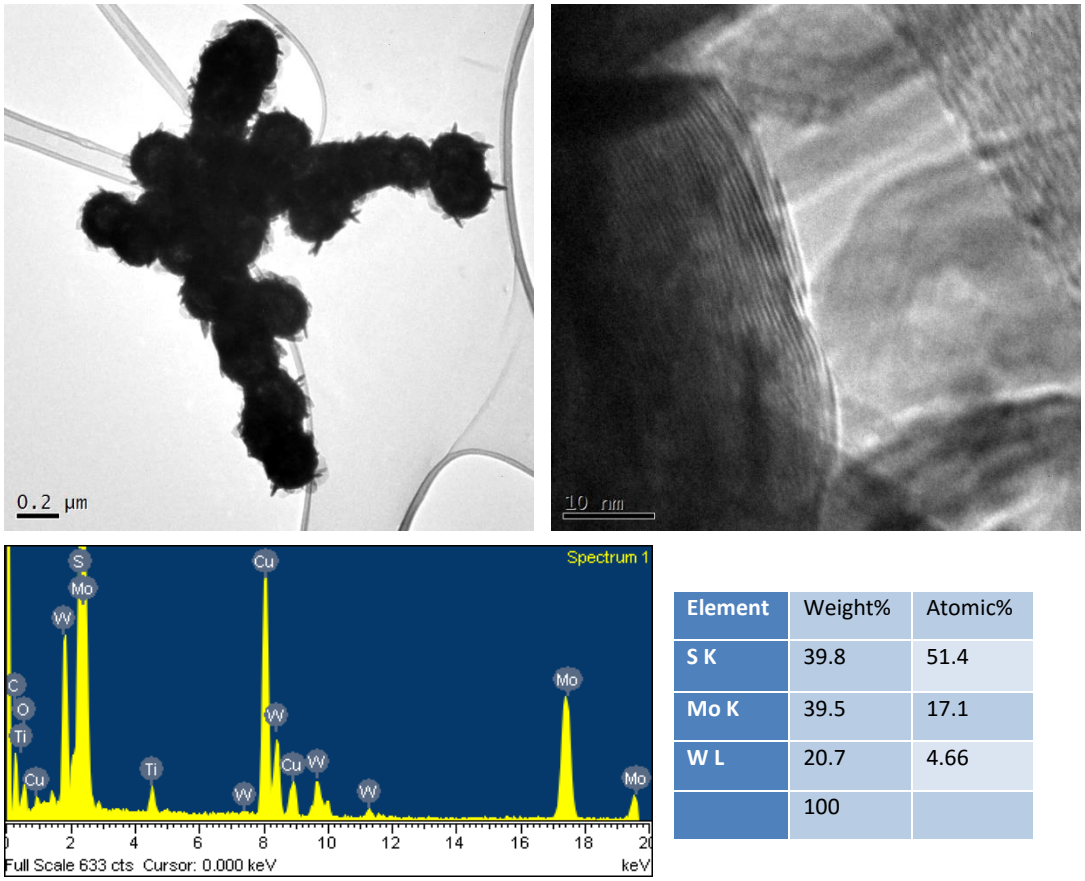
The nanoflowers morphology, as shown in the TEM micrograph (Figure 110) predominantly consisted of Mo and S along with some small amount of W (1.32%) when characterised using EDX. This could indicate a MoS_2 nanoflower morphology with tungsten as dopant. The other predominant morphology was the platelets-like structures which are shown by the TEM micrograph in Figure 111. The TEM image shows the presence of concentric lattice fringes of possibly MoS_2 layers. In addition to this, EDX also detected W (4.66% wt). This could either indicate WS_2 flakes being present alongside the MoS_2 platelets or tungsten atoms serving as dopants in the MoS_2 structures. Given no pure WS_2 flakes were observed it is hypothesised that this is $Mo_{1-x}W_xS_2$. The 4.66% tungsten present in these morphologies is the highest achieved for experiments varying molar ratio of precursors.





Element	Weight%	Atomic%
S K	43.3	60.3
Mo K	51.2	23.8
W L	5.5	1.32
	100	

Figure 110. TEM and EDX of nanoflowers obtained on silicon substrates by using CVD with $WCl_6$and $MoCl_5$ mixed in the molar ratio of 3:2.



Element	Weight%	Atomic%
S K	39.8	51.4
Mo K	39.5	17.1
W L	20.7	4.66
	100	

Figure 111. TEM and EDX of platelet-like structures obtained on silicon substrates by using CVD with $WCl_6$and $MoCl_5$ mixed in the molar ratio of 3:2.

5.3.1.4. Molar ratio 3:1 of WCl_6:$MoCl_5$ precursors

The SEM micrographs for molar ratio of 3:1 consist of predominantly nanoflower-like structure as shown in Figure 112a and Figure 112b. These nanoflowers are high yield and very similar to the WS_2 nanoflowers synthesised previously, as discussed in Chapter 1. The composition of the nanoflowers was verified using XRD (Figure 112c) and Raman spectroscopy (112d). XRD spectrum showed the presence of peaks corresponding to molybdenum oxide (MoO_3) and either 2H WS_2 or MoS_2, due to overlap. Raman spectroscopy technique confirmed the nanoflowers to be WS_2 with the first order present at 350 cm^{-1} (E_{2g}) and 412 cm^{-1} (A_{1g}) and also showed peaks at 700 cm^{-1} and 806 cm^{-1} corresponding to molybdenum oxide phases.

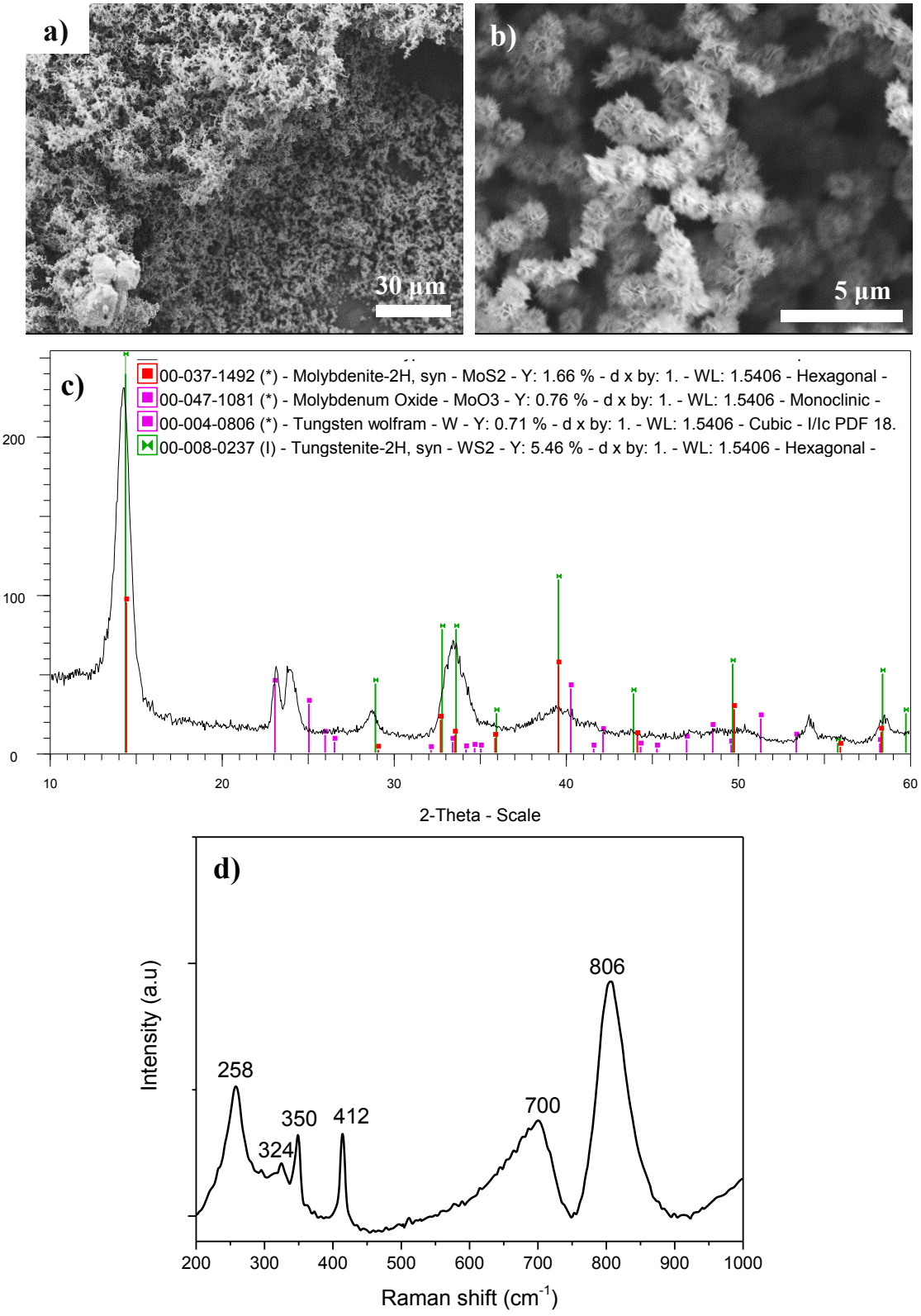


Figure 112. a) SEM micrograph of cluster nanoflowers on silion substratesb) SEM micrograph of nanoflowers; c) XRD showing peak matching for both WS_2 and MoS_2 in addition to MoO_3; d) Raman spectroscopy showing WoS_2 first order modes along with MoO_3 peak obtained by using mixed in the molar ratio of 3:1.

The formation of MoO_3 could be attributed to the aggressive oxidation tendency of the $MoCl_5$ precursor which could possibly result in oxidation during the precursor handling stages. Furthermore, the relative amount of oxidation during the handling process is amplified since the quantity of $MoCl_5$ precursor used was low. As a conclusion the results suggest that the 3:1 molar ratio (WCl_6:$MoCl_5$) of the precursors produced WS_2 nanoflowers as the predominant morphology with MoO_3 as an undesired by-product.

5.3.1.5. Summary of single stage furnace

By varying the molar ratio of the tungsten and molybdenum precursors, it was seen that the morphologies as well as composition of the deposit obtained were altered. The method offered limited control over the final morphology which formed 3D structures from nanoflowers to spiral branched and platelets-like structures. The formation of mixed metal dichalcogenides structures was demonstrated using this setup, even though it proved difficult to establish control over the resultant morphology. A summary of the different morphologies formed along with the phases and atomic percentages of tungsten is shown in Table 5. Also since the morphologies were too thick, visualising the doping in mixed metal dichalcogenide structures using the STEM technique was not feasible. Having to sublime the precursors together at the same temperature of 800 ^{o}C does not offer flexibility to control the precursors individually, which is important especially given the significant differences in sublimation temperature and vapour pressures between them. To overcome some of these drawbacks, the CVD method was performed with the help of a two stage furnace with the precursors placed at the respective sublimation temperatures.

Ratio WCl_6:$MoCl_5$	1:3	1:1	3:2	3:1
Morphology	Nanoflowers	Nanoflowers, Flakes, Spiral-like structure	Nanoflowers, Platelet-like structure	Nanoflowers
Phases	MoS_2, no W	MoS_2 with less than 1% W	MoS_2 with 1-4% W	WS_2, MoO_3, no MoS_2
W atomic %	0	0.3% (flakes), 0.4% (spiral-like structure)	1.3%(nanoflowers) 4.6% (platelet-like structure)	Predominant WS_2 structure

Table 5. Summary of morphologies, phases and atomic percentage of W obtained by varying the molar ratio of WCl_6:$MoCl_5$

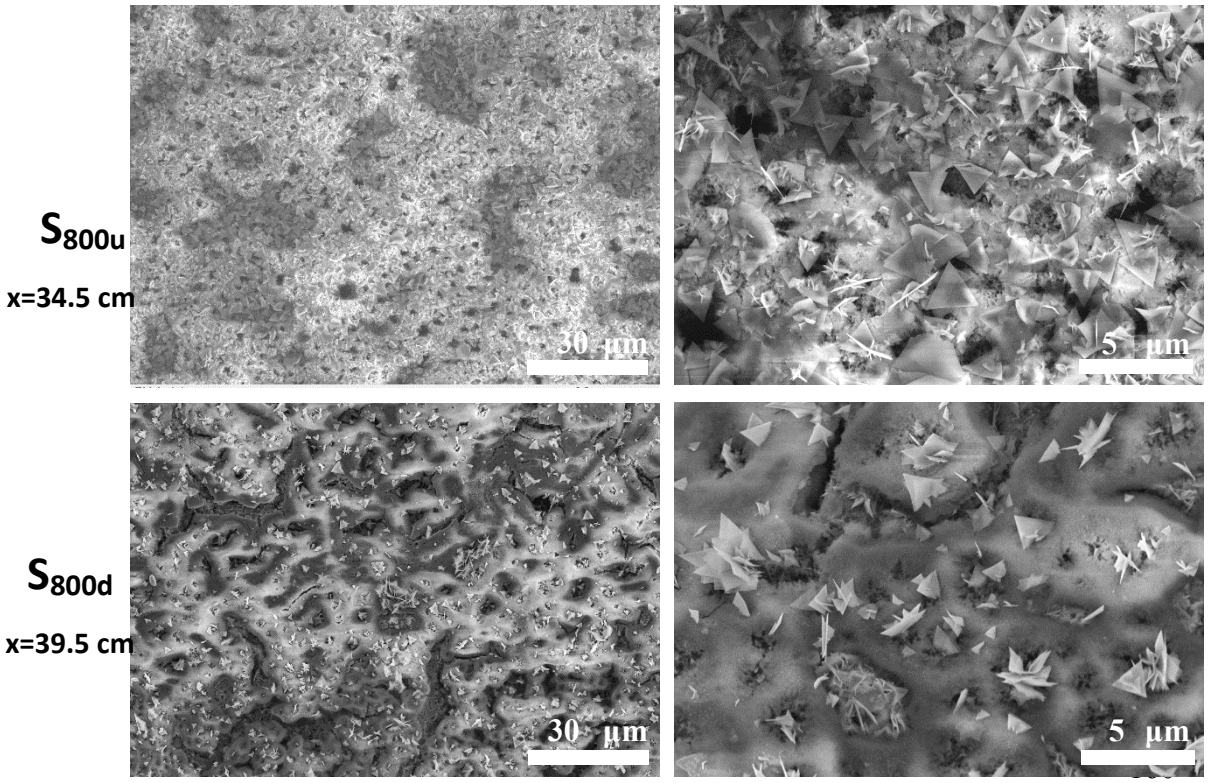
5.3.2. Growth of mixed metal dichalcogenides using two stage furnace

The major limitation of the single stage furnace was the absence of control over the precursors, as they were evaporated together at high temperatures of 800 ^oC. To address this, a two stage furnace with the ability to independently control the sublimation/evaporation temperature of the precursors was developed. This allowed us to study the influence of the precursors on the morphologies, as well as the composition of the final deposit. It also enabled the formation of mixed metal dichalcogenides with composition control. The silicon substrates were placed at definite positions in the furnace. The influence of growth temperature on the morphology, composition and atomic distribution of the deposit grown on the

substrates was studied by employing various characterisation techniques that are detailed below.

5.3.2.1. Scanning Electron Microscopy of deposits from 2-stage furnace

The deposits obtained from different growth temperatures were characterised using the SEM as summarised in Figure 113. The silicon substrate S_{800u} formed large amount of triangular flakes while the substrate S_{800d} maintained at a similar temperature of 800 ^{o}C but downstream formed less quantity of the similar flakes. The substrate S_{750} was found to have grown larger quantity of the triangular flakes, often clustered together. The density and amount of the flakes was much more than S_{800}. This further increased with S_{650} which was the furthest away from the furnace with the lowest temperature, where the flakes completely covered the substrate. This change in the quantity of deposits could be due to the influence of the growth temperature and variation in relative amounts of metal precursors.



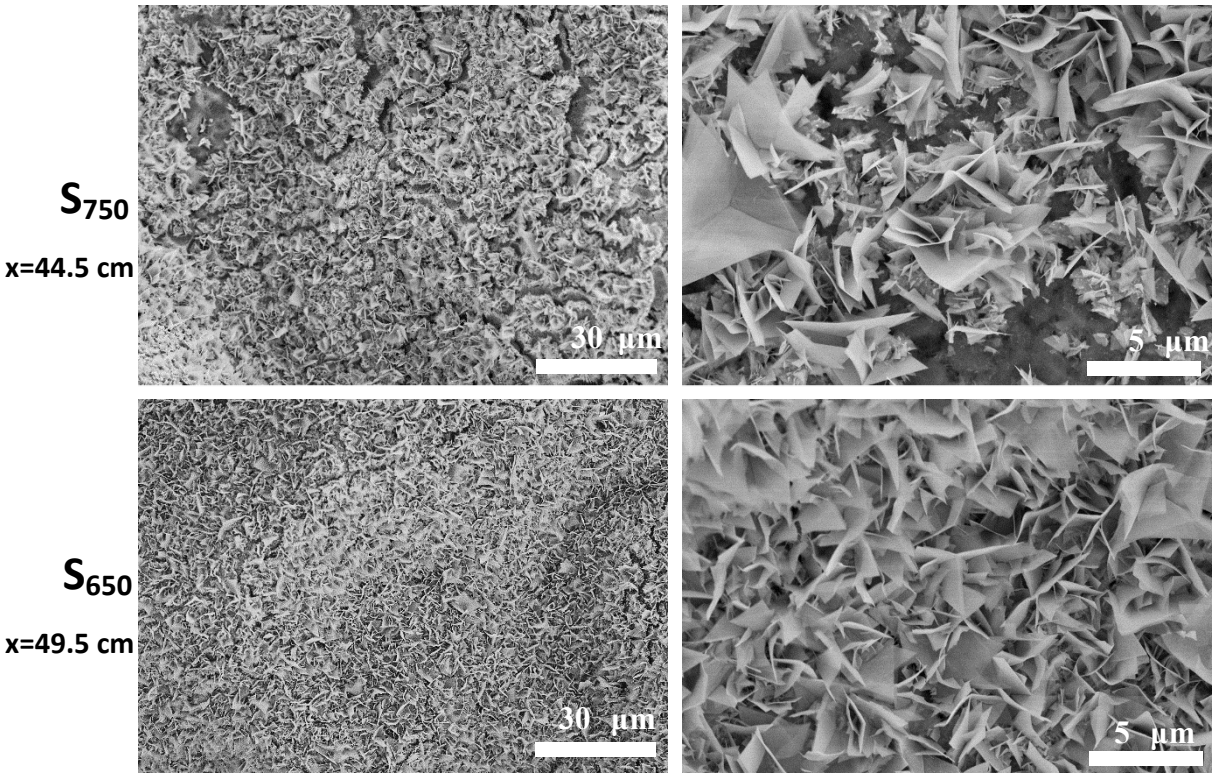


Figure 113. SEM micrographs of deposits showing flakes obtained on silicon substrates maintained at different positions and growth temperatures by using CVD in a two stage furnace.

5.3.2.2. Raman Spectroscopy of mixed metal dichalcogenides

The composition of these flakes observed by the SEM were verified using Raman spectroscopy. Raman spectroscopy was conducted over regions of 20 µm on the deposit of each sample and the cumulative spectrum obtained from the maps is presented in Figure 114. From the spectrum the predominant flakes were MoS_2 as indicated by E_{2g} peak around 380 cm^{-1} (blue region) and A_{1g} peak at 408 cm^{-1}. In addition, samples S_{800d}, S_{750} and S_{650} showed the presence of a small peak around 350 cm^{-1}, (red region) which corresponds to the E_{2g} peak of WS_2 indicating the formation of mixed metal dichalcogenides. It has been reported that the presence of E_{2g} peak at 350 cm^{-1} in mixed chalcogenides was not obvious in $Mo_{0.47}W_{0.53}S_2$, but was visible for larger W compositions.[229] Thus the Raman spectrum indicates formation of mixed

metal dichalcogenides but is inappropriate for quantitatively determining the amount of W in MoS_2.

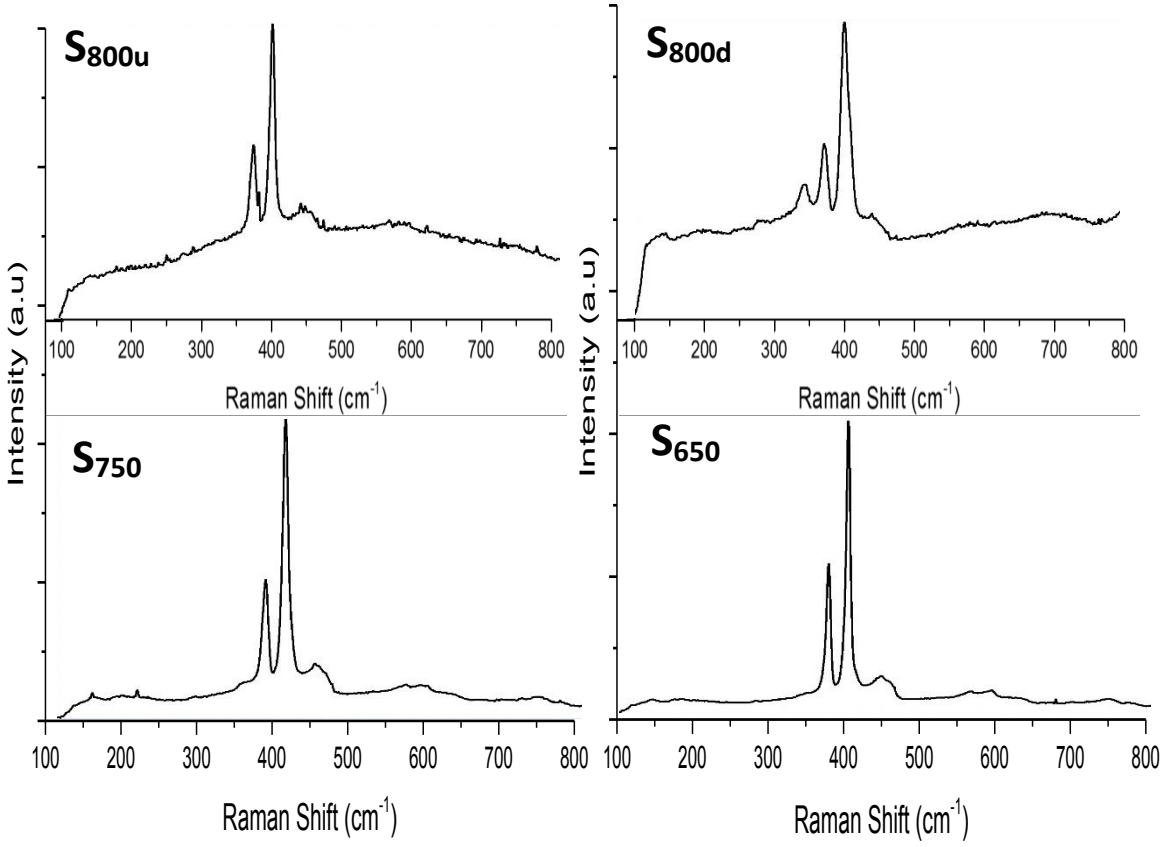


Figure 114. Raman Spectroscopy of deposits obtained on silicon substrates by using CVD in a two stage furnace showing the presence of first order of both MoS_2 and WS_2 peaks indicating formation of $Mo_{1-x}W_xS_2$

5.3.2.3. Electron microscopy of mixed metal dichalcogenides

The flakes obtained from the different growth temperatures were characterised using transmission electron microscopy (TEM) and energy dispersive X-ray spectroscopy (EDX) to identify and determine the atomic proportions Mo and W, and confirm the formation of mixed metal dichalcogenides. Prior to transfer of the deposits onto a TEM grid, they were dissolved in ethanol and sonicated under the tip. The sonication help to exfoliated and isolate the flakes. The morphologies of the various flakes obtained on different substrates are summarised in Figure 115. The flakes are predominantly triangular and often folded up or overlapping each other, possibly

indicating few-layered regions. EDX spectrums were obtained on all these flakes and the results summarising the atomic concentrations of molybdenum (Mo) and tungsten (W) in their structure is tabulated in Figure 116.

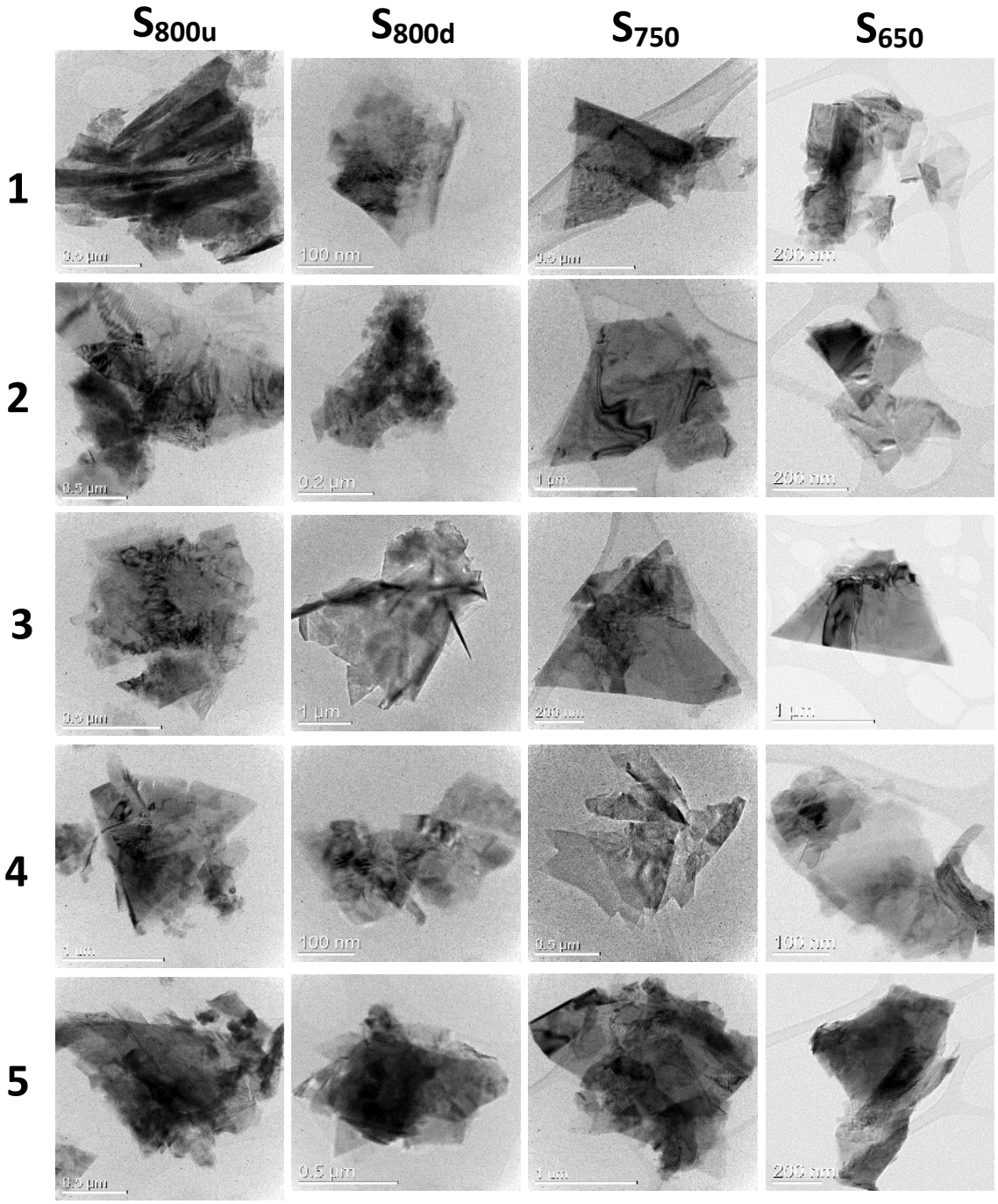


Figure 115. TEM micrographs of deposits on different silicon substrates maintained at different positions obtained by using CVD in a two stage furnace.

S_{800u}

Spectrum	Mo % at.	W % at.
1	92.4	7.6
2	94.9	5.1
3	89.8	10.2
4	97.5	2.5
5	98.2	1.8
Average	**94.6±3.5**	**5.4±3.5**

S_{800d}

Spectrum	Mo % at.	W % at.
1	79.9	20.0
2	62.9	37.0
3	62.2	37.7
4	62.9	37.1
5	71.8	28.1
Average	**67.9±6.9**	**32.0±6.9**

S_{750}

Spectrum	Mo % at.	W % at.
1	58.4	41.6
2	57.9	42.1
3	57.2	42.7
4	42.0	57.9
5	49.1	50.8
Average	**52.9±7.1**	**47.0±7.2**

S_{650}

Spectrum	Mo % at.	W % at.
1	66.8	33.1
2	50.4	49.6
3	57.3	42.6
4	50.9	49.1
5	57.9	42.0
Average	**56.6±5.**	**43.3±6.4**

Figure 116. EDX results indicating the atomic percentage of Mo and W of mixed metal dichalcogenide flakes obtained on different substrates by using CVD in a two stage furnace.

EDX results demonstrate that the atomic concentration of W are quite similar within flakes of the same substrates but vary between the different substrates. Substrate S_{800u} contains the lowest atomic percentage of W (5.4±3.5%), and the W content increases progressively to around 32±6.9% in S_{800d} and 47±7% in S_{750} and drops slightly to 43.3±6.4% in S_{650}. This control of composition of the mixed metal dichalcogenide within the same experiment due to variation in growth temperatures and relative distances to the precursor offers a promising way of producing mixed chalcogenides. This change in composition along the length of the furnace with change in temperature can result from the difference in vapour pressure of the precursors. It is hypothesised that Mo precursor with the higher vapour pressure could influence the reaction at initial part of the furnace largely forming MoS_2 flakes at higher temperature with W precursor taking part at the later stages, indicating an increase in their atomic concentrations.

5.3.2.4. X-ray Photoelectron Spectroscopy of substrates

The XPS spectra corresponding to core binding level of W_{4f} and Mo_{4p} is shown in Figure 117, obtained at various points on the sample across the different growth temperatures. It shows a clear change in intensity indicating variation in the W composition across the different growth substrates. Also the W4f peaks monotonically shift to lower binding energies with increase of W content in the $Mo_{1-x}W_xS_2$ alloys from sample S_{800d} to S_{650}, although the shifts are quite small (less than 1 eV). Chemically, such small shifts in the binding energy of the core levels can be related to a variation in the strength with which the element attracts an electron to itself. A shift of the core level to lower binding energies implies reduced electron-attraction strength. In this regard, the observed shift in W4f core levels manifest themselves as a

weakening factor in the electron-attraction strength of S and a strengthening factor in the electron-attraction strength of Mo induced by the incorporation of W in $Mo_{1-x}W_xS_2$.[233] This phenomenon is physically expected since the electron affinity of W (0.8163 eV) is larger than that of Mo (0.7473 eV).[234] The monotonic shifts in the core levels of W4f, thus suggest that the W atoms were randomly alloyed with MoS_2 by substitutional replacing Mo in the crystal lattice of $Mo_{1-x}W_xS_2$without any phase separations.

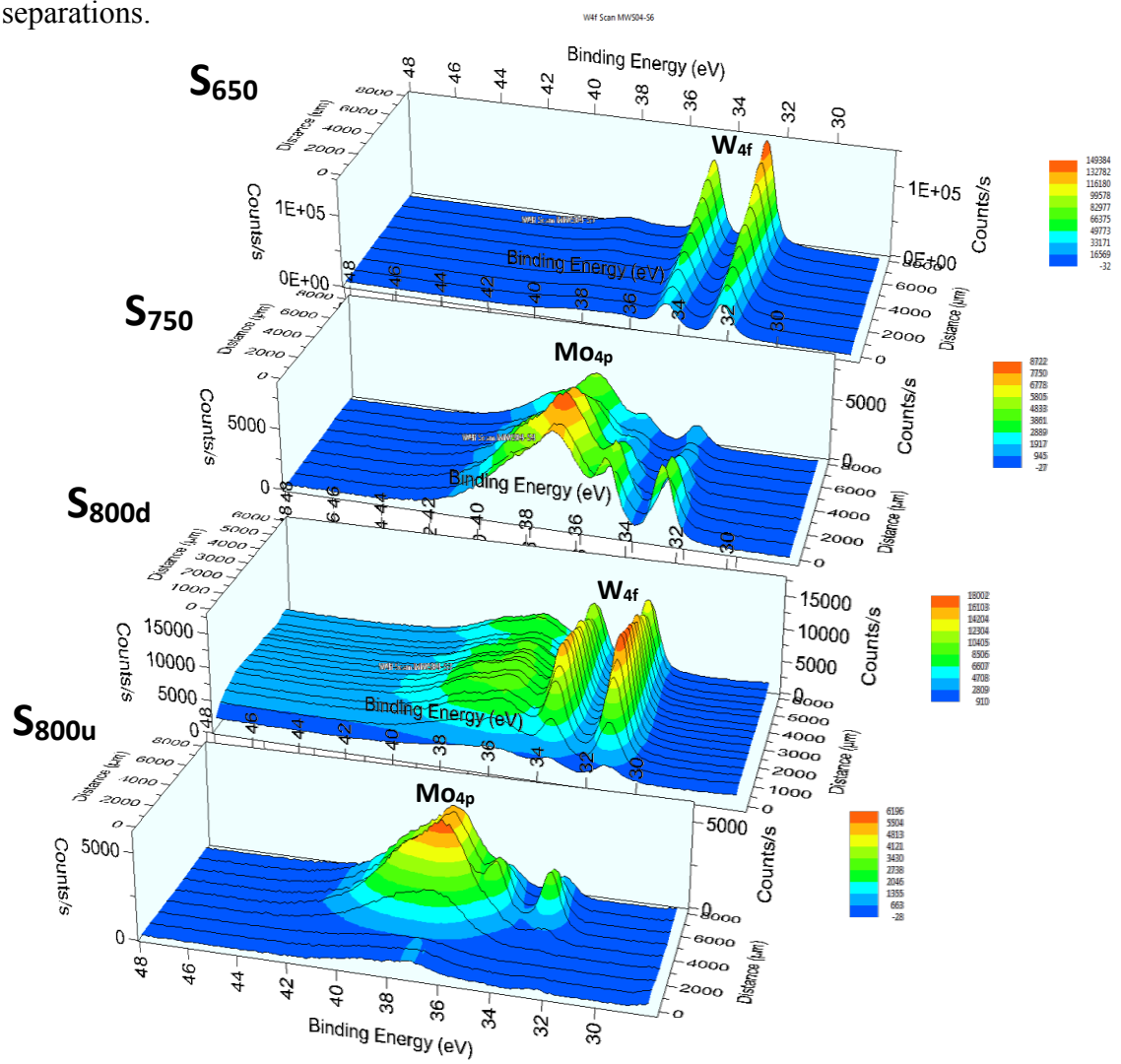


Figure. 117. XPS spectra of deposits at various points on silicon substrates showing the variation of W peaks along the furnace with different growth temperature.

5.3.2.5. STEM imaging of mixed metal dichalcogenides

The scanning transmission electron microscopy (STEM) was employed to visualise the arrangement of Mo and W atoms in mixed metal dichalcogenide lattice. Due to its larger atomic number (Z), the W atom shows brighter annular dark field (ADF) contrast than the Mo atom. This was utilised to visualise the arrangement of the atoms at the thinner regions of the flakes which were usually found at the edges of the exfoliated flakes. These thinner regions could be result of exfoliation using sonication under the tip. The high-resolution STEM obtained on the different samples S_{800u}, S_{800d}, S_{750} and S_{650} are summarised in Figure 118. The amount of bright atoms that would indicate W atom is very less in the multilayer region of sample S_{800u} and this progressively increases in the bilayer regions of samples S_{800d}, S_{750} and S_{650}. The monolayer regions observed at edges of flakes in Figure 118b, Figure 118c and Figure 118d, clearly show the difference in contrast between the Mo and W atoms in samples S_{800d}, S_{750} and S_{650} respectively. The trend of increase in atomic percentages of W obtained from the EDX results corresponds well with the STEM imaging. Thus STEM imaging provided the definite proof of alloying concluding the formation of $Mo_{1-x}W_xS_2$.

Thus the experiment using the two stage furnace provided an efficient and simple method of forming mixed metal dichalcogenides with varying W concerntrations by controlling the growth temperature. The ability to form 2D materials using the two furnace stage setup has been demonstrated in Chapter 4. Thereby, the amount of the precursors could be further reduced and proportions varied to produce 2D alloys which could possess composition-dependent band gaps.

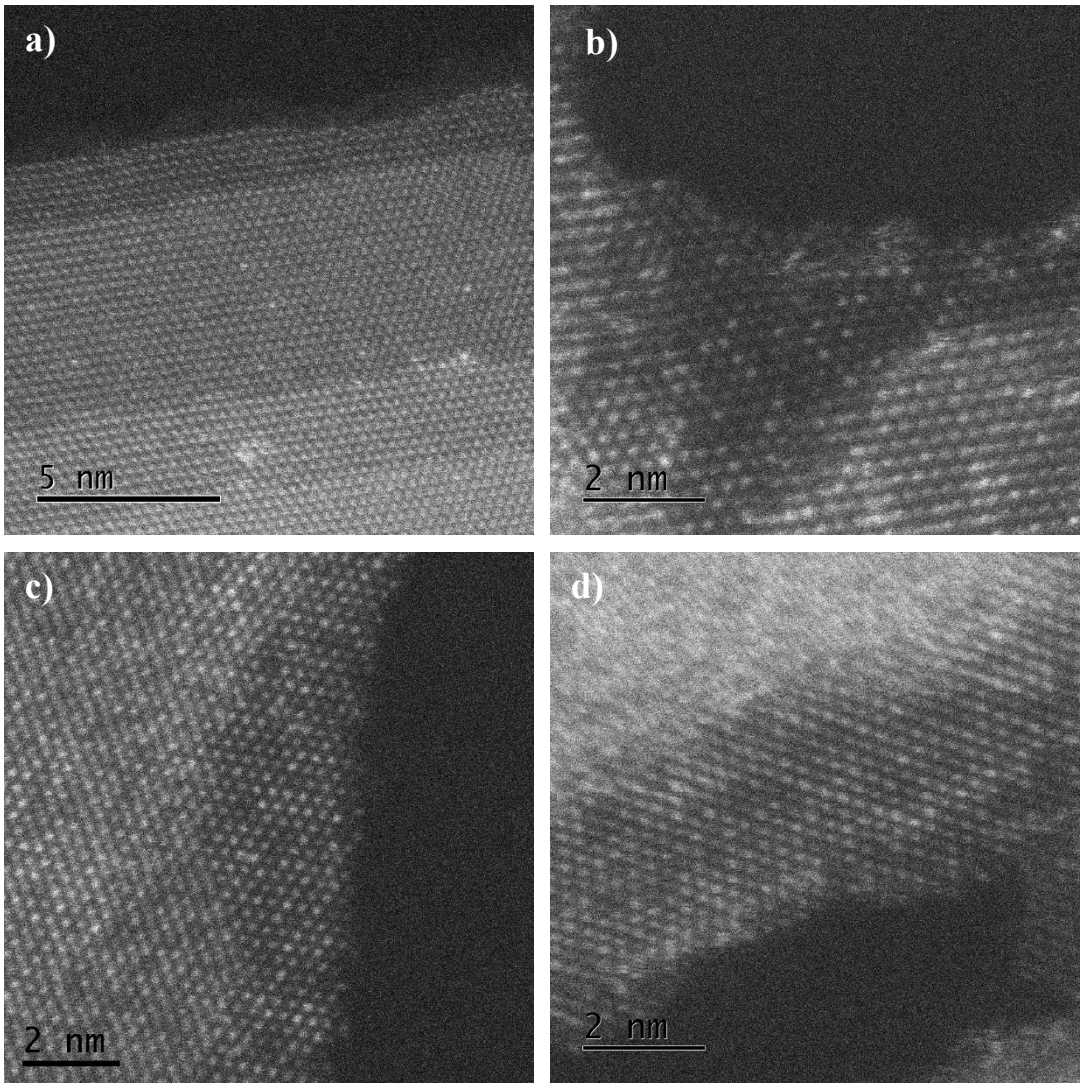


Figure 118. STEM images indicating Mo and W atoms in mixed chalcogenide flakes obtained by using CVD in a two stage furnace of substrates a) S_{800u}; b) S_{800d}; c) S_{750} and d) S_{650}.

5.4. Conclusion

The growth of mixed metal dichalcogenide nanostructures has been realised using chemical vapour deposition, which has not been demonstrated so far. The CVD process offers advantages such as scalability and faster synthesis time (few hours) over chemical vapour transport process which is widely used to form mixed metal

dichalcogenides crystals over a time period of 10 days. The key findings/results are listed below.

- Different molar proportions 1:1, 3:1, 3:2 and 1:3 of WCl_6:$MoCl_5$ using single stage furnace offered composition control up to 4.6% W but limited control over the final morphology which formed 3D structures from nanoflowers to spiral branched and platelet-like structures.
- Individual precursor control using the two-stage furnace demonstrated that the W dopant composition can be varied from as little as a few percent (x=0.98), to over 50% (x=0.42) with variation in different growth temperature and relative distances to the precursor, offering a promising way of producing mixed chalcogenides with controlled composition.
- The atomic-resolution annular dark field (ADF) scanning transmission electron microscopy (STEM) technique showed the substitution of W atoms for Mo atoms within the MoS_2 lattice, confirming the synthesis of alloyed dichalcogenides with varying composition rather than lateral heterojunctions.

Chapter 6. Summary and Future Work

6.1. Summary of research

In this thesis, a simple chemical vapour deposition (CVD) procedure has been used to synthesise different morphologies of WS_2-from three dimensional nanoflowers to two dimensional nanosheets. The process has also been extended to form mixed metal dichalcogenides of $Mo_xW_{1-x}S_2$. This highlights the versatility and potential of the process to serve as a reliable method for the production of TMDs with selective morphologies or controlled composition. The simplicity and scalability of the process offers possibility for upscaling. The advantages of using chloride precursors as metal sources including their higher vapour pressure and lower melting points- was another important aspect of the process that enabled selectivity of the product to be tailored for specific applications. Most transition metals are available in their chloride form which makes this a versatile process attractive for the production of wide range of TMDs.

The reproducible synthesis of nanoflower morphology was established using a simple and scalable CVD process. The process permitted the control of morphology and size distribution of the nanoflowers by the use of only two parameters, namely temperature and time period of synthesis. The nanoflower morphology was studied in great detail using high-resolution microscopy by dissociating the nanomaterials using sonication which revealed the presence of few-layer thin regions at the edges. Dissecting nanoflowers using focussed ion beam (FIB) provided insights into the core of these 3D structures. Novel heterostructures of WS_2 nanoflowers with tungsten oxide nanowires growing on them were also identified using TEM-EDX. The structural evolution of the nanoflower morphology from nucleation through to growth has been

studied along with compositional changes. This shed light on the nucleation process and growth mechanism of these nanostructures. The structural investigation using HRTEM help understand the presence of 2D nanosheets in the 3D nanoflower morphology. Also, as a by-product of this process deposits were obtained on the inside walls of the quartz tube which consisted of faceted microtubes, sheets and wires. These nanomaterials possess relatively high surface area and could be useful in applications such as catalysis and energy storage.

The WS_2 nanoflowers were used as a starting material for exfoliation and applied as catalysts for hydrogen evolution reaction (HER). The exfoliation was carried out using various techniques such as mechanical grinding, liquid exfoliation using surfactants, and solvent exfoliation using sonication, with the aim of forming large micrometer (μm) sized atomically thin flakes with uniform thickness. This interest/application stemmed from the identification of 2D nanosheets in the nanoflower morphology. The mechanical grinding process produced some very thin regions of WS_2 but offered control minimal over the final morphology. A systematic study using liquid exfoliation in surfactants provided limited success in terms of few-layer regions and generally suffered from rolling, breaking and agglomeration of exfoliated flakes as well as problems with contamination. Solvent exfoliation using sonication produced clusters of thin few-layer flakes with an abundance of exposed edges which could serve as ideal electrocatalysts for HER. The exfoliated nanoflowers combined with BP showed excellent HER activity with an overpotential of 100 mV and Tafel slope of 102 mV/decade along with an exchange current density of 15.6 x 10^{-6} A/cm^2. This study shows that CVD and subsequent solvent sonication process forms exfoliated WS_2 nanoflowers in large amounts and provides a promising way to

produce low cost electrocatalysts which could be used for potential application such as energy conversion and storage or sensors.

The synthesis of layered 2D WS_2 domains was also attempted using CVD at atmospheric pressure by employing a two-stage furnace and significantly reducing the amount of metal precursor. The influence of various parameters such as sulphur sublimation temperature, synthesis temperature, time period, substrate's position and precursors on the final deposit were investigated. Also the influence of the substrate on the growth of 2D WS_2 was studied using three widely used substrates namely silicon, 300 nm SiO_2 coated silicon and (0001) c-plane oriented sapphire. The shape, thickness and size of the domains varied for the different substrates depending on the growth condition. The best growth condition for sapphire was found to be 125 ^oC sulphur sublimation temperature and 850 ^oC synthesis temperature which formed thin few-layer domains 10-25 μm in size. For 300 nm SiO_2 coated silicon substrates 150 ^oC sulphur sublimation temperature with 850 ^oC synthesis temperature was suited for growth of bilayer regions of triangular flakes of 5 μm size. Although it is shown that even though mono and bi-layer regions of WS_2 were synthesised on both silicon and sapphire substrates at atmospheric pressure, it was difficult to prevent the secondary nucleation which often leads thicker regions.

The growth of mixed metal dichalcogenide nanostructures was demonstrated using CVD. CVD process was conducted using both single-stage and two-stage furnace. For the single-stage furnace the precursors were mixed together in different molar proportions of 3:1, 1:1, 3:2 and 1:3 (WCl_6:$MoCl_5$). This process formed 3D structures from nanoflowers to spiral branched and platelet-like structures with limited control over their morphology and composition with predominantly MoS_2 structures forming

due to lower sublimation temperature and higher vapour pressure of $MoCl_5$ in comparison to WCl_6 precursor. Using a two-stage, the composition-controlled synthesis of $Mo_xW_{1-x}S_2$ by atmospheric-pressure chemical vapour deposition (CVD) using Mo and W chloride precursors was demonstrated. By controlling the sublimation temperature of the precursors, it was elucidated that the growth temperature, which is varied from 650 ˚C to 800 ˚C, dictates the alloy composition. Complementary Raman spectroscopy, XPS and EDX analysis demonstrates that the W dopant composition can be subsequently varied from as little as a few percent (x=0.98), to over 50% (x=0.42). Through atomic-resolution annular dark field (ADF) scanning transmission electron microscopy (STEM) using a Cs probe corrected JEOL ARM 200F (80-200-kV) the substitution of W atoms for Mo atoms within the MoS_2 lattice was directly observed, confirming the synthesis of alloyed dichalcogenides.

6.2. Future work

6.2.1. Upscaling synthesis of nanoflower morphology

The synthesis of nanoflower morphology can be up-scaled by using large diameter furnace that could host larger silicon substrates. Increasing the length of the furnace would enable more substrates and increase the quantity of deposits. To improve the efficiency of the process, the precursor could be reused by cycling them in the reactor. Subliming the precursors in a separate chamber and introducing them into the furnace would help improve the yield of the process. The nanoflower morphology is attractive for use in catalysis and other energy storage applications due to the large number of exposed edges. This can be further enhanced by the use of simple sonication process as discussed in section 3.3.3.

6.2.2. Improved electrocatalysts for HER

Exfoliated nanoflowers and the nanoflowers morphology have been combined with commercially available BP to be used as electrocatalysts for HER in section 3.3.4. The results show promise in terms of producing electrocatalysts at low cost. However, the performance of these catalysts can be further improved by employing carbon nanomaterials such as graphene and carbon nanotubes or graphene oxide as matrix, since they possess excellent electronic behaviour, greater surface area and increased electron conductivity. This would also improve the chemical and electronic coupling with the WS_2 nanomaterials. It has been shown by Zhou, W. *et al.* [235] that graphene framework with high surface area and good electrical conductivity improve the HER activity of MoS_2 as shown in Figure 119.

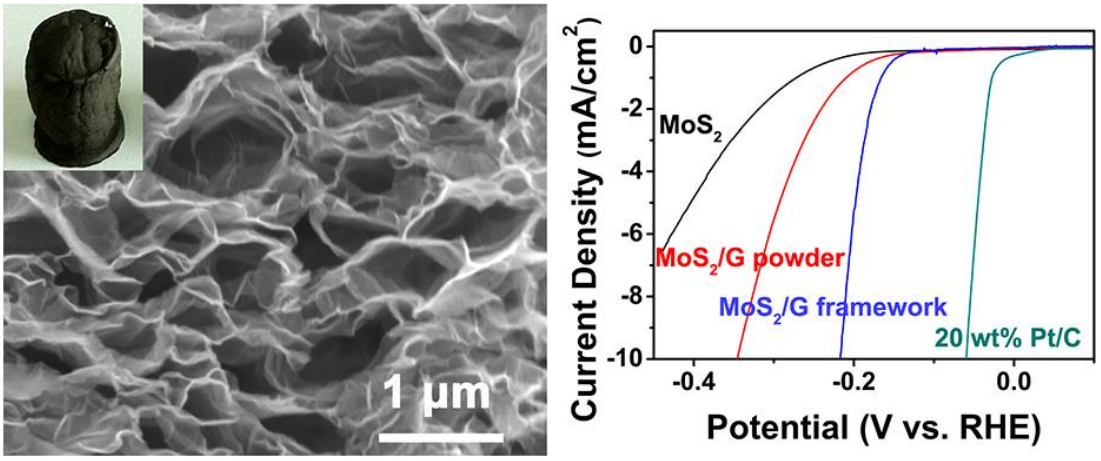


Figure 119. 3D MoS2/Graphene framework and its electrocatalytic activity for HER. Reproduced with permission.[235]

6.2.3. Low-pressure CVD to form thin films

The synthesis of 2D WS_2 using atmospheric pressure CVD was discussed in Chapter 4. The process was successful in producing large-area few-layer WS_2 domains on sapphire substrates with full coverage and bi-layer triangular domains on 300 nm SiO_2/Si substrates. However, it was difficult to prevent the secondary layer growth through nucleation on the already formed regions. One of the ways to prevent this secondary growth is to reduce the total pressure of the system. Yu, Y. *et al.*[214] have shown that the growth of MoS_2 thin films using $MoCl_5$ precursor was dependent on the total pressure of the system and the amount of precursors. By reducing the total pressure of the system the thickness of the films decreased, confirmed by Raman as shown in Figure 120. Hence the low pressure CVD synthesis would help control the partial pressure of the precursors which could in turn reduce the layer number of synthesised thin film.

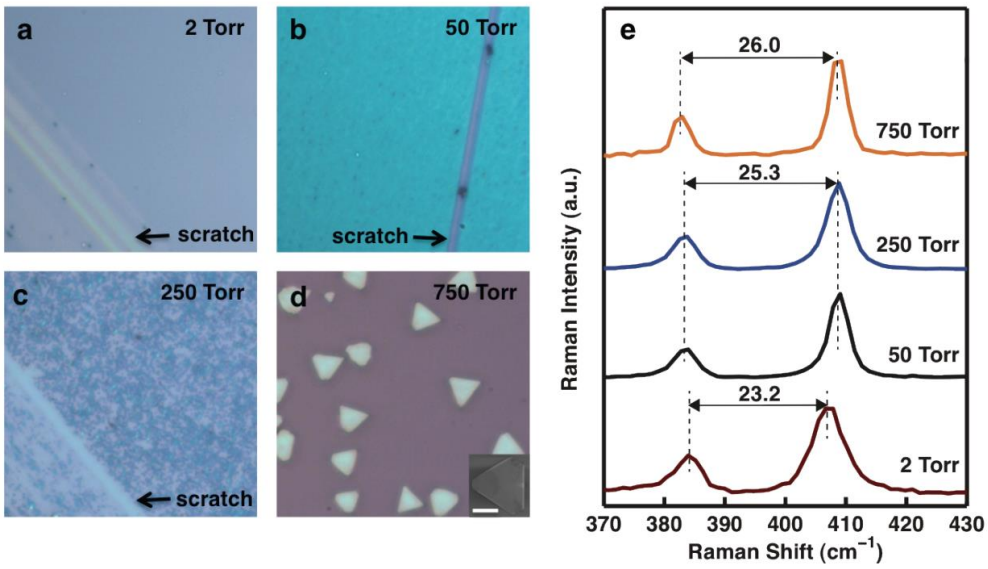


Figure 120. Optical micrographs of MoS_2 deposits under different total pressure of system along with their Raman spectra. Reproduced with permission.[214]

6.2.4. Control of atomic percentage and formation of 2D TMD alloys

The synthesis of mixed metal chalcogenides $Mo_xW_{1-x}S_2$ using CVD was presented in Chapter 5. By using a two-stage furnace and controlling the sublimation of the precursors, composition controlled mixed metal dichalcogenides with varying amount of W content were produced. While the mixed metal dichalcogenides were formed as few-layered flakes which could be suited for catalysis, application involving band gap modulation would require monolayer films. Hence this process could be tuned to form monolayer mixed metal dichalcogenides and investigated for application in optoelectronic application. This could be achieved by independently controlling the precursors input by subliming each in isolated chambers and controlling flow rates using mass flow controllers (MFC) and argon. A schematic of the setup is as shown in the Figure 121. This would help to control the concentration of each reactant during the entire growth period and thus regulate the partial pressure of each reactant. As discussed earlier the partial pressure of the precursors determine the thickness of the resultant deposit and help produce large area monolayer films.

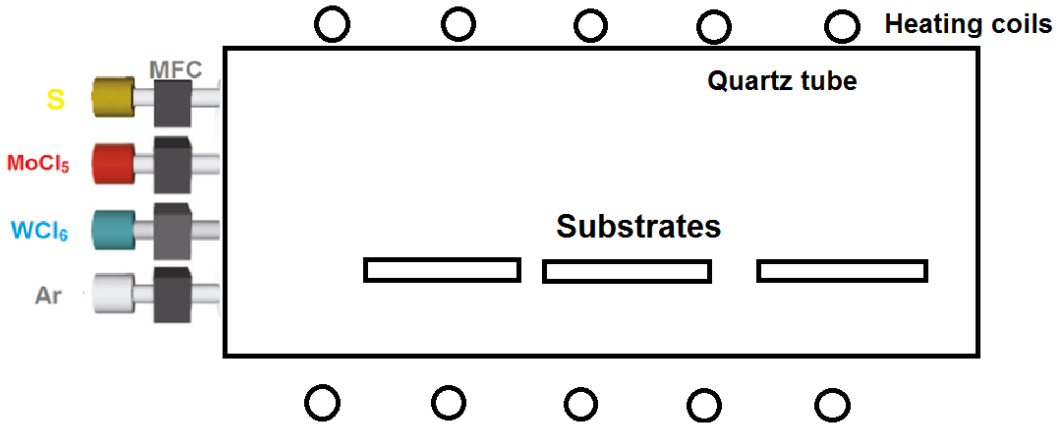


Figure 121. Schematic of proposed CVD setup for synthesis of 2D TMD alloys

Bibliography

1. H.W.Kroto & R.E.Smalley. C60: Buckminsterfullerene. *Lett. to Nat.* (1985).

2. Iijima, S. Helical microtubules of graphitic carbon. *Nature* (1991).

3. Tenne, R. Margulis, L. Genut, M. & Hodes, G. Polyhedral and cylindrical structures of tungsten disulphide. *Nature* **360,** 444–446 (1992).

4. Rao, C. N. R. & Nath, M. Inorganic nanotubes †. 1–24 (2003).

5. Tenne, R. & Seifert, G. Recent Progress in the Study of Inorganic Nanotubes and Fullerene-Like Structures. *Annu. Rev. Mater. Res.* **39,** 387–413 (2009).

6. Feldman, Y., Wasserman, E., Srolovitz, D. J. & Tenne, R. High-Rate, Gas-Phase Growth of MoS2 Nested Inorganic Fullerenes and Nanotubes. *Science* **267,** 222–5 (1995).

7. Feldman, Y. *et al.* Bulk Synthesis of Inorganic Fullerene-like MS 2 (M) Mo , W) from the Respective Trioxides and the Reaction Mechanism. **2,** 5362–5367 (1996).

8. Margolin, a *et al.* Fullerene-like WS(2) nanoparticles and nanotubes by the vapor-phase synthesis of WCl(n) and H(2)S. *Nanotechnology* **19,** 095601 (2008).

9. Tenne, B. R., Margulis, L. & Hodes, G. Fullerene-Like Nanocrystals of Tungsten Disulfide. **76100,**

10. Scheffer, L. *et al.* Scanning tunneling microscopy study of WS2 nanotubes. *Phys. Chem. Chem. Phys.* **4,** 2095–2098 (2002).

11. Seifert, G., Terrones, H., Terrones, M., Jungnickel, G. & Frauenheim, T. Structure and electronic properties of MoS2 nanotubes. *Phys. Rev. Lett.* **85,** 146–9 (2000).

12. Chianelli, R. R. *et al.* Catalytic Properties of Single Layers of Transition Metal Sulfide Catalytic Materials. *Catal. Rev.* **48,** 1–41 (2006).

13. Sobczynski, A. *et al.* Tungsten Dlsulflde : A Novel Hydrogen Evolution Catalyst for Water Decomposition. 2311–2315 (1988).

14. Sobczynski, a. Molybdenum disulfide as a hydrogen evolution catalyst for water photodecomposition on semiconductors. *J. Catal.* **131,** 156–166 (1991).

15. Cohen, S. R. The tribological behavior of type II textured MX 2 ž M s Mo , W ; X s S , Se / films. 190–197 (1998).

16. Rapoport, L., Fleischer, N. & Tenne, R. Applications of WS2(MoS2) inorganic nanotubes and fullerene-like nanoparticles for solid lubrication and for structural nanocomposites. *J. Mater. Chem.* **15,** 1782 (2005).

17. Joly-Pottuz, L. *et al.* Ultralow-friction and wear properties of IF-WS2 under boundary lubrication. *Tribol. Lett.* **18,** 477–485 (2005).

18. Brown, S. *et al.* Bulk vs nanoscale WS2: finite size effects and solid-state lubrication. *Nano Lett.* **7,** 2365–9 (2007).

19. Katz, a., Redlich, M., Rapoport, L., Wagner, H. D. & Tenne, R. Self-lubricating coatings containing fullerene-like WS2 nanoparticles for orthodontic wires and other possible medical applications. *Tribol. Lett.* **21,** 135–139 (2006).

20. Imanishi, N. Synthesis of MoS[sub 2] Thin Film by Chemical Vapor Deposition Method and Discharge Characteristics as a Cathode of the Lithium Secondary Battery. *J. Electrochem. Soc.* **139,** 2082 (1992).

21. Wang, G. X., Bewlay, S., Yao, J., Liu, H. K. & Dou, S. X. Tungsten Disulfide Nanotubes for Lithium Storage. *Electrochem. Solid-State Lett.* **7,** A321 (2004).

22. Furimsky, E. & Canada, L. Catalysis Reviews : Science and Engineering Role of MoS 2 and WS 2 in Hydrodesulfuritation. (2013).

23. Brorson, M., Carlsson, a. & Topsøe, H. The morphology of MoS2, WS2, Co–Mo–S, Ni–Mo–S and Ni–W–S nanoclusters in hydrodesulfurization catalysts revealed by HAADF-STEM. *Catal. Today* **123,** 31–36 (2007).

24. Komarneni, M. R. *et al.* Characterization of Ni-Coated WS 2 Nanotubes for Hydrodesulfurization Catalysis. *Isr. J. Chem.* **52,** 1053–1062 (2012).

25. Chen, J., Kuriyama, N., Yuan, H., Takeshita, H. T. & Sakai, T. Electrochemical hydrogen storage in MoS2 nanotubes. *J. Am. Chem. Soc.* **123,** 11813–11814 (2001).

26. Rothschild, a., Cohen, S. R. & Tenne, R. WS[sub 2] nanotubes as tips in scanning probe microscopy. *Appl. Phys. Lett.* **75,** 4025 (1999).

27. Homyonfer, M. *et al.* Intercalation of inorganic fullerene-like structures yields photosensitive films and new tips for scanning probe microscopy. *J. Am. Chem. Soc.* **119,** 2693–2698 (1997).

28. Xu, F. *et al.* Ultra-toughened nylon 12 nanocomposites reinforced with IF-WS 2. *Nanotechnology* **25,** 325701 (2014).

29. ApNano. at <http://www.apnano.com/>

30. Li, X.-L., Ge, J.-P. & Li, Y.-D. Atmospheric pressure chemical vapor deposition: an alternative route to large-scale MoS2 and WS2 inorganic fullerene-like nanostructures and nanoflowers. *Chemistry* **10,** 6163–71 (2004).

31. Hu, Z. *et al.* MoS 2 Nanoflowers with Expanded Interlayers as High-Performance Anodes for Sodium-Ion Batteries. *Angew. Chemie* **126,** 13008–13012 (2014).

32. Li, Q. *et al.* Molybdenum disulfide nanowires and nanoribbons by electrochemical/chemical synthesis. *J. Phys. Chem. B* **109,** 3169–82 (2005).

33. Wang, Z. *et al.* Ultra-narrow WS2 nanoribbons encapsulated in carbon nanotubes. *J. Mater. Chem.* **21,** 171 (2011).

34. Remskar, M., Virsek, M. & Jesih, A. LETTERS WS 2 Nanobuds as a New Hybrid Nanomaterial. **333,** 2–6 (2008).

35. Bastide, S., Duphil, D., Borra, J.-P. & Lévy-Clément, C. WS2 Closed Nanoboxes Synthesized by Spray Pyrolysis. *Adv. Mater.* **18,** 106–109 (2006).

36. Geim, a K. & Novoselov, K. S. The rise of graphene. *Nat. Mater.* **6,** 183–91 (2007).

37. Geim, a K. & Grigorieva, I. V. Van der Waals heterostructures. *Nature* **499,** 419–25 (2013).

38. Butler, S. Z. *et al.* Opportunities in Two-Dimensional Materials Beyond Graphene. (2013).

39. Jeffrey Zabinski, S. P. WS2 and Graphite structure. *Nature* 761–763 (1997). at <http://www.substech.com/>

40. Wilson, J. a & Yoffe, a D. The transition metal dichalcogenides discussion and interpretation of the observed optical, electrical and structural properties. *Adv. Phys.* **18,** 193–335 (1969).

41. Friend, R. H. & Yoffe, a. D. Electronic properties of intercalation complexes of the transition metal dichalcogenides. *Adv. Phys.* **36,** 1–94 (1987).

42. Chhowalla, M. *et al.* The chemistry of two-dimensional layered transition metal dichalcogenide nanosheets. *Nat. Chem.* **5,** 263–75 (2013).

43. Kuc, a., Zibouche, N. & Heine, T. Influence of quantum confinement on the electronic structure of the transition metal sulfide TS_{2}. *Phys. Rev. B* **83,** 1–4 (2011).

44. Neto, A. H. C. Charge Density Wave , Superconductivity , and Anomalous Metallic Behavior in 2D Transition Metal Dichalcogenides. 1–4 (2001). doi:10.1103/PhysRevLett.86.4382

45. Wilson, J. a., Di Salvo, F. J. & Mahajan, S. Charge-density waves and superlattices in the metallic layered transition metal dichalcogenides. *Adv. Phys.* **24,** 117–201 (1975).

46. Sipos, B. *et al.* From Mott state to superconductivity in 1T-TaS2. *Nat. Mater.* **7,** 960–965 (2008).

47. Ataca, C. & Ciraci, S. (203) Stable, Single-Layer MX2 Transition-Metal Oxides and Dichalcogenides in a Honeycomb-Like Structure.pdf. (2012).

48. Xu, M., Liang, T., Shi, M. & Chen, H. Graphene-Like Two-Dimensional Materials. (2013).

49. Hankare, P. P. *et al.* WS2 thin films: Opto-electronic characterization. *J. Alloys Compd.* **479,** 657–660 (2009).

50. Tenne, R. Fullerene-like materials and nanotubes from inorganic compounds with a layered (2-D) structure. *Colloids Surfaces A Physicochem. Eng. Asp.* **208,** 83–92 (2002).

51. Remškar, M. Inorganic Nanotubes. *Adv. Mater.* **16,** 1497–1504 (2004).

52. Rao, C. N. R. & Nag, A. Inorganic Analogues of Graphene. *Eur. J. Inorg. Chem.* **2010,** 4244–4250 (2010).

53. Ugarte, D. Curling and closure of graphitic networks under electron-beam irradiation. *Nature* **359,** 707–709 (1992).

54. Enyashin, A. N. *et al.* Structure and stability of molybdenum sulfide fullerenes. *Angew. Chem. Int. Ed. Engl.* **46,** 623–7 (2007).

55. Rosentsveig, R. *et al.* Fullerene-like MoS2 Nanoparticles and Their Tribological Behavior. *Tribol. Lett.* **36,** 175–182 (2009).

56. Chen, J., Li, S.-L., Xu, Q. & Tanaka, K. Synthesis of open-ended MoS2 nanotubes and the application as the catalyst of methanation. *Chem. Commun. (Camb).* 1722–1723 (2002). doi:10.1039/b205109e

57. Mak, K. F., Lee, C., Hone, J., Shan, J. & Heinz, T. F. Atomically Thin MoS_{2}: A New Direct-Gap Semiconductor. *Phys. Rev. Lett.* **105,** 136805 (2010).

58. Taylor, P., Wilson, J. A. & Yoffe, A. D. Advances in Physics The transition metal dichalcogenides discussion and interpretation of the observed optical , electrical and structural properties. 37–41 (2013).

59. Podberezskaya, N. V., Magarill, S. a., Pervukhina, N. V. & Borisov, S. V. Crystal chemistry of dichalcogenides MX2. *J. Struct. Chem.* **42,** 654–681 (2001).

60. Bertolazzi, S., Brivio, J. & Kis, A. Stretching and Breaking of Ultrathin. 9703–9709 (2011).

61. Radisavljevic, B., Radenovic, a, Brivio, J., Giacometti, V. & Kis, a. Single-layer MoS2 transistors. *Nat. Nanotechnol.* **6,** 147–50 (2011).

62. Ilatikhameneh, H. *et al.* Tunnel Field-Effect Transistors in 2D Transition Metal Dichalcogenide Materials. 1–7

63. Wang, Q. H., Kalantar-Zadeh, K., Kis, A., Coleman, J. N. & Strano, M. S. Electronics and optoelectronics of two-dimensional transition metal dichalcogenides. *Nat. Nanotechnol.* **7,** 699–712 (2012).

64. Ye, M., Winslow, D., Zhang, D., Pandey, R. & Yap, Y. Recent Advancement on the Optical Properties of Two-Dimensional Molybdenum Disulfide (MoS2) Thin Films. *Photonics* **2,** 288–307 (2015).

65. Zeng, H. *et al.* Optical signature of symmetry variations and spin-valley coupling in atomically thin tungsten dichalcogenides. **21,** 4908–4916 (2012).

66. Cao, T. *et al.* Valley-selective circular dichroism of monolayer molybdenum disulphide. *Nat. Commun.* **3,** 887 (2012).

67. Babaei, H., Khodadadi, J. M. & Sinha, S. Large theoretical thermoelectric power factor of suspended single-layer MoS2. *Appl. Phys. Lett.* **105,** 193901 (2014).

68. Osada, M. & Sasaki, T. Two-dimensional dielectric nanosheets: Novel nanoelectronics from nanocrystal building blocks. *Adv. Mater.* **24,** 210–228 (2012).

69. Rosenfeld Hacohen, Y. *et al.* Synthesis of NiCl2 nanotubes and fullerene-like structures by laser ablation: theoretical considerations and comparison with MoS2 nanotubes. *Phys. Chem. Chem. Phys.* **5,** 1644–1651 (2003).

70. Albu-Yaron, A. *et al.* Preparation and structural characterization of stable Cs2O closed-cage structures. *Angew. Chemie - Int. Ed.* **44,** 4169–4172 (2005).

71. Tenne, R. Nested fullerene-like structures. *Nature* (1993).

72. Oriakhi, C. O. & Lerner, M. M. Layered Metal Chalcogenides. *ChemInform* **36,** (2005).

73. Palosz, B. Reasons for Polytypism of Crystals of the Type MXe. **11,** (1983).

74. Shi, Y., Wan, Y., Liu, R., Tu, B. & Zhao, D. Synthesis of highly ordered mesoporous crystalline WS(2) and MoS(2) via a high-temperature reductive sulfuration route. *J. Am. Chem. Soc.* **129,** 9522–31 (2007).

75. Schuffenhauer, C., Popovitz-Biro, R. & Tenne, R. Synthesis of NbS2 nanoparticles with (nested) fullerene-like structure (IF). *J. Mater. Chem.* **12,** 1587–1591 (2002).

76. Chen, J., Tao, Z. L. & Li, S. L. Lithium intercalation in open-ended TiS2 nanotubes. *Angew. Chemie - Int. Ed.* **42,** 2147–2151 (2003).

77. Etzkorn, J. *et al.* Metal-Organic Chemical Vapor Depostion Synthesis of Hollow Inorganic-Fullerene-Type MoS2 and MoSe2 Nanoparticles. *Adv. Mater.* **17,** 2372–2375 (2005).

78. Margolin, A., Popovitz-Biro, R., Albu-Yaron, A., Rapoport, L. & Tenne, R. Inorganic fullerene-like nanoparticles of TiS2. *Chem. Phys. Lett.* **411,** 162–166 (2005).

79. Zelenski, C. M. & Dorhout, P. K. Template Synthesis of Near-Monodisperse 1 Microscale Nanofibers and Nanotubules of MoS 2. **7863,** 734–742 (1998).

80. Rao, C. N. R. Simple Synthesis of MoS 2 and WS 2 Nanotubes. *Adv. Mater.* 283–286 (2001).

81. Wu, Z., Wang, D., Zan, X. & Sun, A. Synthesis of WS2 nanosheets by a novel mechanical activation method. *Mater. Lett.* **64,** 856–858 (2010).

82. Adeogun, a., Afzaal, M. & O'Brien, P. Studies of Molybdenum Disulfide Nanostructures Prepared by AACVD Using Single-Source Precursors. *Chem. Vap. Depos.* **12,** 597–599 (2006).

83. Smith, R. J. *et al.* Large-scale exfoliation of inorganic layered compounds in aqueous surfactant solutions. *Adv. Mater. Deerf. Beach Fla* **23,** 3944–3948 (2011).

84. Zhou, K.-G., Mao, N.-N., Wang, H.-X., Peng, Y. & Zhang, H.-L. A mixed-solvent strategy for efficient exfoliation of inorganic graphene analogues. *Angew. Chem. Int. Ed. Engl.* **50,** 10839–42 (2011).

85. Lee, Y.-H. *et al.* Synthesis of large-area MoS2 atomic layers with chemical vapor deposition. *Adv. Mater.* **24,** 2320–5 (2012).

86. Van der Zande, A. M. *et al.* Grains and grain boundaries in highly crystalline monolayer molybdenum disulphide. *Nat. Mater.* **12,** 554–561 (2013).

87. Najmaei, S. *et al.* Vapour phase growth and grain boundary structure of molybdenum disulphide atomic layers. *Nat. Mater.* **12,** 1–6 (2013).

88. Elías, A. L. *et al.* Controlled Synthesis and Transfer of Large-Area WS2 Sheets: From Single Layer to Few Layers. *ACS Nano* **7,** 5235–42 (2013).

89. Rothschild, A., Sloan, J. & Tenne, R. Growth of WS 2 Nanotubes Phases. 5169–5179 (2000).

90. Feldman, Y., Zak, A., Popovitz-Biro, R. & Tenne, R. New reactor for production of tungsten disulfide hollow onion-like (inorganic fullerene-like) nanoparticles. *Solid State Sci.* **2,** 663–672 (2000).

91. Tenne, R. Inorganic nanotubes and fullerene-like nanoparticles. *Nat. Nanotechnol.* **1,** 103–111 (2006).

92. Hershfinkel, M. *et al.* Nested Polyhedra of MX2 (M = W, Mo; X = S, Se) Probed by High-Resolution Electron Microscopy and Scanning Tunneling Microscopy. *J. Am. Chem. Soc.* **116,** 1914–1917 (1994).

93. Galun, E. *et al.* Crystallization of layered metal-dichalcogenides films on amorphous substrates. *Appl. Phys. Lett.* **67,** 3474 (1995).

94. Rapoport, L., Bilik, Y., Feldman, Y. & Homyonfer, M. Hollow nanoparticles of WS2 as potential solid-state lubricants. *Nature* **387,** 791–793 (1997).

95. Tenne, R. Scanning Tunneling Microscope Induced Crystallization of Fullerene-like MoS 2. *J. Am. Chem. Soc.* **118,** 7804–7808 (1996).

96. Prasad, T. P., Diemann, E. & Müller, a. Thermal decomposition of (NH4)2MoO2S2, (NH4)2MoS4, (NH4)2WO2S2 and (NH4)2WS4. *J. Inorg. Nucl. Chem.* **35,** 1895–1904 (1973).

97. Decomposition, T., Diemann, E., Muller, a & Aymonino, P. J. Thermal Decomposition. **198,** 191–198 (1981).

98. Mueller, a. *et al.* New method for the preparation of hydrodesulphurization catalysts. Use of the molybdenum sulphur cluster compound (NH4)2[Mo3 IVS13]. *Appl. Catal.* **62,** 13–17 (1990).

99. Diggle, J. W., Downie, T. C. & Goulding, C. W. Anodic oxide films on aluminum. *Chem. Rev.* **69,** 365–405 (1969).

100. Brumlik, C. J. & Martin, C. R. Template synthesis of metal microtubules. *J. Am. Chem. Soc.* **113,** 3174–3175 (1991).

101. Stoffels, E. *et al.* MoS[sub 2] nanoparticle formation in a low pressure environment. *J. Appl. Phys.* **86,** 3442 (1999).

102. Frindt, R. F. Single Crystals of MoS2 Several Molecular Layers Thick. *J. Appl. Phys.* **37,** 1928 (1966).

103. Coleman, J. N. *et al.* Two-dimensional nanosheets produced by liquid exfoliation of layered materials. *Science* **331,** 568–71 (2011).

104. Miremadi, B. K. & Morrison, S. R. The intercalation and exfoliation of tungsten disulfide. *J. Appl. Phys.* **63,** 4970–4974 (1988).

105. Yang, D. & Frindt, R. F. Li-intercalation and exfoliation of WS2. *J. Phys. Chem. Solids* **57,** 1113–1116 (1996).

106. Matte, H. S. S. R. *et al.* MoS2 and WS2 analogues of graphene. *Angew. Chem. Int. Ed. Engl.* **49,** 4059–62 (2010).

107. Matte, H. S. S. R. *et al.* Synthesis, Characterization, and Properties of Few-layer Metal Dichalcogenides and their Nanocomposites with Noble Metal Particles, Polyaniline, and Reduced Graphene Oxide. *Zeitschrift für Anorg. und Allg. Chemie* **638,** 2617–2624 (2012).

108. Novoselov, K. S. *et al.* Electric field effect in atomically thin carbon films. *Science* **306,** 666–9 (2004).

109. Novoselov, K. S. *et al.* Two-dimensional atomic crystals. **102,** 10451–10453 (2005).

110. Hansen, C. *Hansen solubility parameters: a user's handbook.* (CRC Publisher, 2005).

111. Nicolosi, V., Chhowalla, M., Kanatzidis, M. G., Strano, M. S. & Coleman, J. N. Liquid Exfoliation of Layered Materials. *Science (80-.).* **340,** 1226419–1226419 (2013).

112. Benavente, E., Santa Ana, M. a., Mendizábal, F. & González, G. Intercalation chemistry of molybdenum disulfide. *Coord. Chem. Rev.* **224,** 87–109 (2002).

113. Eda, G. *et al.* Photoluminescence from chemically exfoliated MoS 2. *Nano Lett.* **11,** 5111–5116 (2011).

114. Mos, H. S. & Al, E. D. A. E. T. Coherent Atomic and Electronic. 7311–7317 (2012).

115. Zeng, Z. *et al.* An effective method for the fabrication of few-layer-thick inorganic nanosheets. *Angew. Chemie - Int. Ed.* **51,** 9052–9056 (2012).

116. Zeng, Z. *et al.* Single-layer semiconducting nanosheets: high-yield preparation and device fabrication. *Angew. Chem. Int. Ed. Engl.* **50,** 11093–7 (2011).

117. Splendiani, A. *et al.* Emerging photoluminescence in monolayer MoS2. *Nano Lett.* **10,** 1271–5 (2010).

118. Lee, Y. H. *et al.* Synthesis of large-area MoS 2 atomic layers with chemical vapor deposition. *Adv. Mater.* **24,** 2320–2325 (2012).

119. Lin, Y.-C. *et al.* Wafer-scale MoS2 thin layers prepared by MoO3 sulfurization. *Nanoscale* **4,** 6637 (2012).

120. Wang, X., Feng, H., Wu, Y. & Jiao, L. Controlled synthesis of highly crystalline MoS2 flakes by chemical vapor deposition. *J. Am. Chem. Soc.* **135,** 5304–7 (2013).

121. Zhan, Y., Liu, Z., Najmaei, S., Ajayan, P. M. & Lou, J. Large-area vapor-phase growth and characterization of MoS(2) atomic layers on a SiO(2) substrate. *Small* **8,** 966–71 (2012).

122. M. Salmeron, G. A. S. A LEED-AES study of the structure of sulfur monolayers on the Mo(100) crystal face. *Surf. Sci.* **127,** 526–540 (1983).

123. Wilson, J. M. LEED and AES study of the interaction of H2S and Mo (100). *Surf. Sci.* **53,** 330–340 (1975).

124. Shi, Y. *et al.* van der Waals epitaxy of MoS_2 layers using graphene as growth templates. *Nano Lett.* **12,** 2784–91 (2012).

125. Liu, K.-K. *et al.* Growth of large-area and highly crystalline MoS2 thin layers on insulating substrates. *Nano Lett.* **12,** 1538–44 (2012).

126. Rong, Y. *et al.* Controlling sulphur precursor addition for large single crystal domains of WS2. *Nanoscale* **6,** 12096–103 (2014).

127. Enyashin, A. N. Theoretical Studies of Inorganic Fullerenes and Fullerene-Like Nanoparticles. *Isr. J. Chem.* **50,** 468–483 (2010).

128. Tenne, R. & Rao, C. N. R. Inorganic nanotubes. *Philos. Trans. A. Math. Phys. Eng. Sci.* **362,** 2099–125 (2004).

129. Boeker, T. *et al.* Band structure of MoS_2, MoSe_2, and alpha-MoTe_2: Angle-resolved photoelectron spectroscopy and ab-initio calculations. **64,** 12 (2001).

130. Mos, F. *et al.* Anomalous Lattice Vibrations of Single-. **4,** 2695–2700 (2010).

131. Huang, X., Zeng, Z. & Zhang, H. Metal dichalcogenide nanosheets: preparation, properties and applications. *Chem. Soc. Rev.* **42,** 1934–46 (2013).

132. Zhu, Y. Q. *et al.* Shock-absorbing and failure mechanisms of WS2 and MoS2 nanoparticles with fullerene-like structures under shock wave pressure. *J. Am. Chem. Soc.* **127,** 16263–72 (2005).

133. Kaplan-Ashiri, I. & Tenne, R. Mechanical Properties of WS2 Nanotubes. *J. Clust. Sci.* **18,** 549–563 (2007).

134. Kaplan-Ashiri, I. *et al.* On the mechanical behavior of WS2 nanotubes under axial tension and compression. *Proc. Natl. Acad. Sci. U. S. A.* **103,** 523–8 (2006).

135. Kaplan-Ashiri, I. *et al.* Microscopic Investigation of Shear in Multiwalled Nanotube Deformation. *J. Phys. Chem. C* **111,** 8432–8436 (2007).

136. Reeves, C. Graphene : Characterization After Mechanical Exfoliation. 1–23 (2010).

137. Castellanos-Gomez, A., Singh, V., van der Zant, H. S. J. & Steele, G. a. Mechanics of freely-suspended ultrathin layered materials. *Ann. Phys.* n/a–n/a (2014). doi:10.1002/andp.201400153

138. Castellanos-Gomez, A. *et al.* Elastic properties of freely suspended MoS2 nanosheets. *Adv. Mater.* **24,** 772–5 (2012).

139. Miyoshi, K. Solid Lubricants and Coatings for Extreme Environments : State-of-the-Art Survey. 1–23 (2007).

140. Jifen, W., Wensheng, Z. & Guifen, J. Preparation and tribological properties of tungsten disulfide hollow spheres assisted by methyltrioctylammonium chloride. *Tribol. Int.* **43,** 1650–1658 (2010).

141. Lu, W. & Lieber, C. M. Nanoelectronics from the bottom-up. *Nat. Mater.* **6,** 841–850 (2007).

142. Yoon, Y., Ganapathi, K. & Salahuddin, S. How good can monolayer MoS_2 transistors be? *Nano Lett.* **11,** 3768–73 (2011).

143. Wang, Q. H., Kalantar-zadeh, K., Kis, A., Coleman, J. N. & Strano, M. S. transition metal dichalcogenides. *Nat. Publ. Gr.* **7,** 699–712 (2012).

144. M. Arden, W. The International Technology Roadmap for Semiconductors—Perspectives and challenges for the next 15 years. *Curr. Opin. Solid State Mater. Sci.* **6,** 371–377 (2002).

145. Colinge, J. P. Multiple-gate SOI MOSFETs. *Solid. State. Electron.* **48,** 897–905 (2004).

146. Schwierz, F. Graphene transistors. *Nat. Nanotechnol.* **5,** 487–496 (2010).

147. Han, G. & Yoon, Y. Contact-dependent performance variability of monolayer MoS 2 field-effect transistors. **213508,** 2–7 (2014).

148. Radisavljevic, B., Whitwick, M. B. & Kis, A. Integrated circuits and logic operations based on single-layer MoS 2. *ACS Nano* **5,** 9934–9938 (2011).

149. Wang, H. *et al.* Integrated circuits based on bilayer MoS_2 transistors. *Nano Lett.* **12,** 4674–80 (2012).

150. Law, M., Goldberger, J. & Yang, P. Semiconductor Nanowires and Nanotubes. *Annu. Rev. Mater. Res.* **34,** 83–122 (2004).

151. Avouris, P., Freitag, M. & Perebeinos, V. Carbon-nanotube photonics and optoelectronics. *Nat. Photonics* **2,** 341–350 (2008).

152. Scholes, G. D. & Rumbles, G. Excitons in nanoscale systems. *Nat. Mater.* **5,** 683–696 (2006).

153. Kamat, P. V. Quantum Dot Solar Cells. Semiconductor Nanocrystals as Light Harvesters. *J. Phys. Chem. C* **112,** 18737–18753 (2008).

154. Bonaccorso, F., Sun, Z., Hasan, T. & Ferrari, a. C. Graphene Photonics and Optoelectronics. **4,** 611–622 (2010).

155. Dean, C. R. *et al.* Boron nitride substrates for high-quality graphene electronics. *Nat. Nanotechnol.* **5,** 722–726 (2010).

156. Alharbi, F. *et al.* Abundant non-toxic materials for thin film solar cells: Alternative to conventional materials. *Renew. Energy* **36,** 2753–2758 (2011).

157. Gourmelon, E. *et al.* MS2 (M = W, Mo) photosensitive thin films for solar cells. *Sol. Energy Mater. Sol. Cells* **46,** 115–121 (1997).

158. Yin, Z. *et al.* Single-layer MoS2 phototransistors. *ACS Nano* **6,** 74–80 (2012).

159. Polman, A. & Atwater, H. a. Photonic design principles for ultrahigh-efficiency photovoltaics. *Nat. Mater.* **11,** 174–177 (2012).

160. He, Q., Wu, S., Yin, Z. & Zhang, H. Graphene-based electronic sensors. *Chem. Sci.* **3,** 1764 (2012).

161. Huang, X. *et al.* Graphene-based materials: Synthesis, characterization, properties, and applications. *Small* **7,** 1876–1902 (2011).

162. Li, H. *et al.* Fabrication of single- and multilayer MoS 2 film-based field-effect transistors for sensing NO at room temperature. *Small* **8,** 63–67 (2012).

163. He, Q. *et al.* Fabrication of flexible MoS2 thin-film transistor arrays for practical gas-sensing applications. *Small* **8,** 2994–2999 (2012).

164. Wu, S. *et al.* Electrochemically reduced single-layer MoS2 nanosheets: Characterization, properties, and sensing applications. *Small* **8,** 2264–2270 (2012).

165. Yan, Y., Xia, B., Xu, Z. & Wang, X. Recent development of molybdenum sulfides as advanced electrocatalysts for hydrogen evolution reaction. *ACS Catal.* **4,** 1693–1705 (2014).

166. Takasu, Y., Fujii, Y., Yasuda, K., Iwanaga, Y. & Matsuda, Y. Electrocatalytic properties of ultrafine platinum particles for hydrogen electrode reaction in an aqueous solution of sulfuric acid. *Electrochim. Acta* **34,** 453–458 (1989).

167. Jaramillo, T. F. *et al.* Identification of active edge sites for electrochemical H2 evolution from MoS2 nanocatalysts. *Science* **317,** 100–2 (2007).

168. Tributsch, H. & Bennett, J. C. Electrochemistry and photochemistry of MoS2 layer crystals. I. *J. Electroanal. Chem. Interfacial Electrochem.* **81,** 97–111 (1977).

169. Fujishima, A., Noguchi, Y., Honda, K. & Loo, B. H. PHOTOELECTROCHEMICAL STUDIES OF MoS//2 ELECTRODE BY ROTATING RING-DISK ELECTRODE TECHNIQUE. *Bull. Chem. Soc. Jpn.* **55,** 17–22 (1982).

170. Kiesewetter, T., Tomm, Y., Turrión, M. & Tributsch, H. Composite materials for photovoltaics: A realistic aim? *Sol. Energy Mater. Sol. Cells* **59,** 309–323 (1999).

171. Cao, L. Layer-Dependent Electrocatalysis of MoS 2 for Hydrogen Evolution. *Nano Lett.* 1–6 (2014).

172. Frame, F. A. & Osterloh, F. E. CdSe-MoS2: A quantum size-confined photocatalyst for hydrogen evolution from water under visible light. *J. Phys. Chem. C* **114,** 10628–10633 (2010).

173. Liu, Y., Yu, Y.-X. & Zhang, W. MoS 2 /CdS Heterojunction with High Photoelectrochemical Activity for H 2 Evolution Under Visible Light: The Role of MoS 2. *J. Phys. Chem. C* 130530103906008 (2013). doi:10.1021/jp4009652

174. Maitra, U. *et al.* Highly effective visible-light-induced H2 generation by single-layer 1T-MoS2 and a nanocomposite of few-layer 2H-MoS 2 with heavily nitrogenated graphene. *Angew. Chemie - Int. Ed.* **52,** 13057–13061 (2013).

175. Seger, B. *et al.* Hydrogen production using a molybdenum sulfide catalyst on a titanium-protected n +p-silicon photocathode. *Angew. Chemie - Int. Ed.* **51,** 9128–9131 (2012).

176. Structures, F. & Tenne, B. R. Doped and Heteroatom-Containing. (1995).

177. Hsu, W. K. *et al.* An Alternative Route to Molybdenum Disulfide Nanotubes. *J. Am. Chem. Soc.* **122,** 10155–10158 (2000).

178. Remskar, M. *et al.* Self-assembly of subnanometer-diameter single-wall MoS2 nanotubes. *Science* **292,** 479–81 (2001).

179. Legma, J. B., Vacquier, G. & Casalot, a. Chemical vapour transport of molybdenum and tungsten diselenides by various transport agents. *J. Cryst. Growth* **130,** 253–258 (1993).

180. Okada, M. *et al.* Direct Chemical Vapor Deposition Growth of WS2 Atomic Layers on Hexagonal Boron Nitride. *ACS Nano* 2–6 (2014). doi:10.1021/nn503093k

181. Zhang, X. *et al.* Phonon and Raman scattering of two-dimensional transition metal dichalcogenides from monolayer, multilayer to bulk material. **2,** 1–30 (2015).

182. Berkdemir, A. *et al.* Identification of individual and few layers of WS2 using Raman Spectroscopy. *Sci. Rep.* **3,** 1–8 (2013).

183. Brunauer, S., Emmett, P. H. & Teller, E. Adsorption of Gases in Multimolecular Layers. *J. Am. Chem. Soc.* **60,** 309–319 (1938).

184. Webb, P. A. & Orr, C. *Analytical methods in fine particle technology*. (Micromeritics Instrument Corp, 1997).

185. Deepak, F. L., Mayoral, A. & Yacaman, M. J. Faceted MoS2 nanotubes and nanoflowers. *Mater. Chem. Phys.* **118,** 392–397 (2009).

186. Cunningham, G. *et al.* Solvent exfoliation of transition metal dichalcogenides: Dispersibility of exfoliated nanosheets varies only weakly between compounds. *ACS Nano* **6,** 3468–3480 (2012).

187. Zhu, Y. *et al.* Carbon-Based Supercapacitors. **332,** 1537–1542 (2011).

188. Voiry, D. *et al.* Enhanced catalytic activity in strained chemically exfoliated WS_2 nanosheets for hydrogen evolution. *Nat. Mater.* **12,** 850–5 (2013).

189. Lukowski, M. a *et al.* Enhanced Hydrogen Evolution Catalysis from Chemically Exfoliated Metallic MoS2 Nanosheets. *J. Am. Chem. Soc.* 1–4 (2013). doi:10.1021/ja404523s

190. Wu, Z. *et al.* WS2 nanosheets as a highly efficient electrocatalyst for hydrogen evolution reaction. *Appl. Catal. B Environ.* **125,** 59–66 (2012).

191. Durand, R. Des i gn and performance water. **2,**

192. Greeley, J., Jaramillo, T. F., Bonde, J., Chorkendorff, I. B. & Nørskov, J. K. Computational high-throughput screening of electrocatalytic materials for hydrogen evolution. *Nat. Mater.* **5,** 909–913 (2006).

193. Eza, H. HYDROGEN OVERPOTENTIAL FOR TRANSITION. (1992).

194. Chen, Z. *et al.* CoreÀshell MoO 3 ÀMoS 2 Nanowires for Hydrogen Evolution : 4168–4175 (2011).

195. Vesborg, P. C. K., Seger, B. & Chorkendorff, I. Recent Development in Hydrogen Evolution Reaction Catalysts and Their Practical Implementation. *J. Phys. Chem. Lett.* 951–957 (2015). doi:10.1021/acs.jpclett.5b00306

196. Das, D. Hydrogen production by biological processes: a survey of literature. *Int. J. Hydrogen Energy* **26,** 13–28 (2001).

197. Hinnemann, B. *et al.* Biomimetic Hydrogen Evolution : MoS 2 Nanoparticles as Catalyst for Hydrogen Evolution. 5308–5309 (2005).

198. Nørskov, J. K., Bligaard, T., Rossmeisl, J. & Christensen, C. H. Towards the computational design of solid catalysts. *Nat. Chem.* **1,** 37–46 (2009).

199. Karunadasa, H. I. *et al.* A molecular MoS2 edge site mimic for catalytic hydrogen generation. *Science (80-.).* 849–853 (2012).

200. Weiss, K. & Phillips, J. Calculated specific surface energy of molybdenite (MoS_{2}). *Phys. Rev. B* **14,** 5392–5395 (1976).

201. Ambrosi, A., Sofer, Z. & Pumera, M. Lithium Intercalation Compound Dramatically Influences the Electrochemical Properties of Exfoliated MoS2. *Small* 1–8 (2014). doi:10.1002/smll.201400401

202. Chang, Y.-H. *et al.* Highly efficient electrocatalytic hydrogen production by MoS(x) grown on graphene-protected 3D Ni foams. *Adv. Mater.* **25,** 756–60 (2013).

203. Chen, D. *et al.* Double Transition-Metal Chalcogenide as a High-Performance Lithium-Ion Battery Anode Material. (2014).

204. Ge, P. *et al.* Hydrogen evolution across nano-Schottky junctions at carbon supported MoS2 catalysts in biphasic liquid systems. *Chem. Commun.* **48,** 6484 (2012).

205. Conway, B. E. & Tilak, B. V. Interfacial processes involving electrocatalytic evolution and oxidation of H2, and the role of chemisorbed H. *Electrochim. Acta* **47,** 3571–3594 (2002).

206. Kibler, L. a. Hydrogen electrocatalysis. *ChemPhysChem* **7,** 985–991 (2006).

207. Roger, P. The rate of electrocatalytic hydrogen evolution and the heat of adsorption of hydrigen. *Trans. Faraday Soc.* 1053–1063 (1957).

208. Kibsgaard, J., Chen, Z., Reinecke, B. N. & Jaramillo, T. F. Engineering the surface structure of MoS2 to preferentially expose active edge sites for electrocatalysis. *Nat. Mater.* **11,** 963–9 (2012).

209. Merki, D., Fierro, S., Vrubel, H. & Hu, X. Amorphous molybdenum sulfide films as catalysts for electrochemical hydrogen production in water. *Chem. Sci.* **2,** 1262–1267 (2011).

210. Zhou, Z.-Y., Tian, N., Huang, Z.-Z., Chen, D.-J. & Sun, S.-G. Nanoparticle catalysts with high energy surfaces and enhanced activity synthesized by electrochemical method. *Faraday Discuss.* **140,** 81–92; discussion 93–112 (2008).

211. Lukowski, M. a *et al.* Highly active hydrogen evolution catalysis from metallic WS2 nanosheets. *Energy Environ. Sci.* **7,** 2608–2613 (2014).

212. Wiesel, I. *et al.* Synthesis of WS2 and MoS2 fullerene-like nanoparticles from solid precursors. *Nano Res.* **2,** 416–424 (2009).

213. Tehrani, M., Luhrs, C. C., Al-Haik, M. S., Trevino, J. & Zea, H. Synthesis of WS2 nanostructures from the reaction of WO3 with CS2 and mechanical characterization of WS2 nanotube composites. *Nanotechnology* **22,** 285714 (2011).

214. Yu, Y. *et al.* Controlled scalable synthesis of uniform, high-quality monolayer and few-layer MoS2 films. *Sci. Rep.* **3,** 1866 (2013).

215. Wang, Y., Chen, W., Wang, B. & Zheng, Y. Ultrathin Ferroelectric Films: Growth, Characterization, Physics and Applications. *Materials (Basel).* **7,** 6377–6485 (2014).

216. Fu, Q. *et al.* Controllable synthesis of high quality monolayer WS 2 on a SiO 2 /Si substrate by chemical vapor deposition. *RSC Adv.* **5,** 15795–15799 (2015).

217. Murdock, A. T. *et al.* Controlling the orientation, edge geometry, and thickness of chemical vapor deposition graphene. *ACS Nano* **7,** 1351–1359 (2013).

218. Ueno, K. Epitaxial growth of transition metal dichalcogenides on cleaved faces of mica. *J. Vac. Sci. Technol. A Vacuum, Surfaces, Film.* **8,** 68 (1990).

219. Ma, L. *et al.* Epitaxial growth of large area single-crystalline few-layer MoS2 with high space charge mobility of 192 cm2 V−1 s−1. *Appl. Phys. Lett.* **105,** 72105 (2014).

220. Adachi, S. *Properties of semiconductor alloys: group-IV, III-V and II-VI semiconductors*. **28,** (John Wiley & Sons, 2009).

221. Tarrio, C. & Schnatterly, S. E. Interband transitions, plasmons, and dispersion in hexagonal boron nitride. *Phys. Rev. B* **40,** 7852–7859 (1989).

222. Gutiérrez, H. R. *et al.* Extraordinary Room-Temperature Photoluminescence in Triangular WS(2) Monolayers. *Nano Lett.* (2012). doi:10.1021/nl3026357

223. Duesberg, G. S. Heterojunctions in 2D semiconductors: A perfect match. *Nat. Mater.* **13,** 1075–1076 (2014).

224. Hansen, L. P. *et al.* Atomic-scale edge structures on industrial-style MoS 2 nanocatalysts. *Angew. Chemie - Int. Ed.* **50,** 10153–10156 (2011).

225. Merki, D. & Hu, X. Recent developments of molybdenum and tungsten sulfides as hydrogen evolution catalysts. *Energy Environ. Sci.* **4,** 3878 (2011).

226. Dumcenco, D. O., Kobayashi, H., Liu, Z., Huang, Y.-S. & Suenaga, K. Visualization and quantification of transition metal atomic mixing in Mo1-xWxS2 single layers. *Nat. Commun.* **4,** 1351 (2013).

227. Gong, Y. *et al.* Vertical and in-plane heterostructures from WS2/MoS2 monolayers. *Nat. Mater.* (2014). doi:10.1038/nmat4091

228. Duan, X. X. *et al.* Lateral epitaxial growth of two-dimensional layered semiconductor heterojunctions. *Nat. Nanotechnol.* **9,** 1024–1030 (2014).

229. Chen, Y. *et al.* Tunable band gap photoluminescence from atomically thin transition-metal dichalcogenide alloys. *ACS Nano* **7,** 4610–6 (2013).

230. Chen, Y. *et al.* Composition-dependent Raman modes of Mo(1-x)W(x)S2 monolayer alloys. *Nanoscale* **6,** 2833–9 (2014).

231. Lin, Z. *et al.* Facile synthesis of MoS2 and MoxW1-xS2 triangular monolayers. *APL Mater.* **2,** 092804 (2014).

232. Dumcenco, D. O., Chen, K. Y., Wang, Y. P., Huang, Y. S. & Tiong, K. K. Raman study of 2H-Mo1−xWxS2 layered mixed crystals. *J. Alloys Compd.* **506,** 940–943 (2010).

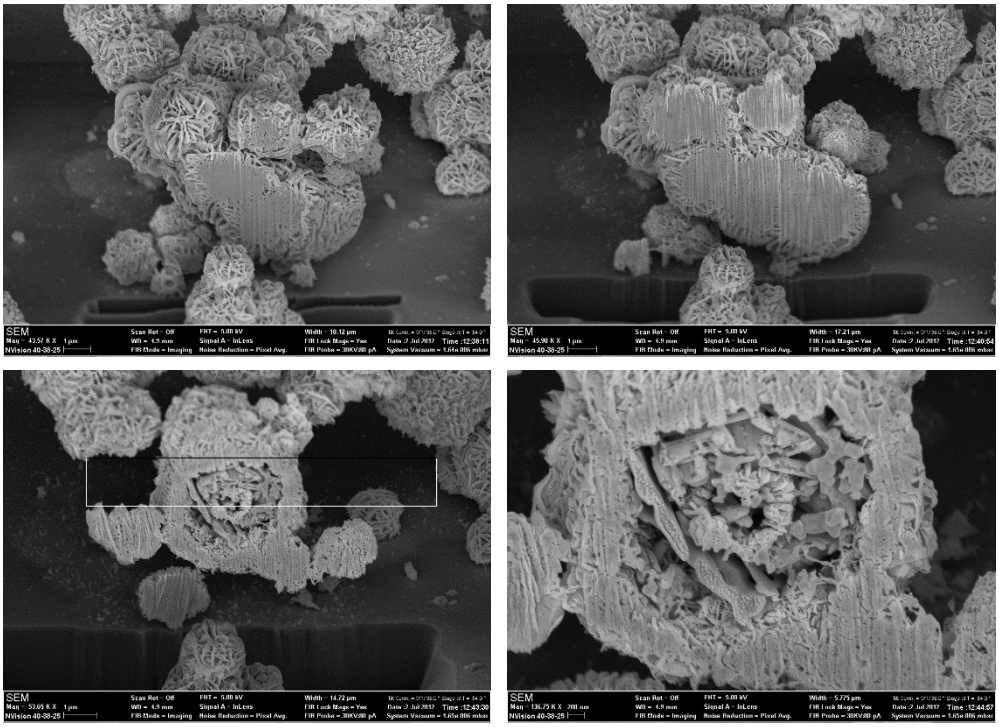
233. Liu, H., Antwi, K., Chua, S. & Chi, D. Vapor-phase growth and characterization of Mo 1− x W x S 2 (0≤ x≤ 1) atomic layers on 2-inch sapphire substrates. *Nanoscale* **6,** 624–9 (2014).

234. Lindahl, a. O. *et al.* The electron affinity of tungsten. *Eur. Phys. J. D* **60,** 219–222 (2010).

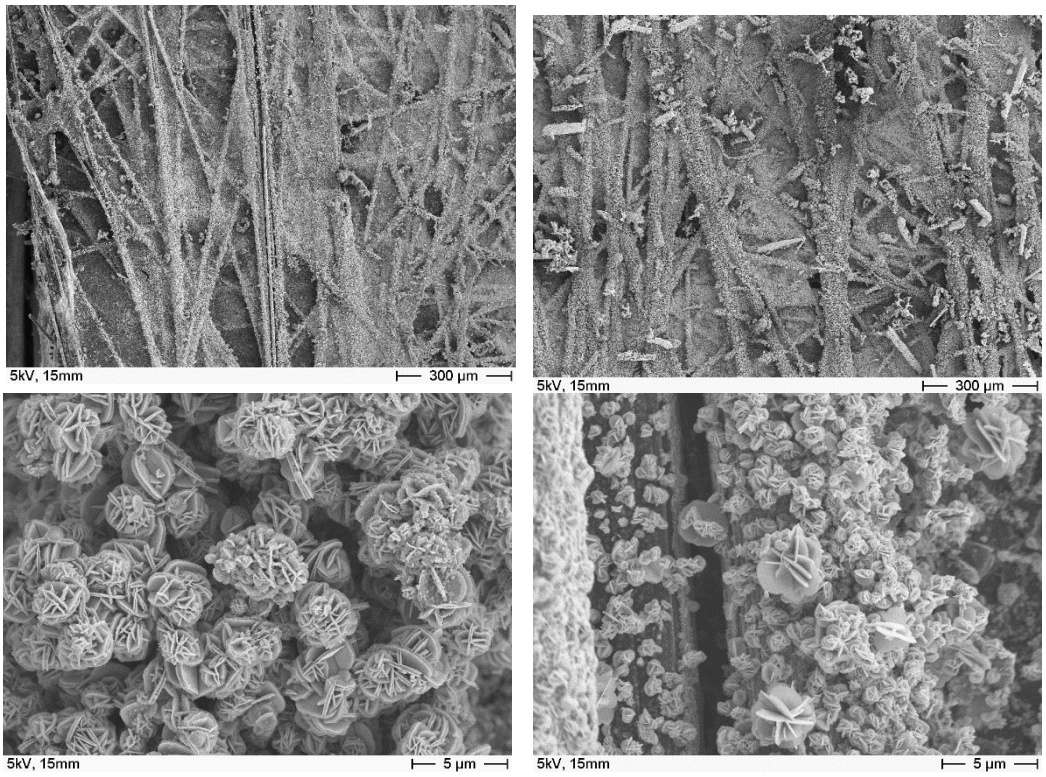
235. Zhou, W. *et al.* Three-Dimensional Hierarchical Frameworks Based on MoS 2 Nanosheets Self-Assembled on Graphene Oxide for E ffi cient Electrocatalytic Hydrogen Evolution. 2–8 (2014).

Appendix

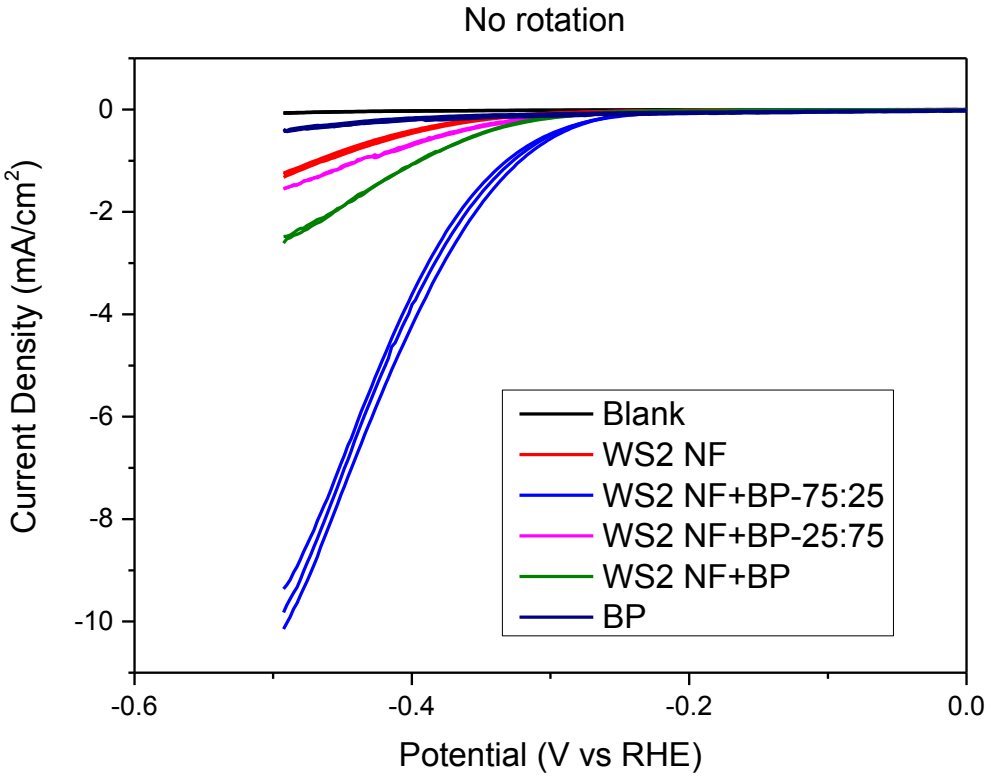
Dissection of nanoflowers using FIB

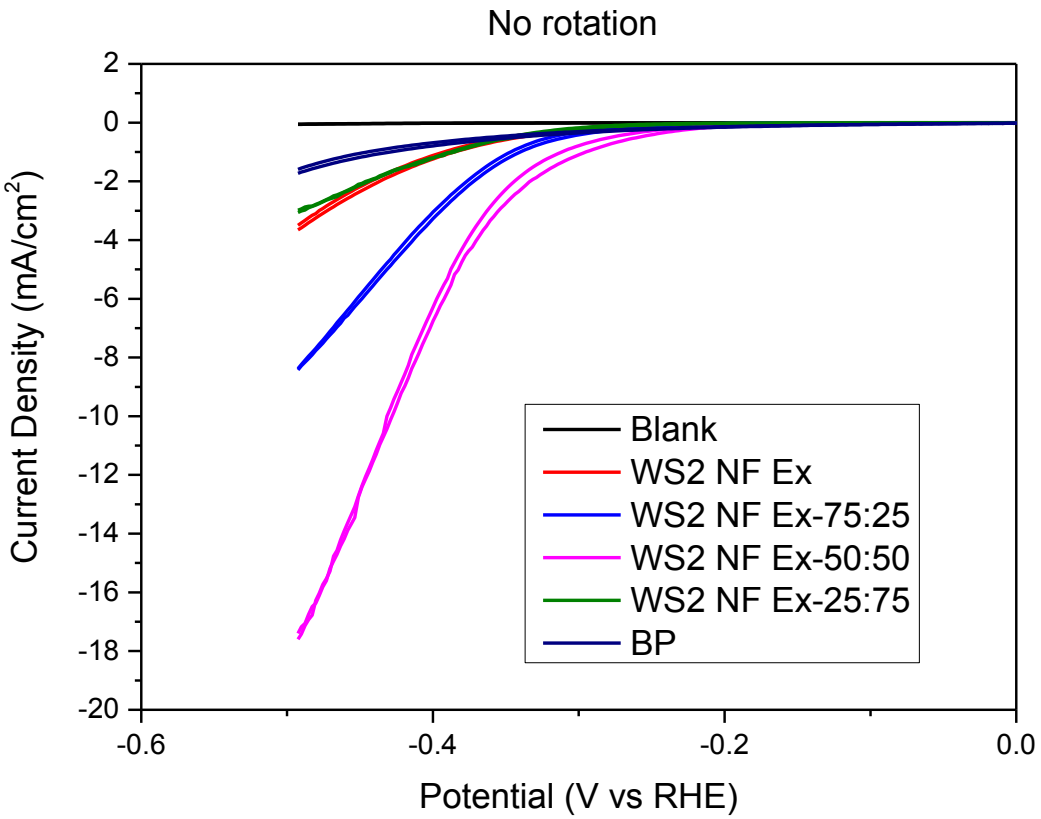


Growth of nanoflowers on carbon paper

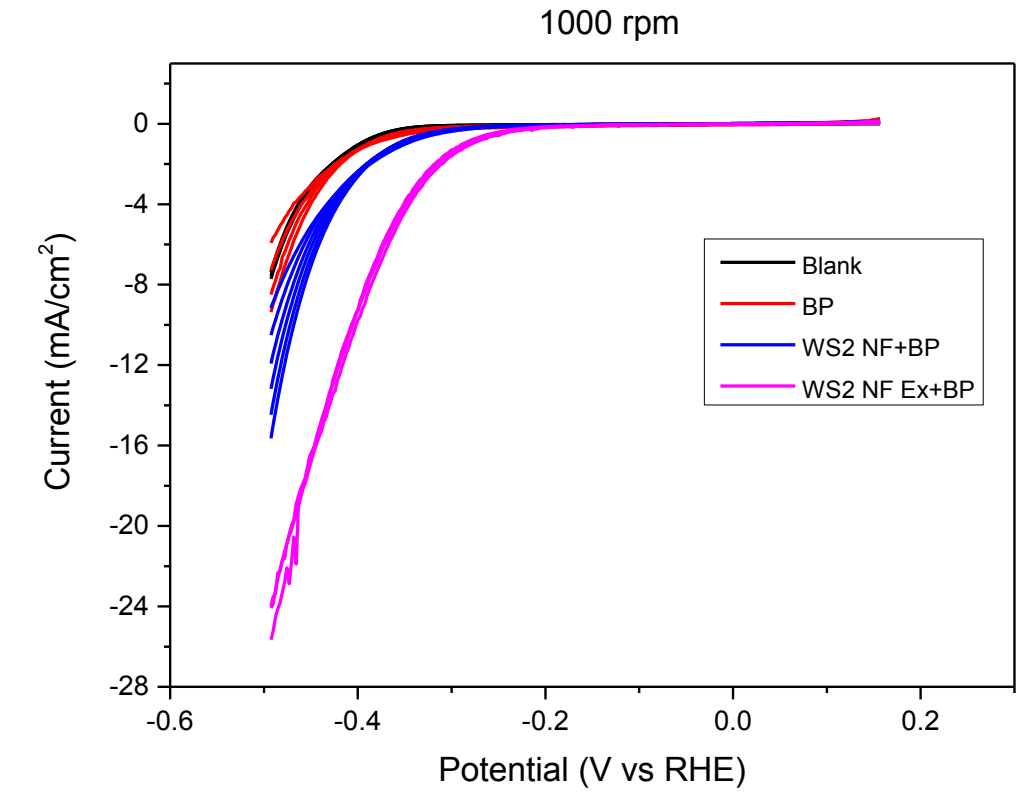


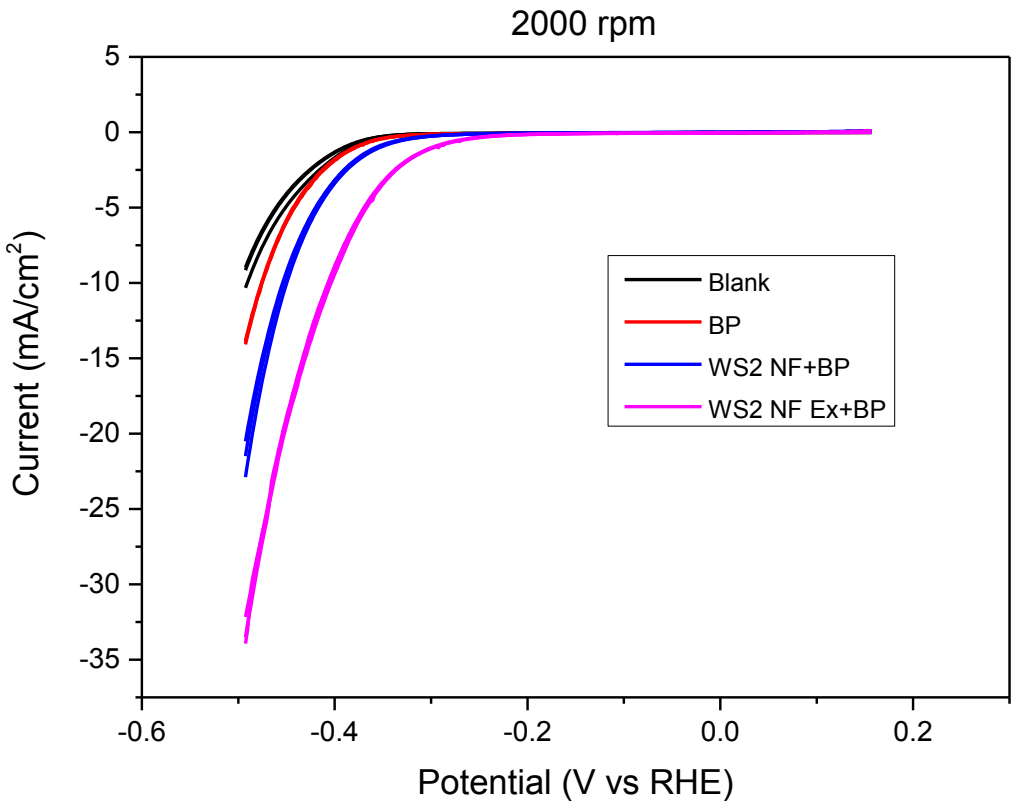
HER activity using different proportions of catalysts+BP





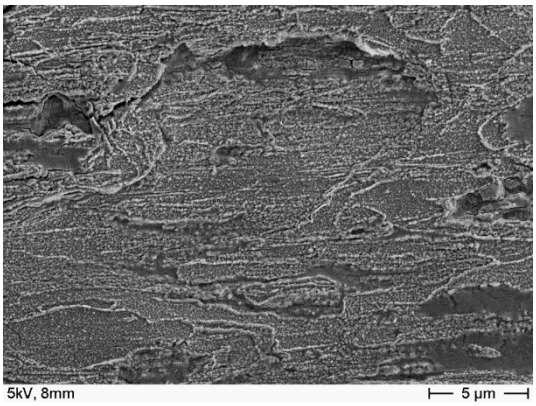
HER activity using rotation of electrode hosting catalysts+BP

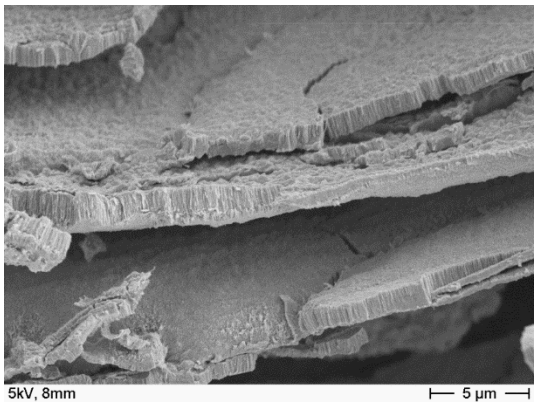


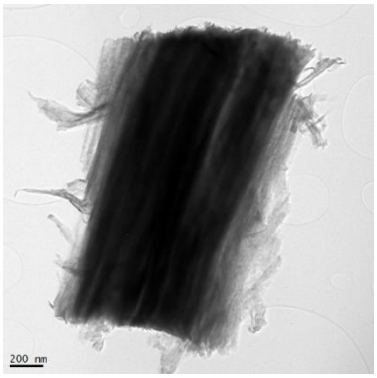


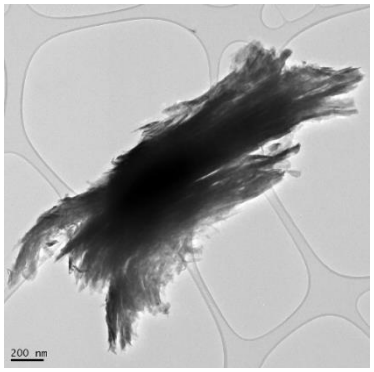
Sulphurisation of metal foils

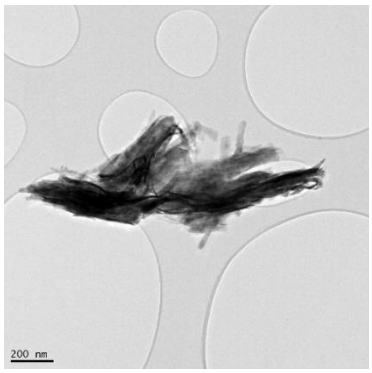
Temperature- 800 ^{o}C , Sulfur–40mmol
Time- 10 min, TEM-scrapped, 1hr bath
Cooling- controlled cooling
Ar flow- 100 sccm

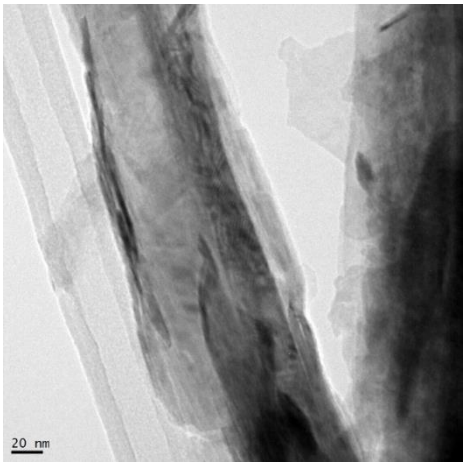


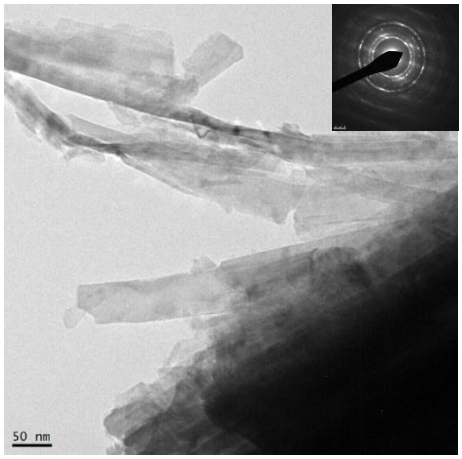


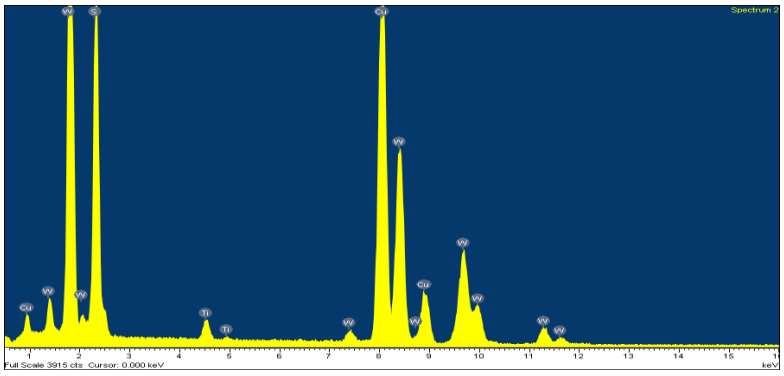






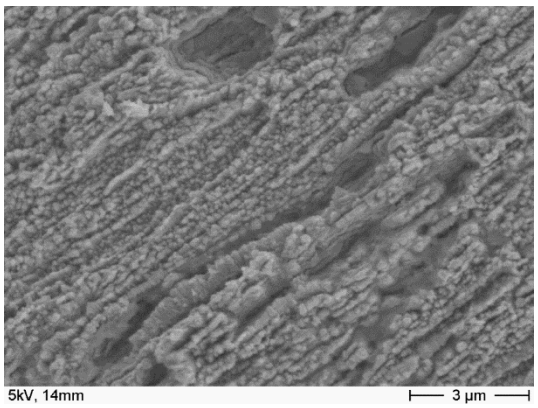


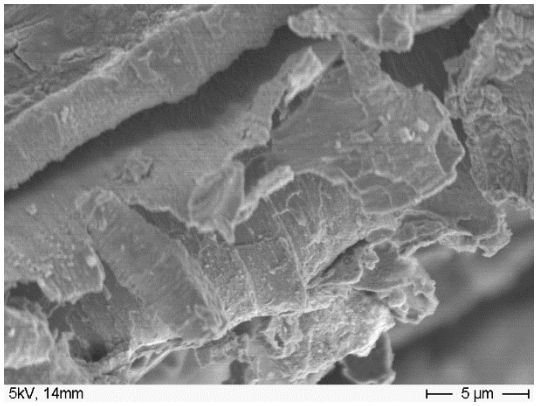


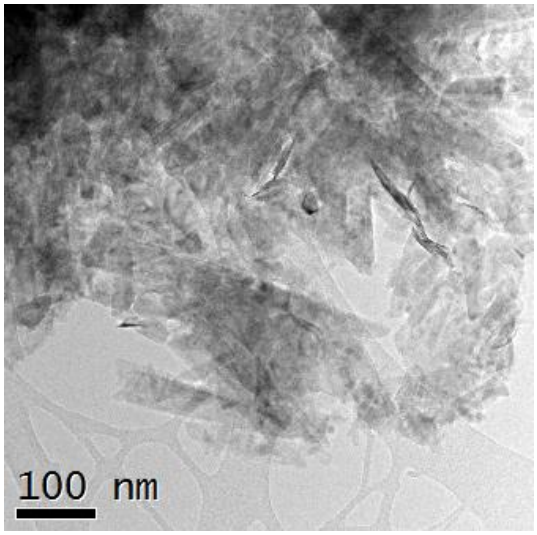


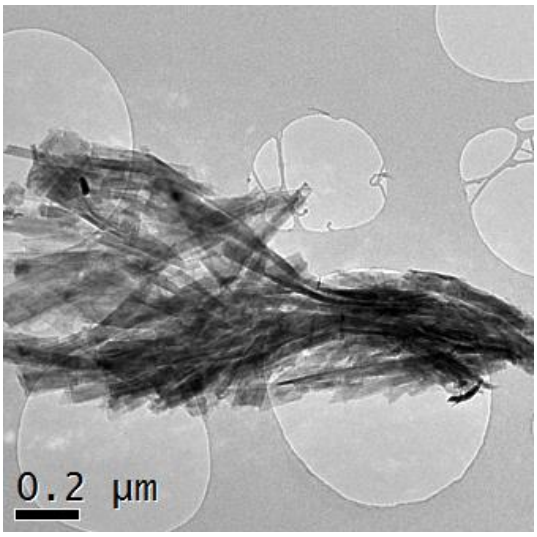
Element	Weight%	Atomic%
C K	0.41	2.71
S K	13.00	32.62
Ti K	1.00	1.67
Cu K	30.86	39.06
W L	54.74	23.94

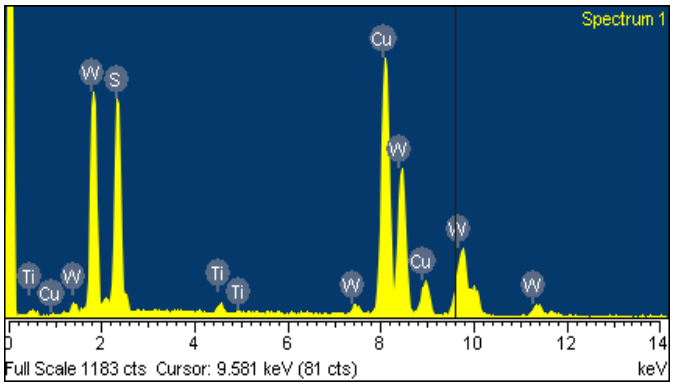
Temperature- 700°C , Sulfur–40mmol
Time- 1 hour, TEM- 1hr bath in ethanol
Cooling- controlled cooling
Ar flow- 100 sccm





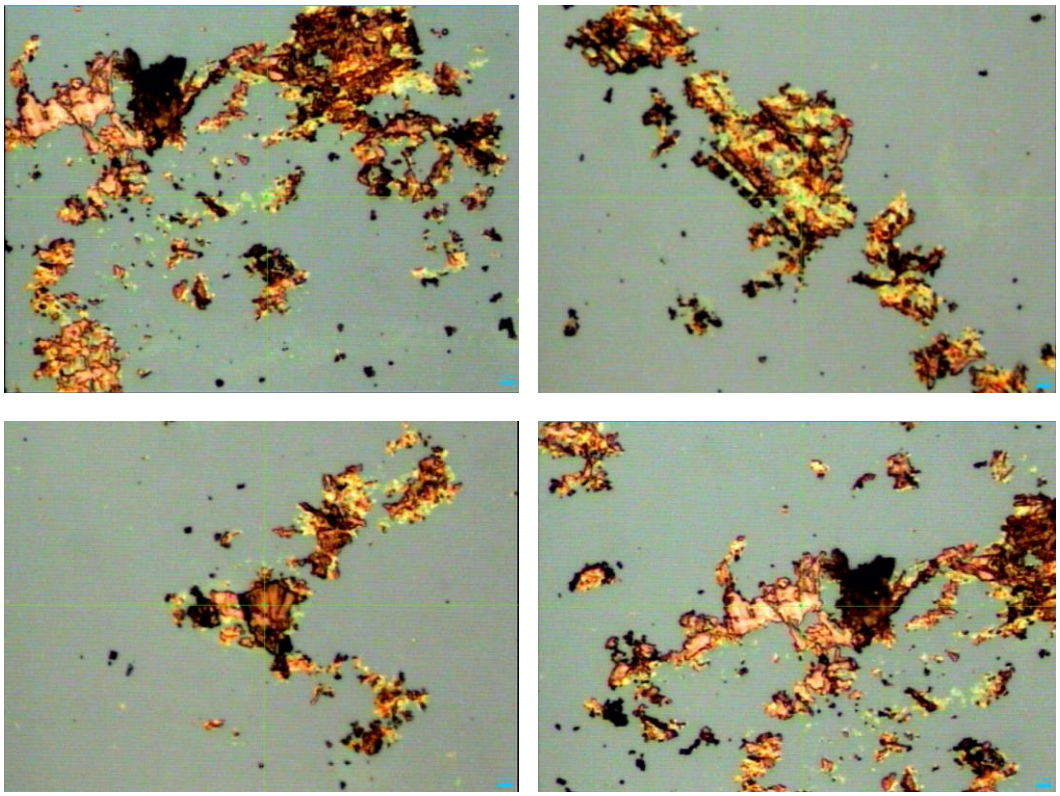


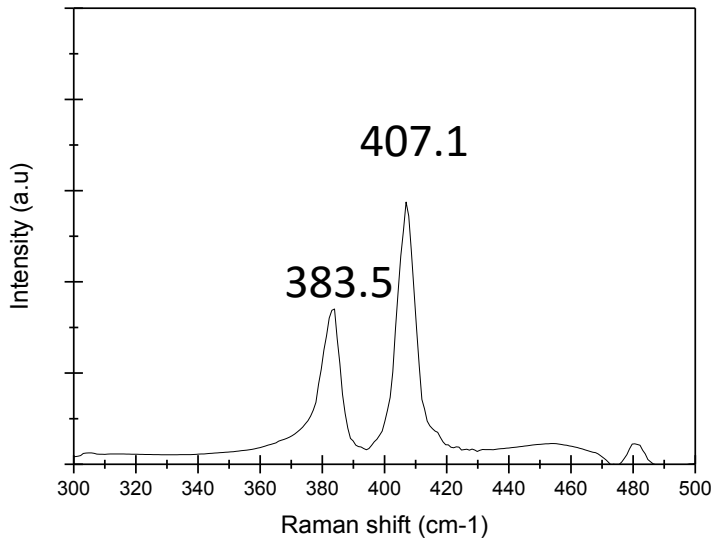




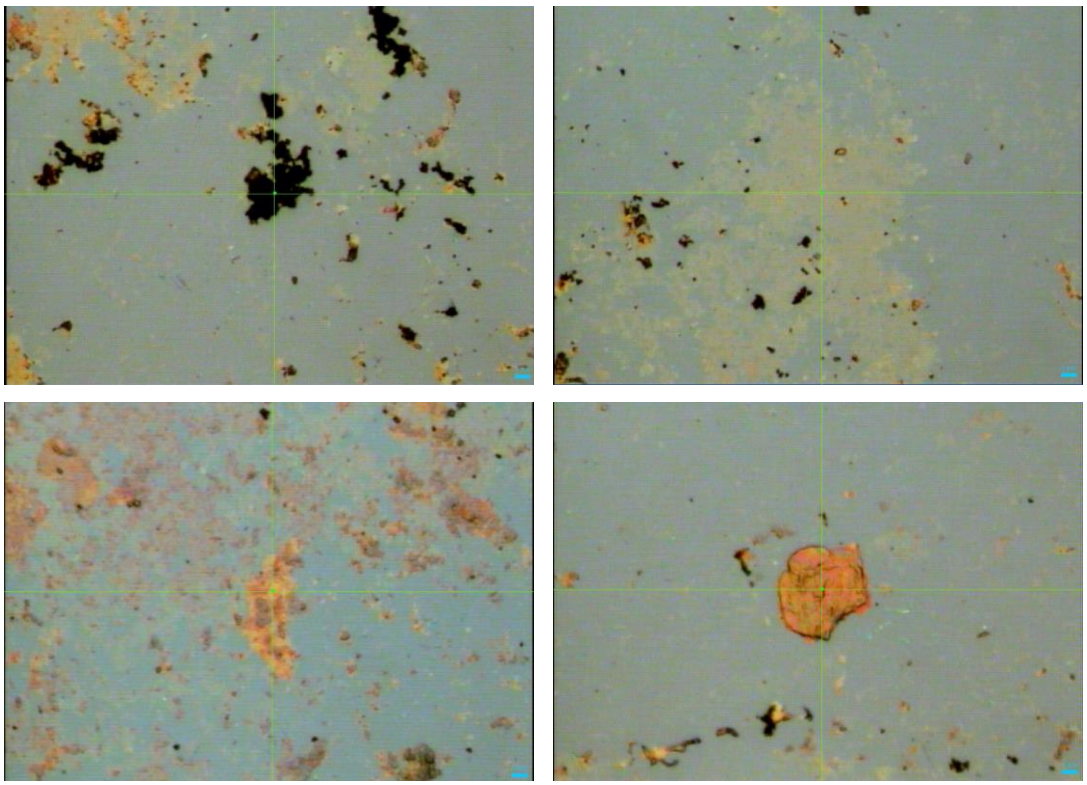
Element	Weight %	Atomic %
S K	16.22	39.18
Ti K	1.01	1.64
Cu K	30.49	37.16
W L	52.27	22.02

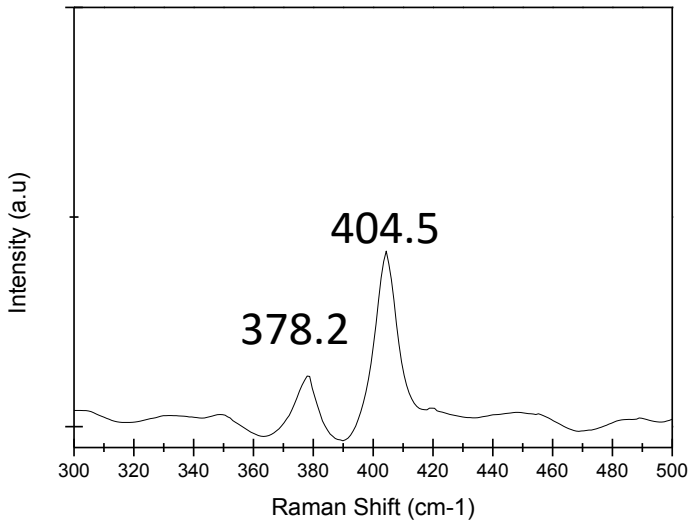
Exfoliation using PMMA





Exfoliation using scotch tape

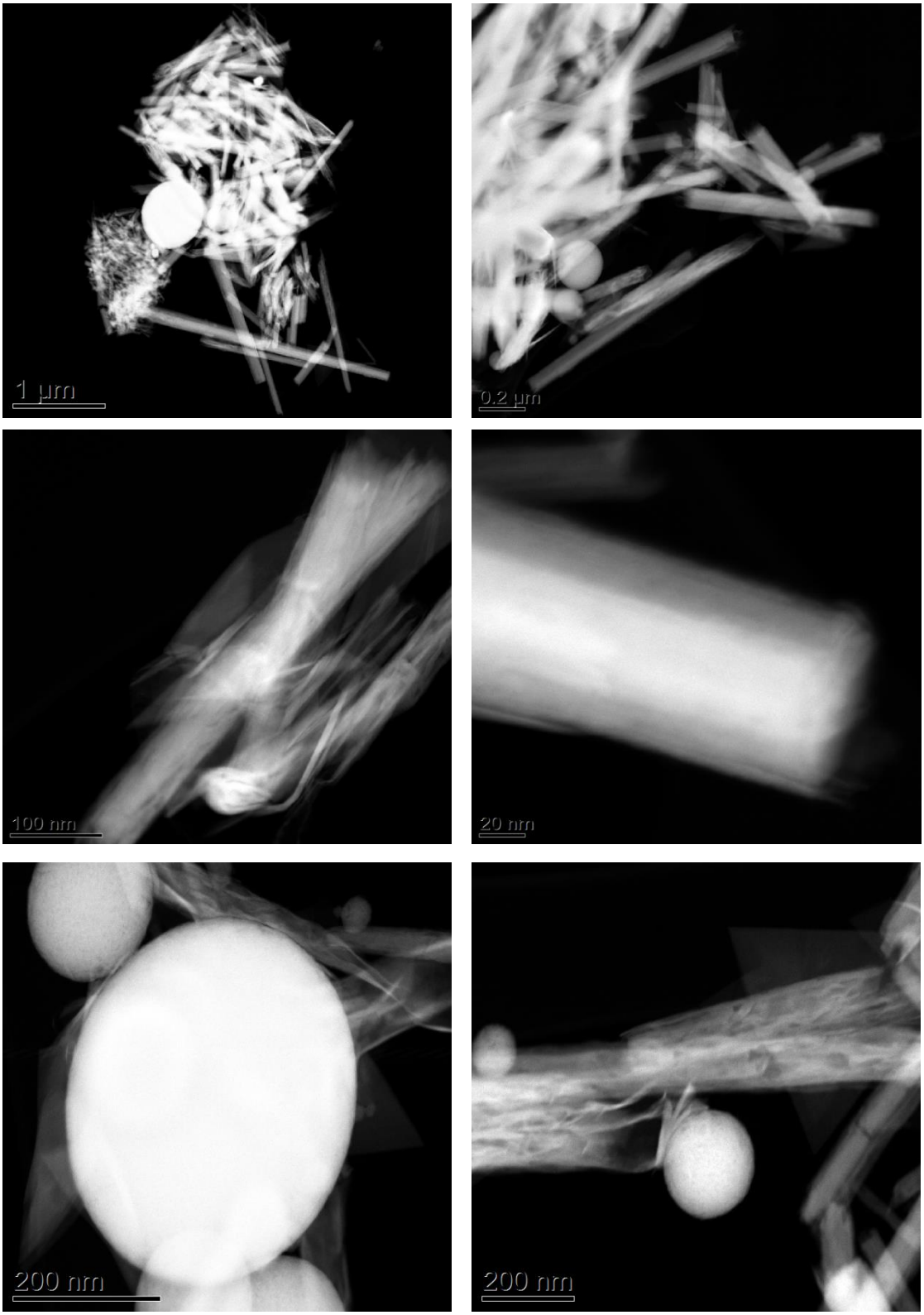


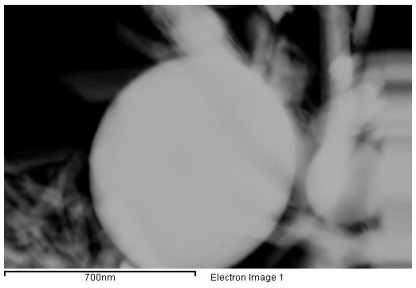


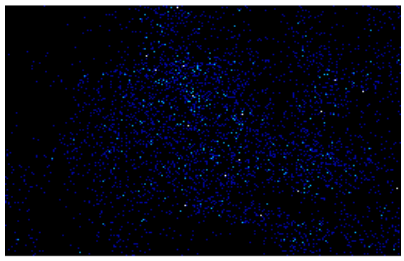
Sulphurisation of metal oxide templates

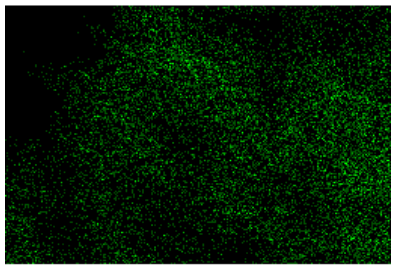
Single stage furnace

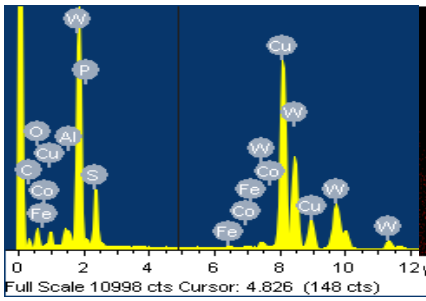
- Temperature (F2) – 550 °C
- Time period – 30 min
- Amount of sulphur – 1 gram
- Flow rate – 100 sccm Argon

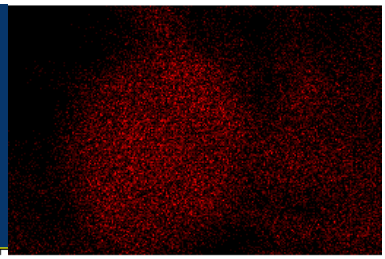




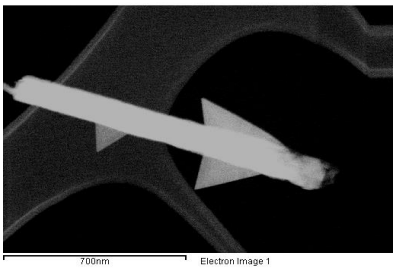


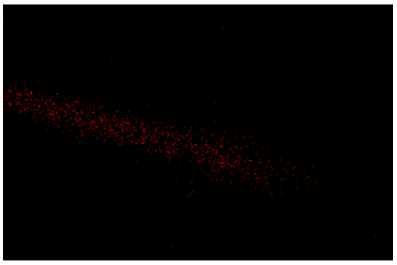


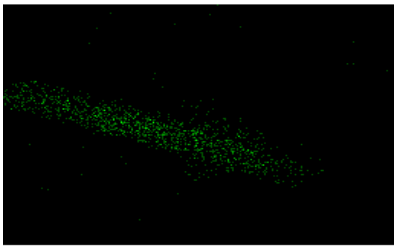


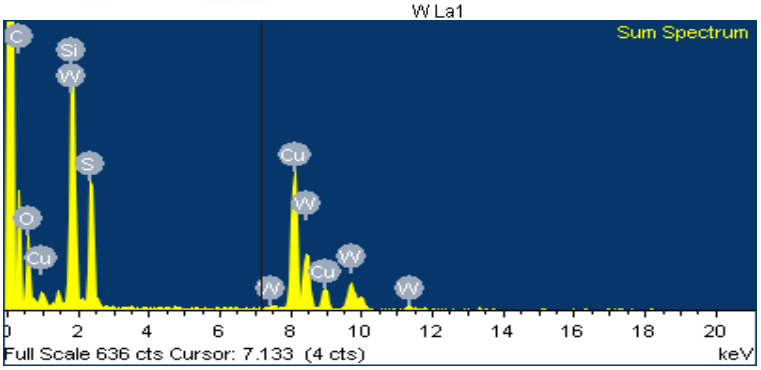


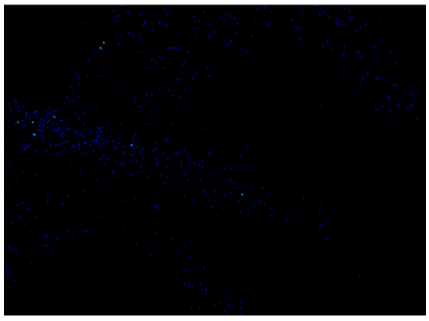
Element	Weight%	Atomic%
O K	5.07	21.89
S K	4.75	10.24
W L	56.58	21.26







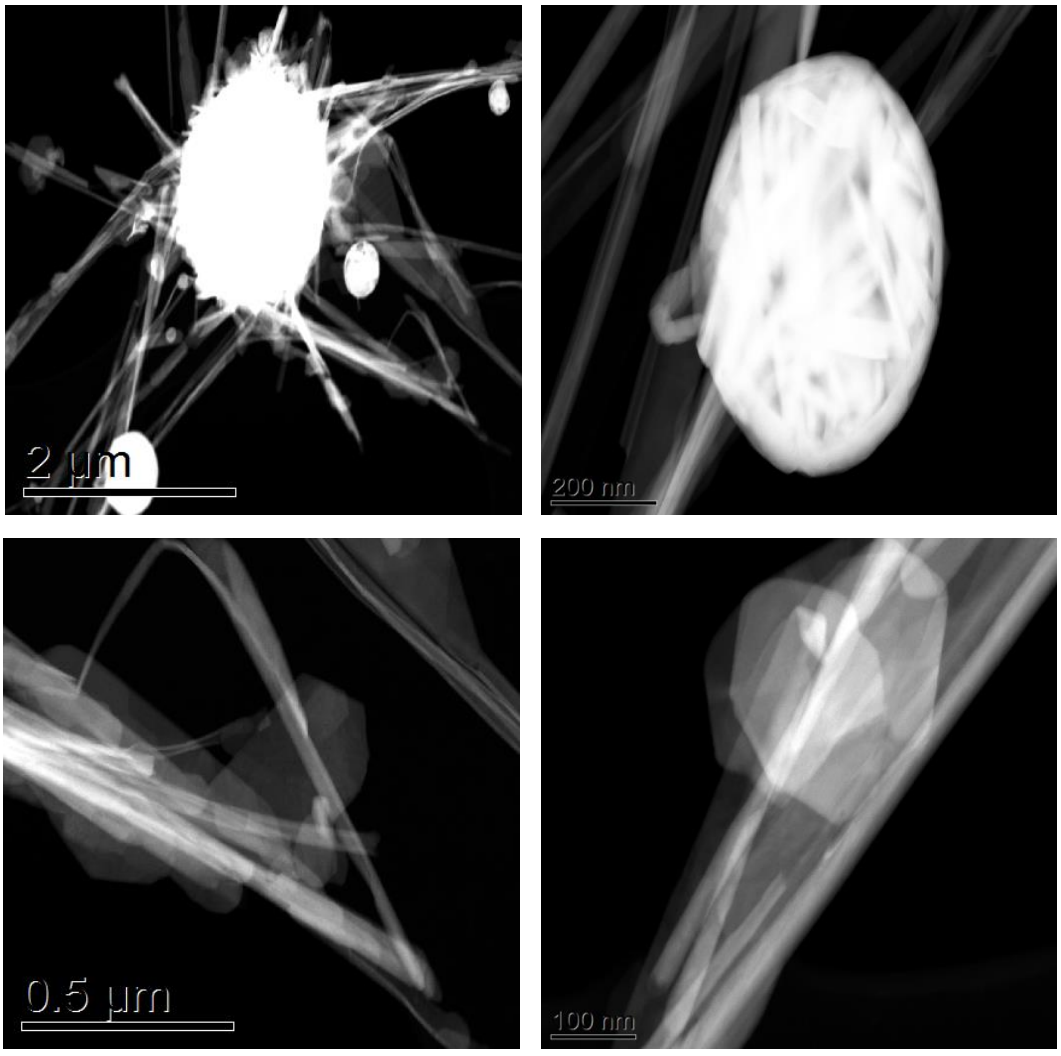


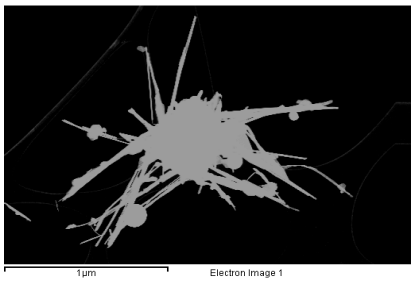


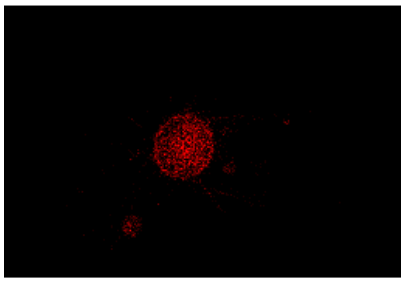
Element	Weight%	Atomic%
O K	8.11	14.73
S K	9.80	8.89
W L	31.01	4.90

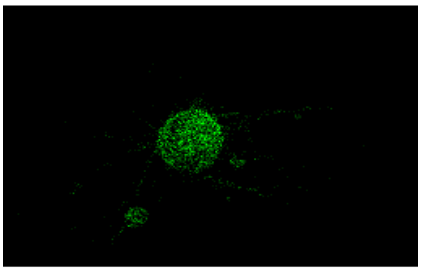
Two stage furnace

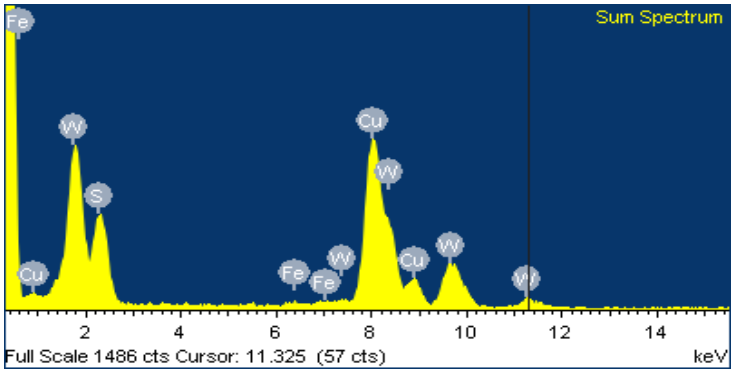
- Temperature (F2) – 850 ^{o}C
- Time period – 30 min
- Amount of sulphur – 1 gram
- Temperature of sulphur (F1)-150 ^{o}C
- Flow rate – 100 sccm Argon



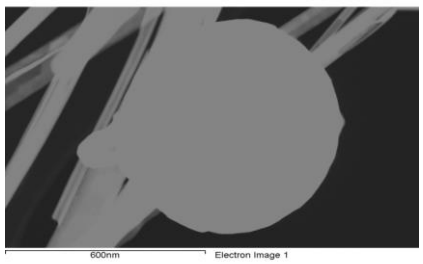


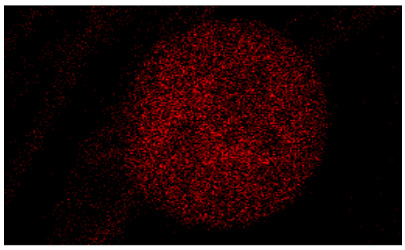


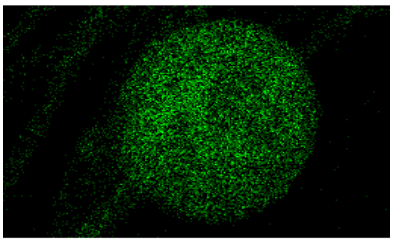


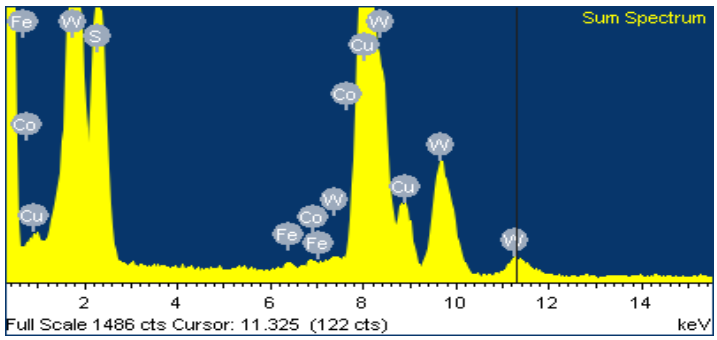


Element	Weight%	Atomic%
S K	14.65	33.45
W M	42.26	16.82





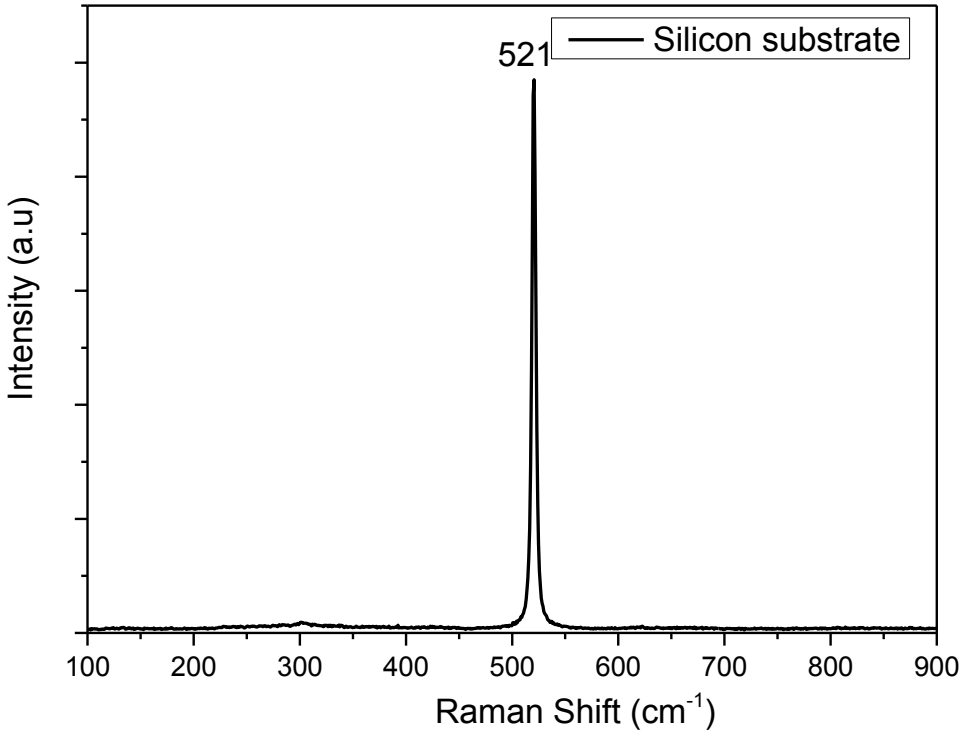




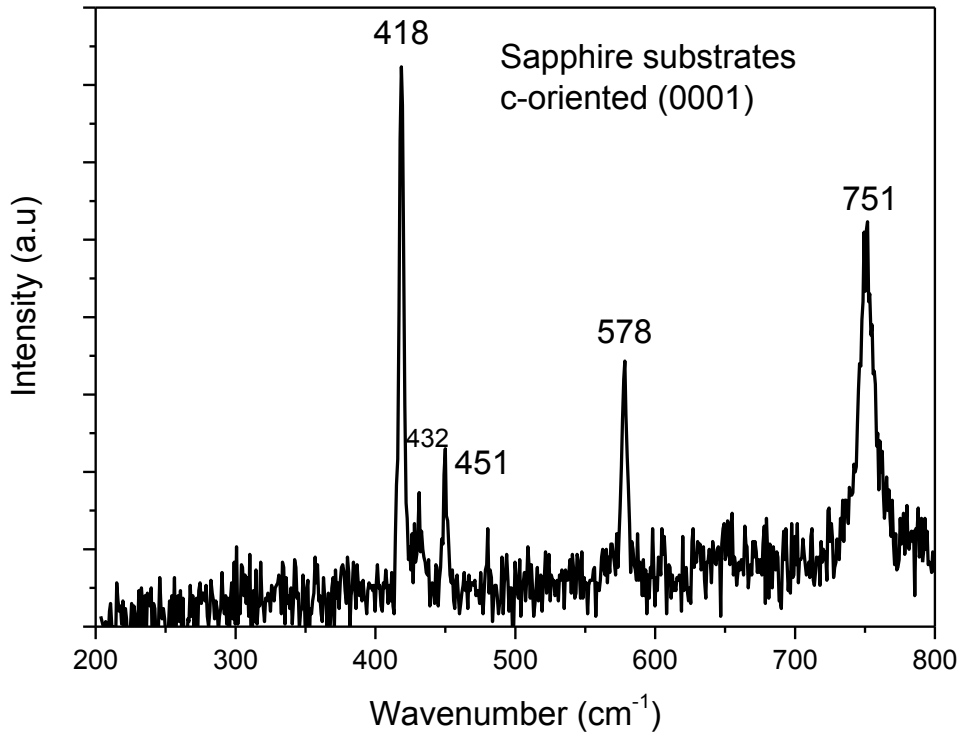
Element	Weight%	Atomic%
S K	16.66	37.62
W M	43.90	17.29

Raman spectroscopy of blank substrates and bulk powders

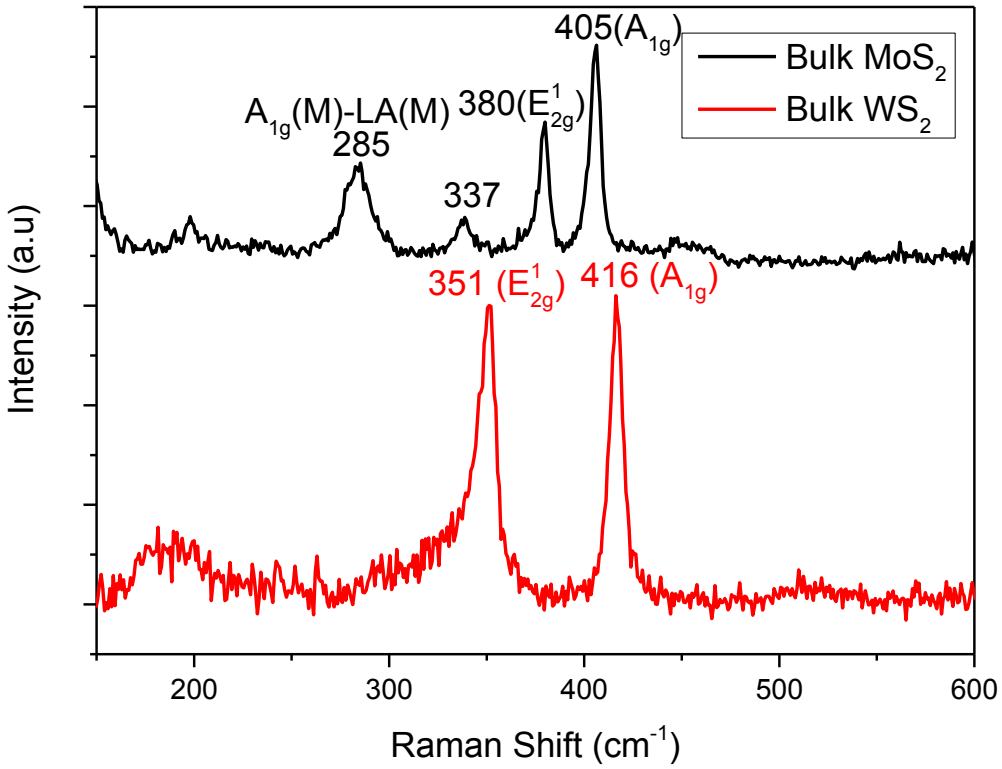
Silicon



Sapphire c-plane oriented



Bulk powder


405(A1g)
Bulk MoS2
Bulk WS2
A1g(M)-LA(M)
285
380(E12g)
337
351 (E12g)
416 (A1g)
Intensity (a.u)
200
300
400
500
600
Raman Shift (cm-1)